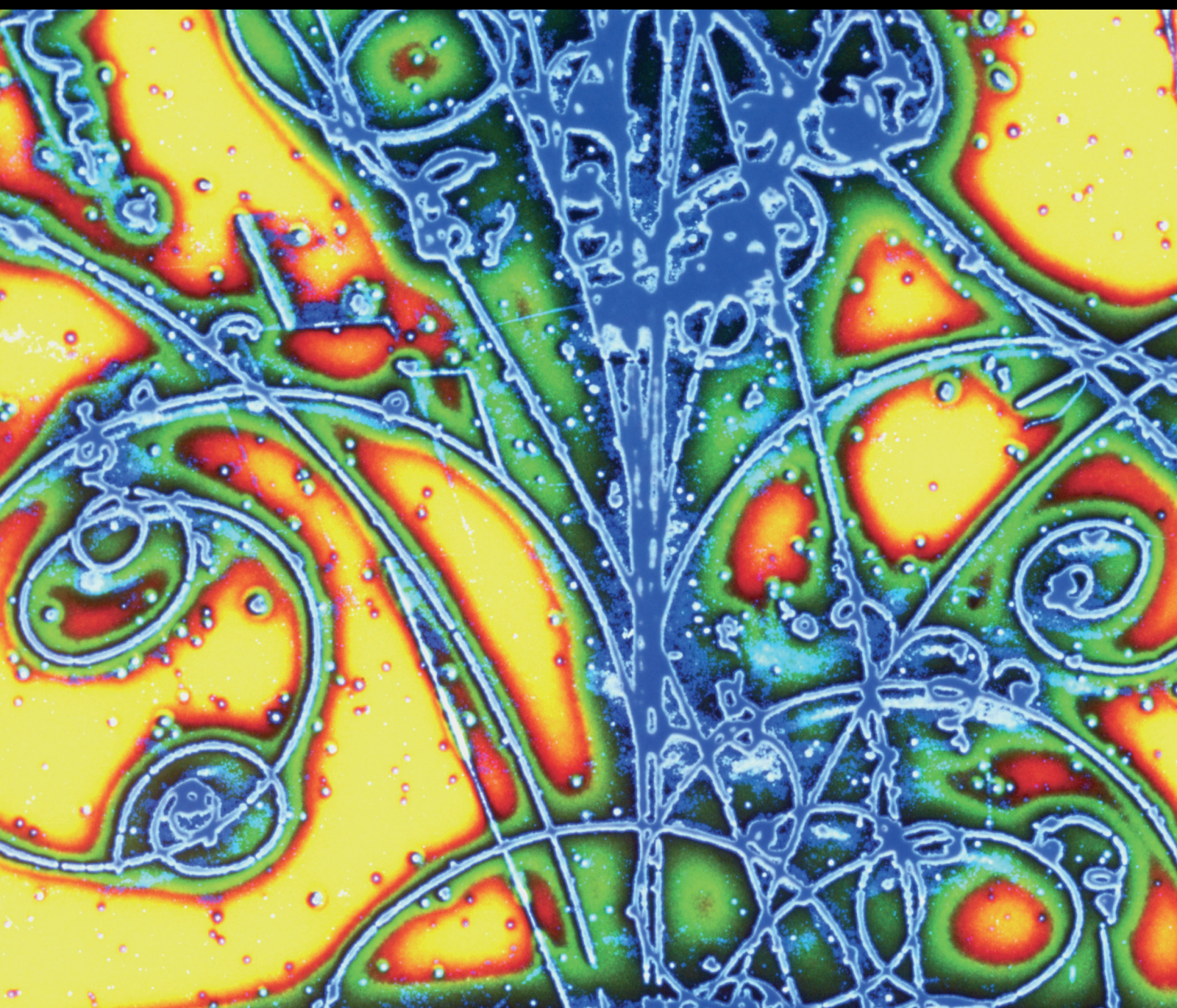


Advances in High Energy Physics

Physics at a Fixed-Target Experiment Using the LHC Beams

Guest Editors: Jean-Philippe Lansberg, Gianluca Cavoto, Cynthia Hadjidakis, Jibo He, Cédric Lorcé, and Barbara Trzeciak





Physics at a Fixed-Target Experiment Using the LHC Beams

Advances in High Energy Physics

Physics at a Fixed-Target Experiment Using the LHC Beams

Guest Editors: Jean-Philippe Lansberg, Gianluca Cavoto, Cynthia Hadjidakis, Jibo He, Cédric Lorcé, and Barbara Trzeciak



Copyright © 2015 Hindawi Publishing Corporation. All rights reserved.

This is a special issue published in “Advances in High Energy Physics.” All articles are open access articles distributed under the Creative Commons Attribution License, which permits unrestricted use, distribution, and reproduction in any medium, provided the original work is properly cited.

Editorial Board

Luis A. Anchordoqui, USA
T. Asselmeyer-Maluga, Germany
Marco Battaglia, Switzerland
Botio Betev, Switzerland
Emil Bjerrum-Bohr, Denmark
Rong-Gen Cai, China
Duncan L. Carlsmith, USA
Ashot Chilingarian, Armenia
Shi-Hai Dong, Mexico
Edmond C. Dukes, USA
Amir H. Fatollahi, Iran
Frank Filthaut, Netherlands
Chao-Qiang Geng, Taiwan

Maria Giller, Poland
Xiaochun He, USA
Filipe R. Joaquim, Portugal
Kyung K. Joo, Korea
Michal Kreps, UK
Ming Liu, USA
Enrico Lunghi, USA
Piero Nicolini, Germany
Seog H. Oh, USA
Sergio Palomares-Ruiz, Spain
Anastasios Petkou, Greece
Alexey A. Petrov, USA
Thomas Rossler, Sweden

Juan José Sanz-Cillero, Spain
Reinhard Schlickeiser, Germany
Sally Seidel, USA
George Siopsis, USA
Luca Stanco, Italy
Satyendra Thoudam, Netherlands
Smarajit Triambak, South Africa
Elias C. Vagenas, Kuwait
Nikos Varelas, USA
Kadayam S. Viswanathan, Canada
Yau W. Wah, USA

Contents

Physics at a Fixed-Target Experiment Using the LHC Beams, Jean-Philippe Lansberg, Gianluca Cavoto, Cynthia Hadjidakis, Jibo He, Cédric Lorcé, and Barbara Trzeciak
Volume 2015, Article ID 319654, 2 pages

Next-to-Leading Order Differential Cross Sections for J/ψ , $\psi(2S)$, and Υ Production in Proton-Proton Collisions at a Fixed-Target Experiment Using the LHC Beams, Yu Feng and Jian-Xiong Wang
Volume 2015, Article ID 726393, 7 pages

The Gluon Sivers Distribution: Status and Future Prospects, Daniël Boer, Cédric Lorcé, Cristian Pisano, and Jian Zhou
Volume 2015, Article ID 371396, 10 pages

Studies of Backward Particle Production with a Fixed-Target Experiment Using the LHC Beams, Federico Alberto Ceccopieri
Volume 2015, Article ID 652062, 9 pages

Bremsstrahlung from Relativistic Heavy Ions in a Fixed Target Experiment at the LHC, Rune E. Mikkelsen, Allan H. Sørensen, and Ulrik I. Uggerhøj
Volume 2015, Article ID 625473, 4 pages

Antishadowing Effect on Charmonium Production at a Fixed-Target Experiment Using LHC Beams, Kai Zhou, Zhengyu Chen, and Pengfei Zhuang
Volume 2015, Article ID 439689, 8 pages

Quarkonium Production and Proposal of the New Experiments on Fixed Target at the LHC, A. B. Kurepin and N. S. Topilskaya
Volume 2015, Article ID 760840, 13 pages


Quarkonium Suppression from Coherent Energy Loss in Fixed-Target Experiments Using LHC Beams, François Arleo and Stéphane Peigné
Volume 2015, Article ID 961951, 6 pages

Transverse Single-Spin Asymmetries in Proton-Proton Collisions at the AFTER@LHC Experiment in a TMD Factorisation Scheme, M. Anselmino, U. D'Alesio, and S. Melis
Volume 2015, Article ID 475040, 12 pages

Transverse Single-Spin Asymmetries in Proton-Proton Collisions at the AFTER@LHC Experiment, K. Kanazawa, Y. Koike, A. Metz, and D. Pitonyak
Volume 2015, Article ID 257934, 9 pages

Feasibility Studies for Quarkonium Production at a Fixed-Target Experiment Using the LHC Proton and Lead Beams (AFTER@LHC), L. Massacrier, B. Trzeciak, F. Fleuret, C. Hadjidakis, D. Kikola, J. P. Lansberg, and H.-S. Shao
Volume 2015, Article ID 986348, 15 pages

Gluon Shadowing Effects on J/ψ and Υ Production in $p + \text{Pb}$ Collisions at $\sqrt{s_{NN}} = 115 \text{ GeV}$ and $\text{Pb} + p$ Collisions at $\sqrt{s_{NN}} = 72 \text{ GeV}$ at AFTER@LHC, R. Vogt
Volume 2015, Article ID 492302, 10 pages



Prospects for Open Heavy Flavor Measurements in Heavy Ion and $p + A$ Collisions in a Fixed-Target Experiment at the LHC, Daniel Kikoła
Volume 2015, Article ID 783134, 8 pages

A Gas Target Internal to the LHC for the Study of pp Single-Spin Asymmetries and Heavy Ion Collisions, Colin Barschel, Paolo Lenisa, Alexander Nass, and Erhard Steffens
Volume 2015, Article ID 463141, 6 pages

A Review of the Intrinsic Heavy Quark Content of the Nucleon, S. J. Brodsky, A. Kusina, F. Lyonnet, I. Schienbein, H. Spiesberger, and R. Vogt
Volume 2015, Article ID 231547, 12 pages

Near-Threshold Production of W^\pm , Z^0 , and H^0 at a Fixed-Target Experiment at the Future Ultrahigh-Energy Proton Colliders, J. P. Lansberg, R. Mikkelsen, and U. I. Uggerhøj
Volume 2015, Article ID 249167, 7 pages

Editorial

Physics at a Fixed-Target Experiment Using the LHC Beams

**Jean-Philippe Lansberg,¹ Gianluca Cavoto,² Cynthia Hadjidakis,¹ Jibo He,³
Cédric Lorcé,⁴ and Barbara Trzeciak⁵**

¹IPNO, Université Paris-Sud, CNRS/IN2P3, 91406 Orsay, France

²INFN Sezione di Roma, Piazzale Aldo Moro 2, 00185 Roma, Italy

³PH Department, CERN, 1211 Geneva 23, Switzerland

⁴CPHT, École Polytechnique, 91128 Palaiseau, France

⁵Faculty of Nuclear Sciences and Physical Engineering, Czech Technical University in Prague, Brehova 7, 115 19 Prague 1, Czech Republic

Correspondence should be addressed to Jean-Philippe Lansberg; jean-philippe.lansberg@in2p3.fr

Received 9 September 2015; Accepted 9 September 2015

Copyright © 2015 Jean-Philippe Lansberg et al. This is an open access article distributed under the Creative Commons Attribution License, which permits unrestricted use, distribution, and reproduction in any medium, provided the original work is properly cited. The publication of this article was funded by SCOAP³.

The collisions of the high-energy LHC beams with fixed targets, including polarized and nuclei targets, can greatly expand the range of fundamental physics phenomena accessible at CERN. The fixed-target mode allows for an intensive study of rare processes, novel spin-correlations, high x_F dynamics, diffractive physics, and nuclear phenomena as well as the novel spectroscopy of hadrons carrying multiple heavy quarks.

The extraordinary energy of the LHC beams would make such a LHC fixed-target physics program, referred to as AFTER@LHC thereafter, unique. We believe that such a facility is of much interest to a wide range of hadron, nuclear, and particle physicists and we are glad that this volume gathers fifteen state-of-the-art contributions supporting such an endeavour.

The contributions to this volume are of different kinds, ranging from theoretical articles reviewing the theory of some effects to be studied with such a facility to experimental contributions detailing the techniques and the performances of specific targets and feasibility studies of key measurements. We briefly outline them below topic by topic.

On the theory side, the volume gathers two very important reviews. The first one entitled “A Review of the Intrinsic Heavy Quark Content of the Nucleon” by S. J. Brodsky et al. summarizes the current knowledge on the charm content in the proton. This is a hot topic which has direct implications, for instance, with neutrino astrophysics. The

second theory review by D. Boer et al. entitled “The Gluon Sivers Distribution: Status and Future Prospects” focuses on the gluon Sivers effect which encapsulates the connection between the gluon angular momentum and the proton spin.

The nucleon-spin-structure topic is complemented by two theoretical predictions for the transverse single-spin asymmetries for pions, jets, and photons, one by M. Anselmino et al. entitled “Transverse Single-Spin Asymmetries in Proton-Proton Collisions at the AFTER@LHC Experiment in a TMD Factorisation Scheme” and the other by K. Kanazawa et al. entitled “Transverse Single-Spin Asymmetries in Proton-Proton Collisions at the AFTER@LHC Experiment.”

This sets the context for measurements using polarised gas targets which is precisely the scope of the contribution of C. Barschel et al. entitled “A Gas Target Internal to the LHC for the Study of pp Single-Spin Asymmetries and Heavy Ion Collisions” which paves the way for a polarised internal gas target in the LHC complex. Such a proposal follows from the successful target system of the HERMES experiment at DESY. In this contribution, the luminosities expected for unpolarised and polarised hydrogen and nuclear gas targets are estimated.

Continuing with contributions dealing with the hadron structure and the perturbative regime of Quantum Chromodynamics, the contribution by F. A. Ceccopieri entitled “Studies of Backward Particle Production with a Fixed-Target

Experiment Using the LHC Beams” explores the possibility of studying in hadronic collisions with AFTER@LHC the *fracture* functions using the production of a hard dilepton, just as in the Drell-Yan process, but in association with an observed final-state hadron.

Quarkonium production is also known to be an ideal probe of Quantum Chromodynamics at the interface between its perturbative and nonperturbative domain. The contribution of Y. Feng and J.-X. Wang entitled “Next-to-Leading Order Differential Cross Sections for J/ψ , $\psi(2S)$, and Υ Production in Proton-Proton Collisions at a Fixed-Target Experiment Using the LHC Beams” presents a next-to-leading order analysis of the quarkonium yields at the energies reached by AFTER@LHC and demonstrates how such measurements in a new energy domain would constrain the long-distance physics parameters needed to predict the quarkonium yields even at collider energies.

The use of nuclear targets with the LHC lead beam provides a new window to study nuclear phenomena, such as the quark-gluon plasma in the target rest frame (or over a large rapidity range). The contribution of K. Zhou et al. entitled “Antishadowing Effect on Charmonium Production at a Fixed-Target Experiment Using LHC Beams” analyses the impact of the antishadowing of gluons in heavy nuclei on the production of charmonia at AFTER@LHC. This work clearly demonstrates that the study of heavy-ion collisions in an energy domain between SPS and RHIC, never explored before with high luminosities, can perfectly complement the RHIC and LHC heavy-ion program and provide measurements of phenomena inaccessible otherwise.

Along these lines, one of the superior advantages of the fixed-target mode is to provide extremely precise analyses of proton-nucleus collisions. These are mandatory baselines to interpret nucleus-nucleus results and are extremely useful to learn more about the nuclear phenomena in the subfemtometer domain. The contribution of F. Arleo and S. Peigné entitled “Quarkonium Suppression from Coherent Energy Loss in Fixed-Target Experiments Using LHC Beams” studies the impact of a coherent energy loss on charmonium production in proton-lead collisions whereas the contribution of R. Vogt entitled “Gluon Shadowing Effects on J/ψ and Υ Production in $p+Pb$ Collisions at $\sqrt{s_{NN}} = 115$ GeV and $Pb+p$ Collisions at $\sqrt{s_{NN}} = 72$ GeV at AFTER@LHC” studies in detail the impact of the nuclear modification of the gluon densities on the quarkonium yields.

These studies are nicely complemented by a paper entitled “Feasibility Studies for Quarkonium Production at a Fixed-Target Experiment Using the LHC Proton and Lead Beams (AFTER@LHC)” by L. Massacrier et al. which is the first of its kind and which paves the way for the elaboration of a number of figures-of-merit which would support a forthcoming *Expression of Interest* for AFTER@LHC. In addition to these detailed feasibility studies, D. Kikoła in his contribution entitled “Prospects for Open Heavy Flavor Measurements in Heavy Ion and $p+A$ Collisions in a Fixed-Target Experiment at the LHC” looks at the feasibility to perform state-of-the-art studies of open charm and beauty production in proton-nucleus and nucleus-nucleus collisions at AFTER@LHC. Finally, A. B. Kurepin and N. S. Topilskaya

review in their contribution entitled “Quarkonium Production and Proposal of the New Experiments on Fixed Target at the LHC” the current knowledge of quarkonium studies in heavy-ion collisions and discuss the opportunities offered by an internal solid target at the ALICE experiment interaction point.

The list of studies linked to heavy-ion collisions is completed by the contribution of R. E. Mikkelsen et al. entitled “Bremsstrahlung from Relativistic Heavy Ions in a Fixed Target Experiment at the LHC” which focuses on the emission process of high-energy photon in ultraperipheral heavy-nucleus collisions. Such measurements would enable us to extract the charge distributions of nuclei with a lifetime down to femtoseconds.

The last contribution by J. P. Lansberg et al. entitled “Near-Threshold Production of W^\pm , Z^0 , and H^0 at a Fixed-Target Experiment at the Future Ultrahigh-Energy Proton Colliders” is to our knowledge the first work ever dealing with the possibility offered by a possible fixed-target experiment at the future ultrahigh-energy hadron facilities such as HE-LHC, FCC-hh, and SppC.

Overall, we are very hopeful that the contributions gathered in the present volume will give a new impetus to initiatives in favour of a fixed-target program at the LHC. In particular, they will certainly serve as a solid background for the writing of a forthcoming *Expression of Interest* for such a facility.

Jean-Philippe Lansberg
Gianluca Cavoto
Cynthia Hadjidakis
Jibo He
Cédric Lorcé
Barbara Trzeciak

Research Article

Next-to-Leading Order Differential Cross Sections for J/ψ , $\psi(2S)$, and Υ Production in Proton-Proton Collisions at a Fixed-Target Experiment Using the LHC Beams

Yu Feng and Jian-Xiong Wang

Institute of High Energy Physics, Chinese Academy of Sciences, P.O. Box 918(4), Beijing 100049, China

Correspondence should be addressed to Yu Feng; yfeng@ihep.ac.cn

Received 17 April 2015; Accepted 4 June 2015

Academic Editor: Cynthia Hadjidakis

Copyright © 2015 Y. Feng and J.-X. Wang. This is an open access article distributed under the Creative Commons Attribution License, which permits unrestricted use, distribution, and reproduction in any medium, provided the original work is properly cited. The publication of this article was funded by SCOAP³.

Using nonrelativistic QCD (NRQCD) factorization, we calculate the yields for J/ψ , $\psi(2S)$, and $\Upsilon(1S)$ hadroproduction at $\sqrt{s} = 72$ GeV and 115 GeV including the next-to-leading order QCD corrections. Both these center-of-mass energies correspond to those obtained with 7 TeV and 2.76 TeV nucleon beam impinging a fixed target. We study the cross section integrated in p_t as a function of the (center-of-mass) rapidity as well as the p_t differential cross section in the central rapidity region. Using different NLO fit results of the NRQCD long-distance matrix elements, we evaluate a theoretical uncertainty which is certainly much larger than the projected experimental uncertainties with the expected 20 fb^{-1} to be collected per year with AFTER@LHC for pp collision at the center of mass energy $\sqrt{s} \approx 115$ GeV.

1. Introduction

Nonrelativistic quantum chromodynamics (NRQCD) [1] is the most systematic factorization scheme to describe the decay and production of heavy quarkonia. It allows one to organize the theoretical calculations as double expansions in both the coupling constant α_s and the heavy-quark relative velocity v . In the past few years, significant progress has been made in next-to-leading order (NLO) QCD calculations based on NRQCD. Calculations and fits of NRQCD long-distance matrix elements (LDMEs) for both the J/ψ yield and polarization in hadroproduction have been carried out [2–6] as well as for Υ hadroproduction [7, 8]. Using these LDMEs, one can in principle predict the transverse momentum p_t differential cross section at any energies. In addition, in a recent study [9], we have discussed the implication of these fits on the energy dependence of the cross sections integrated in p_t .

In this paper, we predict these differential cross sections for the kinematics of a fixed-target experiment using the LHC beams (AFTER@LHC) [10]. In practice, 7 TeV protons on targets yield to a c.m.s energy close to 115 GeV and 72 GeV for 2.76 TeV nucleons (as in the case of a Pb beam).

This corresponds to a range very seldom explored so far, significantly higher than that at CERN-SPS and not far from BNL-RHIC. With the typical luminosity of the fixed-target mode, which allows for yearly luminosities as large as 20 fb^{-1} in pp collision at $\sqrt{s} \approx 115$ GeV, AFTER@LHC is expected to be a quarkonium and heavy-flavor observatory [10, 11]. In general, the opportunities of a fixed-target experiment using the LHC beam for spin and heavy-ion physics are discussed in [10, 12–14]. With the calculation at $\sqrt{s} = 72$ GeV, which is supposed to be a baseline rate where nuclear effects would be added, we confirm that charmonium yields can easily reach 10^9 per year and 10^6 for bottomonium at $\sqrt{s} \approx 115$ GeV.

2. Next-to-Leading Order Calculation

Following the NRQCD factorization formalism [1], the cross section for quarkonium hadroproduction H can be expressed as

$$d\sigma [pp \rightarrow H + X] = \sum_{i,j,n} \int dx_1 dx_2 G_p^i G_p^j d\hat{\sigma} [ij \rightarrow (Q\bar{Q})_n X] \langle \mathcal{O}_n^H \rangle, \quad (1)$$

where p is either a proton or an antiproton, $G_p^{i(j)}$ is the parton distribution function (PDF) of p , the indices i, j run over all possible partonic species, and n denotes the color, spin, and angular momentum states of the intermediate $Q\bar{Q}$ pair. For ψ and Υ , namely, the 3S_1 quarkonium states, their leading CO states of relative order $\mathcal{O}(v^4)$ are $^1S_0^{[8]}$, $^3S_1^{[8]}$, and $^3P_J^{[8]}$. Along with the CS transition $^3S_1^{[1]}$, we call the total CS + CO contributions as direct production. The short-distance coefficient (SDC) $d\hat{\sigma}$ will be calculated perturbatively, while the long-distance matrix elements (LDMEs) $\langle \mathcal{O}_n^H \rangle$ are governed by nonperturbative QCD effects.

Now let us take a look at the parton level processes relevant to this work. As it is well known, the CO contributions to hadroproduction appear at α_s^2 [15] and their Born contributions are

$$\begin{aligned} q + \bar{q} &\longrightarrow Q\bar{Q} \left[^3S_1^{[8]} \right], \\ g + g &\longrightarrow Q\bar{Q} \left[^1S_0^{[8]}, ^3P_{J=0,2}^{[8]} \right], \end{aligned} \quad (2)$$

where $q(\bar{q})$ denotes the light quarks (antiquarks).

Up to α_s^3 , QCD corrections include real and virtual corrections. One inevitably encounters ultra-violet (UV), infrared (IR), and Coulomb divergences when dealing with the virtual corrections. UV divergences from self-energy and triangle diagrams are canceled upon the renormalization procedure. For the real emission corrections, three kinds of processes should be considered:

$$\begin{aligned} g + g &\longrightarrow Q\bar{Q} \left[^3S_1^{[1]}, ^1S_0^{[8]}, ^3S_1^{[8]}, ^3P_{J=0,2}^{[8]} \right] + g, \\ g + q(\bar{q}) &\longrightarrow Q\bar{Q} \left[^1S_0^{[8]}, ^3S_1^{[8]}, ^3P_{J=0,2}^{[8]} \right] + q(\bar{q}), \\ q + \bar{q} &\longrightarrow Q\bar{Q} \left[^1S_0^{[8]}, ^3S_1^{[8]}, ^3P_{J=0,1,2}^{[8]} \right] + g, \end{aligned} \quad (3)$$

some of which involve IR singularities in phase space integration and we adopt the two-cutoff phase space slicing method [16] to isolate these singularities by introducing two small cutoffs, δ_s and δ_c . For technical details, we refer readers to [17, 18].

One has to note that in (3), the $^3S_1^{[1]}$ production in gg fusion is not really correction. Strictly speaking, it is only the Born-order contribution for hadroproduction with a jet. In fact, all the real emission processes in (3) will be taken as Born-order contributions of quarkonium-jet production.

As regards to the p_t dependent differential cross section, and the QCD NLO corrections in this case are up to α_s^4 , which involves the real emission processes

$$\begin{aligned} g + g &\longrightarrow (Q\bar{Q})_n + g + g, \\ g + g &\longrightarrow (Q\bar{Q})_n + q + \bar{q}, \\ g + q(\bar{q}) &\longrightarrow (Q\bar{Q})_n + g + q(\bar{q}), \end{aligned}$$

$$\begin{aligned} q + \bar{q} &\longrightarrow (Q\bar{Q})_n + g + g, \\ q + \bar{q} &\longrightarrow (Q\bar{Q})_n + q + \bar{q}, \\ q + \bar{q} &\longrightarrow (Q\bar{Q})_n + q' + \bar{q}', \\ q + q &\longrightarrow (Q\bar{Q})_n + q + q, \\ q + q' &\longrightarrow (Q\bar{Q})_n + q + q', \end{aligned} \quad (4)$$

where q, q' denote light quarks with different flavors and $(Q\bar{Q})_n$ can be either $^3S_1^{[1]}$, $^1S_0^{[8]}$, $^3S_1^{[8]}$, or $^3P_J^{[8]}$. One can find the details of such computations at this order in [18, 19] and some examples in [2, 3, 6–8].

All of these calculations are made with the newly updated Feynman Diagram Calculation package [20].

3. Constrains on the LDMEs

The color-singlet (CS) LDMEs are estimated from the wave functions at the origin by $\langle \mathcal{O}^H(^3S_1^{[1]}) \rangle = (3N_c/2\pi)|R_H(0)|^2$, where the wave functions are obtained via potential model calculation [21]. This gives $|R_{J/\psi}(0)|^2 = 0.81 \text{ GeV}^3$, $|R_{\psi(2S)}(0)|^2 = 0.53 \text{ GeV}^3$, and $|R_{\Upsilon(1S)}(0)|^2 = 6.5 \text{ GeV}^3$. In the following, we will refer to this contribution as the CSM results when performed separately.

The color-octet (CO) LDMEs can only be extracted from data. As for now, SDC are known up to NLO accuracy and the fits of LDMEs can be thus performed at NLO. However, different results are obtained when different dataset is used. We made a selection of these fits in order to assess the theoretical uncertainty induced by the LDMEs. We briefly discuss below these different fit results.

In the J/ψ case, seven groups of LDMEs [2, 5, 6, 22–25] are collected in Table 1. They are extracted by fitting the data of hadroproduction yield [2] or combined with polarization [5, 6] on pp collisions. The first one [22] was based on a wider set of data including ep and $\gamma\gamma$ system with $p_t > 1 \text{ GeV}$. In [5, 6], the data with $p_t < 7 \text{ GeV}$ are excluded in their fit. The fit in [23, 24] took the η_c measurement ($p_t \geq 6 \text{ GeV}$) into consideration. Only one of them is used [24] since their results are almost the same. The last one incorporates the leading-power fragmentation corrections together with the QCD NLO corrections, which results in a different SDC and may result in different LDMEs. In [2], Ma et al. fit the data with $p_t > 7 \text{ GeV}$ by two linear combinations of LDMEs:

$$\begin{aligned} M_{0,r_0}^{J/\psi} &= \langle \mathcal{O}^{J/\psi}(^1S_0^{[8]}) \rangle + \frac{r_0}{m_c^2} \langle \mathcal{O}^{J/\psi}(^3P_0^{[8]}) \rangle, \\ M_{1,r_1}^{J/\psi} &= \langle \mathcal{O}^{J/\psi}(^3S_1^{[8]}) \rangle + \frac{r_1}{m_c^2} \langle \mathcal{O}^{J/\psi}(^3P_0^{[8]}) \rangle, \end{aligned} \quad (5)$$

from which we extract the value of LDMEs by restricting $\langle \mathcal{O}^{J/\psi}(^1S_0^{[8]}) \rangle$ and $\langle \mathcal{O}^{J/\psi}(^3S_1^{[8]}) \rangle$ to be positive to get a loose constraint on the $\langle \mathcal{O}^{J/\psi}(^3P_0^{[8]}) \rangle$ range, from which we choose

TABLE 1: The values of LDMEs for J/ψ hadroproduction (in units of GeV^3).

References	$\langle \mathcal{O}^{J/\psi}({}^3S_1^{[1]}) \rangle$	$\langle \mathcal{O}^{J/\psi}({}^1S_0^{[8]}) \rangle$	$\langle \mathcal{O}^{J/\psi}({}^3S_1^{[8]}) \rangle$	$\langle \mathcal{O}^{J/\psi}({}^3P_0^{[8]}) \rangle / m_Q^2$
Butenschoen and Kniehl (2011) [22]	1.32	3.0×10^{-2}	1.7×10^{-3}	-4.0×10^{-3}
Chao et al. (2012) [5]	1.16	8.9×10^{-2}	3.0×10^{-3}	5.6×10^{-3}
Ma et al. (2011) [2]	1.16	3.9×10^{-2}	5.6×10^{-3}	8.9×10^{-3}
Gong et al. (2013) [6]	1.16	9.7×10^{-2}	-4.6×10^{-3}	-9.5×10^{-3}
Zhang et al. (2014) [23]	0.24~0.90	$(0.4\sim 1.1) \times 10^{-2}$	1.0×10^{-2}	1.7×10^{-2}
Han et al. (2015) [24]	1.16	0.7×10^{-2}	1.0×10^{-2}	1.7×10^{-2}
Bodwin et al. (2014) [25]	0	9.9×10^{-2}	1.1×10^{-2}	4.9×10^{-3}

TABLE 2: The values of LDMEs for $\psi(2S)$ and $Y(1S)$ hadroproduction (in units of GeV^3).

H	References	$\langle \mathcal{O}^H({}^3S_1^{[1]}) \rangle$	$\langle \mathcal{O}^H({}^1S_0^{[8]}) \rangle$	$\langle \mathcal{O}^H({}^3S_1^{[8]}) \rangle$	$\langle \mathcal{O}^H({}^3P_0^{[8]}) \rangle / m_Q^2$
$\psi(2S)$	Gong et al. (2013) [6]	0.76	-1.2×10^{-4}	3.4×10^{-3}	4.2×10^{-3}
	Ma et al. (2011) [2]	0.76	1.4×10^{-2}	2.0×10^{-3}	1.6×10^{-3}
$Y(1S)$	Gong et al. (2014) [8]	9.28	11.2×10^{-2}	-4.1×10^{-3}	-6.7×10^{-3}
	Han et al. (2014) [26]	9.28	3.5×10^{-3}	5.8×10^{-2}	3.6×10^{-2}
	Feng et al. (2015) [27]	9.28	13.6×10^{-2}	6.1×10^{-3}	-9.3×10^{-3}

the center value in order to obtain the three LDMEs (Ma et al. (2011) in Table 1).

As regards the $\psi(2S)$, only two NLO analyses have been done (see [2, 6]), both of which excluded the data with $p_t < 7 \text{ GeV}$ in their fit. To extract the LDME values from the fit results of Ma et al., the same method is used as for the J/ψ . For $Y(1S)$, we use three groups of LDMEs [8, 26, 27]. Both of them have exactly accounted for the direct production and the feed-down contributions. In the fit of [26], only the data in $p_t > 15 \text{ GeV}$ region are used, while in [8, 27] the region is $p_t > 8 \text{ GeV}$. They all describe the high p_t yield data at Tevatron and LHC very well. We gather the LDMEs of $\psi(2S)$ and $Y(1S)$ in Table 2.

4. Numerical Results

The differential cross sections as a function of (center-of-mass) rapidity and transverse momentum are considered in this section. In both cases, the CTEQ6M parton distribution functions [28] and the corresponding two-loop QCD coupling constants α_s are used. The charm quark mass is set to be $m_c = 1.5 \text{ GeV}$, while the bottom quark mass is taken to be $m_b = 4.75 \text{ GeV}$. The renormalization and factorization scales are chosen as $\mu_r = \mu_f = 2m_Q$ for rapidity distribution plots, while for the plots of transverse momentum distribution they are $\mu_r = \mu_f = \mu_T$, with $\mu_T = \sqrt{(2m_Q)^2 + p_t^2}$. The NRQCD scale is chosen as $\mu_\Lambda = m_Q$. It is important to note that different choices of these scales may be adopted which can bring some additional uncertainties in our predictions. We show these uncertainties from the scales combined to those from the quark masses for the plot of the rapidity distribution of the yield (and only for the CO contributions). The scale dependence is estimated by varying μ_r, μ_f , by a factor of 1/2 and 2 with respect to their central values and quark masses varying 0.1 GeV up and down for J/ψ , as well as 0.25 GeV for Y . Branching ratios are taken from PDG [29], which give

$\mathcal{B}[J/\psi \rightarrow \mu\mu] = 0.0596$, $\mathcal{B}[\psi(2S) \rightarrow \mu\mu] = 0.0079$, and $\mathcal{B}[Y(1S) \rightarrow \mu\mu] = 0.0248$, respectively. The two phase space cutoffs $\delta_s = 10^3$ and $\delta_c = \delta_s/50$ are chosen and the insensitivity of the results on different choices for these cutoffs has been checked.

4.1. $d\sigma/dy$ up to α_s^3 . First, we study the p_t -integrated cross section (where the whole p_t region is integrated) as a function of rapidity. The QCD NLO corrections are up to α_s^3 in this case. In Figures 1 and 2, we show the rapidity distribution of direct J/ψ , $\psi(2S)$, and $Y(1S)$ production cross section at center of mass energy $\sqrt{s} = 72 \text{ GeV}$ and 115 GeV , respectively. We first discuss the “unnormalized” CO channel contributions shown in Figure 1, where the CO LDMEs are set to unity for all three production channels. For $\psi(2S)$, the CSM is different from J/ψ only by a factor, we therefore do not perform it separately. Obviously, the CSM results (red lines) for both J/ψ and $Y(1S)$ are small compared with the CO channels. The dominant CO channel for J/ψ is ${}^3P_J^{[8]}$ transition, while for $Y(1S)$ it is ${}^1S_0^{[8]}$. Besides, these “unnormalized” contributions for J/ψ display a clear hierarchy, but for $Y(1S)$, little difference between ${}^3S_1^{[8]}$ and ${}^3P_J^{[8]}$ contributions shows up.

Adopting the LDMEs in Tables 1 and 2, we present the rapidity distribution of cross section for various cases in Figure 2. The lines are the central values with different groups of LDMEs, while the colored areas are the uncertainties from scales and quark masses. Only the boundary lines are shown with scales and mass uncertainties. For the J/ψ , six groups of NRQCD results are shown as a band, the boundaries of which has a distance within factor 10. The values of the cross sections are roughly in the region of $10^4 \sim 10^5 \text{ pb}$. The CSM results are systematically below the full NRQCD band, again by a factor 10. Without a surprise, the CSM seems to be negligible for total NRQCD results. However, some words of cautious are in order here. In fact, as we have

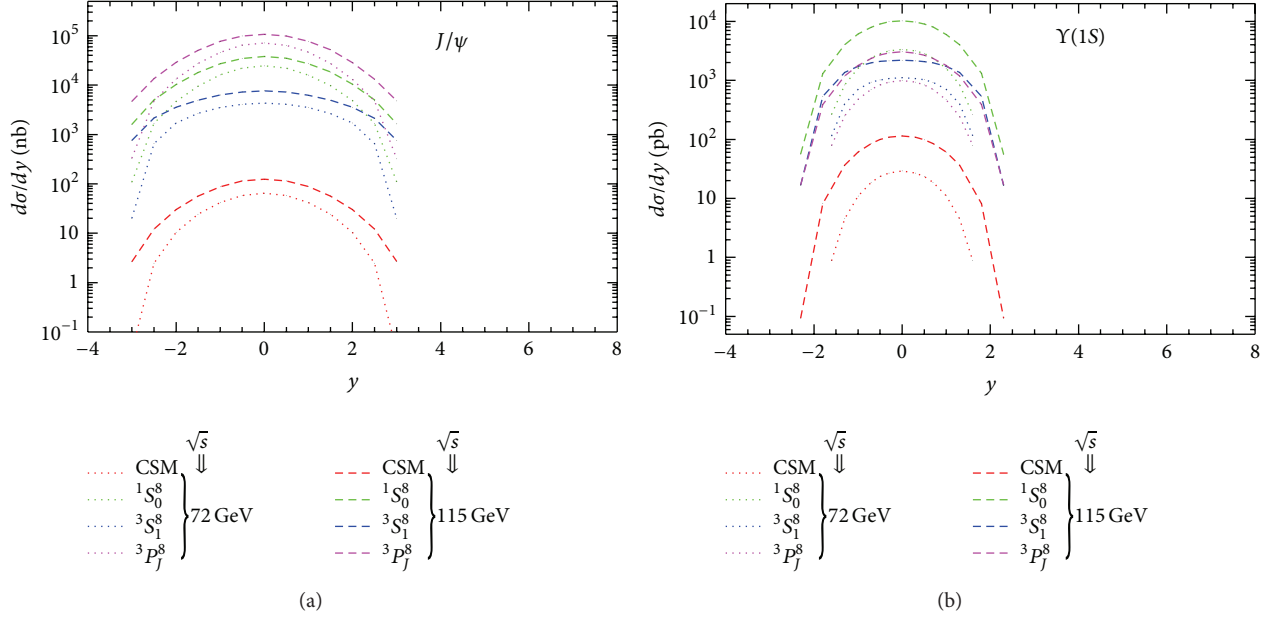


FIGURE 1: The “unnormalized” CO channel contributions for direct J/ψ (a) and $\Upsilon(1S)$ (b) hadroproduction at the c.m.s energy 72 GeV (dot lines) and 115 GeV (dashed lines), respectively. The CO LDMEs for all the channels are set to unity.

discussed in [9], the LO CSM contribution explains the data very well from the RHIC to LHC energies, while the CO LDMEs extracted from p_t -differential NLO correction would lead to p_t -integrated cross sections overshooting the data. Only the fit from Butenschoen and Kniehl [22], including rather low p_t data, provides an acceptable description of the p_t -integrated cross section. In other words, most of the predictions in Figure 2 may overshoot the data. One should indeed stress that most of the fits which we used are based on large p_t data, while this rapidity distribution bears on the whole p_t region. We suppose the band from the LDMEs of Butenschoen and Kniehl [22]; namely, the lowest band (red dashed line) would probably give the best prediction of the J/ψ yields, although their LDMEs clearly face difficulty to describe the polarization data. To be complete, let us mention that, following an observations also done in [9], the CSM yield may underestimate the measurements below RHIC energy.

As regards the $\psi(2S)$, two groups of LDMEs lead to a consistent predictions which give a cross section around 10^3 pb at both $\sqrt{s} = 72$ GeV and 115 GeV. Accounting for the uncertainties of the scales and quark masses, the cross sections reach 10^4 pb in the central rapidity region. Nevertheless, these results overestimated the data as discussed in [9].

In the $\Upsilon(1S)$ case, two curves are close and a third one is slightly different. Yet, their difference is only in pb units. At RHIC energies and below [9], this reproduces quite well the $\Upsilon(1S)$ data. This should thus also be the case at the energies considered here.

4.2. $d\sigma/dp_t$ up to α_s^4 . Now let us discuss the differential cross sections in the transverse momentum p_t . In Figure 3, the p_t distributions of direct J/ψ , $\psi(2S)$, and $\Upsilon(1S)$

hadroproduction are presented. For J/ψ and $\psi(2S)$, the yields are dominated by the CO contributions, which is larger than that of the CSM at NLO by at least one order of magnitude. The various groups of LDMEs predict J/ψ and $\psi(2S)$ differential yields which are much less spread than for the p_t integrated yields; this is expected since the fits are based on a similar distribution but at different energies. Only the one from [25] (the light blue dot-dashed line) seems to depart from the other ones, being from 2 to 10 times larger in J/ψ case. This may be understood by the fact that the fits in [25] have a different SDC compared with others, which would be the source of the difference.

For $\Upsilon(1S)$, the red dashed and blue dot-dashed lines are almost parallel with a tiny difference, while the green dot line is obviously lower at low p_t region and crosses the other ones as p_t increases. This explains the behavior of $d\sigma/dy$ in Figure 2 with a visible difference between the green curve and the other two.

5. Summary

We evaluated the NLO QCD corrections for the direct J/ψ , $\psi(2S)$, and $\Upsilon(1S)$ production at fixed-target LHC energies. We studied the cross section integrated in p_t as a function of the rapidity as well as the p_t differential cross section in the central rapidity region, including QCD corrections up to α_s^3 and α_s^4 contributions, respectively. To perform a reliable prediction, various sets of NRQCD long-distance matrix elements obtained from different fitting methods are considered as well as the uncertainties from the scales and quark masses. With the typical luminosity of the fixed-target mode, which allows for yearly luminosities as large as 20 fb^{-1} with 7 TeV proton beams, our predictions confirm

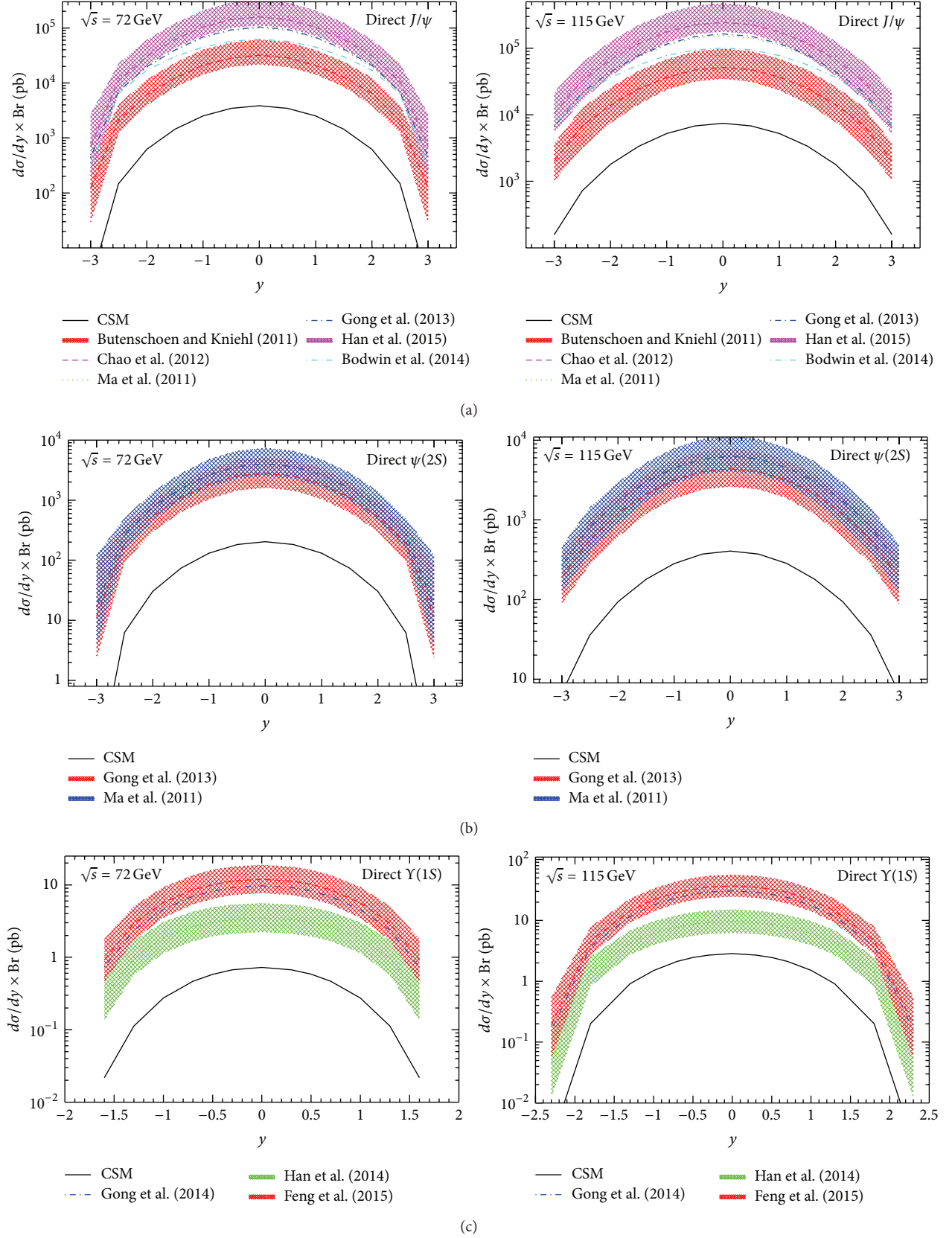


FIGURE 2: Rapidity distribution of differential cross section for direct J/ψ (a), $\psi(2S)$ (b), and $\Upsilon(1S)$ (c) hadroproduction at the center of mass energy $\sqrt{s} = 72$ GeV and $\sqrt{s} = 115$ GeV, respectively. The lines are the uncertainty from LDMEs values while the color areas are scales and masses uncertainties.

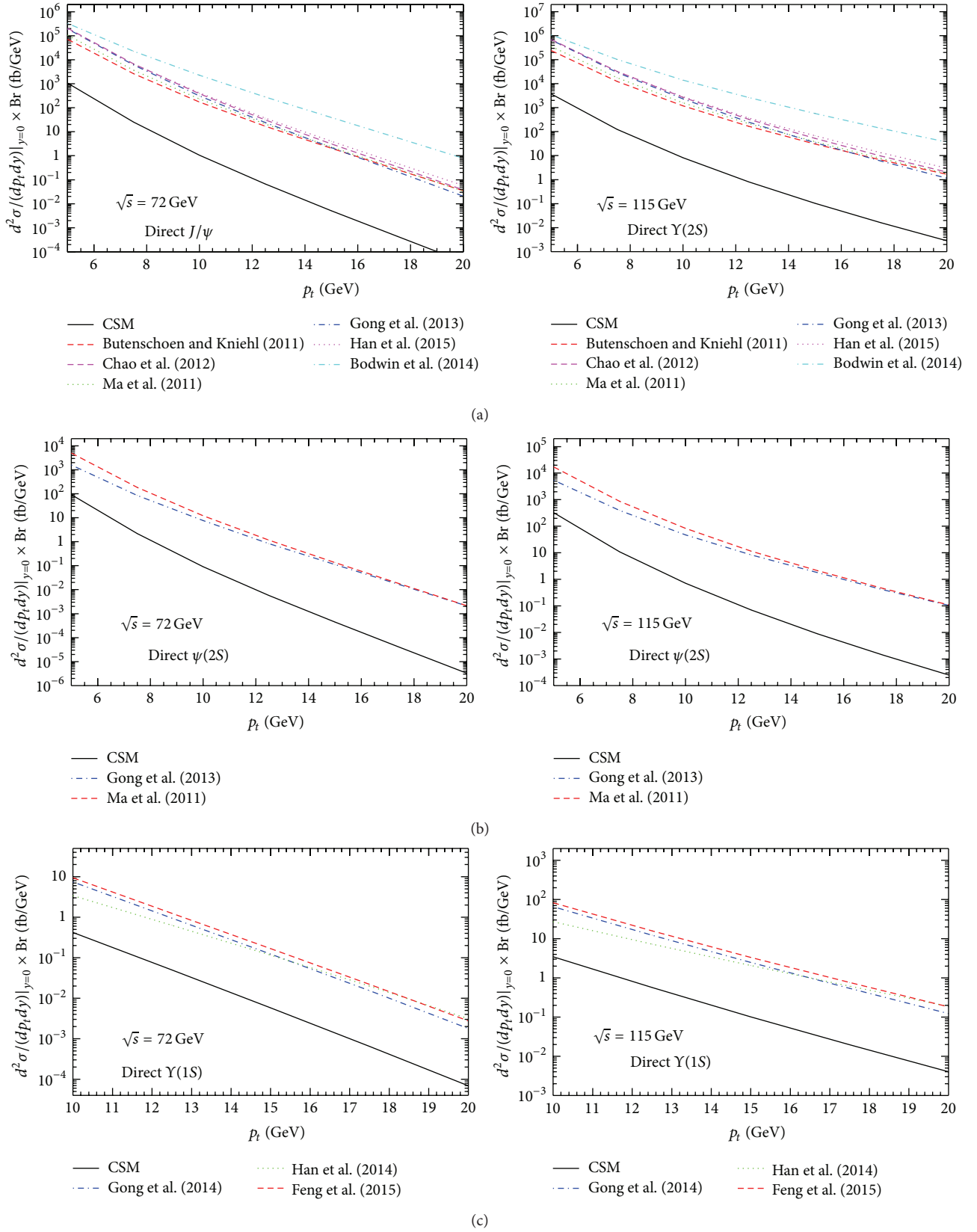


FIGURE 3: Transverse momentum distribution of differential cross section with the rapidity $y = 0$ for direct J/ψ , $\psi(2S)$, and $\Upsilon(1S)$ hadroproduction from (a) to (c), respectively.

that charmonium yields can easily reach 10^9 per year and 10^6 for bottomonium at the center of mass energy $\sqrt{s} \approx 115$ GeV in pp collision.

Conflict of Interests

The authors declare that there is no conflict of interests regarding the publication of this paper.

Acknowledgment

The authors are grateful to Jean-Philippe Lansberg for his generous help in this work.

References

- [1] G. T. Bodwin, E. Braaten, and G. P. Lepage, "Rigorous QCD analysis of inclusive annihilation and production of heavy quarkonium," *Physical Review D*, vol. 51, no. 3, pp. 1125–1171, 1995.
- [2] Y.-Q. Ma, K. Wang, and K.-T. Chao, " $J/\psi(\psi')$ Production at the Tevatron and LHC at $\mathcal{O}(\alpha_s^4)$ in Nonrelativistic QCD," *Physical Review Letters*, vol. 106, Article ID 042002, 2011.
- [3] M. Butenschoen and B. A. Kniehl, "Reconciling J/ψ production at HERA, RHIC, Tevatron, and LHC with nonrelativistic QCD factorization at next-to-leading order," *Physical Review Letters*, vol. 106, Article ID 022003, 2011.
- [4] M. Butenschoen and B. A. Kniehl, " J/ψ polarization at the Tevatron and the LHC: nonrelativistic-QCD factorization at the crossroads," *Physical Review Letters*, vol. 108, Article ID 172002, 2012.
- [5] K.-T. Chao, Y.-Q. Ma, H.-S. Shao, K. Wang, and Y.-J. Zhang, " J/ψ polarization at Hadron colliders in nonrelativistic QCD," *Physical Review Letters*, vol. 108, Article ID 242004, 2012.
- [6] B. Gong, L.-P. Wan, J.-X. Wang, and H.-F. Zhang, "Polarization for prompt J/ψ and $\psi(2s)$ production at the Tevatron and LHC," *Physical Review Letters*, vol. 110, Article ID 042002, 2013.
- [7] K. Wang, Y.-Q. Ma, and K.-T. Chao, " $\Upsilon(1S)$ prompt production at the Tevatron and LHC in nonrelativistic QCD," *Physical Review D*, vol. 85, Article ID 114003, 2012.
- [8] B. Gong, L.-P. Wan, J.-X. Wang, and H.-F. Zhang, "Complete next-to-leading-order study on the yield and polarization of $\Upsilon(1S, 2S, 3S)$ at the Tevatron and LHC," *Physical Review Letters*, vol. 112, Article ID 032001, 2014.
- [9] Y. Feng, J.-P. Lansberg, and J.-X. Wang, "Energy dependence of direct-quarkonium production in pp collisions from fixed-target to LHC energies: complete one-loop analysis," <http://arxiv.org/abs/1504.00317>.
- [10] S. J. Brodsky, F. Fleuret, C. Hadjidakis, and J. P. Lansberg, "Physics opportunities of a fixed-target experiment using LHC beams," *Physics Reports*, vol. 522, no. 4, pp. 239–255, 2013.
- [11] J. P. Lansberg, S. J. Brodsky, F. Fleuret, and C. Hadjidakis, "Quarkonium physics at a fixed-target experiment using the LHC beams," *Few-Body Systems*, vol. 53, no. 1-2, pp. 11–25, 2012.
- [12] L. Massacrier, M. Anselmino, R. Arnaldi et al., "Studies of transverse-momentum-dependent distributions with A Fixed-Target Experiment using the LHC beams (AFTER@LHC)," <http://arxiv.org/abs/1502.00984>.
- [13] J. P. Lansberg, M. Anselmino, R. Arnaldi et al., "Spin physics and TMD studies at a fixed-target experiment at the LHC (AFTER@LHC)," *EPJ Web of Conferences*, vol. 85, Article ID 02038, 2015.
- [14] A. Rakotozafindrabe, R. Arnaldi, S. Brodsky et al., "Ultra-relativistic heavy-ion physics with AFTER@LHC," *Nuclear Physics A*, vol. 904-905, pp. 957c–960c, 2013.
- [15] P. L. Cho and A. K. Leibovich, "Color-octet quarkonia production. II," *Physical Review D*, vol. 53, pp. 6203–6217, 1996.
- [16] B. Harris and J. Owens, "Two cutoff phase space slicing method," *Physical Review D*, vol. 65, Article ID 094032, 2002.
- [17] B. Gong and J.-X. Wang, "QCD corrections to polarization of J/ψ and Υ at Fermilab Tevatron and CERN LHC," *Physical Review D*, vol. 78, Article ID 074011, 2008.
- [18] B. Gong, X. Q. Li, and J.-X. Wang, "QCD corrections to J/ψ production via color-octet states at the Tevatron and LHC," *Physics Letters B*, vol. 673, no. 3, pp. 197–200, 2009.
- [19] B. Gong, J.-X. Wang, and H.-F. Zhang, "QCD corrections to Υ production via color-octet states at the Tevatron and LHC," *Physical Review D*, vol. 83, Article ID 114021, 2011.
- [20] J.-X. Wang, "Progress in FDC project," *Nuclear Instruments and Methods in Physics Research Section A: Accelerators, Spectrometers, Detectors and Associated Equipment*, vol. 534, no. 1-2, pp. 241–245, 2004.
- [21] E. J. Eichten and C. Quigg, "Quarkonium wave functions at the origin," *Physical Review D*, vol. 52, pp. 1726–1728, 1995.
- [22] M. Butenschoen and B. A. Kniehl, "World data of J/ψ production consolidate nonrelativistic QCD factorization at next-to-leading order," *Physical Review D*, vol. 84, Article ID 051501, 2011.
- [23] H.-F. Zhang, Z. Sun, W.-L. Sang, and R. Li, "Impact of η_c hadroproduction data on charmonium production and polarization within the nonrelativistic QCD framework," *Physical Review Letters*, vol. 114, Article ID 092006, 2014.
- [24] H. Han, Y.-Q. Ma, C. Meng, H.-S. Shao, and K.-T. Chao, " η_c production at LHC and implications for the understanding of J/ψ production," *Physical Review Letters*, vol. 114, Article ID 092005, 2015.
- [25] G. T. Bodwin, H. S. Chung, U.-R. Kim, and J. Lee, "Fragmentation contributions to J/ψ production at the Tevatron and the LHC," *Physical Review Letters*, vol. 113, Article ID 022001, 2014.
- [26] H. Han, Y.-Q. Ma, C. Meng, H.-S. Shao, and Y.-J. Zhang, 1410.8537, 2014.
- [27] Y. Feng, B. Gong, L.-P. Wan, and J.-X. Wang, "An updated study for Υ production and polarization at the Tevatron and LHC," <http://xxx.tau.ac.il/abs/1503.08439>.
- [28] J. Pumplin, D. Stump, J. Huston, H.-L. Lai, P. M. Nadolsky, and W.-K. Tung, "New generation of parton distributions with uncertainties from global QCD analysis," *Journal of High Energy Physics*, vol. 2002, no. 7, article 12, 2002.
- [29] K. Olive, K. Agashe, C. Amsler et al., "Review of particle physics," *Chinese Physics C*, vol. 38, Article ID 090001, 2014.

Review Article

The Gluon Sivers Distribution: Status and Future Prospects

Daniël Boer,¹ Cédric Lorcé,^{2,3} Cristian Pisano,⁴ and Jian Zhou⁵

¹Van Swinderen Institute, University of Groningen, Nijenborgh 4, 9747 AG Groningen, Netherlands

²SLAC National Accelerator Laboratory, Stanford University, Menlo Park, CA 94025, USA

³IFPA, AGO Department, University of Liège, Sart-Tilman, 4000 Liège, Belgium

⁴Department of Physics, University of Antwerp, Groenenborgerlaan 171, 2020 Antwerp, Belgium

⁵Nikhef and Department of Physics and Astronomy, VU University Amsterdam, De Boelelaan 1081, 1081 HV Amsterdam, Netherlands

Correspondence should be addressed to Daniël Boer; d.boer@rug.nl

Received 16 April 2015; Accepted 28 June 2015

Academic Editor: Jibo He

Copyright © 2015 Daniël Boer et al. This is an open access article distributed under the Creative Commons Attribution License, which permits unrestricted use, distribution, and reproduction in any medium, provided the original work is properly cited. The publication of this article was funded by SCOAP³.

We review what is currently known about the gluon Sivers distribution and what are the opportunities to learn more about it. Because single transverse spin asymmetries in $p^\uparrow p \rightarrow \pi X$ provide only indirect information about the gluon Sivers function through the relation with the quark-gluon and tri-gluon Qiu-Sterman functions, current data from hadronic collisions at RHIC have not yet been translated into a solid constraint on the gluon Sivers function. SIDIS data, including the COMPASS deuteron data, allow for a gluon Sivers contribution of natural size expected from large N_c arguments, which is $\mathcal{O}(1/N_c)$ times the nonsinglet quark Sivers contribution. Several very promising processes to measure the gluon Sivers effect directly have been suggested, which besides RHIC investigations, would strongly favor experiments at AFTER@LHC and a possible future Electron-Ion Collider. Due to the inherent process dependence of TMDs, the gluon Sivers TMD probed in the various processes are different linear combinations of two universal gluon Sivers functions that have different behavior under charge conjugation and that therefore satisfy different theoretical constraints. For this reason both hadronic and DIS type of collisions are essential in the study of the role of gluons in transversely polarized protons.

1. The Sivers Function and Its Definition

The distribution of quarks and gluons in a proton (or any other spin-1/2 hadron) that is polarized transversely to its momentum need not be left-right symmetric with respect to the plane spanned by the momentum and spin directions. This asymmetry is called the Sivers effect [1]. It results in angular asymmetries of produced particles in high energy scattering processes involving a transversely polarized hadron. Experimental data in support for such a left-right asymmetry in the quark distribution was first obtained from semi-inclusive DIS process by the HERMES collaboration [2]. This review is about what is currently known about the gluonic Sivers effect distribution. The Sivers effect is of great interest theoretically as it is very sensitive to the color flow in the scattering process and to the multitude of color exchanges among initial and final states. It is the first quantity for which this has been recognized and for which color flow sensitivity

can be tested unambiguously [3]. Verification of its unusual properties will provide a strong test of the formalism of Transverse-Momentum-Dependent parton distributions. It is an important quantity of nonperturbative QCD to consider both qualitatively and quantitatively. This review discusses these aspects for the gluon Sivers distribution specifically. We first start with its proper definition.

The number density in momentum space of a generic parton (quark, antiquark, and gluon) inside a hadron with mass M , transverse polarization \mathbf{S}_T , and momentum \mathbf{P} can be written as

$$\hat{f}(x, \mathbf{k}_\perp; \mathbf{S}_T) = f_1(x, \mathbf{k}_\perp^2) - \frac{(\hat{\mathbf{P}} \times \mathbf{k}_\perp) \cdot \hat{\mathbf{S}}_T}{M} f_{1T}^\perp(x, \mathbf{k}_\perp^2), \quad (1)$$

where $f_1(x, \mathbf{k}_\perp^2)$ is the unpolarized Transverse-Momentum-Dependent (TMD) parton distribution, $\hat{\mathbf{S}}_T \equiv \mathbf{S}_T/|\mathbf{S}_T|$, and $\hat{\mathbf{P}} \equiv \mathbf{P}/|\mathbf{P}|$. The function $f_{1T}^\perp(x, \mathbf{k}_\perp^2)$ describing the distortion

in the distribution of unpolarized partons with light-front momentum fraction x and transverse momentum \mathbf{k}_\perp due to the transverse polarization of the hadron is called the Sivers function. The notation used here comes from [4], but also the notation $\Delta^N f_{g/h^\dagger}$ from [5, 6] is sometimes used, where $\Delta^N f_{g/h^\dagger} = -2 (|\mathbf{k}_\perp|/M) f_{1T}^{\perp g}$ (analogous to the quark case [7]).

The Sivers function satisfies the following positivity bound [8]:

$$\frac{|\mathbf{k}_\perp|}{M} |f_{1T}^\perp(x, \mathbf{k}_\perp^2)| \leq f_1(x, \mathbf{k}_\perp^2). \quad (2)$$

In [8] the operator definition of the gluon Sivers function, which was called $G_T = -f_{1T}^{\perp g}$ [9], was first given without gauge links. The definition including gauge links then appeared in [10, 11]

$$\begin{aligned} & -\frac{(\hat{\mathbf{P}} \times \mathbf{k}_\perp) \cdot \hat{\mathbf{S}}_T}{M} f_{1T}^{\perp g}(x, \mathbf{k}_\perp^2) \\ & = \frac{1}{2} [\hat{f}(x, \mathbf{k}_\perp; \mathbf{S}_T) - \hat{f}(x, \mathbf{k}_\perp; -\mathbf{S}_T)] \end{aligned} \quad (3)$$

with

$$\begin{aligned} \hat{f}(x, \mathbf{k}_\perp; \mathbf{S}_T) &= \frac{\delta_T^{jl}}{xP^+} \int \frac{dz^- d^2 z_\perp}{(2\pi)^2} e^{ik \cdot z} \langle P, S_T | 2 \\ & \cdot \text{Tr} [F^{+j}(0) U_{[0,z]} F^{+l}(z) U_{[z,0]}] | P, S_T \rangle \Big|_{z^+=0}, \end{aligned} \quad (4)$$

where $U_{[a,b]}$ is a Wilson line connecting the points a and b along a contour determined by the physical process and $k^+ = xP^+$ is the fraction of parton light-front momentum. For a proper definition that is free from rapidity divergences associated with gauge links with paths (partly) along the light front, a redefinition involving the so-called soft factor is necessary [12–15]. This will however not play a significant role here and can simply be considered as implicit.

2. Sivers Effect, A_N , and Qiu-Sterman Effect

The Sivers effect (for both quarks and gluons) was first suggested in [1] as an explanation for the large left-right single transverse spin asymmetries (A_N) observed in $p^\uparrow p \rightarrow \pi X$ [16–23] (and similar asymmetries in K [22], in η [24], and tentatively in J/ψ [25] production). The Sivers effect was first studied phenomenologically in [5]. However, extraction of the Sivers TMD presumes all-order TMD factorization. A factorized description of the process $pp \rightarrow \pi X$ only applies for large transverse momentum p_T of the produced pions (say for $p_T \gtrsim 1$ GeV), where in fact collinear factorization is appropriate [26], rather than TMD factorization. Although TMDs do appear in the phenomenological description of A_N in [5] and subsequent studies (see [27]), that description is thus not based on a TMD factorization theorem. Rather it should be considered as an effective model description, now commonly referred to as the Generalized Parton Model (GPM). As a phenomenological approach it has proven

useful in the quest to disentangle the possible underlying mechanisms of the spin asymmetries; see [27, 28] for more discussion, but the extracted “effective” TMDs may differ from the TMDs extracted from TMD-factorizing processes. What is known about the effective gluon Sivers TMD will be discussed below.

In collinear factorization the single spin asymmetry (SSA) will arise at the twist-3 level [29]. In this description A_N probes the (quark-gluon) Qiu-Sterman function (sometimes one factor of the coupling constant g is included in the definition of Qiu-Sterman functions, because one always encounters them multiplied by g) [30, 31]

$$\begin{aligned} T_{q,F}(x, x) &= \frac{M}{P^+} \int \frac{dz^- d\eta}{2\pi} e^{ik \cdot z} \frac{(\hat{\mathbf{P}} \times \hat{\mathbf{S}}_T)^j}{2M} \langle P, S | \bar{\psi}(0) \\ & \cdot \gamma^+ F^{+j}(\eta z) \psi(z) | P, S \rangle \Big|_{z^+=|z_\perp|=0}, \end{aligned} \quad (5)$$

and its trigluon correlation analogues $T_G^{(f)}(x, x) = T_G^{(+)}(x, x)$ and $T_G^{(d)}(x, x) = T_G^{(-)}(x, x)$ [32–35]

$$\begin{aligned} T_G^{(\pm)}(x, x) &= -\frac{2M\delta_T^{lm}}{x(P^+)^2} \int \frac{dz^- d\eta}{2\pi} e^{ik \cdot z} \frac{(\hat{\mathbf{P}} \times \hat{\mathbf{S}}_T)^j}{2M} \langle P, S | \\ & \cdot C_\pm^{abc} F_a^{+l}(0) F_b^{+j}(\eta z) F_c^{+m}(z) | P, S \rangle \Big|_{z^+=|z_\perp|=0}, \end{aligned} \quad (6)$$

where $C_+^{abc} = if^{abc}$ and $C_-^{abc} = d^{abc}$ and where the light-front gauge $A^+ = 0$ has been considered for convenience.

In [36] the quark-gluon Qiu-Sterman function has been related to the first transverse moment of the quark Sivers function, that is, $f_{1T}^{\perp(1)q}(x) \propto T_{q,F}(x, x)/M$, where

$$f_{1T}^{\perp(1)q}(x) \equiv \int d^2 k_\perp \frac{\mathbf{k}_\perp^2}{2M^2} f_{1T}^{\perp q}(x, \mathbf{k}_\perp^2). \quad (7)$$

However, that relation was only established at tree level (beyond tree level the relation will be affected by the considered regularized definition of the Sivers TMD including its dependence on the soft factor). A similar tree level relation can be established in the gluon sector as well: $f_{1T}^{\perp(1)g}(x) \propto T_G(x, x)/M$ (where T_G that appears in this relation depends on the gauge links; see the discussion in Section 5).

Another relation has been established in [37]:

$$f_{1T}^{\perp q}(x, \mathbf{k}_\perp^2) \Big|_{\mathbf{k}_\perp^2 \gg M^2} \sim \alpha_s \frac{M}{\mathbf{k}_\perp^4} (K \otimes T_{q,F})(x), \quad (8)$$

which means that the quark-gluon Qiu-Sterman function determines the large transverse momentum tail of the quark Sivers function. Here it should be emphasized that the function $(K \otimes T_{q,F})(x)$ consists not only of a convolution of $T_{q,F}(x, x)$ but also of its derivative $x \partial T_{q,F}(x, x) / \partial x$ and of the more general $T_{q,F}(x, y)$ with $y \neq x$. It corresponds to the fact that the evolution of $T_{q,F}$ is nonautonomous and inhomogeneous; see [38]. Note that here we have discussed the nonsinglet contributions only that apply to combinations like u minus d quarks; otherwise also gluonic contributions need to be taken into account.

Similarly, the tail of the gluon Sivers function is determined by several Qiu-Sterman functions [39]. It receives contributions from the quark-gluon Qiu-Sterman functions $T_{q,F}(x, x)$ and $T_{q,F}(x, y)$ with $y \neq x$ and from the trigluon functions $T_G^{(f/d)}(x, x)$ (whose contribution to the gluon Sivers function depends on the gauge links; see Section 5). At small x the situation simplifies: the contributions from $T_{q,F}(x, x)$ and $T_{q,F}(x, y)$ with $y \neq x$ to the tail of the gluon Sivers function cancel each other [39], leaving only the trigluon correlators. Moreover, $T_G^{(d)}(x, x)$ evolves with the same $1/x$ behavior at small x as the unpolarized gluon distribution and is therefore not necessarily suppressed at high energies and small values of x , whereas $T_G^{(f)}(x, x)$ lacks this $1/x$ enhancement [35]. As the large p_T A_N data from RHIC are generally not in the small- x region of the polarized proton, except for negative x_F , any simplifications at small x should of course first be tested for validity.

Information from A_N measurements at sufficiently large p_T (in order to consider a collinear factorization description in the first place) can thus *in principle* reflect some information on Sivers functions (i.e., on the tails and perhaps also on first transverse moments), but *in practice* other twist-3 contributions beside the mentioned Qiu-Sterman functions, namely, chiral-odd and fragmentation function analogues, contribute to A_N [28, 40–42]. From the smallness of A_N in the midrapidity and backward (negative x_F) regions, one would generally conclude that gluonic and sea quark contributions to the transverse single spin asymmetry are not large, but a detailed analysis is required to determine precisely the size of the various contributions.

A_N for π^0 production at midrapidity has been measured by the PHENIX experiment in polarized pp collisions at RHIC and was found to be consistent with zero, for p_T values below 5 GeV at the permille level and for higher p_T values (up to 11 GeV) at the few percent level [21, 43]. These data taken at $\sqrt{s} = 200$ GeV probe x values only down to $x \sim 0.006$, where still a combination of Qiu-Sterman functions is expected to contribute. In [44] these π^0 data were discussed, using two models for the trigluon Qiu-Sterman functions that were constrained from A_N in D -meson production [45, 46]. The midrapidity π^0 data are shown to mostly constrain $T_G^{(f)}(x, x)$ (their $N(x)$) at low p_T . The authors conclude that “both models give tiny asymmetry due to the small partonic cross sections, so the form of the three-gluon correlation functions is not much constrained by the data in this region.” From this limited model study of both π^0 and D production one would conclude that $T_G^{(f)}(x, x)$ and $T_G^{(d)}(x, x)$ are in any case small, a permille fraction of x times the unpolarized gluon distribution. This should be investigated further with more general model forms that adhere to the correct small- x behavior and with more precise data. The experimental precision of A_N can be improved much further both at RHIC and especially at the AFTER@LHC experiment [47], which would have a luminosity factor of 10–100 times higher, if not more. Such improvement and the measurements of asymmetries for many different types of produced particles are required to separately constrain or determine the various Qiu-Sterman contributions.

In the GPM the smallness of A_N at midrapidity puts strong constraints on the effective gluon Sivers function. As explained, this gluon Sivers function captures the combined effect from several Qiu-Sterman contributions and may thus differ from the actual gluon Sivers function obtained from TMD-factorizing processes. In a recent GPM analysis [48], which is an updated analysis of [49], the *best fits* to the PHENIX midrapidity $\pi^0 A_N$ data indeed correspond to a small effective gluon Sivers function with respect to its theoretical bound determined by the unpolarized gluon. For example, for $x < 0.1$ it is at most only a few percent of the bound. However, the maximally allowed effective gluon Sivers function is still sizable though. Its first transverse moment is still found to be around 30% of the up quark Sivers function in the region $0.06 < x < 0.3$, which is consistent with findings from semi-inclusive DIS for the actual gluon Sivers function and also with theoretical expectations, as discussed in the next section. In addition, it should be mentioned that this GPM analysis assumes a Gaussian k_\perp dependence, which corresponds neither to the correct power-law tail of the Sivers function, (8), nor to the unpolarized gluon distribution. Given all the caveats that come with these results, one should be careful to draw a definite conclusion about the size of the actual gluon Sivers TMD from A_N data.

One should also specify clearly what one calls a small gluon Sivers function. It will depend on what one compares to, that is, whether that is to the unpolarized gluon that grows very rapidly at small x or to the up or down quark Sivers function for not too small x . At small x it becomes very important whether one discusses the f or d type contribution (see Section 5), which is an issue not addressed in the GPM studies of A_N .

3. Sivers Asymmetry in SIDIS

The Sivers effect leads to a $\sin(\phi_h - \phi_s)$ asymmetry in semi-inclusive DIS (SIDIS) [4], which has been observed in experiments using a proton target by HERMES [2, 50] and COMPASS [51] and using ^3He target by Jefferson Lab Hall A [52, 53]. The data follow to quite a good extent the expectations of a valence quark picture in the target and of favored fragmentation. In the proton case, π^+ thus shows the largest asymmetry (for large z values, the asymmetry is around 4–5% or even somewhat larger when a lower cut of $Q^2 > 4 \text{ GeV}^2$ is implemented instead of $Q^2 > 1 \text{ GeV}^2$ [50]). The π^- asymmetries are smaller and still compatible with zero. The K^\pm asymmetries are similar to the π^\pm asymmetries, but with larger errors. Sivers asymmetries on a deuteron target [54] are all consistent with zero. Fits to all these HERMES and COMPASS data, including the deuteron data using isospin symmetry, indicate that the Sivers function (f_{1T}^\perp) for u quarks in a proton is negative and for a d quark in a proton is positive and approximately equal in absolute value [55]. This fits the expectations from the limit of a large number of colors N_c [56, 57]:

$$f_{1T}^{\perp u}(x, \mathbf{k}_\perp^2) = -f_{1T}^{\perp d}(x, \mathbf{k}_\perp^2) + \mathcal{O}\left(\frac{1}{N_c}\right). \quad (9)$$

The flavor singlet combination of u and d is of the same order as the gluon contribution in N_c counting [58]. The latter is thus $1/N_c$ suppressed with respect to the flavor nonsinglet quark Sivers effect at not too small x ($x \sim 1/N_c$) [59].

Within the current accuracy, the SIDIS data do not require any sea quark or gluon contributions, which among other considerations (see Section 6) led Brodsky and Gardner to conclude that the gluon Sivers function is small or even zero (“absence of gluon orbital angular momentum”) [60]. The SIDIS data from HERMES, COMPASS, and Jefferson Lab Hall A are of course at rather modest Q^2 and not too small- x values, that is, in the valence region. One cannot yet draw any conclusions about the gluon Sivers function at higher Q^2 and smaller values of x . Moreover, the data certainly still allow for gluon Sivers contributions of the order of $1/N_c$ times the valence quark Sivers functions. This is evident from the fits by Anselmino et al. [55], where the first transverse moment of the u and d Sivers functions has error bands that are at least around 30% of the central values.

Note that the SSA in the “inclusive” process $ep \rightarrow hX$, where the back-scattered lepton is not observed [61, 62], does not allow for an interpretation in terms of TMDs, as the data are dominated by $Q^2 \approx 0$. Even for large p_T the appropriate factorization would be collinear factorization and the Sivers type of asymmetry would probe the Qiu-Sterman functions instead [63], which as discussed above have some relation to the Sivers TMDs, but only via the tail or possibly via the first transverse moment. The asymmetries for $p_T > 1$ GeV are found to be at the level of 5–10% for positive hadrons. Fits will need to make clear how much room there is for a gluon Qiu-Sterman effect. Given the fact that the gluon Qiu-Sterman function does not enter at leading order in α_s in this process, this room may be considerable.

4. Sivers Asymmetry in Other Processes

Several other pp scattering processes to access the gluon Sivers function have been suggested over the past years: $p^\uparrow p \rightarrow \text{jet jet}X$ [64], $p^\uparrow p \rightarrow DX$ [34, 44, 65], $p^\uparrow p \rightarrow \gamma X$ [66], $p^\uparrow p \rightarrow \gamma \text{jet}X$ [66, 67], $p^\uparrow p \rightarrow \gamma^* X \rightarrow \mu^+ \mu^- X$ [66], $p^\uparrow p \rightarrow \text{jet}X$ (single transverse spin asymmetries in jet production measured at RHIC [68, 69] at forward rapidities (the valence region) show very small asymmetries, which is probably due to a cancellation among u and d quark contributions [70]), $p^\uparrow p \rightarrow \pi \text{jet}X$ [71], and $p^\uparrow p \rightarrow \eta_{c/b} X$ [39]. Several of these processes are like A_N in (high- p_T) pion production, which means that they deal with twist-3 collinear factorization and only provide indirect or limited information about the gluon Sivers TMD. Several other processes run into the problem of TMD factorization breaking contributions [72] and hence are not safe. In principle they do probe TMDs but as a result of TMD factorization breaking contributions, conclusions about the gluon Sivers function from their measurements cannot be drawn safely. This applies, for instance, to the process $p^\uparrow p \rightarrow \text{jet jet}X$ (measured at RHIC to be small at the few percent level [73]), which moreover suffers from cancellations between u and d contributions and between the effects of initial and final state

interactions [74–76]. TMD factorization breaking would also apply to open heavy quark production: $p^\uparrow p \rightarrow Q\bar{Q}X$, such as $p^\uparrow p \rightarrow D^0 \bar{D}^0 X$; compare, for example, [77]. Whether the problem also applies to double heavy quarkonium production remains to be seen, because in practice the color singlet contributions may give the dominant contribution in that case. Among the hadronic collisions the processes having one or two color singlets in the final state would in any case be the safest. One very promising example is $p^\uparrow p \rightarrow \gamma \text{jet}X$ [67], where it depends on the rapidity of the photon and the jet, that is, on the x fraction of the parton in polarized proton, whether the gluon Sivers function dominates over the quark one or vice versa. Another very promising example is $p^\uparrow p \rightarrow J/\psi \gamma X$, which is predominantly initiated by gluon-gluon scattering (which is an order in α_s higher than the gluon contribution in $p^\uparrow p \rightarrow \gamma \text{jet}X$) and for which the color singlet contribution dominates over the color octet one to a large extent [78, 79]. The same applies to $p^\uparrow p \rightarrow J/\psi J/\psi X$ (see the contribution by Lansberg and Shao in this special issue). AFTER@LHC would be very well-suited for studying these processes.

SSA experiments could be done at AFTER@LHC where the beam of protons or lead ions of the LHC would collide with a fixed target that is transversely polarized. Such pp^\uparrow and $Pb p^\uparrow$ collisions would have a center-of-mass energy $\sqrt{s_{NN}}$ of 115 and 72 GeV, respectively, and have high luminosity and good coverage in the rapidity region of the transversely polarized target (mid and large x_p^\uparrow) [47]. Polarized Drell-Yan and prompt photon production studies could be done to measure the quark Sivers function very precisely, perhaps to the level that the gluon Sivers function becomes relevant, despite the large values of x in the polarized target. As mentioned γjet and $J/\psi \gamma$ production could be used to study the gluon Sivers effect directly, where the former would need specific selection of the rapidities. In addition, the comparison of $Pb p^\uparrow \rightarrow \gamma \text{jet}X$ and $pp^\uparrow \rightarrow \gamma \text{jet}X$ would give a further handle on determining the relative sizes of quark and gluon Sivers functions. Other processes, such as D -meson or J/ψ production, would allow a similar study of Qiu-Sterman functions, including the trigluon ones, which are of course interesting in their own right. See [28] for a more detailed and quantitative study of twist-3 transverse single spin asymmetries in proton-proton collisions at the AFTER@LHC experiment. All these possibilities offer a very interesting complementary opportunity or even a competitive alternative to the other existing high-energy particle physics spin projects aiming at studying the role of gluons in transversely polarized protons.

In electron-proton scattering one of the most promising processes to directly probe the gluon Sivers function is open charm production, $ep^\uparrow \rightarrow e' c \bar{c} X$, which could ideally be studied with an Electron-Ion Collider (EIC). By selecting the charm (or bottom) quark, one effectively eliminates the subprocesses $\gamma^* q \rightarrow qg$ and $\gamma^* \bar{q} \rightarrow \bar{q}g$ and becomes essentially (this assumes that intrinsic charm contributions are suppressed by selecting sufficiently small- x values) sensitive to $\gamma^* g \rightarrow c \bar{c}$ and thus to the gluon Sivers function (a similar

argument is used in the study of high- p_T hadron pairs in muon-deuteron and muon-proton scattering [80, 81], where photon-gluon fusion is expected to dominate. The relevant asymmetry $A_{UT}^{\sin(\phi_{2h}-\phi_S)}$ is found to be $-0.14 \pm 0.15(\text{stat.}) \pm 0.06(\text{syst.})$ at $\langle x_G \rangle = 0.13$ for the deuteron and $-0.26 \pm 0.09(\text{stat.}) \pm 0.08(\text{syst.})$ at $\langle x_G \rangle = 0.15$ for the proton. For the interpretation of the data in terms of the gluon Sivvers effect, Q^2 and p_T of each hadron need to be sufficiently large to trust factorization). Here the transverse momenta of the heavy quarks are considered to be almost back-to-back. There is no problem with TMD factorization breaking contributions of the type discussed in [72], but that does not mean that the process is as straightforward as SIDIS. Even in the case where one considers charm jets, one has to include a description of the transverse momentum distribution inside such a jet. It may be easier to consider $D^0 \bar{D}^0$ measurements (for a study of the twist-3 SSA in large $p_T D$ meson production in SIDIS, that is, $ep^\dagger \rightarrow e' DX$, see [33, 82]). In either case one deals with 3 TMDs. Such processes involve a different soft factor (in this case a vacuum correlator of 6 Wilson lines) compared to processes involving 2 TMDs as in SIDIS, affecting the predictability. This has been discussed at the one-loop level in [83]. The SSA in $ep^\dagger \rightarrow e' D^0 \bar{D}^0 X$ has been studied for some models of the gluon Sivvers function in [84]; compare Section 2.3.1 of [84]. This may be the “smoking gun” process for the gluonic Sivvers effect at an EIC. It should be mentioned though that it actually probes a different gluon Sivvers TMD than the hadronic processes discussed above. This is discussed in the next section. It shows that hadronic processes are complementary to DIS processes.

For completeness we mention that when comparing extractions of the gluon Sivvers TMD from different processes, one has to take care not only of the process dependence but also of the different energy scales. Under TMD evolution from one scale to another, the transverse momentum distribution changes. For details we refer to [85–90].

5. Process Dependence of the Gluon Sivvers Function

Once a set of processes that in principle allow probing the gluon Sivvers TMD has been obtained, one still has to take into account the fact that such TMD is process-dependent. For quarks the famous overall sign change between the Sivvers TMD probed in SIDIS and the one probed in Drell-Yan is expected [3, 91–93] and is currently under experimental investigation. For gluons the situation is more complicated as each gluon TMD depends on two gauge links (in the fundamental representation), so there are more possibilities [11, 94, 95]. The gauge link structure of the gluon distributions in $ep \rightarrow e' D^0 \bar{D}^0 X$ differs from the one in, for instance, $pp \rightarrow \gamma \text{jet} X$ (cf. [96] for the comparison at small x). Clearly, this will complicate the analysis of gluon Sivvers effect which will involve more than one gluon Sivvers function. In [11] it was demonstrated that any gluon Sivvers function

can be expressed in terms of two “universal” gluon Sivvers functions:

$$f_{1T}^{\perp g[U]}(x, \mathbf{k}_\perp^2) = \sum_{c=1}^2 C_{G,c}^{[U]} f_{1T}^{\perp g(Ac)}(x, \mathbf{k}_\perp^2), \quad (10)$$

where the coefficients $C_{G,c}^{[U]}$ are calculable for each partonic subprocess. The first transverse moments of the two distinct gluon Sivvers functions are related (at least at tree level) to the two distinct trigluon Qiu-Sterman functions $T_G^{(f/d)}$. Therefore, we will refer to the universal gluon Sivvers functions as $f_{1T}^{\perp g(f)}$ and $f_{1T}^{\perp g(d)}$. The two functions have different behavior under charge conjugation, just like $T_G^{(f)}$ is a matrix element of a C -even operator and $T_G^{(d)}$ of a C -odd operator.

The process $ep^\dagger \rightarrow e' D^0 \bar{D}^0 X$ is dominated by just one partonic subprocess $\gamma g \rightarrow q \bar{q}$ and thus probes the gluon Sivvers function with two future-pointing (+) links [97], which is $f_{1T}^{\perp g(f)}$ [11]. The process $p^\dagger p \rightarrow \gamma \text{jet} X$ probes the subprocesses $qg \rightarrow \gamma q$ and $q \bar{q} \rightarrow \gamma g$. If one selects kinematics such that one probes small- x values in the polarized proton, such that $qg \rightarrow \gamma q$ dominates, then this process accesses the gluon Sivvers with a future- and past-pointing link, which corresponds to $f_{1T}^{\perp g(d)}$. The theoretical expectations are different for these two cases.

6. Theoretical Constraints on Sivvers Function

Constraints on the unintegrated gluon Sivvers TMD $f_{1T}^{\perp g}(x, \mathbf{k}_\perp^2)$ from fits have to take into account that it is theoretically possible that both the quark and the gluon Sivvers TMD can have nodes in x and/or k_\perp [98, 99]. The possibility of a node in x is supported by the observation [35] that the splitting function for $T_G^{(f)}$ is negative at small x , in analogy to the Δg case. Fits to SIDIS data (studied with a rather restrictive parameterization and in a restricted kinematic range) do not appear to require a node [100], but that does not exclude this possibility. Especially when comparing data from different kinematic regions and different processes, this option should be kept in mind. Nodes can of course have a large effect on integrals of Sivvers functions, such as the first transverse moment (7) and its first Mellin moment (for parton a)

$$\langle \mathbf{k}_{\perp a} \rangle = -M(\hat{\mathbf{S}}_T \times \hat{\mathbf{P}}) \int dx f_{1T}^{\perp(1)a}(x), \quad (11)$$

which is the average transverse momentum inside a transversely polarized target. The notation $\langle \mathbf{k}_{\perp a} \rangle$ comes from [101]. This quantity is related to the Sivvers shift [102], the average transverse momentum shift orthogonal to the transverse spin direction, which is normalized to the zeroth transverse moment of the unpolarized TMD $f_1^{(0)}(x) \equiv \int d^2 k_\perp f_1(x, \mathbf{k}_\perp^2)$:

$$\langle k_\perp^y(x) \rangle_{UT_x} = M \frac{f_{1T}^{\perp(1)}(x; \mu, \zeta)}{f_1^{(0)}(x; \mu, \zeta)}. \quad (12)$$

Here only the y -component perpendicular to the transverse spin direction x is nonzero and therefore considered. Note

that the Sivers shift depends in principle on the renormalization scale μ and a rapidity variable ζ but also depends on the path of the gauge link (see below). Furthermore, there is the theoretical issue whether the transverse moments converge. For that reason a regularized version using Bessel moments has been suggested in [102], which for quarks has been evaluated on the lattice in [103]. The lattice calculation of the Sivers shift for $u - d$ is consistent with negative u and positive d Sivers functions in SIDIS, which are expectations that follow from general arguments on final state interactions [104], from a model-dependent relation to GPDs [105, 106] (see below) and from fits [107, 108].

As said above, $f_{1T}^{\perp(1)q}(x)$ has a (process-dependent!) relation to the Qiu-Sterman function $T_{q,F}(x, x)$, which so far only has been established at tree level and for quarks. In addition, Burkardt has suggested a model-dependent relation between the integrated quantity $f_{1T}^{\perp(1)}(x)$ and an integral over the GPD $E(x, \xi, \Delta^2)$ at zero skewness $\xi = 0$ (and only for quarks) [105]:

$$f_{1T}^{\perp(1)}(x) \propto \int d^2 b_{\perp} \bar{\mathcal{F}}(\mathbf{b}_{\perp}) \frac{\partial}{\partial b_y} \mathcal{E}(x, \mathbf{b}_{\perp}^2), \quad (13)$$

for a nucleon polarized in the transverse x direction. Here $\mathcal{E}(x, \mathbf{b}_{\perp}^2) \equiv \int (d^2 \Delta_{\perp} / (2\pi)^2) e^{-i\mathbf{b}_{\perp} \cdot \Delta_{\perp}} E(x, 0, -\Delta_{\perp}^2)$ and $\bar{\mathcal{F}}(\mathbf{b}_{\perp})$ is called the lensing function. This relation has been obtained in models [9, 105, 106, 109]. It allows relating $\langle \mathbf{k}_{\perp q} \rangle$ to the anomalous magnetic moment κ_q associated with the quark q :

$$\int dx \int d^2 b_{\perp} \mathcal{E}_q(x, \mathbf{b}_{\perp}^2) = \kappa_q, \quad (14)$$

albeit in a model-dependent and (due to the different integrals involved) only qualitative way. This relation does confirm the expectations for the relative signs between the u and d Sivers functions and has been used in [110] to fit SIDIS data for the Sivers effect with the integral constrained by the anomalous magnetic moments. Interestingly, this led to a new estimation of the quark total angular momentum which turned out to be in agreement with most common GPD extractions [111–115]. The relation between $\langle \mathbf{k}_{\perp q} \rangle$ and κ_q is also at the heart of the argument by Brodsky and Gardner of why a gluon Sivers function is expected to be small. Using that $\kappa_u^p = 2\kappa_p + \kappa_n = 1.673$ and $\kappa_d^p = 2\kappa_n + \kappa_p = -2.033$, one sees the opposite signs reflected, but since $|(\kappa_p + \kappa_n)/2| = 0.06 \ll \kappa_{p/n} \approx 1.8 - 1.9$ this suggests that there is little room for gluon contributions [60]. If $(\kappa_u^p + \kappa_d^p)/2$ is taken as a measure for κ_g^p , the latter is about 10% smaller than κ_q^p . This would suggest that κ_g^p is of order $1/N_c^2$ rather than $1/N_c$, which in turn would suggest a similar additional $1/N_c$ suppression for the gluon Sivers function. Clearly there are various (strong!) assumptions going into this type of argument, such that the conclusion can certainly not be taken at face value. Apart from the assumptions on the relation to the gluon Sivers function, it is not clear that one can use very low-energy quantities to deduce something about the size of the gluon contributions at energies around or above 1 GeV to begin with.

Burkardt derived a further constraint on the fully integrated quantity $\langle \mathbf{k}_{\perp a} \rangle$, nowadays referred to as the Burkardt

sum rule (BSR) [101], stating that the total transverse momentum of all partons in a transversely polarized proton must vanish [116]:

$$\langle \mathbf{k}_{\perp} \rangle = \sum_{a=q,\bar{q},g} \langle \mathbf{k}_{\perp a} \rangle = \mathbf{0}. \quad (15)$$

In terms of the Sivers function, the BSR takes the form [59]

$$\sum_{a=q,\bar{q},g} \int dx f_{1T}^{\perp(1)a}(x) = 0. \quad (16)$$

Its validity has been checked explicitly in a diquark spectator model in [117]. The fits to SIDIS data from [108] at the scale $Q^2 = 2.4 \text{ GeV}^2$ almost saturate the BSR already with the u and d quark contributions alone:

$$\begin{aligned} \langle k_{\perp u} \rangle &= 96_{-28}^{+60} \text{ MeV}, \\ \langle k_{\perp d} \rangle &= -113_{-51}^{+45} \text{ MeV}. \end{aligned} \quad (17)$$

The contributions of the sea quarks are all small and together allow the following range for the gluon contribution:

$$-10 \leq \langle k_{\perp g} \rangle \leq 48 \text{ MeV}. \quad (18)$$

This means there is certainly still room for a 30% contribution from gluons with respect to the valence quarks. Of course, it should be emphasized that these values were obtained under assumptions on the k_{\perp} dependence, the absence of nodes, and extrapolations outside the kinematic region accessed by the SIDIS experiments.

The derivation of the BSR by Burkardt [101] considers gauge links as they appear in SIDIS and involves a gluon correlator containing the antisymmetric f_{abc} structure constant of $SU(3)$. As shown in [94, 95], there is also a gluon correlator with the symmetric d_{abc} structure constant. As a consequence, inclusion of gauge links in the operator definition of TMD distributions gives rise to two distinct gluon Sivers functions, $f_{1T}^{\perp g(f)}$ and $f_{1T}^{\perp g(d)}$ (corresponding to the (Ac) label used in [11]). However, the BSR essentially expresses transverse momentum conservation. Since the momentum operator in QCD is C-even, only the gluon Sivers function $f_{1T}^{\perp g(f)}$ which is associated with a C-even operator is constrained by the BSR. The gluon Sivers function $f_{1T}^{\perp g(d)}$, which is associated with a C-odd operator, is not expected to satisfy a BSR where quark and gluon contributions cancel each other. Judging from the small- x behavior of $T_G^{(d)}(x, x)$ expected from its evolution equation, the integral of $f_{1T}^{\perp g(d)}$ over x may even not converge.

7. Conclusions

In summary, no hard constraints on the size of the gluon Sivers function exist apart from the positivity bound, although the theoretical expectation from large N_c considerations (expected to hold approximately for not too small x) favors a 30% gluon to quark Sivers ratio, which

is still completely allowed by all SIDIS data, including the COMPASS deuteron data. It may turn out that the ratio is smaller, but much smaller than 10% may in turn be considered unnaturally small. Strictly speaking, no direct conclusion about the size of the gluon Sivers function can be drawn from A_N data. Like $p^\uparrow p \rightarrow \pi X$, many other processes suggested in the literature to probe the gluon Sivers function actually deal with collinear factorization and as such they are sensitive to complicated linear combinations of quark-gluon and trigluon Qiu-Sterman functions (and chiral-odd and fragmentation function versions of them) rather than to Sivers functions directly. Inferring constraints on the gluon Sivers function, even on its large transverse momentum tail, must therefore be done with much care. In the Generalized Parton Model description of A_N at midrapidity, the *effective* gluon Sivers function is currently still allowed to be 30% of the up quark Sivers function, despite the smallness of the asymmetry. Other suggested processes that in principle probe TMDs may suffer from TMD factorization breaking contributions and any results on the gluon Sivers function from measurements of such processes cannot be trusted. This applies, for instance, to the process $p^\uparrow p \rightarrow \text{jet jet} X$.

The most promising processes that directly give access to the gluon Sivers effect are $p^\uparrow p \rightarrow \gamma \text{jet} X$, $p^\uparrow p \rightarrow J/\psi \gamma X$, and $ep^\uparrow \rightarrow e' c \bar{c} X$. The first process can be studied at RHIC and at a polarized fixed-target experiment at LHC (AFTER@LHC), the second process also at AFTER@LHC, and the third process at a possible future Electron-Ion Collider. Due to the inherent process dependence of TMDs, the gluon Sivers TMD probed is in principle different in these processes. They can be expressed in terms of two universal gluon Sivers functions that appear in different linear combinations in different processes. Extracting and comparing these universal functions is very interesting from a theoretical point of view. The fact that a difference can exist is a consequence of the non-Abelian nature of QCD. Both functions satisfy different theoretical constraints. Although TMD factorization is expected to hold for these processes, that has not been demonstrated yet to all orders. Apart from the process dependence, there is also the issue of modified soft factors to contend with still. Nevertheless, as far as experimentally demonstrating and measuring a gluon Sivers effect in transversely polarized protons, several complementary future possibilities exist, in which AFTER@LHC can play a very important role.

Conflict of Interests

The authors declare that there is no conflict of interests regarding the publication of this paper.

Acknowledgments

The authors wish to thank Mauro Anselmino, Maarten Buffing, Umberto D'Alesio, Jean-Philippe Lansberg, Piet Mulders, and Francesco Murgia for useful discussions and/or feedback on the text. C. Lorcé acknowledges support by the Belgian Fund F.R.S.-FNRS via the contract of Chargé de

Recherches. C. Pisano acknowledges support by the “Fonds Wetenschappelijk Onderzoek-Vlaanderen” (FWO) through a postdoctoral Pegasus Marie Curie Fellowship.

References

- [1] D. W. Sivers, “Single-spin production asymmetries from the hard scattering of pointlike constituents,” *Physical Review D*, vol. 41, no. 1, pp. 83–90, 1990.
- [2] A. Airapetian, N. Akopov, Z. Akopov et al., “Single-spin asymmetries in semi-inclusive deep-inelastic scattering on a transversely polarized hydrogen target,” *Physical Review Letters*, vol. 94, Article ID 012002, 2005.
- [3] J. C. Collins, “Leading-twist single-transverse-spin asymmetries: Drell–Yan and deep-inelastic scattering,” *Physics Letters B*, vol. 536, no. 1-2, pp. 43–48, 2002.
- [4] D. Boer and P. J. Mulders, “Time-reversal odd distribution functions in lepton production,” *Physical Review D: Particles, Fields, Gravitation and Cosmology*, vol. 57, no. 9, pp. 5780–5786, 1998.
- [5] M. Anselmino, M. Boglione, and F. Murgia, “Single spin asymmetry for $p^\uparrow p \rightarrow \pi X$ in perturbative QCD,” *Physics Letters B*, vol. 362, no. 1-4, pp. 164–172, 1995.
- [6] M. Anselmino, M. Boglione, U. D'Alesio, E. Leader, S. Melis, and F. Murgia, “General partonic structure for hadronic spin asymmetries,” *Physical Review D*, vol. 73, no. 1, Article ID 014020, 23 pages, 2006.
- [7] A. Bacchetta, U. D'Alesio, M. Diehl, and C. A. Miller, “Single-spin asymmetries: the Trento conventions,” *Physical Review D*, vol. 70, no. 11, Article ID 117504, 2004.
- [8] P. J. Mulders and J. Rodrigues, “Transverse momentum dependence in gluon distribution and fragmentation functions,” *Physical Review D*, vol. 63, Article ID 094021, 2001.
- [9] S. Meißner, A. Metz, and K. Goeke, “Relations between generalized and transverse momentum dependent parton distributions,” *Physical Review D*, vol. 76, Article ID 034002, 2007.
- [10] C. Lorcé and B. Pasquini, “Structure analysis of the generalized correlator of quark and gluon for a spin-1/2 target,” *Journal of High Energy Physics*, vol. 2013, no. 9, article 138, 2013.
- [11] M. G. A. Buffing, A. Mukherjee, and P. J. Mulders, “Generalized universality of definite rank gluon transverse momentum dependent correlators,” *Physical Review D*, vol. 88, Article ID 054027, 2013.
- [12] J. Collins, *Foundations of Perturbative QCD*, Cambridge University Press, 2011.
- [13] J. Collins, “New definition of tmd parton densities,” *International Journal of Modern Physics: Conference Series*, vol. 4, no. 85, 2011.
- [14] M. G. Echevarría, A. Idilbi, and I. Scimemi, “Soft and collinear factorization and transverse momentum dependent parton distribution functions,” *Physics Letters B*, vol. 726, no. 4-5, pp. 795–801, 2013.
- [15] M. G. Echevarría, T. Kasemets, P. J. Mulders, and C. Pisano, “QCD evolution of (un)polarized gluon TMDPDFs and the Higgs q_T -distribution,” *Journal of High Energy Physics*, 2015.
- [16] J. Antille, L. Dick, L. Madansky et al., “Spin dependence of the inclusive reaction $p + p$ (polarized) $\rightarrow \pi^0 + X$ at 24 GeV/c for high- $p_T \pi^0$ produced in the central region,” *Physics Letters B*, vol. 94, no. 4, pp. 523–526, 1980.
- [17] D. L. Adams, N. Akchurin, N. I. Belikov et al., “Analyzing power in inclusive π^+ and π^- production at high x_F with a 200 GeV

- polarized proton beam,” *Physics Letters B*, vol. 264, pp. 462–466, 1991.
- [18] D. L. Adams, N. Akchurin, N. I. Belikov et al., “Comparison of spin asymmetries and cross sections in π^0 production by 200 GeV polarized antiprotons and protons,” *Physics Letters B*, vol. 261, no. 1-2, pp. 201–206, 1991.
 - [19] K. Krueger, C. Allgower, T. Kasprzyk et al., “Large analyzing power in inclusive π^\pm production at high X_F with a 22-GeV/c polarized proton beam,” *Physics Letters B*, vol. 459, no. 1-3, pp. 412–416, 1999.
 - [20] J. Adams, C. Adler, M. M. Aggarwal et al., “Cross sections and transverse single-spin asymmetries in forward neutral-pion production from proton collisions at $\sqrt{s} = 200$ GeV,” *Physical Review Letters*, vol. 92, no. 17, Article ID 171801, 6 pages, 2004.
 - [21] S. S. Adler, S. Afanasiev, C. Aidala et al., “Measurement of transverse single-spin asymmetries for midrapidity production of neutral pions and charged hadrons in polarized $p + p$ collisions at $\sqrt{s} = 200$ GeV,” *Physical Review Letters*, vol. 95, no. 20, Article ID 202001, 6 pages, 2005.
 - [22] I. Arsene, I. G. Bearden, D. Beavis et al., “Single-transverse-spin asymmetries of identified charged hadrons in polarized pp collisions at $\sqrt{s} = 62.4$ GeV,” *Physical Review Letters*, vol. 101, Article ID 042001, 2008.
 - [23] B. I. Abelev, M. M. Aggarwal, Z. Ahammed et al., “Forward neutral-pion transverse single-spin asymmetries in $p + p$ collisions at $\sqrt{s}=200$ GeV,” *Physical Review Letters*, vol. 101, no. 22, Article ID 222001, 2008.
 - [24] L. Adamczyk, G. Agakishiev, M. M. Aggarwal et al., “Transverse single-spin asymmetry and cross section for π^0 and η mesons at large Feynman x in $p^\dagger + p$ collisions at $\sqrt{s} = 200$ GeV,” *Physical Review D*, vol. 86, Article ID 051101, 2012.
 - [25] A. Adare, S. Afanasiev, C. Aidala et al., “Measurement of transverse single-spin asymmetries for J/ψ production in polarized $p + p$ collisions at $\sqrt{s} = 200$ GeV,” *Physical Review D*, vol. 82, Article ID 112008, 2010, Erratum in *Physical Review D*, vol. 86, Article ID 099904, 2012.
 - [26] J. C. Collins, D. E. Soper, and G. Sterman, “Factorization of hard processes in QCD,” *Advanced Series on Directions in High Energy Physics*, vol. 5, pp. 1–9, 1988.
 - [27] M. Anselmino, U. D’Alesio, and S. Melis, “Transverse single-spin asymmetries in proton-proton collisions at the AFTER@LHC experiment in a TMD factorisation scheme,” <http://arxiv.org/abs/1504.03791>.
 - [28] K. Kanazawa, Y. Koike, A. Metz, and D. Pitonyak, “Transverse single-spin asymmetries in proton-proton collisions at the AFTER@LHC experiment,” <http://arxiv.org/abs/1502.04021>.
 - [29] M. Luo, J. Qiu, and G. Sterman, ITP-SB-91-56, C91-08-18.
 - [30] J. Qiu and G. Sterman, “Single transverse spin asymmetries,” *Physical Review Letters*, vol. 67, no. 17, pp. 2264–2267, 1991.
 - [31] J. Qiu and G. Sterman, “Single transverse-spin asymmetries in hadronic pion production,” *Physical Review D*, vol. 59, Article ID 014004, 1998.
 - [32] X. D. Ji, “Gluon correlations in the transversely polarized nucleon,” *Physics Letters B*, vol. 289, no. 1-2, pp. 137–142, 1992.
 - [33] Z. B. Kang and J. W. Qiu, “Single transverse-spin asymmetry for D -meson production in semi-inclusive deep inelastic scattering,” *Physical Review D*, vol. 78, no. 3, Article ID 034005, 11 pages, 2008.
 - [34] Z. B. Kang, J. W. Qiu, W. Vogelsang, and F. Yuan, “Accessing trigluon correlations in the nucleon via the single spin asymmetry in open charm production,” *Physical Review D*, vol. 78, no. 11, Article ID 114013, 9 pages, 2008.
 - [35] A. Schäfer and J. Zhou, “A note on the scale evolution of tri-gluon correlations,” <http://arxiv.org/abs/1308.4961>.
 - [36] D. Boer, P. J. Mulders, and F. Pijlman, “Universality of T-odd effects in single spin and azimuthal asymmetries,” *Nuclear Physics B*, vol. 667, no. 1-2, pp. 201–241, 2003.
 - [37] X. Ji, J. W. Qiu, W. Vogelsang, and F. Yuan, “Unified picture for single transverse-spin asymmetries in hard-scattering processes,” *Physical Review Letters*, vol. 97, Article ID 082002, 2006.
 - [38] V. M. Braun, A. N. Manashov, and B. Pirnay, “Scale dependence of twist-three contributions to single spin asymmetries,” *Physical Review D*, vol. 80, Article ID 114002, 2009, Erratum in: *Physical Review D*, vol. 86, Article ID 119902, 2012.
 - [39] A. Schäfer and J. Zhou, “Transverse single spin asymmetry in hadronic $\eta_{c,b}$ production,” *Physical Review D*, vol. 88, Article ID 014008, 2013.
 - [40] K. Kanazawa and Y. Koike, “New analysis of the single transverse-spin asymmetry for hadron production at RHIC,” *Physical Review D*, vol. 82, no. 3, Article ID 034009, 12 pages, 2010.
 - [41] K. Kanazawa and Y. Koike, “A phenomenological study of single transverse-spin asymmetry for inclusive light-hadron productions at RHIC,” *Physical Review D*, vol. 83, Article ID 114024, 2011.
 - [42] K. Kanazawa, Y. Koike, A. Metz, and D. Pitonyak, “Towards an explanation of transverse single-spin asymmetries in proton-proton collisions: the role of fragmentation in collinear factorization,” *Physical Review D*, vol. 89, no. 11, Article ID 111501, 5 pages, 2014.
 - [43] A. Adare, S. Afanasiev, C. Aidala et al., “Measurement of transverse-single-spin asymmetries for midrapidity and forward-rapidity production of hadrons in polarized $p + p$ collisions at $\sqrt{s} = 200$ and 62.4 GeV,” *Physical Review D*, vol. 90, Article ID 012006, 2014.
 - [44] H. Beppu, K. Kanazawa, Y. Koike, and S. Yoshida, “Three-gluon contribution to the single spin asymmetry for light hadron production in pp collision,” *Physical Review D*, vol. 89, Article ID 034029, 2014.
 - [45] H. Liu, “Transverse single spin asymmetry in heavy flavor production in polarized $p + p$ collisions at PHENIX,” *AIP Conference Proceedings*, vol. 1149, no. 1, pp. 439–442, 2009.
 - [46] Y. Koike and S. Yoshida, “Probing the three-gluon correlation functions by the single spin asymmetry in $p^\dagger p \rightarrow DX$,” *Physical Review D*, vol. 84, Article ID 014026, 2011.
 - [47] S. J. Brodsky, F. Fleuret, C. Hadjidakis, and J. P. Lansberg, “Physics opportunities of a fixed-target experiment using LHC beams,” *Physics Reports*, vol. 522, no. 4, pp. 239–255, 2013.
 - [48] U. D’Alesio, F. Murgia, and C. Pisano, “Towards a first estimate of the gluon Sivers function from A_N data in pp collisions at RHIC,” <http://arxiv.org/abs/1506.03078>.
 - [49] M. Anselmino, U. D’Alesio, S. Melis, and F. Murgia, “Constraints on the gluon Sivers distribution via transverse single spin asymmetries at midrapidity in $p^\dagger p \rightarrow \pi^0 X$ processes at BNL RHIC,” *Physical Review D*, vol. 74, no. 9, Article ID 094011, 7 pages, 2006.
 - [50] A. Airapetian, N. Akopov, Z. Akopov et al., “Observation of the naive- T -odd sivers effect in deep-inelastic scattering,” *Physical Review Letters*, vol. 103, Article ID 152002, 2009.
 - [51] C. Adolph, M. G. Alekseev, V. Y. Alexakhin et al., “II—experimental investigation of transverse spin asymmetries in μ - p SIDIS processes: sivers asymmetries,” *Physics Letters B*, vol. 717, no. 4-5, pp. 383–389, 2012.

- [52] X. Qian, K. Allada, C. Dutta et al., “Single spin asymmetries in charged pion production from semi-inclusive deep inelastic scattering on a transversely polarized ^3He target at $Q^2 = 1.4\text{--}2.7\text{ GeV}^2$,” *Physical Review Letters*, vol. 107, Article ID 072003, 2011.
- [53] Y. X. Zhao, Y. Wang, K. Allada et al., “Single spin asymmetries in charged kaon production from semi-inclusive deep inelastic scattering on a transversely polarized ^3He target,” *Physical Review C*, vol. 90, no. 5, Article ID 055201, 6 pages, 2014.
- [54] M. Alekseev, A. Amoroso, and V. Y. Alexakhin, “Collins and Sivers asymmetries for pions and kaons in muon–deuteron DIS,” *Physics Letters B*, vol. 673, no. 2, pp. 127–135, 2009.
- [55] M. Anselmino, M. Boglione, U. D’Alesio, S. Melis, F. Murgia, and A. Prokudin, “Sivers distribution functions and the latest SIDIS data,” <http://arxiv.org/abs/1107.4446>.
- [56] P. V. Pobylitsa, “Transverse-momentum dependent parton distributions in large- N_c QCD,” <http://arxiv.org/abs/hep-ph/0301236>.
- [57] A. Drago, “Time-reversal-odd distribution functions in chiral models with vector mesons,” *Physical Review D*, vol. 71, no. 5, Article ID 057501, 4 pages, 2005.
- [58] A. V. Efremov, K. Goeke, and P. V. Pobylitsa, “Gluon and quark distributions in large $N(c)$ QCD: theory versus phenomenology,” *Physics Letters, Section B: Nuclear, Elementary Particle and High-Energy Physics*, vol. 488, no. 2, pp. 182–186, 2000.
- [59] A. V. Efremov, K. Goeke, S. Menzel, A. Metz, and P. Schweitzer, “Sivers effect in semi-inclusive DIS and in the Drell-Yan process,” *Physics Letters B*, vol. 612, no. 3–4, pp. 233–244, 2005.
- [60] S. J. Brodsky and S. Gardner, “Evidence for the absence of gluon orbital angular momentum in the nucleon,” *Physics Letters B*, vol. 643, no. 1, pp. 22–28, 2006.
- [61] A. Airapetian, N. Akopov, Z. Akopov et al., “Transverse target single-spin asymmetry in inclusive electroproduction of charged pions and kaons,” *Physics Letters B*, vol. 728, pp. 183–190, 2014.
- [62] K. Allada, Y. X. Zhao, K. Aniol et al., “Single spin asymmetries of inclusive hadrons produced in electron scattering from a transversely polarized ^3He target,” *Physical Review C*, vol. 89, Article ID 042201, 2014.
- [63] Z. B. Kang, A. Metz, J. W. Qiu, and J. Zhou, “Exploring the structure of the proton through polarization observables in $l_p \rightarrow \text{jetX}$,” *Physical Review D*, vol. 84, Article ID 034046, 2011.
- [64] D. Boer and W. Vogelsang, “Asymmetric jet correlations in pp^\uparrow scattering,” *Physical Review D*, vol. 69, Article ID 094025, 2004.
- [65] M. Anselmino, M. Boglione, U. D’Alesio, E. Leader, and F. Murgia, “Accessing Sivers gluon distribution via transverse single spin asymmetries in $p^\uparrow p \rightarrow DX$ processes at BNL RHIC,” *Physical Review D—Particles, Fields, Gravitation and Cosmology*, vol. 70, no. 7, Article ID 74025, 2004.
- [66] I. Schmidt, J. Soffer, and J. J. Yang, “Transverse single spin asymmetries in photon production,” *Physics Letters B*, vol. 612, no. 3–4, pp. 258–262, 2005.
- [67] A. Bacchetta, C. Bomhof, U. D’Alesio, P. J. Mulders, and F. Murgia, “Sivers single-spin asymmetry in photon-jet production,” *Physical Review Letters*, vol. 99, no. 21, Article ID 212002, 2007.
- [68] L. Adamczyk, G. Agakishiev, M. M. Aggarwal et al., “Longitudinal and transverse spin asymmetries for inclusive jet production at mid-rapidity in polarized $p + p$ collisions at $\sqrt{s}=200\text{ GeV}$,” *Physical Review D*, vol. 86, p. 032006, 2012.
- [69] L. C. Bland, E. J. Brash, H. J. Crawford et al., “Cross sections and transverse single-spin asymmetries in forward jet production from proton collisions at $\sqrt{s} = 500\text{ GeV}$,” <http://arxiv.org/abs/1304.1454>.
- [70] M. Anselmino, M. Boglione, U. D’Alesio, S. Melis, F. Murgia, and A. Prokudin, “Sivers effect and the single spin asymmetry AN in $p^\uparrow p \rightarrow hX$ processes,” *Physical Review D: Particles, Fields, Gravitation and Cosmology*, vol. 88, no. 5, Article ID 054023, 2013.
- [71] U. D’Alesio, F. Murgia, and C. Pisano, “Azimuthal asymmetries for hadron distributions inside a jet in hadronic collisions,” *Physical Review D—Particles, Fields, Gravitation and Cosmology*, vol. 83, no. 3, Article ID 034021, 2011.
- [72] T. C. Rogers and P. J. Mulders, “No generalized transverse momentum dependent factorization in the hadroproduction of high transverse momentum hadrons,” *Physical Review D*, vol. 81, no. 9, Article ID 094006, 17 pages, 2010.
- [73] B. I. Abelev, M. M. Aggarwal, Z. Ahammed et al., “Measurement of transverse single-spin asymmetries for Dijet production in proton-proton collisions at $\sqrt{s} = 200\text{ GeV}$,” *Physical Review Letters*, vol. 99, Article ID 142003, 2007.
- [74] C. J. Bomhof, P. J. Mulders, W. Vogelsang, and F. Yuan, “Single-transverse spin asymmetry in dijet correlations at hadron colliders,” *Physical Review D*, vol. 75, no. 7, Article ID 074019, 2007.
- [75] J. W. Qiu, W. Vogelsang, and F. Yuan, “Single transverse-spin asymmetry in hadronic dijet production,” *Physical Review D*, vol. 76, Article ID 074029, 2007.
- [76] W. Vogelsang and F. Yuan, “Hadronic dijet imbalance and transverse-momentum-dependent parton distributions,” *Physical Review D*, vol. 76, no. 9, Article ID 094013, 6 pages, 2007.
- [77] S. Catani, M. Grazzini, and A. Torre, “Transverse-momentum resummation for heavy-quark hadroproduction,” *Nuclear Physics B*, vol. 890, pp. 518–538, 2015.
- [78] W. J. den Dunnen, J.-P. Lansberg, C. Pisano, and M. Schlegel, “Accessing the transverse dynamics and polarization of gluons inside the proton at the LHC,” *Physical Review Letters*, vol. 112, no. 21, Article ID 212001, 2014.
- [79] J. P. Lansberg, M. Anselmino, R. Arnaldi et al., “Spin physics and TMD studies at a fixed-target experiment at the LHC (AFTER@LHC),” *EPJ Web of Conferences*, vol. 85, Article ID 02038, 6 pages, 2015.
- [80] A. Szabelski, “Gluon contribution to the Sivers effect. COMPASS results on deuteron target,” *EPJ Web of Conferences*, vol. 85, Article ID 02006, 6 pages, 2015.
- [81] A. Szabelski and COMPASS Collaboration, “Results of the gluon Sivers asymmetry extraction from COMPASS data with transversely polarised targets,” in *Proceedings of the 7th International Conference on Quarks and Nuclear Physics (QNP ’15)*, Valparaiso, Chile, March 2015, <http://www.compass.cern.ch/compass/publications/talks/t2015/szabelski.qnp2015.pdf>.
- [82] H. Beppu, Y. Koike, K. Tanaka, and S. Yoshida, “Single transverse-spin asymmetry in large P_T open charm production at an electron-ion collider,” *Physical Review D*, vol. 85, Article ID 114026, 2012.
- [83] R. Zhu, P. Sun, and F. Yuan, “Low transverse momentum heavy quark pair production to probe gluon tomography,” *Physics Letters B*, vol. 727, no. 4–5, pp. 474–479, 2013.
- [84] D. Boer, M. Diehl, R. Milner et al., “Gluons and the quark sea at high energies: distributions, polarization, tomography,” <http://arxiv.org/abs/1108.1713>.
- [85] Z. B. Kang, B. W. Xiao, and F. Yuan, “QCD resummation for single spin asymmetries,” *Physical Review Letters*, vol. 107, Article ID 152002, 2011.

- [86] S. M. Aybat, J. C. Collins, J. W. Qiu, and T. C. Rogers, “QCD evolution of the Sivers function,” *Physical Review D: Particles, Fields, Gravitation and Cosmology*, vol. 85, no. 3, Article ID 034043, 2012.
- [87] M. Anselmino, M. Boglione, and S. Melis, “Strategy towards the extraction of the Sivers function with transverse momentum dependent evolution,” *Physical Review D*, vol. 86, no. 1, Article ID 014028, 2012.
- [88] P. Sun and F. Yuan, “Energy evolution for the Sivers asymmetries in hard processes,” *Physical Review D*, vol. 88, p. 034016, 2013.
- [89] D. Boer, “TMD evolution of the Sivers asymmetry,” *Nuclear Physics B*, vol. 874, no. 1, pp. 217–229, 2013.
- [90] M. G. Echevarria, A. Idilbi, Z. B. Kang, and I. Vitev, “QCD evolution of the Sivers asymmetry,” *Physical Review D*, vol. 89, no. 7, Article ID 074013, 2014.
- [91] S. J. Brodsky, D. S. Hwang, and I. Schmidt, “Final-state interactions and single-spin asymmetries in semi-inclusive deep inelastic scattering,” *Physics Letters B*, vol. 530, no. 1–4, pp. 99–107, 2002.
- [92] S. J. Brodsky, D. S. Hwang, and I. Schmidt, “Initial-state interactions and single-spin asymmetries in Drell-Yan processes,” *Nuclear Physics B*, vol. 642, no. 1–2, pp. 344–356, 2002.
- [93] A. V. Belitsky, X. Ji, and F. Yuan, “Final state interactions and gauge invariant parton distributions,” *Nuclear Physics B*, vol. 656, no. 1–2, pp. 165–198, 2003.
- [94] C. J. Bomhof and P. J. Mulders, “Gluonic pole cross sections and single spin asymmetries in hadron-hadron scattering,” *Journal of High Energy Physics*, vol. 2007, no. 2, article 029, 2007.
- [95] C. J. Bomhof and P. J. Mulders, “Non-universality of transverse momentum dependent parton distribution functions,” *Nuclear Physics B*, vol. 795, no. 1–2, pp. 409–427, 2008.
- [96] F. Dominguez, C. Marquet, B. W. Xiao, and F. Yuan, “Universality of unintegrated gluon distributions at small x ,” *Physical Review D*, vol. 83, no. 10, Article ID 105005, 27 pages, 2011.
- [97] C. Pisano, D. Boer, S. J. Brodsky, M. G. A. Buffing, and P. J. Mulders, “Linear polarization of gluons and photons in unpolarized collider experiments,” *Journal of High Energy Physics*, vol. 2013, no. 10, article 024, 2013.
- [98] D. Boer, “On a possible node in the Sivers and Qiu-Sterman functions,” *Physics Letters B*, vol. 702, no. 4, pp. 242–245, 2011.
- [99] Z. B. Kang, J. W. Qiu, W. Vogelsang, and F. Yuan, “Observation concerning the process dependence of the Sivers functions,” *Physical Review D*, vol. 83, no. 9, Article ID 094001, 9 pages, 2011.
- [100] Z. B. Kang and A. Prokudin, “Global fitting of single spin asymmetry: an attempt,” *Physical Review D*, vol. 85, Article ID 074008, 2012.
- [101] M. Burkardt, “Sivers mechanism for gluons,” *Physical Review D*, vol. 69, no. 9, Article ID 091501, 4 pages, 2004.
- [102] D. Boer, L. Gamberg, B. Musch, and A. Prokudin, “Bessel-weighted asymmetries in semi-inclusive deep inelastic scattering,” *Journal of High Energy Physics*, vol. 2011, no. 10, article 021, 2011.
- [103] B. U. Musch, P. Hägler, M. Engelhardt, J. W. Negele, and A. Schäfer, “Sivers and Boer-Mulders observables from lattice QCD,” *Physical Review D: Particles, Fields, Gravitation and Cosmology*, vol. 85, Article ID 094510, 2012.
- [104] M. Burkardt, “Impact parameter dependent parton distributions and transverse single spin asymmetries,” *Physical Review D*, vol. 66, Article ID 114005, 2002.
- [105] M. Burkardt, “Chromodynamic lensing and transverse single spin asymmetries,” *Nuclear Physics A*, vol. 735, no. 1–2, pp. 185–199, 2004.
- [106] M. Burkardt and D. S. Hwang, “Sivers effect and generalized parton distributions in impact parameter space,” *Physical Review D*, vol. 69, Article ID 074032, 2004.
- [107] M. Anselmino, M. Boglione, U. D’Alesio, A. Kotzinian, F. Murgia, and A. Prokudin, “Extracting the Sivers function from polarized semi-inclusive deep inelastic scattering data and making predictions,” *Physical Review D*, vol. 72, Article ID 094007, 2005, Erratum in: *Physical Review D*, vol. 72, Article ID 099903, 2005.
- [108] M. Anselmino, M. Boglione, U. D’Alesio et al., “Sivers effect for pion and kaon production in semi-inclusive deep inelastic scattering,” *The European Physical Journal A*, vol. 39, no. 1, pp. 89–100, 2009.
- [109] L. Gamberg and M. Schlegel, “Final state interactions and the transverse structure of the pion using non-perturbative eikonal methods,” *Physics Letters B*, vol. 685, no. 1, pp. 95–103, 2010.
- [110] A. Bacchetta and M. Radici, “Constraining quark angular momentum through semi-inclusive measurements,” *Physical Review Letters*, vol. 107, Article ID 212001, 2011.
- [111] M. Guidal, M. V. Polyakov, A. V. Radyushkin, and M. Vanderhaeghen, “Nucleon form factors from generalized parton distributions,” *Physical Review D—Particles, Fields, Gravitation and Cosmology*, vol. 72, no. 5, Article ID 054013, 2005.
- [112] M. Diehl, T. Feldmann, R. Jakob, and P. Kroll, “Generalized parton distributions from nucleon form factor data,” *European Physical Journal C*, vol. 39, no. 1, 2005.
- [113] S. Ahmad, H. Honkanen, S. Liuti, and S. K. Taneja, “Generalized parton distributions from hadronic observables: zero skewness,” *Physical Review D*, vol. 75, no. 9, Article ID 094003, 19 pages, 2007.
- [114] S. V. Goloskokov and P. Kroll, “The target asymmetry in hard vector-meson electroproduction and parton angular momenta,” *European Physical Journal C*, vol. 59, no. 4, pp. 809–819, 2009.
- [115] M. Diehl and P. Kroll, “Nucleon form factors, generalized parton distributions and quark angular momentum,” *The European Physical Journal C*, vol. 73, article 2397, 2013.
- [116] C. Lorcé, “The light-front gauge-invariant energy-momentum tensor,” <http://xxx.tau.ac.il/abs/1502.06656>.
- [117] K. Goeke, S. Meissner, A. Metz, and M. Schlegel, “Checking the Burkardt sum rule for the Sivers function by model calculations,” *Physics Letters B*, vol. 637, no. 4–5, pp. 241–244, 2006.

Review Article

Studies of Backward Particle Production with a Fixed-Target Experiment Using the LHC Beams

Federico Alberto Ceccopieri

IFPA, Université de Liège, Allée du 6 Août, 4000 Liège, Belgium

Correspondence should be addressed to Federico Alberto Ceccopieri; federico.alberto.ceccopieri@cern.ch

Received 19 March 2015; Revised 28 May 2015; Accepted 17 June 2015

Academic Editor: Jean-Philippe Lansberg

Copyright © 2015 Federico Alberto Ceccopieri. This is an open access article distributed under the Creative Commons Attribution License, which permits unrestricted use, distribution, and reproduction in any medium, provided the original work is properly cited. The publication of this article was funded by SCOAP³.

The foreseen capability to cover the far backward region at a Fixed-Target Experiment using the LHC beams allows one to explore the dynamics of the target fragmentation in hadronic collisions. In this report we briefly outline the required theoretical framework and discuss a number of studies of forward and backward particle production. By comparing this knowledge with the one accumulated in Deep Inelastic Scattering on target fragmentation, the basic concept of QCD factorisation could be investigated in detail.

1. Introduction

In hadronic collisions a portion of the produced particle spectrum is characterised by hadrons carrying a sizeable fraction of the available centre-of-mass energy, the so-called leading particle effect. It is phenomenologically observed that for such hadrons their valence-parton composition is almost or totally conserved with respect to the one of initial-state hadrons [1]. In pp collisions, for example, protons, neutrons, and lambdas show a significant leading particle effect. For such processes, the production cross section peaks at very small transverse momenta with respect to the collision axis, a regime where perturbative techniques cannot be applied, giving insight into nonperturbative aspects of QCD dynamics in high energy collisions.

Quite interestingly, the leading particle effect has been observed in Semi-Inclusive Deep Inelastic Scattering (SIDIS). At variance with the hadronic processes mentioned above, such a process naturally involves a large momentum transfer. The presence of a hard scale enables the derivation of a dedicated factorisation theorem [2–5] which ensures that QCD factorisation holds for backward particle production in DIS. The relevant cross sections can then be factorised into perturbatively calculable short distance cross sections and new distributions, fracture functions, which simultaneously encode information both on the interacting parton and on the spectator fragmentation into the observed hadron. Despite of

being nonperturbative in nature, their scale dependence can be calculated within perturbative QCD [6]. The factorisation theorem [2–5] guarantees that fracture functions are universal distributions, at least in the context of SIDIS.

Detailed experimental studies of hard diffraction at HERA have shown to support the hypothesis of QCD factorisation and evolution inherent the fracture function formalism. Furthermore, they led to a quite accurate knowledge of diffractive parton distributions [7–11], a special case of fracture functions in the very backward kinematic limit. For particles other than protons, proton-to-neutron fracture functions have been extracted from a pQCD analysis of forward neutron production in DIS in [12]. A set of proton-to-lambda fracture functions has been obtained by performing a combined pQCD fit to a variety of semi-inclusive DIS lambda production data in [13].

As theoretically anticipated in [2–4, 14, 15] and experimentally observed in hard diffraction in $p\bar{p}$ collisions at Tevatron [16, 17], QCD factorisation is violated for fracture functions in hadronic collisions. On general grounds, it might be expected, in fact, that the dynamics of target-remnants hadronisation is affected by the coloured environment resulting from the scattering in a rather different way with respect to the Deep Inelastic Scattering case.

Nonetheless, the tools mentioned above allow us to investigate quantitatively particle production mechanisms in

the very backward and forward regions, to test the concept of factorisation at the heart of QCD, and to study the dependencies of factorisation breaking upon the species and the kinematics of the selected final state particle.

This physics program could be successfully carried on at a Fixed-Target Experiment using the LHC beams [18]. Novel experimental techniques are, in fact, available to extract beam-halo protons or heavy ions from LHC beams without affecting LHC performances. Such a resulting beam would be then impinged on a high-density and/or long-length fixed target, guaranteeing high luminosities. Furthermore, most importantly for the physics program to be discussed here, the entire backward hemisphere (in the centre-of-mass system of the collision) would be accessible with standard experimental techniques allowing high precision studies of the target fragmentation. Although measurements of particle production in the very forward region (close to the beam axis) might be challenging experimentally due to the high particle densities and large energy flow, the installation of dedicated detectors, like forward neutron calorimeters and/or proton taggers, could further broaden the physics program outlined above giving access to the beam fragmentation region.

The paper is organised as follows. In Section 2 we first give a brief theoretical introduction on the fracture functions formalism and to higher order corrections to the semi-inclusive Drell-Yan process. In Section 3 we outline different analyses which could be performed at AFTER@LHC with special focus on single hard diffraction. In Section 4 we summarise our results.

2. Collinear Factorisation Formula

Fracture functions, originally introduced in DIS, do depend on a large momentum transfer. Therefore, in order to use them in hadronic collisions, a hard process must be selected. We consider here the semi-inclusive version of the Drell-Yan process:

$$H_1(P_1) + H_2(P_2) \longrightarrow H(h) + \gamma^*(q) + X, \quad (1)$$

in which one hadron H is measured in the final state together with a Drell-Yan pair. In such a process the high invariant mass of the lepton pair, $q^2 = Q^2$, allows the applicability of perturbative QCD, while the detected hadron H can be used, without any phase space restriction, as a local probe to investigate particle production mechanisms.

The associated production of a particle and a Drell-Yan pair in terms of partonic degrees of freedom starts at $\mathcal{O}(\alpha_s)$. One of the contributing diagrams is depicted in Figure 1.

Assuming that the hadronic cross sections admit a factorisation in terms of long distance nonperturbative distributions and short distance perturbative calculable matrix elements for the partonic process $i(p_1) + j(p_2) \rightarrow l(k) + \gamma^*(q)$, predictions based on perturbative QCD are obtained convoluting the relevant partonic subprocess cross sections, $d\hat{\sigma}^{ij \rightarrow l\gamma^*}$, with parton distribution functions, f_{i/H_1} and f_{j/H_2} ,

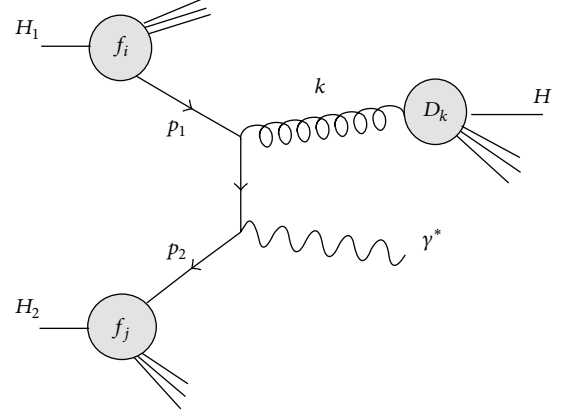


FIGURE 1: Example of diagram contributing to hadron production in the central fragmentation region to order $\mathcal{O}(\alpha_s)$ in (2).

and fragmentation functions, $D^{H/l}$. The hadronic cross section, at centre of mass energy squared $s = (P_1 + P_2)^2$, can be symbolically written as [19, 20]

$$\frac{d\sigma^{H,C,(1)}}{dQ^2 dz} \propto \sum_{i,j,l} \int \frac{dx_1}{x_1} \int \frac{dx_2}{x_2} \int \frac{d\rho}{\rho} f_i^{[1]}(x_1) f_j^{[2]}(x_2) \cdot D^{H/l}\left(\frac{z}{\rho}\right) \frac{d\hat{\sigma}^{ij \rightarrow l\gamma^*}}{dQ^2 d\rho}, \quad (2)$$

where the convolutions are over the momentum fractions of the incoming and outgoing partons. The partonic indices i , j , and l in the sum run on the available partonic subprocesses. The superscripts label the incoming hadrons and the presence of crossed terms is understood. This type of factorised hadronic cross section is expected to hold for hadrons produced at sufficiently high transverse momentum and it is widely and successfully used to compute cross sections for large momentum transfer processes in hadronic collisions. The Lorentz-invariant variable z in (2) is defined by

$$z = \frac{2h \cdot (P_1 + P_2)}{s} \equiv \frac{2E_H^*}{\sqrt{s}}. \quad (3)$$

In the hadronic centre-of-mass frame, where the second identity holds, z is just the observed hadron energy, E_H^* , scaled down by the beam energy $\sqrt{s}/2$. The variable ρ , appearing in (2), is its partonic equivalent. Within this production mechanism, the observed hadron H is generated by the fragmentation of the final state parton l , and for this reason we address it as *central*. The amplitudes squared [21], however, are singular when the transverse momentum of the final state parton vanishes. In such configurations, the parent parton l of the observed hadron H is collinear either to the incoming parton i or j . As these phase space regions are approached, perturbation theory loses its predictivity. This class of collinear singularities escape the usual renormalisation procedure which amounts to reabsorb collinear divergences into a redefinition of bare parton distribution and fragmentation functions. Such singularities are likely to

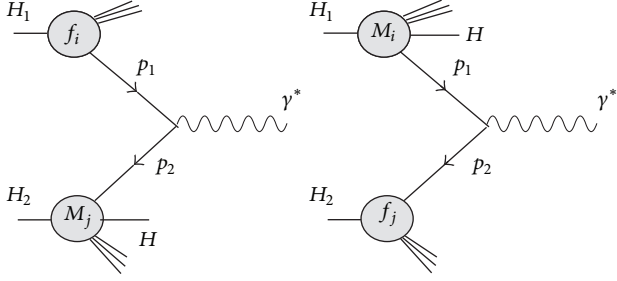


FIGURE 2: Pictorial representation of the parton model formula (4) for the associated production of a Drell-Yan pair and a particle in the target fragmentation regions.

appear in every fixed order calculation in the same kinematical limits spoiling the convergence of the perturbative series. In [19, 20] a generalised procedure for the factorisation of such additional collinear singularities is proposed. The latter is the same as the one proposed in Deep Inelastic Scattering [22] where the same singularities pattern is also found, confirming the universality of collinear radiation between different hard processes. Such a generalised collinear factorisation makes use of fracture functions. These distributions obey DGLAP-type evolution equations which contain an additional inhomogeneous term resulting from the subtraction of collinear singularities in the target fragmentation region [6, 22]. Such equations allow us to resume the corresponding large logarithmic corrections to all orders in perturbation theory. Bare fracture functions, $M_i^{H/H_1}(x, z)$, describe the hadronization of the spectators system in hadron-induced reactions. They express the conditional probability to find a parton i initiating the hard scattering while a hadron H is produced with fractional momentum z in the target fragmentation region of the incoming hadron H_1 .

The use of fracture functions allows for particles production already to $\mathcal{O}(\alpha_s^0)$, since the hadron H can be nonperturbatively produced by a fracture function itself. Therefore, the lowest order parton model formula can be symbolically written as

$$\frac{d\sigma^{H,T,(0)}}{dQ^2 dz} \propto \sum_{i,j} \int \frac{dx_1}{x_1} \int \frac{dx_2}{x_2} \cdot [M_i^{[1]}(x_1, z) f_j^{[2]}(x_2) + M_i^{[2]}(x_2, z) f_j^{[1]}(x_1)] \cdot \frac{d\hat{\sigma}^{ij \rightarrow \gamma^*}}{dQ^2} \quad (4)$$

and it is sketched in Figure 2. The superscripts in (4) indicate from which incoming hadron, H_1 or H_2 , the outgoing hadron H is produced through a fracture function. In order to complete the calculation to $\mathcal{O}(\alpha_s)$ accuracy we should consider higher order corrections to (4). Since in this case the hadron H is already produced by fracture functions, final state parton radiation should be integrated and the resulting contribution added to virtual corrections. One of

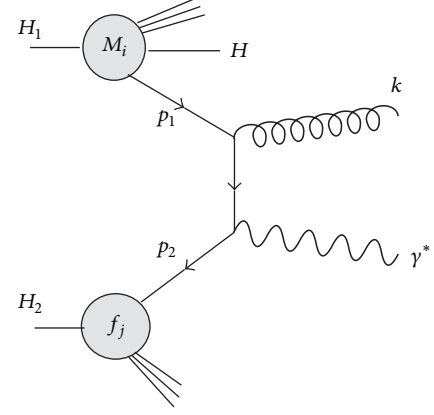


FIGURE 3: Example of diagram contributing to $\mathcal{O}(\alpha_s)$ corrections in the target fragmentation region (5).

the contributing diagrams is depicted in Figure 3. The general structure of these terms is

$$\frac{d\sigma^{H,T,(1)}}{dQ^2 dz} \propto \sum_{i,j} \int \frac{dx_1}{x_1} \int \frac{dx_2}{x_2} \cdot [M_i^{[1]}(x_1, z) f_j^{[2]}(x_2) + M_i^{[2]}(x_2, z) f_j^{[1]}(x_1)] \cdot \frac{d\hat{\sigma}^{ij \rightarrow (l)\gamma^*}}{dQ^2}. \quad (5)$$

We refer to them as to the *target fragmentation contributions*. Their calculation is, apart from minor differences in kinematics, completely analogous to the one of the inclusive Drell-Yan case. The factorisation procedure, first elaborated in [22] in the context of SIDIS, amounts to substitute in (4) the bare fracture and parton distributions functions with their renormalised version [19, 20]. Renormalised parton distributions and fracture functions homogeneous terms do cancel, as in the inclusive Drell-Yan case, all singularities present in (5). The additional singularities in (2) are cancelled by the combination of parton distributions and fracture functions inhomogeneous renormalisation terms. Adding all the various contributions, the resulting hadron- p_t integrated cross section, up to order $\mathcal{O}(\alpha_s)$, is then infrared finite [19, 20] and can be symbolically written as

$$\frac{d\sigma^H}{dQ^2 dz} = \frac{\sigma_0}{N_c s} \sum_{i,j} [M_i^{[1]} \otimes f_j^{[2]} + M_i^{[2]} \otimes f_j^{[1]}] \left(1 + \frac{\alpha_s}{2\pi} C^{ij} \right) + \frac{\sigma_0}{N_c s} \frac{\alpha_s}{2\pi} \sum_{i,j,l} f_i^{[1]} \otimes f_j^{[2]} \otimes D^{H/l} \otimes K_l^{ij}, \quad (6)$$

where $\sigma_0 = 4\pi\alpha_{em}^2/3Q^2$ and N_c is the number of colors. We refer to the previous equation as to the collinear factorisation formula for the process under study. The next-to-leading order coefficients C^{ij} and K_l^{ij} have been calculated

in [20], making the whole calculation ready for numerical implementation.

We stress, however, that our ability to consistently subtract collinear singularities in such a semi-inclusive process is a necessary but not sufficient condition for factorisation to hold in hadronic collisions. The one-loop calculation outlined above in fact does involve only the so-called active partons. It completely ignores multiple soft parton exchanges between active and spectators partons, whose effects should be accounted for in any proof of QCD factorisation. Therefore, there is no guarantee that fracture functions extracted from SIDIS can be successfully used to describe forward or backward particle production in hadronic collisions. Reversing the argument, such a comparison may instead offer new insights into nonperturbative aspects of QCD and to the breaking of factorisation.

3. Single Hard Diffraction at AFTER@LHC

As an application of the formalism presented in the previous sections we will consider single hard diffractive production of a Drell-Yan pair:

$$p_1(P_1) + p_2(P_2) \longrightarrow p(P) + \gamma^*(q) + X, \quad (7)$$

where we have indicated in parentheses the four momenta of the relevant particles. We present in the following cross sections differential in the virtual photon variables. The subsequent decay of the virtual photon into a lepton pair can be easily included so that realistic cuts on leptons rapidity and transverse momentum can then be applied. We consider the AFTER@LHC kinematic setting in which a 7 TeV proton beam collides on a fixed target proton leading to a centre-of-mass energy of $\sqrt{s} = 115$ GeV. We consider the projectile proton p_1 moving in the positive z direction and p_2 at rest in the laboratory. The diffractively produced proton p has in general almost the incoming projectile proton p_1 energy and very small transverse momentum as measured with respect to the collision axis. The detection of such fast protons will in general require the installation of forward proton taggers. The lepton pair instead will be measured by the main AFTER@LHC detector. This kinematical configuration is pictorially represented in the right plot of Figure 2.

Diffractive processes have been intensively analysed in DIS at HERA ep collider, revealing their leading twist nature. From scaling violations of the diffractive structure functions [7, 10, 11] and dijet production in the final state [8, 9] quite precise diffractive parton distributions functions (dPDFs) have been extracted from HERA data, which parametrise the parton content of the color singlet exchanged in the t -channel. The comparison of QCD predictions for single diffractive hard processes based on diffractive parton distributions measured at HERA against data measured at Tevatron [16, 17] ($\sqrt{s} = 1.96$ TeV), adopting a factorised ansatz as in (4), has indeed revealed that these processes are, not unexpectedly [14, 15], significantly suppressed in hadronic collisions. This conclusion persists even after the inclusion of higher order QCD corrections [23]. Complementing these results with the forthcoming ones from LHC at higher centre-of-mass

energies ($\sqrt{s} = 13$ TeV) and the ones from AFTER@LHC at $\sqrt{s} = 115$ GeV will give insight into the energy dependence of the so-called rapidity gap survival (RGS) probability in a wide range in \sqrt{s} . Since the theoretical computation of the RGS factor is highly model dependent, we decided not to include it in our predictions. Therefore, the latter must be considered as upper bounds.

Diffractive parton distributions f_i^D are in general proton-to-proton fracture functions M_i . They depend upon the final state proton fractional energy loss, $x_{\text{IP}} = 1 - z$ with z given in (3), the fractional momentum of the interacting parton with respect to the pomeron momentum, $\beta = x/x_{\text{IP}}$ and the virtuality Q^2 . In general fracture functions may depend also upon the invariant momentum transfer $t = (P - P_1)^2$ at the proton vertex [24]. In all diffractive structure functions measurements at HERA, out of which dPDFs are determined, t is integrated up to some $t^{\text{max}} \ll Q^2$. In this case dPDFs obey ordinary DGLAP evolution equations [25] as their extended, t -dependent version [24]. In the present paper we use dPDFs form [7] which are defined by $|t| < 1 \text{ GeV}^2$. Since they are extracted from large rapidity gap data where the proton is not directly measured, they contain a contribution (23%) from the so-called proton dissociation contribution. In order to use dPDFs in the present context we first note that

$$M_i(x_1, z, Q^2) = x_{\text{IP}}^{-1} f_i^D(\beta, x_{\text{IP}}, Q^2). \quad (8)$$

The extra factor x_{IP}^{-1} comes from the Jacobian of the change $x_1 = \beta x_{\text{IP}}$. We then rearrange (4) in terms of new variables obtaining

$$\begin{aligned} & \frac{d\sigma^D}{dQ^2 dx_{\text{IP}}} \\ &= \frac{\sigma_0}{N_c s} \int_{\tau/x_{\text{IP}}}^1 \frac{d\beta}{\beta} \sum_{q, \bar{q}} e_q^2 x_{\text{IP}}^{-1} f_q^D(\beta, x_{\text{IP}}, \mu_F^2) f_{\bar{q}}\left(\frac{\tau}{\beta x_{\text{IP}}}, \mu_F^2\right), \end{aligned} \quad (9)$$

with $\tau = Q^2/s$. For simplicity we consider here leading order formulas but the extension to higher order is straightforward. In (9) we use parton distribution functions from [26]. We show explicitly the dependence of fracture and parton distributions functions upon the factorisation scale, μ_F^2 . Predictions are obtained with this scale set to $\mu_F^2 = Q^2$. Theoretical errors associated with higher order corrections are instead estimated varying such scale in the range $\mu_F^2 = 1/4 Q^2$ and $\mu_F^2 = 4 Q^2$.

In Figure 4 we present predictions for the x_{IP} distribution. In left plot we consider a Drell-Yan pair of mass $Q^2 = 100 \text{ GeV}^2$. The distribution shrinks as lower x_{IP} -values are approached whereas, from hard diffraction at HERA, it is well known that diffractive cross sections rise as an inverse power of x_{IP} . Such an effect therefore is then attributed to phase space threshold effects. The Drell-Yan invariant mass constraint can be rewritten in the diffractive case as $Q^2 = \beta x_{\text{IP}} x_2 s$, which can be cast (for $\beta \rightarrow 1$ and $x_2 \rightarrow 1$) in upper bound on the invariant mass $Q^2 < x_{\text{IP}} s$ at fixed x_{IP} and s . This hypothesis is further supported in the right plot of Figure 4, where differential distributions are presented for three values of Q^2 . The lowest values of x_{IP} are then accessed

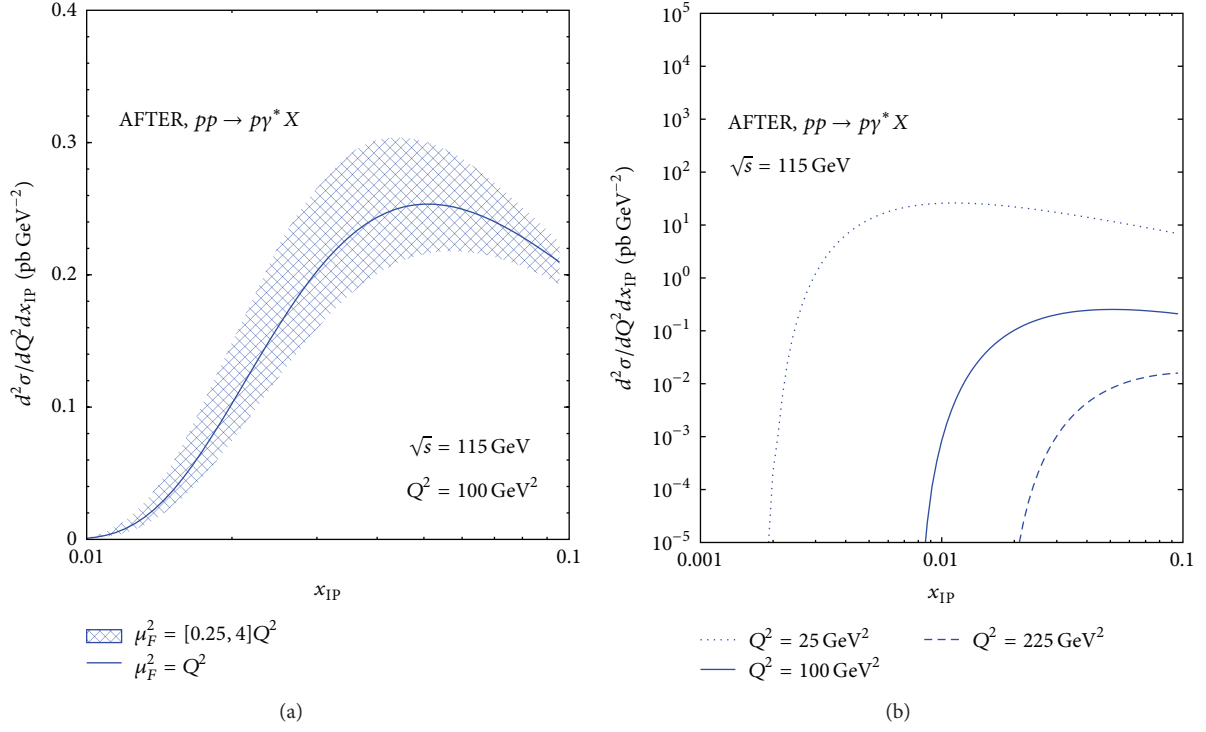


FIGURE 4: (a) Double differential cross sections for the production of a Drell-Yan pair of mass $Q^2 = 100 \text{ GeV}^2$. Blue error bands represent theoretical errors estimation, as described in the text. (b) Double differential cross sections for three different invariant masses.

only by lowering the invariant mass of the pair. We note that, even considering the maximum value of $x_{\text{IP}} = 0.1$, single diffractive production of W^\pm and Z is beyond the kinematic reach at AFTER@LHC. In the left panel of Figure 5 we present the prediction for the Q^2 distribution at a fixed value of $x_{\text{IP}} = 0.05$. The cross section, as expected, is fast falling as an inverse power of Q^2 . The Q^2 distribution is particularly instructive since it allows us to study the possible dependence of the RGS factor on Q^2 and therefore to get an insight into the underlying dynamics. In the right panel of Figure 5 we present the Q^2 -differential cross section multiplied by a factor Q^4 , which compensates the fast fall off of the electromagnetic cross section so that all the Q^2 dependence is accounted for by that of fracture and parton distributions. These curves and the corresponding slopes, however, can not be readily interpreted as genuine results of QCD evolution of fracture and parton distributions functions because of the threshold effect mentioned above appearing at such moderate values of \sqrt{s} .

By changing variable from β to the virtual photon centre-of-mass rapidity, y^{CM} ,

$$\begin{aligned} \beta &= \frac{\sqrt{\tau}}{x_{\text{IP}}} e^{y^{\text{CM}}}, \\ x_2 &= \sqrt{\tau} e^{-y^{\text{CM}}}, \end{aligned} \quad (10)$$

equation (9) can be further manipulated to give the three-differential cross section:

$$\begin{aligned} \frac{d\sigma^D}{dQ^2 dx_{\text{IP}} dy^{\text{CM}}} &= \frac{\sigma_0}{N_c s} \sum_{q, \bar{q}} e_q^2 x_{\text{IP}}^{-1} f_q^D(\beta, x_{\text{IP}}, \mu_F^2) f_{\bar{q}}(x_2, \mu_F^2). \end{aligned} \quad (11)$$

The rapidity range for diffractive Drell-Yan production reads

$$\ln \sqrt{\tau} < y^{\text{CM}} < \ln \frac{\sqrt{\tau}}{x_{\text{IP}}} \quad (12)$$

which, as expected, turns out to be asymmetric given the kinematic constraint $x_1 < x_{\text{IP}}$. The rapidity range for the inclusive Drell-Yan case is recovered simply setting $x_{\text{IP}} = 1$. The rapidity distribution is particularly sensitive to the shape of the diffractive parton distributions. This distribution will be useful to investigate any possible kinematic dependence of the RGS factor. In the left panel of Figure 6 we present the centre-of-mass rapidity distribution at fixed $Q^2 = 100 \text{ GeV}^2$ and $x_{\text{IP}} = 0.05$. In this frame the distribution is shifted at negative values of y^{CM} . Therefore, on average, the parton originating from the target proton carries more momentum than the one originating from the pomeron. Since the rapidity

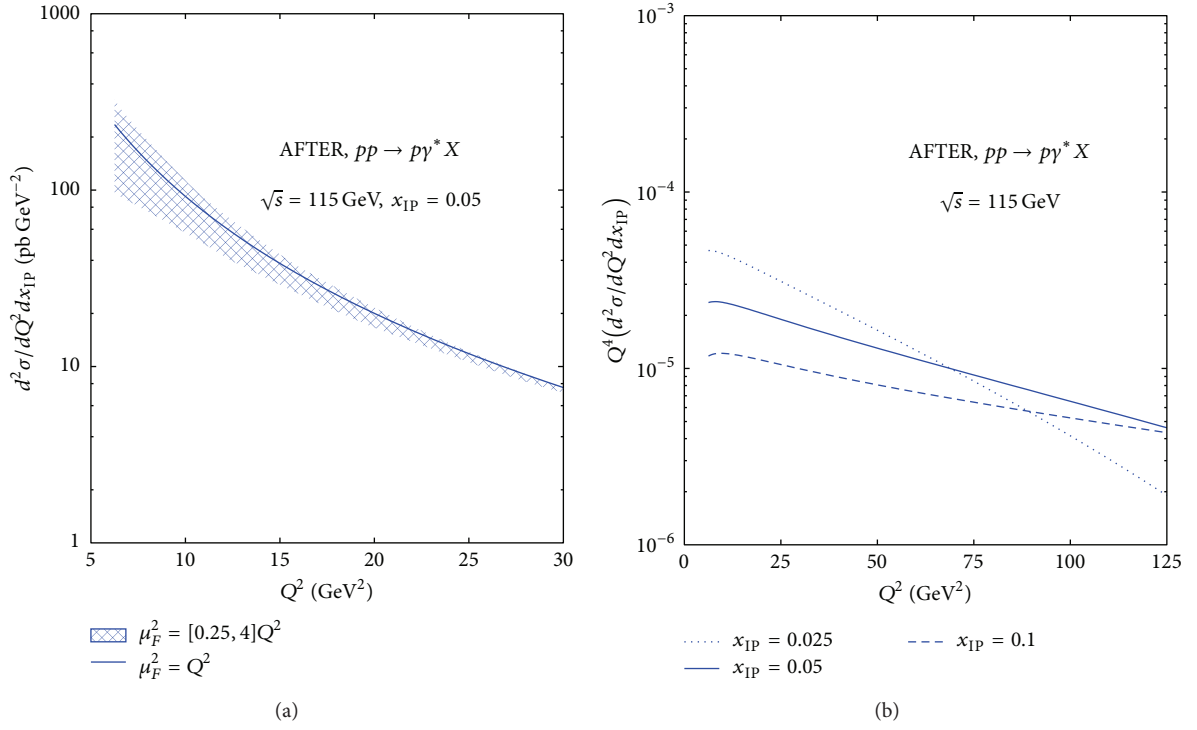


FIGURE 5: (a) Double differential cross sections for the production of a Drell-Yan pair at $x_{IP} = 0.05$. Blue error bands represent theoretical errors estimation, as described in the text. (b) Double differential cross sections times Q^4 for three different x_{IP} -values.

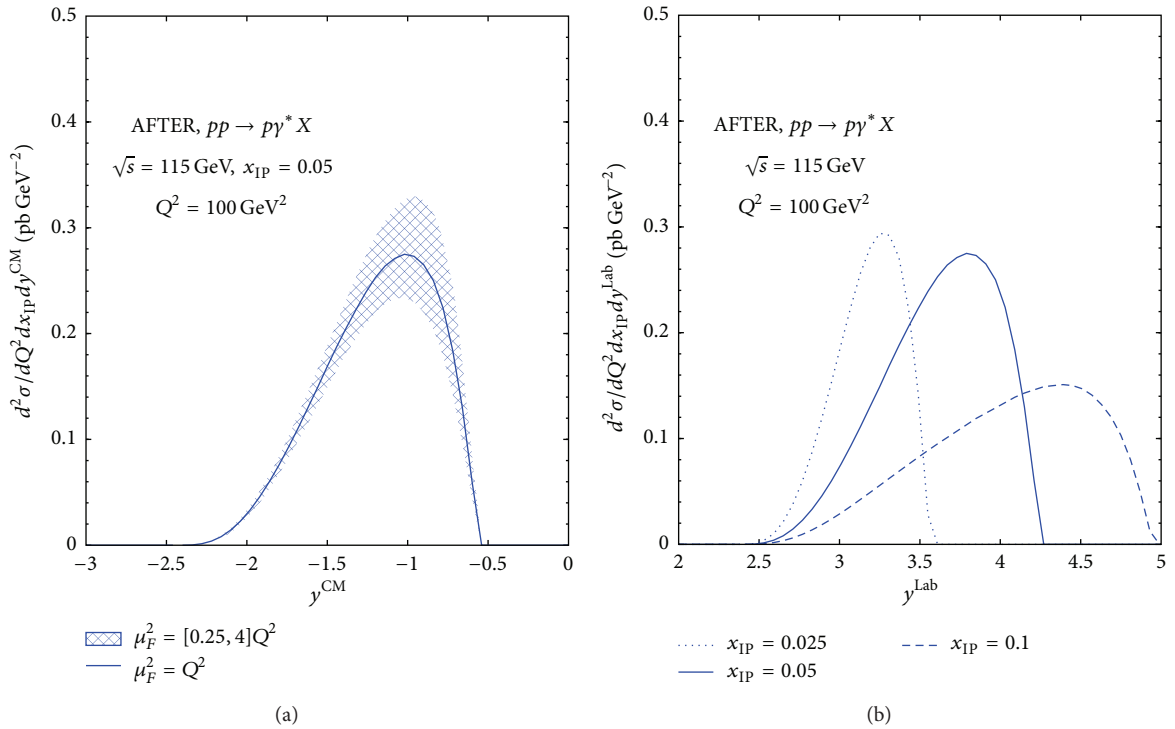


FIGURE 6: (a) Triple differential cross sections for the production of a Drell-Yan pair at $x_{IP} = 0.05$ and of mass $Q^2 = 100 \text{ GeV}^2$. Blue error bands represent theoretical errors estimation, as described in the text. (b) Triple differential cross sections for three different x_{IP} -values.

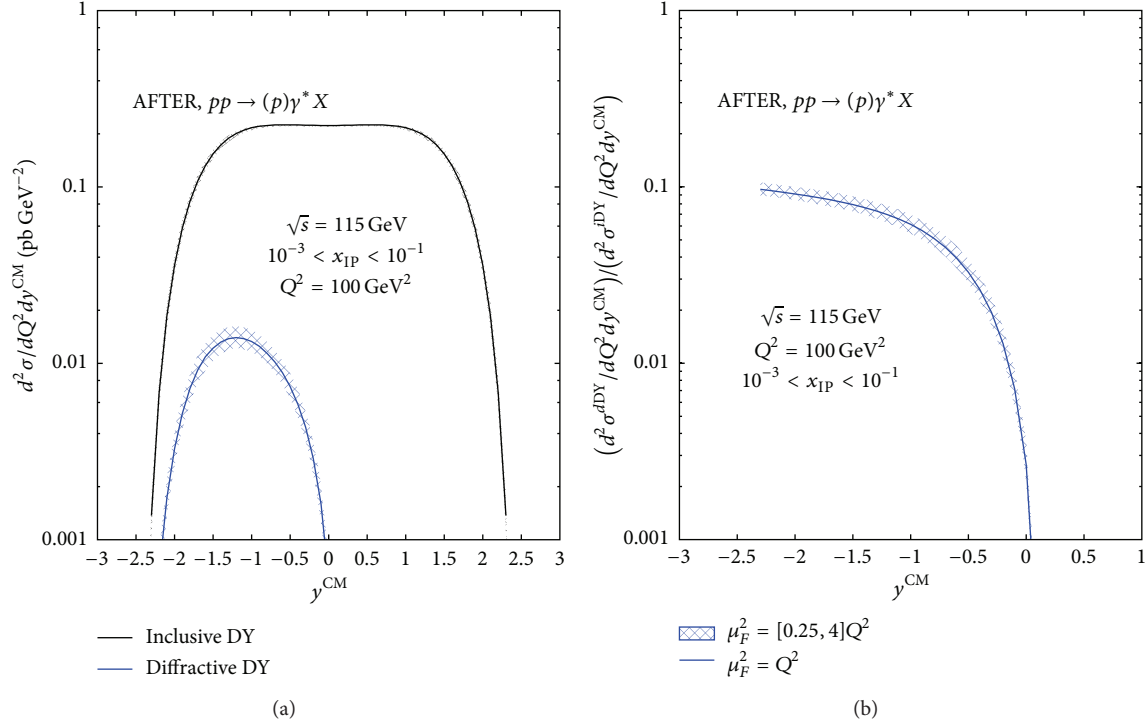


FIGURE 7: (a) Rapidity distributions for inclusive and diffractive Drell-Yan of mass $Q^2 = 100$ GeV². Blue error bands represent theoretical errors estimation, as described in the text. (b) Diffractive to inclusive Drell-Yan rapidity distributions ratio.

is additive under boost along the collision axis we may easily boost the y^{CM} to the laboratory frame by using

$$y^{\text{Lab}} = \frac{1+c}{1-c} y^{\text{CM}} \quad \text{with } c = \sqrt{1 - \frac{4m_p^2}{s}} \quad (13)$$

with m_p the proton mass. In the AFTER@LHC kinematics this implies a rapidity shift $\Delta y = y^{\text{Lab}} - y^{\text{CM}} = 4.8$. The rapidity distributions in the laboratory frame for a Drell-Yan pair of mass $Q^2 = 100$ GeV² and for three different x_{IP} values are presented in the right panel of Figure 6. One may notice from the plot that for increasing x_{IP} the Drell-Yan pair spans a wider rapidity range and the corresponding spectrum is increasingly more forward. It might be useful to discuss the single diffractive Drell-Yan pair production in conjunction with the analogous inclusive process. Such a comparison is presented for the centre-of-mass rapidity distributions in the left plot of Figure 7 for a common Drell-Yan pair of mass squared $Q^2 = 100$ GeV² and, for the diffractive case, integrated in the range $10^{-3} < x_{\text{IP}} < 10^{-1}$. The rapidity distribution in the single diffractive case is strongly asymmetric whereas in the inclusive case it is symmetric around $y^{\text{CM}} = 0$. This effect is primarily due to the different kinematics of the two processes and to the different fractional momentum distributions between parton and fracture distributions. In the right plot of Figure 7 the ratio between the two previous distributions is presented. The ratio gives direct information on the suppression factor between the single diffractive to the inclusive process,

assuming a factorised expression for the former (11). Such a ratio might be convenient from the experimental side since many lepton detection systematics will cancel. On the theoretical one it is expected to be more stable against the inclusion of higher order corrections. In the present case, for example, the factorisation scale is simultaneously varied both on the numerator and denominator resulting in a reduced theoretical error band with respect to the one obtained for absolute cross sections.

We wish to end this section with a brief overview of other possible applications of the proposed formalism. A completely analogous program can be performed for the associated production of forward neutron and a Drell-Yan pair, $p + p \rightarrow n + \gamma^* + X$. The production of forward neutron in DIS at HERA has shown a leading twist nature. From scaling violations of the semi-inclusive neutron structure functions a set of proton-to-neutron fracture functions has been extracted from data in [12] which can be used to predict forward neutron rate in hadronic collisions. As in the case of hard diffraction, both physics programs would highly benefit from the installation of a dedicated instrumentation for the measurements of fast neutrons and protons quite close to the beam axis. Measurements in the forward region, although problematic experimentally, give in fact direct access to the study of the beam fragmentation region.

As a third application we consider hyperon production associated with a Drell-Yan pair, $p + p \rightarrow V + \gamma^* + X$, where V generically indicates either a Λ^0 or $\bar{\Lambda}^0$ hyperon. At very low transverse momentum, the Λ^0 longitudinal momentum

spectrum should show a significant leading particle effect, which can be predicted, assuming factorisation as in $d\sigma^{H,T}$, by the proton-to-lambda fracture functions set obtained from a fit to SIDIS data in [13]. On the other hand, the $\bar{\Lambda}^0$ spectrum in the same kinematical conditions should instead show almost no leading particle effect, giving access to the proton-to- $\bar{\Lambda}^0$ fracture functions. We note, in general, that the particle-to-antiparticle fracture function is indeed an interesting and almost unknown distribution. On the other hand, if one considers Λ^0 or $\bar{\Lambda}^0$ at sufficiently large transverse momentum, their combined analysis, described by $d\sigma^{H,C}$, should allow for the investigation of parton hadronisation into hyperons in the QCD vacuum as parametrised by fragmentation functions.

As a last application we consider the associated production of one particle and a Drell-Yan pair in the context of multiparton interactions. The latter process has already been used to investigate the contamination of the so-called underlying event [27] to jet observable and has been successfully used to study underlying event properties [28]. If the detected hadron is measured at sufficiently large transverse momentum, the latter constitutes a natural infrared regulator for the partonic matrix elements. In this kinematical conditions we also expect a rather small contribution from fracture functions. Therefore, the central term, $d\sigma^{H,C,(1)}$, can be used to estimate the single parton scattering contribution to the process. The latter might be considered as the baseline to study the double (or multiple) parton scattering contributions to the same final state, where, for example, the primary scatterer produces a Drell-Yan pair while the secondary one produces the detected hadron H .

4. Conclusions

We have briefly reviewed a perturbative approach to single particle production associated with a Drell-Yan pair in hadronic collisions. On the theoretical side we have shown that the introduction of fracture functions allows a consistent factorisation of new class of collinear singularities arising in this type of processes. The factorisation procedure coincides with the one used in DIS confirming, as expected, the universal structure of collinear singularities and supports the proposed collinear factorisation formula. On the phenomenological side we have outlined some areas in which the formalism can be fully tested. In particular, focusing on the AFTER@LHC kinematical range, we have presented numerical predictions for the single diffractive production of virtual photons. The study of such a process might improve our understanding of nonperturbative aspects of QCD and it allows one to explore in detail the nature of factorisation breaking at intermediate energies.

Conflict of Interests

The author declares that there is no conflict of interests regarding the publication of this paper.

References

- [1] M. Basile, G. Cara Romeo, L. Cifarelli et al., “The ‘leading’-particle effect in hadron physics,” *Nuovo Cimento A*, vol. 66, no. 2, pp. 129–163, 1981.
- [2] J. C. Collins, “Proof of factorization for diffractive hard scattering,” *Physical Review D*, vol. 57, no. 5, pp. 3051–3056, 1998.
- [3] J. C. Collins, “Erratum: proof of factorization for diffractive hard scattering [Phys. Rev. D 57, 3051 (1998)],” *Physical Review D*, vol. 61, no. 1, Article ID 019902, 1 page, 1999.
- [4] J. C. Collins, “Factorization in hard diffraction,” *Journal of Physics G: Nuclear and Particle Physics*, vol. 28, no. 5, pp. 1069–1077, 2002.
- [5] M. Grazzini, L. Trentadue, and G. Veneziano, “Fracture functions from cut vertices,” *Nuclear Physics B*, vol. 519, no. 1-2, pp. 394–404, 1998.
- [6] L. Trentadue and G. Veneziano, “Fracture functions. An improved description of inclusive hard processes in QCD,” *Physics Letters B*, vol. 323, no. 2, pp. 201–211, 1994.
- [7] A. Aktas, V. Andreev, T. Anthonis et al., “Measurement and QCD analysis of the diffractive deep-inelastic scattering cross section at HERA,” *The European Physical Journal C—Particles and Fields*, vol. 48, no. 3, pp. 715–748, 2006.
- [8] H1 Collaboration, “Dijet cross sections and parton densities in diffractive DIS at HERA,” *Journal of High Energy Physics*, vol. 2007, no. 10, article 042, 2007.
- [9] ZEUS Collaboration, S. Chekanov, M. Derrick et al., “A QCD analysis of ZEUS diffractive data,” *Nuclear Physics B*, vol. 831, no. 1-2, pp. 1–25, 2010.
- [10] F. A. Ceccopieri and L. Favart, “Revisiting QCD fits in diffractive DIS,” <http://arxiv.org/abs/1205.6356>.
- [11] F. A. Ceccopieri and L. Favart, “QCD fits in diffractive DIS revisited,” <http://arxiv.org/abs/1110.4829>.
- [12] F. A. Ceccopieri, “QCD analysis of forward neutron production in DIS,” *The European Physical Journal C*, vol. 74, article 3029, 2014.
- [13] F. A. Ceccopieri and D. Mancusi, “QCD analysis of Lambda hyperon production in DIS target-fragmentation region,” *The European Physical Journal C*, vol. 73, article 2435, 2013.
- [14] A. Berera and D. E. Soper, “Diffractive jet production in a simple model with applications to DESY HERA,” *Physical Review D*, vol. 50, article 4328, 1994.
- [15] J. C. Collins, L. Frankfurt, and M. Strikman, “Diffractive hard scattering with a coherent pomeron,” *Physics Letters B*, vol. 307, no. 1-2, pp. 161–168, 1993.
- [16] CDF Collaboration, “Diffractive dijets with a leading antiproton in $\bar{p}p$ collisions at $\sqrt{s} = 1800$ GeV,” *Physical Review Letters*, vol. 84, p. 5043, 2000.
- [17] T. Aaltonen, A. González, S. Amerio et al., “Diffractive W and Z production at the Fermilab Tevatron,” *Physical Review D*, vol. 82, no. 11, Article ID 112004, 10 pages, 2010.
- [18] S. J. Brodsky, F. Fleuret, C. Hadjidakis, and J. P. Lansberg, “Physics opportunities of a fixed-target experiment using LHC beams,” *Physics Reports*, vol. 522, no. 4, pp. 239–255, 2013.
- [19] F. A. Ceccopieri and L. Trentadue, “NLO semi-inclusive Drell-Yan cross-section in quantum chromodynamics as a factorization analyzer,” *Physics Letters B*, vol. 668, no. 4, pp. 319–323, 2008.
- [20] F. A. Ceccopieri, “Associated production of one particle and a Drell-Yan pair in hadronic collisions,” *Physics Letters B*, vol. 703, no. 4, pp. 491–497, 2011.

- [21] G. Altarelli, R. K. Ellis, and G. Martinelli, “Large perturbative corrections to the Drell-Yan process in QCD,” *Nuclear Physics B*, vol. 157, no. 3, pp. 461–497, 1979.
- [22] D. Graudenz, “One-particle inclusive processes in deeply inelastic lepton-nucleon scattering,” *Nuclear Physics B*, vol. 432, no. 1-2, pp. 351–373, 1994.
- [23] M. Klasen and G. Kramer, “Survival probability for diffractive dijet production in $p\bar{p}$ collisions from next-to-leading order calculations,” *Physical Review D*, vol. 80, Article ID 074006, 2009.
- [24] G. Camici, M. Grazzini, and L. Trentadue, “Fracture functions and Jet Calculus,” *Physics Letters, Section B*, vol. 439, no. 3-4, pp. 382–388, 1998.
- [25] F. A. Ceccopieri and L. Trentadue, “A new fracture function approach to QCD initial state radiation,” *Physics Letters B*, vol. 655, no. 1-2, pp. 15–25, 2007.
- [26] A. D. Martin, R. G. Roberts, W. J. Stirling, and R. S. Thorne, “NNLO global parton analysis,” *Physics Letters B*, vol. 531, no. 3-4, pp. 216–224, 2002.
- [27] T. Affolder, H. Akimoto, A. Akopian et al., “Charged jet evolution and the underlying event in proton-antiproton collisions at 1.8 TeV,” *Physical Review D*, vol. 65, no. 9, Article ID 092002, 22 pages, 2002.
- [28] T. Aaltonen, J. Adelman, B. Álvarez González et al., “Studying the underlying event in Drell-Yan and high transverse momentum jet production at the Tevatron,” *Physical Review D*, vol. 82, Article ID 034001, 2010.

Research Article

Bremsstrahlung from Relativistic Heavy Ions in a Fixed Target Experiment at the LHC

Rune E. Mikkelsen, Allan H. Sørensen, and Ulrik I. Uggerhøj

Department of Physics and Astronomy, Aarhus University, Ny Munkegade 120, 8000 Aarhus C, Denmark

Correspondence should be addressed to Rune E. Mikkelsen; rune@phys.au.dk

Received 20 March 2015; Accepted 13 May 2015

Academic Editor: Gianluca Cavoto

Copyright © 2015 Rune E. Mikkelsen et al. This is an open access article distributed under the Creative Commons Attribution License, which permits unrestricted use, distribution, and reproduction in any medium, provided the original work is properly cited. The publication of this article was funded by SCOAP³.

We calculate the emission of bremsstrahlung from lead and argon ions in ultraperipheral collisions in a fixed target experiment (AFTER) that uses the LHC beams. With nuclear charges of Ze equal to $82e$ and $18e$, respectively, these ions are accelerated to energies of $7\text{ TeV} \times Z$. The bremsstrahlung peaks around $\approx 100\text{ GeV}$ and the spectrum exposes the nuclear structure of the incoming ion. The peak structure is significantly different from the flat power spectrum pertaining to a point charge. Photons are predominantly emitted within an angle of $1/\gamma$ to the direction of ion propagation. Our calculations are based on the Weizsäcker-Williams method of virtual quanta with application of existing experimental data on photonuclear interactions.

1. Introduction

The structure of stable nuclei, in particular the charge distribution, may be investigated by impact of photons and electrons as, for example, shown in pioneering works by McAllister and Hofstadter; see, for example, [1]. This method, however, is not possible for unstable nuclei with short lifetimes as, for example, hypernuclei. Instead, essentially with a change of reference frame, one may let the nucleus under investigation impinge on a suitable target, for example, an amorphous foil, and measure the delta electrons and/or photons emitted in the process. The interaction thus proceeds between the nucleus and a target electron or a virtual photon similarly originating from the target. With this method the charge distribution may be measured, in this case of the projectile, which might be a nucleus of very short lifetime, $\gamma c\tau \approx 1\text{ mm}$, where γ is the Lorentz factor, c the speed of light, and τ the lifetime. With the proposal to extract protons and heavy ions from the LHC for fixed target physics, the so-called AFTER@LHC, such measurements would in principle enable charge distributions, or at least sphericity, for nuclei with lifetimes down to femtoseconds to be extracted. We report calculations of bremsstrahlung emission from Pb and Ar nuclei, with energies corresponding to the maximum of the LHC. We are restricted to cases where the projectile is left

intact, that is, to ultraperipheral collisions in which projectile and target nuclei do not overlap. The interaction between the collision partners is electromagnetic but the structure of the composite projectile nucleus, namely, the strong nuclear force, plays a significant role in the photon emission through the giant dipole resonance.

2. Bremsstrahlung

We study bremsstrahlung emission by relativistic heavy ions. When traversing an amorphous target, the projectile ions interact with the target electrons and nuclei. This causes radiation emission and energy loss to the projectiles. We focus on the radiation and assume the ion beam to be monoenergetic; that is, we consider targets sufficiently thin that the projectile energy loss is minimal. We further assume impact parameters in excess of the sum of the radii of collision partners.

To establish a reference value for the cross section, we first consider the incoming ion as a point particle of electric charge Ze colliding with target atoms of nuclear charge $Z_t e$. The major part of the radiation is due to the interaction of the projectile with target nuclei which, in turn, are screened by target electrons at distances beyond the Thomas-Fermi

distance, a_{TF} . The cross section differential in energy for the emission of bremsstrahlung photons from an ion with atomic number A then reads [2]

$$\frac{d\chi}{d\hbar\omega} = \frac{16}{3} \frac{Z_t^2 Z^4}{A^2} \alpha r_u^2 L, \quad (1)$$

where $\alpha \equiv e^2/\hbar c$ is the fine structure, e the unit electric charge, and \hbar the reduced Planck constant. The classical nucleon radius is defined as $r_u \equiv e^2/M_u c^2$, where M_u is the atomic mass unit. Expression (1) gives the radiation cross section or power spectrum; it is the number spectrum weighted by the photon energy, $\hbar\omega$. The factor L is given by

$$L \approx \ln \left(\frac{233M}{Z_t^{1/3} m} \right) - \frac{1}{2} \left[\ln(1+r^2) - \frac{1}{1+r^{-2}} \right], \quad (2)$$

$$r = \frac{96\hbar\omega}{\gamma\gamma' Z_t^{1/3} m c^2},$$

where $\gamma \equiv E/Mc^2$, $\gamma' \equiv (E - \hbar\omega)/Mc^2$, m is the electron mass, and M is the mass of the projectile. The material-dependent factor L accounts for the electronic screening of the target nuclei. It is essentially the logarithm of the ratio between the effective maximum ($\sim 2Mc$) and minimum ($\sim \hbar/a_{\text{TF}}$) momentum transfers to the scattering center. The reference power spectrum extends all the way up to the energy of the primary ion and varies only slightly with energy. However, as we will study in this paper, photons with energy $\hbar\omega \gtrsim \gamma\hbar c/R$ have wavelengths smaller than the radius of the ions which cause the emission, making them sensitive to the nuclear structure and collective dynamics of the constituent protons. Taking this into account causes significant change in the shape of the bremsstrahlung spectrum.

3. The Weizsäcker-Williams Method

When the emitted bremsstrahlung photons have a wavelength that is small compared to the nucleus, the size and structure of the nucleus affect the emission. We can investigate this by using the Weizsäcker-Williams method of virtual quanta [2–5]. In this approach, we represent a moving charged particle by a spectrum of virtual photons which scatter on a stationary charged particle. There are contributions to bremsstrahlung from scattering both on target constituents and on the projectile ion. The latter is the dominant contribution. Hence we change to a reference frame in which the incoming ion is at rest and where we represent the screened target nuclei by a bunch of virtual photons. These photons scatter off the ion and are subsequently Lorentz boosted back to the laboratory frame—resulting in an energy increase by a factor of up to 2γ . This means that the bremsstrahlung can be calculated using the Weizsäcker-Williams method of virtual quanta, photonuclear interaction theory, and a Lorentz transformation. For the cross section we take the elastic photonuclear interaction cross section as this ensures that the scatterer remains intact; that is, the incoming ion does not disintegrate in the process of radiation emission. The spectrum of virtual photons is given in [2, 6]. Multiplying

this with the photonuclear scattering cross section differential in angle results in the scattering cross section differential in energy and angle. The transformation to the laboratory frame is performed by utilizing an invariance relation [2] and produces the bremsstrahlung power spectrum differential in energy and angle; for details, see [6–8].

In [6], one of us used this procedure to calculate the bremsstrahlung spectrum of relativistic bare lead ions. This was possible by using the photonuclear interaction data provided in [9]. However, data for other nuclei is not abundantly available. We therefore developed a procedure to derive the necessary elastic scattering cross sections taking total photonuclear absorption cross sections as input; these are available in the ENDF database for about 100 different nuclei [10]. We obtain the elastic scattering cross sections at low to moderate energies, that is, at energies covering the giant dipole resonance by applying the optical theorem and a dispersion relation to the total photonuclear absorption data; see [7]. At higher energies additional constraints are invoked to ensure coherence. With this construct, the bremsstrahlung spectrum can be calculated for any ion for which the total photon absorption cross section is known. Due to the available data, our approach is most exact for lead ions which have already been successfully accelerated to $4 \text{ TeV} \times Z$ in the LHC machine. Also, this allowed us to cross-check the earlier calculations for the bremsstrahlung from lead. It has not been finally decided if other ions will ever be used in the LHC. But argon ions are frequently discussed as a possibility if the physics case requires lower mass ions to be accelerated [11]. Supporting this idea, in 2015, the CERN accelerator complex is successfully accelerating argon ions in the Super Proton Synchrotron at energies up to 150 GeV/n . We therefore also provide bremsstrahlung calculations for argon ions at LHC energy in the next section.

4. Results: Bremsstrahlung

In this section, we present calculations of bremsstrahlung spectra in ultraperipheral collision for bare argon and lead ions at $7 \text{ TeV} \times Z$ incident on a fixed target. Figure 1 shows the power spectrum of bremsstrahlung for lead ions aimed at a lead target. The spectrum obtained by integrating over all emission angles has a pronounced peak around a photon energy of about 80 GeV . This corresponds to the collective interaction of the projectile nucleons with the virtual photons of the target—the giant dipole resonance. This well-known resonance in the photonuclear cross sections is also apparent in the bremsstrahlung spectrum, albeit here multiplied by a factor of 2γ from the Lorentz boost. At energies above the peak, significantly fewer photons are predicted by the current model. This is because coherence is restricted to a decreasing range of photon scattering angles such that most scattering events correspond to incoherent interaction with the projectile protons. Incoherent interaction of an energetic virtual photon with a target proton generally leads to breakup of the nucleus and hence does not contribute to the spectrum. This decreasing contribution from coherent scattering leads to a depletion of the elastic scattering cross section at higher energies, which is apparent also in the

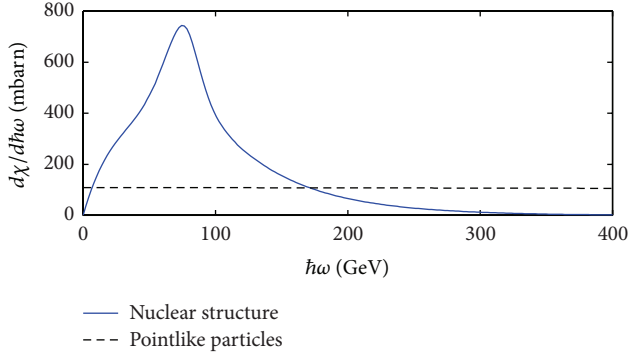


FIGURE 1: Bremsstrahlung calculations for a Pb-208 projectile with energy $7 \text{ TeV} \times Z$ incident on a lead target. The dashed line shows reference cross section (1) and the full drawn curve shows the present results.

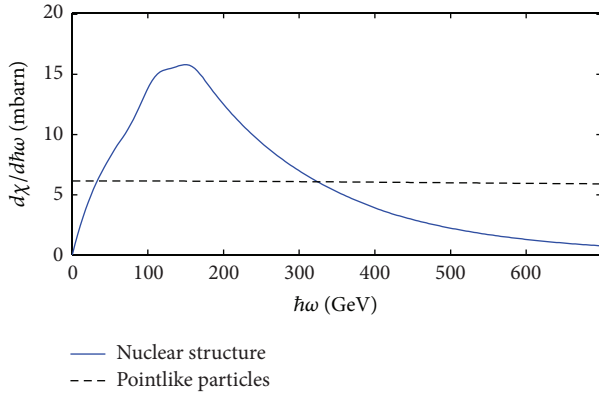


FIGURE 2: The same as Figure 1 except for the projectile which is here Ar-40.

bremsstrahlung spectrum. Since the dashed line in Figure 1 extends all the way up to the energy of the ion, the integrated difference between the two curves is very large. Note that Figure 1 pertains to cases where the projectile is left intact. The photoproduction in collisions with nuclear overlap is drastically different [6].

The spectrum for argon projectiles is shown in Figure 2. It is largely similar to that for lead except that the overall values are much lower. The peak height is approximately 50 times lower, and it must be noted that there is no simple scaling between the heights and shapes of the two spectra (scaling the heights with Z^2 off-shoots by a factor of 2-3 here). The lack of such scaling is traced back to differences in the photonuclear scattering cross sections. The argon spectrum is somewhat broader than that for lead and the high energy tail extends to larger energies than for lead. This difference reflects a similar difference at the elastic scattering cross sections and is due to the different shapes of the argon and lead nuclei. Lead is almost spherically symmetric and this leads to a very narrow giant dipole resonance peak. For argon on the other hand, the nucleus is much less symmetric, and the photonuclear as well as the bremsstrahlung cross sections actually consist of two individual but close-lying peaks (for bremsstrahlung this will show through collimation).

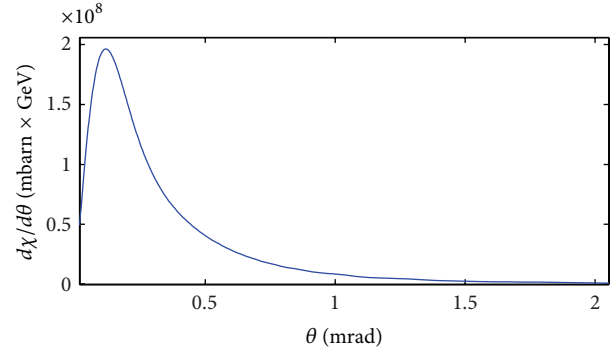


FIGURE 3: The angular distribution of bremsstrahlung from a Pb-208 projectile with energy $7 \text{ TeV} \times Z$ incident on a lead target. Note that the cross section is shown to be differential in the polar emission angle θ rather than in solid angle and hence includes a factor of $2\pi\sin(\theta)$. The majority of the bremsstrahlung photons are indeed emitted in the very near forward direction.

Figure 3 shows the bremsstrahlung spectrum obtained for lead ions by integration over emission energy, that is, differential in angle instead of energy. As expected, there is a peak in the radiation intensity at an angle corresponding to $1/\gamma$. For LHC beam energies this means that the bremsstrahlung photons are emitted at angles of order less than 1 mrad.

5. Summary and Conclusions

We have presented calculations of the bremsstrahlung emission from relativistic heavy ions with energy corresponding to that of the LHC beam. The calculations, which are restricted to ultraperipheral collisions between projectile and target nuclei, are novel in the way that knowledge on nuclear structure is taken into account using existing data on photonuclear cross sections. In addition, our approach has not before been applied to energies above that available at the SPS. We demonstrate that substantial cross sections for the emission of high energy photons are expected around energies of $\hbar\omega \approx 100 \text{ GeV}$. Here our model produces a radiation peak which overshoots the result for a pointlike particle of the same charge and mass by a factor of roughly 2 and 6 for argon and lead, respectively. In the energy regions below and above the peak, however, our model produces significantly fewer bremsstrahlung photons than what is otherwise expected. If this holds true against experiments, it implies that the energy loss of the ions through the bremsstrahlung channel is much less severe than previously expected by some authors (cf. [6]).

Our calculations can of course also be performed at lower energies; see [7] for calculated cross sections for energies of about $150 \text{ GeV}/n$. The SPS can accelerate to about $450 \text{ GeV} \times Z$ so that experiments located in the SPS fixed target hall should be able to see this signal. The COMPASS experiment [12] may be a candidate. See also [13] for calculations on delta electron emission from a similar experimental condition as discussed here. Along with bremsstrahlung measurements, such electrons would be highly sensitive to the nuclear charge structure.

If a fixed target facility using the LHC beams is constructed, one could hope for the option to produce secondary beams. With such beams, one could study the bremsstrahlung from short-lived nuclei. If traversing a 1 mm target, the lifetime would be $\gamma c\tau = 1$ mm, which leads to $\tau \approx 4 \cdot 10^{-16}$ s.

Exploiting the Lorentz time dilation, the nuclear structure of these rare nuclei could be exposed. Potentially, along with these short-lived species, one may also study exotic beams where the nucleus contains a strange quark. It is presently unknown whether the presence of a strange quark increases or decreases the radius of the nuclear charge. Whereas such effects may be visible in the bremsstrahlung spectrum, they would certainly be impossible to study using conventional electron scattering.

Conflict of Interests

The authors declare that there is no conflict of interests regarding the publication of this paper.

References

- [1] R. W. McAllister and R. Hofstadter, "Elastic scattering of 188-Mev electrons from the proton and the alpha particle," *Physical Review*, vol. 102, no. 3, pp. 851–856, 1956.
- [2] J. D. Jackson, *Classical Electrodynamics*, John Wiley & Sons, New York, NY, USA, 2nd edition, 1975.
- [3] E. J. Williams, "Nature of the high energy particles of penetrating radiation and status of ionization and radiation formulae," *Physical Review*, vol. 45, p. 729, 1934.
- [4] E. J. Williams, "Correlation of certain collision problems with radiation theory," *Mathematisk-Fysiske Meddelelser*, vol. 13, no. 4, pp. 1–4, 1935.
- [5] C. F. Weizsäcker, "Ausstrahlung bei Stößen sehr schneller Elektronen," *Zeitschrift für Physik*, vol. 88, no. 9-10, pp. 612–625, 1934.
- [6] A. H. Sørensen, "Bremsstrahlung from relativistic heavy ions in matter," *Physical Review A*, vol. 81, Article ID 022901, 2010.
- [7] R. E. Mikkelsen, A. H. Sørensen, and U. I. Uggerhøj, Submitted to *Physical Review C*.
- [8] T. V. Jensen and A. H. Sørensen, "Bremsstrahlung from relativistic bare heavy ions: nuclear and electronic contributions in amorphous and crystalline materials," *Physical Review A*, vol. 87, no. 2, Article ID 022902, 15 pages, 2013.
- [9] K. P. Schelhaass, J. M. Henneberg, M. Sanzone-Arenhövel et al., "Nuclear photon scattering by ^{208}Pb ," *Nuclear Physics A*, vol. 489, pp. 189–224, 1988.
- [10] M. B. Chadwick, M. Herman, P. Obložinský et al., "ENDF/B-VII.1 nuclear data for science and technology: cross sections, covariances, fission product yields and decay data," *Nuclear Data Sheets*, vol. 112, no. 12, pp. 2887–2996, 2011.
- [11] M. Benedikt, P. Collier, V. Mertens, J. Poole, and K. Schindl, *LHC Design Report (CERN)*, vol. 3, chapter 33, 2004.
- [12] D. von Harrach, "The COMPASS experiment at CERN," *Nuclear Physics A*, vol. 629, no. 1-2, pp. 245–254, 1998.
- [13] A. H. Sørensen, "Electron-ion momentum transfer at ultra-relativistic energy," in *Proceedings of the 20th International Conference on the Physics of Electronic and Atomic Collisions*, F. Aumayr and H. Winter, Eds., p. 475, World Scientific, Singapore, 1998.

Research Article

Antishadowing Effect on Charmonium Production at a Fixed-Target Experiment Using LHC Beams

Kai Zhou,^{1,2} Zhengyu Chen,¹ and Pengfei Zhuang¹

¹Physics Department, Tsinghua University and Collaborative Innovation Center of Quantum Matter, Beijing 100084, China

²Institute for Theoretical Physics, Goethe-University Frankfurt am Main, Max-von-Laue-Strasse 1, 60438 Frankfurt am Main, Germany

Correspondence should be addressed to Pengfei Zhuang; zhuangpf@mail.tsinghua.edu.cn

Received 17 April 2015; Revised 25 June 2015; Accepted 5 August 2015

Academic Editor: Cynthia Hadjidakis

Copyright © 2015 Kai Zhou et al. This is an open access article distributed under the Creative Commons Attribution License, which permits unrestricted use, distribution, and reproduction in any medium, provided the original work is properly cited. The publication of this article was funded by SCOAP³.

We investigate charmonium production in Pb + Pb collisions at LHC beam energy $E_{\text{lab}} = 2.76A$ TeV at fixed-target experiment ($\sqrt{s_{\text{NN}}} = 72$ GeV). In the frame of a transport approach including cold and hot nuclear matter effects on charmonium evolution, we focus on the antishadowing effect on the nuclear modification factors R_{AA} and r_{AA} for the J/ψ yield and transverse momentum. The yield is more suppressed at less forward rapidity ($y_{\text{lab}} \approx 2$) than that at very forward rapidity ($y_{\text{lab}} \approx 4$) due to the shadowing and antishadowing in different rapidity bins.

1. Introduction

Recently a fixed-target experiment using the LHC beams has been proposed [1], where the study on quarkonia in nuclear collisions becomes specifically important, due to the wide parton distributions in phase space which is helpful to reveal the charmonium production mechanism [2]. Corresponding to the LHC beam energy $E_{\text{lab}} = 2.76A$ TeV, where A is the nucleon number of the incident nucleus, the center-of-mass energy $\sqrt{s_{\text{NN}}} = 72$ GeV is in between the SPS and RHIC energies, and a quark-gluon plasma is expected to be created in the early stage of heavy ion collisions. Taking into account the advantage of high luminosity in fixed-target experiments, which is helpful for detailed study of rare particles, the J/ψ yield in Pb + Pb collisions at $E_{\text{lab}} = 2.76A$ TeV per LHC run year is about 100 times larger than the J/ψ yield in Au + Au collisions at $\sqrt{s_{\text{NN}}} = 62.4$ GeV per RHIC run year [1]. With the high statistics, one may precisely distinguish between different cold and hot nuclear matter effects on charmonium production [3]. As is well known, the shadowing effect [4, 5], namely, the difference between the parton distributions in a nucleus and in a free nucleon, depends strongly on the parton momentum fraction x . Since x runs in a wide region, $0.001 \leq x \leq 0.5$, in the fixed-target experiments,

it provides a chance to see clearly the shadowing effect on the charmonium distributions in different rapidity bins. In this paper, we study the shadowing effect on the nuclear modification factors for J/ψ yield and transverse momentum in Pb + Pb collisions at LHC beam energy $E_{\text{lab}} = 2.76A$ TeV.

2. Evolution of Quark-Gluon Plasma

The medium created in heavy ion collision at $\sqrt{s_{\text{NN}}} = 72$ GeV is assumed to reach local equilibrium at a proper time $\tau_0 = 0.6$ fm/c [6]; its consequent space-time evolution can be controlled by the ideal hydrodynamic equations:

$$\begin{aligned}\partial_\mu T^{\mu\nu} &= 0, \\ \partial_\mu j^\mu &= 0,\end{aligned}\tag{1}$$

where $T_{\mu\nu} = (\epsilon + p)u_\mu u_\nu - g_{\mu\nu}p$, $j_\mu = nu_\mu$, and u_μ , ϵ , p , and n are, respectively, the energy-momentum tensor, baryon current, four-velocity of the fluid cell, energy density, pressure, and baryon density of the system. The solution of the hydrodynamic equations provides the local temperature $T(x)$, baryon chemical potential $\mu(x)$, and fluid velocity $u_\mu(x)$ of the medium which will be used in the calculation

of the charmonium suppression and regeneration rates [7]. Taking the assumption of Hubble-like expansion and initial boost invariance along the colliding direction for high energy nuclear collisions, we can employ the well tested 2 + 1-dimensional version of the hydrodynamics in describing the evolution of the medium created at $\sqrt{s_{\text{NN}}} = 72$ GeV. Introducing the proper time $\tau = \sqrt{t^2 - z^2}$ and space-time rapidity $\eta = 1/2 \ln[(t + z)/(t - z)]$ instead of the time t and longitudinal coordinate z , the conservation equations can be simplified as [8]

$$\begin{aligned} \partial_\tau E + \nabla \mathbf{M} &= -\frac{E + p}{\tau}, \\ \partial_\tau M_x + \nabla (M_x \mathbf{v}) &= -\frac{M_x}{\tau} - \partial_x p, \\ \partial_\tau M_y + \nabla (M_y \mathbf{v}) &= -\frac{M_y}{\tau} - \partial_y p, \\ \partial_\tau R + \nabla (R \mathbf{v}) &= -\frac{R}{\tau} \end{aligned} \quad (2)$$

with the definitions $E = (\epsilon + p)\gamma^2 - p$, $\mathbf{M} = (\epsilon + p)\gamma^2 \mathbf{v}$, and $R = \gamma n$, where \mathbf{v} and γ are the three-velocity of the fluid cell and Lorentz factor in the transverse plane.

To close the hydrodynamical equations one needs to know the equation of state of the medium. From recent studies on particle elliptic flow and shear viscosity, the matter created in heavy ion collisions at RHIC and LHC energies is very close to a perfect fluid [9]. Considering that the momentum integrated particle yield, especially for heavy quarkonia, is not sensitive to the equation of state, we follow [10] where the deconfined phase at high temperature is an ideal gas of gluons and massless u and d quarks plus 150 MeV massed s quarks, and the hadron phase at low temperature is an ideal gas of all known hadrons and resonances with mass up to 2 GeV [11]. There is a first-order phase transition between these two phases. In the mixed phase, the Maxwell construction is used. The mean field repulsion parameter and the bag constant are chosen as $K = 450 \text{ MeV fm}^3$ and $B^{1/4} = 236 \text{ MeV}$ to obtain the critical temperature $T_c = 165 \text{ MeV}$ [10] at vanishing baryon number density. Note that when one calculates the rapidity or transverse momentum distribution of quarkonia, the choice of the equation of state may result in sizeable difference.

The initialization of the hot medium is taken as the same treatment in [8]. We use the final charged multiplicity to determine the initial entropy density. For $\sqrt{s_{\text{NN}}} = 72$ GeV, the charged multiplicity at central rapidity in center-of-mass frame is estimated to be $dN_{\text{ch}}/d\eta = 515$ based on the empirical formula [12]:

$$\frac{dN_{\text{ch}}}{d\eta} = 312.5 \log_{10} \sqrt{s_{\text{NN}}} - 64.8. \quad (3)$$

The initial baryon density is obtained by adjusting the entropy per baryon to be 250 [13]. From the empirical relation $\sigma_{\text{NN}} = 29.797 + 0.141(\ln \sqrt{s_{\text{NN}}})^{2.624}$ [14] between the inelastic nucleon-nucleon cross section σ_{NN} in unit of mb and the

colliding energy $\sqrt{s_{\text{NN}}}$ in unit of GeV, we have $\sigma_{\text{NN}} = 36 \text{ mb}$ at $\sqrt{s_{\text{NN}}} = 72 \text{ GeV}$. These initial conditions lead to a maximum medium temperature $T_0 = 310 \text{ MeV}$ at the initial time $\tau_0 = 0.6 \text{ fm/c}$. The medium maintains local chemical and thermal equilibrium during the evolution. If we do not consider the charmonium interaction with the hadron gas, the charmonium distributions in the final state will be fixed at time τ_c corresponding to the critical temperature T_c of the deconfinement phase transition.

3. Charmonium Transport in Quark-Gluon Plasma

Since a charmonium is so heavy, its equilibrium with the medium can hardly be reached; we use a Boltzmann transport equation to describe its phase space distribution function $f_\Psi(x, \mathbf{p} | \mathbf{b})$ in heavy ion collisions at impact parameter \mathbf{b} :

$$p^\mu \partial_\mu f_\Psi = -C_\Psi f_\Psi + D_\Psi, \quad (4)$$

where the loss and gain terms $C_\Psi(x, \mathbf{p} | \mathbf{b})$ and $D_\Psi(x, \mathbf{p} | \mathbf{b})$ come from the charmonium dissociation and regeneration in the created hot medium. We have neglected here the elastic scattering, since the charmonium mass is much larger than the typical medium temperature. Considering that the feed-down from the excited states ψ' and χ_c to the ground state J/ψ [15] happens after the medium evolution, we should take transport equations for $\Psi = J/\psi$, ψ' and χ_c when we calculate the J/ψ distribution $f_{J/\psi}$ in the final state.

Introducing the momentum rapidity $y = 1/2 \ln[(E + p_z)/(E - p_z)]$ and transverse energy $E_t = \sqrt{E^2 - p_z^2}$ to replace the longitudinal momentum p_z and energy $E = \sqrt{m^2 + \mathbf{p}^2}$, the transport equation can be rewritten as

$$\begin{aligned} \left[\cosh(y - \eta) \partial_\tau + \frac{\sinh(y - \eta)}{\tau} \partial_\eta + \mathbf{v}_t \cdot \nabla_t \right] f_\Psi \\ = -\alpha_\Psi f_\Psi + \beta_\Psi \end{aligned} \quad (5)$$

with the dissociation and regeneration rates $\alpha_\Psi(x, \mathbf{p} | \mathbf{b}) = C_\Psi(x, \mathbf{p} | \mathbf{b})/E_t$ and $\beta_\Psi(x, \mathbf{p} | \mathbf{b}) = D_\Psi(x, \mathbf{p} | \mathbf{b})/E_t$, where the third term in the square bracket arises from the free streaming of Ψ with transverse velocity $\mathbf{v}_t = \mathbf{p}_t/E_t$ which leads to a strong leakage effect at SPS energy [16].

Considering the gluon dissociation $\Psi + g \rightarrow c + \bar{c}$ in the quark-gluon plasma, the dissociation rate α can be expressed as

$$\begin{aligned} \alpha_\Psi = \frac{1}{2E_t} \int \frac{d^3 \mathbf{k}}{(2\pi)^3 2E_g} \sigma_{g\Psi}(\mathbf{p}, \mathbf{k}, T) 4F_{g\Psi}(\mathbf{p}, \mathbf{k}) \\ \cdot f_g(\mathbf{k}, T, u_\mu), \end{aligned} \quad (6)$$

where E_g is the gluon energy, $F_{g\Psi} = \sqrt{(pk)^2 - m_\Psi^2 m_g^2} = pk$ the flux factor, and f_g the gluon thermal distribution as a function of the local temperature $T(x | \mathbf{b})$ and fluid velocity $u_\mu(x | \mathbf{b})$ determined by the hydrodynamics. The dissociation cross section in vacuum $\sigma_{g\Psi}(\mathbf{p}, \mathbf{k}, 0)$ can be

derived through the operator production expansion (OPE) method with a perturbative Coulomb wave function [17–21]. However, the method is no longer valid for loosely bound states at high temperature. To reasonably describe the temperature dependence of the cross section, we take the geometric relation between the averaged charmonium size and the cross section:

$$\sigma_{g\Psi}(\mathbf{p}, \mathbf{k}, T) = \frac{\langle r^2 \rangle_{\Psi}(T)}{\langle r^2 \rangle_{\Psi}(0)} \sigma_{g\Psi}(\mathbf{p}, \mathbf{k}, 0). \quad (7)$$

The averaged radial square $\langle r^2 \rangle_{\Psi}(T)$ is calculated via potential model [22] with lattice simulated heavy quark potential [23] at finite temperature. When T approaches the charmonium dissociation temperature T_d , the averaged radius square and in turn the cross section go to infinity, which means a complete charmonium melting induced by color screening [24]. Using the internal energy U as the heavy quark potential V , the dissociation temperature T_d is calculated to be $2.1T_c$, $1.16T_c$, and $1.12T_c$ for J/ψ , χ_c , and ψ' , respectively [22].

The regeneration rate β is connected to the dissociation rate α via the detailed balance between the gluon dissociation process and its inverse process [25, 26]. To obtain the regeneration rate, we also need the charm quark distribution function in medium. Although the initially produced charm quarks would carry high transverse momentum, they lose energy (momentum) when passing through the medium. Considering the experimentally observed large open charm quench factor [27–29] and elliptic flow [30, 31], we take as a first approximation a kinetically thermalized momentum spectrum for the charm quark distribution $f_c(x, \mathbf{q} \mid \mathbf{b})$. Neglecting the creation and annihilation of charm-anticharm pairs inside the medium, the spatial density of charm quark number $\rho_c(x \mid \mathbf{b}) = \int d^3\mathbf{q}/(2\pi)^3 f_c(x, \mathbf{q} \mid \mathbf{b})$ satisfies the conservation law

$$\partial_\mu (\rho_c u^\mu) = 0 \quad (8)$$

with the initial density determined by the nuclear geometry $\rho_c(x_0 \mid \mathbf{b}) = T_A(\mathbf{x}_t)T_B(\mathbf{x}_t - \mathbf{b}) \cosh \eta / \tau_0 d\sigma_{cc}^{\text{NN}}/d\eta$, where $T_{A,B}(\mathbf{x}_t) = \int_{-\infty}^{+\infty} \rho_{A,B}(\vec{r}) dz$ are the thickness functions and $d\sigma_{cc}^{\text{NN}}/d\eta$ is the charm quark rapidity distribution in $p + p$ collisions.

For the regeneration rate β , we also considered the canonical effect which is shown to be important in explaining the suppression of strange mesons [32]. When there are only few pairs or even less than one pair of charm quarks produced in an event, one needs to consider the canonical effect to guarantee the exact charm number conservation. Taking into account the fact that the charm and anticharm quarks inside a pair are produced at the same rapidity, we simply multiply the regeneration rate β in a unit rapidity bin by a canonical enhancement factor [33]

$$C_{cc} = 1 + \frac{1}{(dN_{cc}/dy)}. \quad (9)$$

To take into account the relativistic effect on the dissociation cross section to avoid the divergence in the regeneration

cross section, we should replace the charmonium binding energy by the gluon threshold energy in the calculations of α and β [34].

In the hadron phase of the fireball with temperature $T < T_c$, there are many effective models that can be used to calculate the inelastic cross sections between charmonia and hadrons [35]. For J/ψ the dissociation cross section is about a few mb which is comparable with the gluon dissociation cross section. However, considering that the hadron phase appears in the later evolution of the fireball, the ingredient density of the system is much more dilute in comparison with the early hot and dense period [7]. Taking, for instance, the regeneration processes $c + \bar{c} \rightarrow g + J/\psi$ in quark matter and $D + \bar{D}^* \rightarrow \pi + J/\psi$ in hadron matter, the density ratio between charm quarks at initial temperature $T_0 = 310 \text{ MeV}$ and D mesons at critical temperature $T_c = 165 \text{ MeV}$ is around 30. Considering further the life time of the quark matter $\sim 6 \text{ fm/c}$ and the life time of the hadron matter $\sim 2 \text{ fm/c}$ calculated from the hydrodynamics in Section 2, we neglect the charmonium production and suppression in hadron gas, to simplify the numerical calculations. Note that the suppression and regeneration in hadron gas may become important for excited charmonium states [36].

The transport equation can be solved analytically with the explicit solution [7, 37]

$$\begin{aligned} f_\Psi(\mathbf{p}_t, y, \mathbf{x}_t, \eta, \tau) &= f_\Psi(\mathbf{p}_t, y, \mathbf{X}_t(\tau_0), H(\tau_0), \tau_0) \\ &\cdot e^{-\int_{\tau_0}^{\tau} d\tau' / \Delta(\tau') \alpha_\Psi(\mathbf{p}_t, y, \mathbf{X}_t(\tau'), H(\tau'), \tau')} \\ &+ \int_{\tau_0}^{\tau} \frac{d\tau'}{\Delta(\tau')} \beta_\Psi(\mathbf{p}_t, y, \mathbf{X}_t(\tau'), H(\tau'), \tau') \\ &\cdot e^{-\int_{\tau'}^{\tau} d\tau'' / \Delta(\tau'') \alpha_\Psi(\mathbf{p}_t, y, \mathbf{X}_t(\tau''), H(\tau''), \tau'')} \end{aligned} \quad (10)$$

with

$$\begin{aligned} \mathbf{X}_t(\tau') &= \mathbf{x}_t - \mathbf{v}_T [\tau \cosh(y - \eta) - \tau' \Delta(\tau')], \\ H(\tau') &= y - \arcsin\left(\frac{\tau}{\tau'} \sinh(y - \eta)\right), \\ \Delta(\tau') &= \sqrt{1 + \left(\frac{\tau}{\tau'}\right)^2 \sinh^2(y - \eta)}. \end{aligned} \quad (11)$$

The first and second terms on the right-hand side of solution (10) indicate the contributions from the initial production and continuous regeneration, respectively, and both suffer from the gluon dissociation in the medium. Since the regeneration happens in the deconfined phase, the regenerated quarkonia would have probability to be dissociated again by the surrounding gluons. The coordinate shifts $\mathbf{x}_t \rightarrow \mathbf{X}_t$ and $\eta \rightarrow H$ in solution (10) reflect the leakage effect in the transverse and longitudinal directions.

For fixed-target nuclear collisions at $E_{\text{lab}} = 2.76 \text{ A TeV}$, the collision time for the two Pb nuclei to pass through each other in the center of mass frame is $2R_{\text{Pb}} m_N / (\sqrt{s_{\text{NN}}}/2) \sim 0.35 \text{ fm/c}$, which is compatible with the charmonium formation time but shorter than the QGP formation time $\tau_0 = 0.6 \text{ fm}$.

Therefore, all the cold nuclear matter effects can be reflected in the initial charmonium distribution f_Ψ at time τ_0 . We take into account nuclear absorption, nuclear shadowing, and Cronin effect. The initial distribution in solution (10) can be obtained from a superposition of $p + p$ collisions, along with the modifications from these cold nuclear matter effects.

The nuclear absorption is important in explaining the J/ψ suppression in $p + A$ and $A + A$ collisions at low energies. It is due to the inelastic collision between the initially produced charmonia and the surrounding nucleons, and its effect on the charmonium surviving probability can be described by an effective absorption cross section σ_{abs} . The value of σ_{abs} is usually measured in $p + A$ collisions and is several mb at SPS energy. Since the nuclear absorption becomes weaker at higher colliding energy due to the shorter collision time [38, 39], we take $\sigma_{\text{abs}} = 2 \text{ mb}$ at $E_{\text{lab}} = 2.76 A \text{ TeV}$ [39] and the nuclear absorption factor

$$S_{\text{abs}} = e^{-\sigma_{\text{abs}}(\int_{z_A}^{\infty} \rho(z, \mathbf{x}_t) dz + \int_{-\infty}^{z_B} \rho(z, \mathbf{x}_t - \mathbf{b}) dz)}. \quad (12)$$

The Cronin effect broadens the momentum distribution of the initially produced charmonia in heavy ion collisions [7]. In $p + A$ and $A + A$ collisions, the incoming partons (both gluons and quarks) experience multiple scatterings with surrounding nucleons via soft gluon exchanges. The initial scatterings lead to an additional transverse momentum broadening of partons which is then inherited by produced hadrons [40]. Since the Cronin effect is caused by soft interactions, rigorous calculations for the effect are not available. However, the effect is often treated as a random motion. Inspired from a random-walk picture, we take a Gaussian smearing [41, 42] for the modified transverse momentum distribution:

$$\begin{aligned} \bar{f}_\Psi^{\text{NN}}(\mathbf{x}, \mathbf{p}, z_A, z_B | \mathbf{b}) \\ = \frac{1}{\pi a_{gN}^2} \int d^2 \mathbf{p}'_t e^{-\mathbf{p}'_t{}^2 / a_{gN}^2} \bar{f}_\Psi^{\text{NN}}(|\mathbf{p}_t - \mathbf{p}'_t|, p_z) S_{\text{abs}}, \end{aligned} \quad (13)$$

where

$$\begin{aligned} l(\mathbf{x}, z_A, z_B | \mathbf{b}) \\ = \frac{1}{\rho} \left(\int_{-\infty}^{z_A} \rho(z, \mathbf{x}_t) dz + \int_{z_B}^{+\infty} \rho(z, \mathbf{x}_t - \mathbf{b}) dz \right) \end{aligned} \quad (14)$$

is the path length of the two initial gluons in nuclei before fusing into a charmonium at \mathbf{x}, z_A and z_B , a_{gN} is the averaged charmonium transverse momentum square gained from the gluon scattering with a unit of length of nucleons, and $\bar{f}_\Psi^{\text{NN}}(\mathbf{p})$ is the charmonium momentum distribution in a free $p + p$ collision. The Cronin parameter a_{gN} is usually extracted from corresponding $p + A$ collisions. Considering the absence of $p + A$ collision data at $\sqrt{s_{\text{NN}}} = 72 \text{ GeV}$, we take $a_{gN} = 0.085 (\text{GeV}/c)^2/\text{fm}$ from some empirical estimations [4, 25, 43]. As a comparison, for collisions at SPS ($\sqrt{s_{\text{NN}}} \sim 20 \text{ GeV}$) and RHIC ($\sqrt{s_{\text{NN}}} = 200 \text{ GeV}$) we take $a_{gN} = 0.075$ [8] and 0.1 [44] $(\text{GeV}/c)^2/\text{fm}$, respectively.

Assuming that the emitted gluon in the gluon fusion process $g + g \rightarrow \Psi + g$ is soft in comparison with the initial

gluons and the produced charmonium and can be neglected in kinematics, the charmonium production becomes a $2 \rightarrow 1$ process approximately, and the longitudinal momentum fractions of the two initial gluons are calculated from the momentum conservation:

$$x_{1,2} = \frac{\sqrt{m_\Psi^2 + p_t^2}}{\sqrt{s_{\text{NN}}}} e^{\pm y}. \quad (15)$$

The free distribution $\bar{f}_\Psi^{\text{NN}}(\mathbf{p})$ can be obtained by integrating the elementary partonic process:

$$\begin{aligned} \frac{d\sigma_\Psi^{\text{NN}}}{dp_t dy} \\ = \int dy_g x_1 x_2 f_g(x_1, \mu_F) f_g(x_2, \mu_F) \frac{d\sigma_{gg \rightarrow \Psi g}}{d\hat{t}}, \end{aligned} \quad (16)$$

where $f_g(x, \mu_F)$ is the gluon distribution in a free proton, y_g the emitted gluon rapidity, $d\sigma_{gg \rightarrow \Psi g}/d\hat{t}$ the charmonium momentum distribution produced from a gluon fusion process, and μ_F the factorization scale of the fusion process.

Now we consider the shadowing effect. The distribution function $\bar{f}_i(x, \mu_F)$ for parton i in a nucleus differs from a superposition of the distribution $f_i(x, \mu_F)$ in a free nucleon. The nuclear shadowing can be described by the modification factor $R_i = \bar{f}_i/(Af_i)$. To account for the spatial dependence of the shadowing in a finite nucleus, one assumes that the inhomogeneous shadowing is proportional to the parton path length through the nucleus [45], which amounts to considering the coherent interaction of the incident parton with all the target partons along its path length. Therefore, we replace the homogeneous modification factor $R_i(x, \mu_F)$ by an inhomogeneous one [46]

$$\mathcal{R}_i(x, \mu_F, \mathbf{x}_t) = 1 + \frac{A(R_i(x, \mu_F) - 1)T_A(\mathbf{x}_t)}{T_{AB}(0)} \quad (17)$$

with the definition $T_{AB}(\mathbf{b}) = \int d^2 \mathbf{x}_t T_A(\mathbf{x}_t) T_B(\mathbf{x}_t - \mathbf{b})$. We employ in the following the EKS98 package [5] to evaluate the homogeneous ratio R_i , and the factorization scale is taken as $\mu_F = \sqrt{m_\Psi^2 + p_t^2}$.

Replacing the free distribution f_g in (16) by the modified distribution $\bar{f}_g = Af_g \mathcal{R}_g$ and then taking into account the Cronin effect (13), we finally get the initial charmonium distribution for solution (10):

$$\begin{aligned} f_\Psi(x_0, \mathbf{p} | \mathbf{b}) &= \frac{(2\pi)^3}{E_t \tau_0} \int dz_A dz_B \rho_A(\mathbf{x}_t, z_A) \rho_B(\mathbf{x}_t, z_B) \\ &\cdot \mathcal{R}_g(x_1, \mu_F, \mathbf{x}_t) \mathcal{R}_g(x_2, \mu_F, \mathbf{x}_t - \mathbf{b}) \\ &\cdot \bar{f}_\Psi^{\text{NN}}(\mathbf{x}, \mathbf{p}, z_A, z_B | \mathbf{b}) S_{\text{abs}}. \end{aligned} \quad (18)$$

Now the only thing left is the distribution \bar{f}_Ψ^{NN} in a free $p + p$ collision which can be fixed by experimental data or some model simulations.

4. Numerical Results

The beam energy $E_{\text{lab}} = 2.76A$ TeV in fixed-target experiments corresponds to a colliding energy $\sqrt{s_{\text{NN}}} = 72$ GeV, and the rapidity in the center-of-mass frame is boosted in the laboratory frame with a rapidity shift $\Delta y = \tanh^{-1}\beta_{\text{cms}} = 4.3$. Let us first focus on the central rapidity region around $y_{\text{cms}} = 0$ in the center-of-mass frame, which corresponds to $y_{\text{lab}} = 4.3$ in the laboratory frame. The centrality and momentum dependent antishadowing for initially produced charmonia is reflected in the inhomogeneous modification factor \mathcal{R}_g for gluons. The longitudinal momentum fractions are $x_{1,2} = \sqrt{m_\psi^2 + p_t^2}/\sqrt{s_{\text{NN}}} \sim 0.05$ for the two gluons, which are located at the strong antishadowing region [47] by some parametrization of parton distribution shadowing like EKS98 [5], EPS08 [48], and EPS09 [49]. The antishadowing changes not only the gluon distribution but also the charm quark production cross section used in the regeneration. For the process $g + g \rightarrow c + \bar{c}$, the antishadowing for gluons leads to an antishadowing factor, $\sim (\mathcal{R}_g)^2$ for the cross section. Considering that in peripheral collisions the regeneration is weak and its contribution is not remarkably affected by the antishadowing, we take a centrality averaged antishadowing factor for the cross section to simplify the numerical calculation for regeneration. Estimated from the EKS98 evolution [5], we take a 20% enhancement of the charm quark production cross section compared to free p + p collisions. From FONLL calculation [50], the upper limit for $d\sigma_{c\bar{c}}^{\text{NN}}/dy$ is 0.047 mb at $\sqrt{s_{\text{NN}}} = 62.4$ GeV. Note that the experimental data for charm quark cross section in free p + p collisions are close to the upper limit of perturbative calculation; we take $d\sigma_{c\bar{c}}^{\text{NN}}/dy = 0.05$ mb at $\sqrt{s_{\text{NN}}} = 72$ GeV. After taking into account the antishadowing effect in A + A collisions, it becomes 0.06 mb. For p + p collisions, we assume a constant hidden to open charm ratio $(d\sigma_\psi/dy)/(d\sigma_{c\bar{c}}/dy) = \text{const}$ at any colliding energy. From the ratio extracted from the RHIC data [51], we have $d\sigma_{J/\psi}/dy = 0.35 \mu\text{b}$ at $\sqrt{s_{\text{NN}}} = 72$ GeV. The transverse momentum distribution for J/ψ in free p + p collisions can be simulated by PYTHIA [52] and the mean transverse momentum square is $\langle p_t^2 \rangle_{\text{pp}} = 2.7$ (GeV/c) 2 .

Figure 1 shows our calculated centrality dependence of J/ψ nuclear modification factor $R_{\text{AA}} = N_\psi^{\text{AA}}/(N_{\text{coll}}N_\psi^{\text{pp}})$ in Pb + Pb collisions at LHC beam energy $E_{\text{lab}} = 2.76A$ TeV in laboratory frame ($\sqrt{s_{\text{NN}}} = 72$ GeV in center-of-mass frame) at forward rapidity $y_{\text{lab}} = 4.3$ (central rapidity $y_{\text{cms}} = 0$), where N_ψ^{pp} and N_ψ^{AA} are charmonium yields in p + p and A + A collisions, and N_{coll} and N_{part} are numbers of binary collisions and participants. For comparison, we show also the RHIC data at $\sqrt{s_{\text{NN}}} = 62.4$ GeV [53] at central rapidity. Since the shadowing/antishadowing effect is still an open question and its degree depends strongly on the models we used, we show in Figure 1 two calculations for the total J/ψ R_{AA} in Pb + Pb collisions at $\sqrt{s_{\text{NN}}} = 72$ GeV: one is with the above discussed antishadowing and the other is without antishadowing. The hatched band is due to this uncertainty in the antishadowing. With increasing collision centrality, the initial contribution drops down, while the regeneration goes up. The canonical

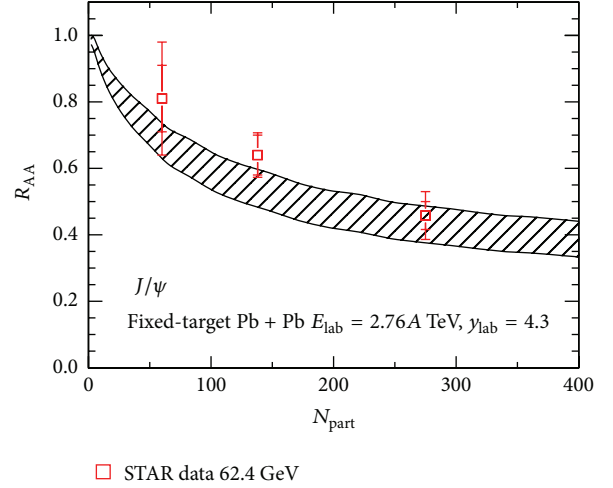


FIGURE 1: The centrality dependence of the J/ψ nuclear modification factor R_{AA} at very forward rapidity $y_{\text{lab}} = 4.3$ ($y_{\text{cms}} = 0$) in Pb + Pb collisions at LHC beam energy $E_{\text{lab}} = 2.76A$ TeV. The hatched band is the model result with the upper and lower borders corresponding to the calculations with and without antishadowing effect. The RHIC data [53] are for Au + Au collisions at $y_{\text{cms}} = 0$.

effect is important in peripheral collisions where the number of charm quark pairs is less than one and the inclusion of the canonical effect enhances sizeably the charmonium yield. In most central collisions, the regeneration can contribute about 25% to the total charmonium yield. The antishadowing at very forward rapidity in the laboratory frame (central rapidity in the center-of-mass frame) enhances the charm quark cross section and in turn the initial charmonium yield by a factor of 1.2. As a consequence, the enhancement factor for the regenerated charmonium number is $1.2^2 = 1.44$ which leads to a strong charmonium enhancement! If we do not consider the antishadowing effect on the charmonium regeneration and initial production, the total R_{AA} is significantly reduced.

To see more clearly the charmonium production mechanism, we turn to the transverse momentum information. In Figure 2 we show the J/ψ nuclear modification factor [54]

$$r_{\text{AA}} = \frac{\langle p_t^2 \rangle_{\text{AA}}}{\langle p_t^2 \rangle_{\text{pp}}} \quad (19)$$

in Pb + Pb collisions at beam energy $E_{\text{lab}} = 2.76A$ TeV, where $\langle p_t^2 \rangle_{\text{AA}}$ and $\langle p_t^2 \rangle_{\text{pp}}$ are averaged J/ψ transverse momentum square in Pb + Pb and p + p collisions at very forward rapidity $y_{\text{lab}} = 4.3$. If we neglect the contribution from the regeneration and consider only the initial production, the ratio r_{AA} goes up monotonously with centrality due to the Cronin effect and leakage effect [54]. The inclusion of regeneration (upper border of the band) remarkably reduces the averaged transverse momentum, because the regenerated charmonia possess a soft momentum distribution induced by the charm quark energy loss. Since the degree of regeneration increases with centrality, the increased soft component leads to a decreasing r_{AA} in most central collisions. The canonical effect can reduce the r_{AA} further, since it enhances the regeneration

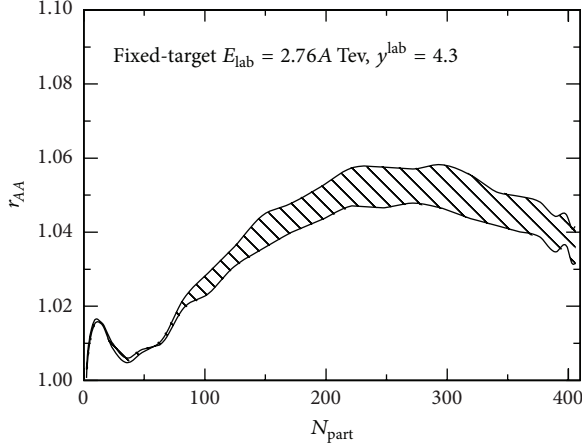


FIGURE 2: The centrality dependence of the J/ψ nuclear modification factor r_{AA} at forward rapidity $y_{lab} = 4.3$ ($y_{cms} = 0$) in Pb + Pb collisions at LHC beam energy $E_{lab} = 2.76A$ TeV. The upper and lower borders of the band correspond to the calculations with and without antishadowing effect.

especially in peripheral collisions. However, we should note that the assumption of charm quark thermalization indicates a full energy loss and it may not be reached in peripheral and semicentral collisions at beam energy $E_{lab} = 2.76A$ TeV. When we switch off the antishadowing (lower border of the band), both the hard component controlled by the initial production and the soft component dominated by the regeneration would be reduced. Considering that the enhancement factor resulted from the antishadowing is 1.2 for the initial production but 1.2^2 for the regeneration, the strong antishadowing in the soft component leads to only a slight difference between with and without considering the antishadowing, shown in Figure 2. It is obvious that, compared to the nuclear modification factor R_{AA} for the yield, the modification factor r_{AA} for the transverse momentum is less sensitive to the shadowing effect [54].

From the simulations of parton distributions in cold nuclear matter [5, 48, 49], the nuclear shadowing region is located at very small x . In the following we consider the shadowing and see its difference from the antishadowing in J/ψ R_{AA} and r_{AA} in fixed-target Pb + Pb collisions. The maximum J/ψ rapidity in the center-of-mass frame is $y_{cms}^{max} = \cosh^{-1}[\sqrt{s_{NN}}/(2m_{J/\psi})] = 3.13$ at $\sqrt{s_{NN}} = 72$ GeV. Considering the expected amount of measured events, we focus on the backward rapidity region around $y_{cms} = -2$ which corresponds to the less forward rapidity $y_{lab} = \Delta y + y_{cms} = 4.3 - 2 = 2.3$ in laboratory frame. From the kinematics, the momentum fractions for the two gluons involved in the gluon fusion process are $x_1 = (\sqrt{m_{\psi}^2 + p_t^2}/\sqrt{s_{NN}})e^2 = 0.35$ and $x_2 = (\sqrt{m_{\psi}^2 + p_t^2}/\sqrt{s_{NN}})e^{-2} = 0.006$. One is located in the EMC region and the other in the shadowing region [5, 48, 49], leading to a reduction of 15% for the charm quark production cross section from EKS98 evolution [5] (20% from EPS09 NLO evolution [49]). Taking the same ratio of charm quark cross section between $y_{cms} = -2$ and $y_{cms} = 0$ calculated from

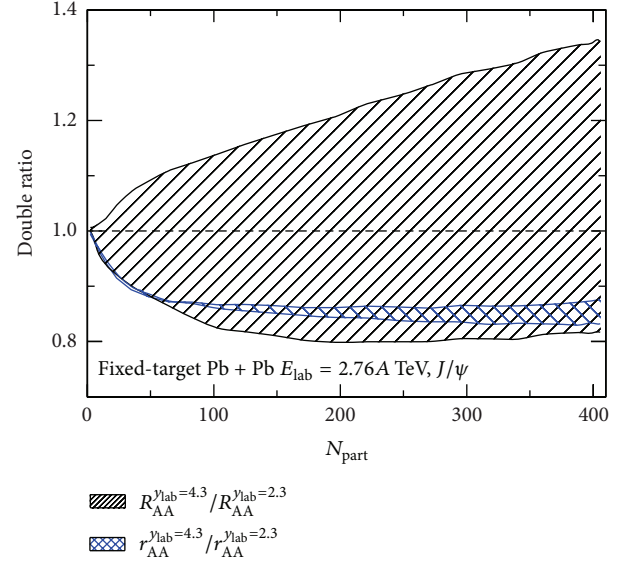


FIGURE 3: The centrality dependence of the double ratios $R_{AA}^{y_{lab}=4.3}/R_{AA}^{y_{lab}=2.3}$ and $r_{AA}^{y_{lab}=4.3}/r_{AA}^{y_{lab}=2.3}$ for J/ψ yield and transverse momentum in Pb + Pb collisions at LHC beam energy $E_{lab} = 2.76A$ TeV. The upper and lower borders of the two bands correspond to the calculations with and without shadowing and antishadowing effects.

FONLL [50] and including the 15% shadowing reduction, we obtain $d\sigma_{cc}^{NN}/dy = 0.01$ mb at $y_{cms} = -2$. For the medium evolution at this backward rapidity region, we initialize the entropy density to be half of that at central rapidity [6, 55] which leads to a maximum temperature of $T_0 = 245$ MeV. Figure 3 shows the two double ratios $R_{AA}^{y_{lab}=4.3}/R_{AA}^{y_{lab}=2.3}$ and $r_{AA}^{y_{lab}=4.3}/r_{AA}^{y_{lab}=2.3}$ of J/ψ ; the upper and lower borders of the two bands correspond to the calculations with and without considering the nuclear shadowing and antishadowing. While the double ratio for the transverse momentum is not sensitive to the shadowing and antishadowing, as we discussed above, the strong antishadowing at $y_{lab} = 4.3$ and shadowing at $y_{lab} = 2.3$ lead to a strong enhancement of the double ratio for the yield. Without considering the shadowing and antishadowing, the stronger charmonium suppression in the hotter medium at $y_{lab} = 4.3$ ($T_0 = 310$ MeV) compared with the weaker suppression in the relatively colder medium at $y_{lab} = 2.3$ ($T_0 = 245$ MeV) makes the double ratio less than unit. However, the inclusion of the yield enhancement due to the antishadowing at $y_{lab} = 4.3$ and the yield suppression due to the shadowing at $y_{lab} = 2.3$ changes significantly the behavior of the double ratio; it becomes larger than unit and can reach 1.3 in most central collisions. Note that the rapidity dependent shadowing effect was used to qualitatively interpret the stronger suppression at forward rapidity than that at midrapidity in Au + Au collisions at RHIC [56, 57].

5. Summary

We investigated with a transport approach the charmonium production in fixed-target Pb + Pb collisions at LHC beam

energy $E_{\text{lab}} = 2.76A$ TeV. We focused on the rapidity dependent shadowing effect on the nuclear modification factors for the charmonium yield and transverse momentum. While the averaged transverse momentum is not sensitive to the shadowing effect, the antishadowing leads to a strong yield enhancement at very forward rapidity $y_{\text{lab}} \approx 4$, and the shadowing results in a strong yield suppression at less forward rapidity $y_{\text{lab}} \approx 2$. The double ratio between the nuclear modification factors R_{AA} in the two rapidity regions amplifies the shadowing effect; it is larger than unit and can reach 1.3 in most central collisions.

From the model studies on gluon distribution in nuclei, see, for instance [5, 47–49], there are large uncertainties in the domain of large x (> 0.1), which is probably due to the unknown EMC effect. From our calculation here, the double ratio of the nuclear modification factor for J/ψ yield is very sensitive to the gluon shadowing effect in different x region. A precise measurement of the ratio may provide a sensitive probe to the gluon distribution.

Conflict of Interests

The authors declare that there is no conflict of interests regarding the publication of this paper.

Acknowledgments

The work is supported by the NSFC under Grant no. 11335005 and the MOST under Grant nos. 2013CB922000 and 2014CB845400.

References

- [1] S. J. Brodsky, F. Fleuret, C. Hadjidakis, and J. P. Lansberg, “Physics opportunities of a fixed-target experiment using LHC beams,” *Physics Reports*, vol. 522, no. 4, pp. 239–255, 2013.
- [2] J. P. Lansberg, S. J. Brodsky, F. Fleuret, and C. Hadjidakis, “Quarkonium physics at a fixed-target experiment using the LHC beams,” *Few-Body Systems*, vol. 53, no. 1–2, pp. 11–25, 2012.
- [3] A. Andronic, F. Arleo, R. Arnaldi et al., “Heavy-flavour and quarkonium production in the LHC era: from proton-proton to heavy-ion collisions,” <http://arxiv.org/abs/1506.03981>.
- [4] R. Vogt, “The A-dependence of open charm and bottom production,” *International Journal of Modern Physics E*, vol. 12, no. 2, p. 211, 2003.
- [5] K. J. Eskola, V. J. Kolhinen, and C. A. Salgado, “The scale dependent nuclear effects in parton distributions for practical applications,” *The European Physical Journal C*, vol. 9, no. 1, pp. 61–68, 1999.
- [6] C. Shen and U. Heinz, “Collision energy dependence of viscous hydrodynamic flow in relativistic heavy-ion collisions,” *Physical Review C*, vol. 85, no. 5, Article ID 054902, 12 pages, 2012.
- [7] Z. Tang, N. Xu, K. Zhou, and P. Zhuang, “Charmonium transverse momentum distribution in high energy nuclear collisions,” *Journal of Physics G: Nuclear and Particle Physics*, vol. 41, no. 12, Article ID 124006, 2014.
- [8] X. Zhu, P. Zhuang, and N. Xu, “ J/ψ transport in QGP and p_t distribution at SPS and RHIC,” *Physics Letters B*, vol. 607, no. 1–2, pp. 107–114, 2005.
- [9] H. Song, S. Bass, U. Heinz, T. Hirano, and C. Shen, “200 A GeV Au + Au collisions serve a nearly perfect Quark-Gluon liquid,” *Physical Review Letters*, vol. 106, Article ID 192301, 2012.
- [10] J. Sollfrank, P. Huovinen, M. Kataja, P. V. Ruuskanen, M. Prakash, and R. Venugopalan, “Hydrodynamical description of 200A GeV/c S+Au collisions: hadron and electromagnetic spectra,” *Physical Review C*, vol. 55, article 392, 1997.
- [11] K. Hagiwara, K. Hikasa, K. Nakamura et al., “Review of particle properties,” *Physical Review D*, vol. 66, no. 1, Article ID 010001, 2002.
- [12] G. Kestin and U. Heinz, “Hydrodynamic radial and elliptic flow in heavy-ion collisions from AGS to LHC energies,” *The European Physical Journal C*, vol. 61, no. 4, pp. 545–552, 2009.
- [13] P. Kolb and R. Rapp, “Transverse flow and hadrochemistry in Au + Au collisions at $\sqrt{s_{NN}} = 200$ GeV,” *Physical Review C*, vol. 67, Article ID 044903, 2003.
- [14] Particle Data Group, “Review of particle properties,” *Physical Review D*, vol. 45, no. 11, pp. S1–S574, 1992.
- [15] A. Zoccoli, I. Abt, M. Adams et al., “Charm, beauty and charmonium production at HERA-B,” *The European Physical Journal C*, vol. 43, no. 1–4, pp. 179–186, 2005.
- [16] J. Hüfner and P. Zhuang, “Time structure of anomalous J/ψ and ψ' suppression in nuclear collisions,” *Physics Letters B*, vol. 559, no. 3–4, pp. 193–200, 2003.
- [17] G. Bhanot and M. E. Peskin, “Short-distance analysis for heavy-quark systems: (I). Diagrammatics,” *Nuclear Physics B*, vol. 156, no. 3, pp. 365–390, 1979.
- [18] G. Bhanot and M. E. Peskin, “Short-distance analysis for heavy-quark systems: (II). Applications,” *Nuclear Physics B*, vol. 156, no. 3, pp. 391–416, 1979.
- [19] F. Arleo, P.-B. Gossiaux, T. Gousset, and J. Aichelin, “Heavy-quarkonium hadron cross section in QCD at leading twist,” *Physical Review D*, vol. 65, no. 1, Article ID 014005, 2002.
- [20] Y. S. Oh, H. C. Kim, and S. H. Lee, “Quarkonium-hadron interactions in QCD,” *Physical Review C*, vol. 65, Article ID 067901, 2002.
- [21] X. N. Wang, “Azimuthal asymmetry of J/ψ suppression in non-central heavy-ion collisions,” *Physics Letters B*, vol. 540, no. 1–2, pp. 62–67, 2002.
- [22] H. Satz, “Colour deconfinement and quarkonium binding,” *Journal of Physics G*, vol. 32, no. 3, p. R25, 2006.
- [23] P. Petreczky, “Quarkonium in a hot medium,” *Journal of Physics G: Nuclear and Particle Physics*, vol. 37, no. 9, Article ID 094009, 2010.
- [24] T. Matsui and H. Satz, “ J/ψ suppression by quark-gluon plasma formation,” *Physics Letters B*, vol. 178, pp. 416–422, 1986.
- [25] R. L. Thews and M. L. Mangano, “Momentum spectra of charmonium produced in a quark-gluon plasma,” *Physical Review C*, vol. 73, Article ID 014904, 2006.
- [26] L. Yan, P. Zhuang, and N. Xu, “ J/ψ production in quark-gluon plasma,” *Physical Review Letters*, vol. 97, Article ID 232301, 2006.
- [27] B. I. Abelev, M. M. Aggarwal, Z. Ahammed et al., “Transverse momentum and centrality dependence of high- p_T nonphotonic electron suppression in Au + Au collisions at $\sqrt{s_{NN}} = 200$ GeV,” *Physical Review Letters*, vol. 98, Article ID 192301, 2007.
- [28] L. Adamczyk, J. K. Adkins, G. Agakishiev et al., “Observation of D^0 Meson nuclear modifications in Au+Au collisions at $\sqrt{s_{NN}} = 200$ GeV,” *Physical Review Letters*, vol. 113, no. 14, Article ID 142301, 7 pages, 2014.

- [29] B. Abelev, J. Adam, D. Adamová et al., “Suppression of high transverse momentum D mesons in central Pb-Pb collisions at $\sqrt{s_{NN}} = 2.76$ TeV,” *Journal of High Energy Physics*, vol. 2012, no. 9, article 112, 2012.
- [30] A. Adare, S. Afanasiev, C. Aidala et al., “Energy loss and flow of heavy quarks in Au+Au collisions at $\sqrt{s_{NN}} = 200$ GeV,” *Physical Review Letters*, vol. 98, Article ID 172301, 2007.
- [31] B. Abelev, J. Adam, D. Adamová et al., “D meson elliptic flow in noncentral Pb-Pb collisions at $\sqrt{s_{NN}} = 2.76$ TeV,” *Physical Review Letters*, vol. 111, Article ID 102301, 2013.
- [32] C. M. Ko, V. Koch, Z.-W. Lin, K. Redlich, M. Stephanov, and X.-N. Wang, “Kinetic equation with exact charge conservation,” *Physical Review Letters*, vol. 86, pp. 5438–5441, 2001.
- [33] Y. Liu, C. Ko, and T. Song, “Hot medium effects on J/ψ production in p+Pb collisions at $\sqrt{s_{NN}} = 5.02$,” *Physics Letters B*, vol. 728, pp. 437–442, 2014.
- [34] A. Polleri, T. Renk, R. Schneider, and W. Weise, “Kinetic description of charmonium production in high-energy nuclear collisions,” *Physical Review C*, vol. 70, Article ID 044906, 2004.
- [35] T. Barnes, E. S. Swanson, C.-Y. Wong, and X.-M. Xu, “Dissociation cross sections of ground state and excited charmonia with light mesons in the quark model,” *Physical Review C*, vol. 68, Article ID 014903, 2003.
- [36] X. Du and R. Rapp, “Sequential regeneration of charmonia in heavy-ion collisions,” <http://arxiv.org/abs/1504.00670>.
- [37] Y. Liu, Z. Qu, N. Xu, and P. Zhuang, “Rapidity dependence of J/ψ production at the RHIC and LHC,” *Journal of Physics G: Nuclear and Particle Physics*, vol. 37, no. 7, Article ID 075110, 2010.
- [38] A. Capella and E. G. Ferreira, “ J/ψ Suppression and the decrease of nuclear absorption with increasing energy,” *Physical Review C*, vol. 76, Article ID 064906, 2007.
- [39] C. Lourenço, R. Vogt, and H. K. Wöhri, “Energy dependence of J/ψ absorption in proton-nucleus collisions,” *Journal of High Energy Physics*, vol. 2009, no. 2, article 014, 2009.
- [40] S. Esumi, U. Heinz, and N. Xu, “Collective flow or random walk?” *Physics Letters B*, vol. 403, no. 1-2, pp. 145–148, 1997.
- [41] X. Zhao and R. Rapp, “Transverse momentum spectra of J/ψ in heavy-ion collisions,” *Physics Letters B*, vol. 664, no. 4-5, pp. 253–257, 2008.
- [42] Y. Liu, B. Chen, N. Xu, and P. Zhuang, “ Υ production as a probe for early state dynamics in high energy nuclear collisions at RHIC,” *Physics Letters B*, vol. 697, no. 1, pp. 32–36, 2011.
- [43] X. N. Wang, “Where is the jet quenching in Pb + Pb collisions at 158 A GeV?” *Physical Review Letters*, vol. 81, pp. 2655–2658, 1998.
- [44] Y. Liu, Z. Qu, N. Xu, and P. Zhuang, “Spacetime evolution of J/ψ production in high energy nuclear collisions,” *Journal of Physics G*, vol. 36, no. 6, Article ID 064057, 2009.
- [45] S. R. Klein and R. Vogt, “Inhomogeneous shadowing effects on J/ψ production in dA collisions,” *Physical Review Letters*, vol. 91, Article ID 142301, 2003.
- [46] R. Vogt, “Shadowing and absorption effects on J/ψ production in dA collisions,” *Physical Review C*, vol. 71, Article ID 054902, 2005.
- [47] J. Dias de Deus, “Nuclear anti-shadowing and the quarkonium nucleon elastic scattering amplitude,” *Physics Letters B*, vol. 335, no. 2, pp. 188–191, 1994.
- [48] K. Eskola, H. Paukkunen, and C. Salgado, “An improved global analysis of nuclear parton distribution functions including RHIC data,” *Journal of High Energy Physics*, vol. 2008, no. 7, article 102, 2008.
- [49] K. J. Eskola, H. Paukkunen, and C. A. Salgado, “EPS09—a new generation of NLO and LO nuclear parton distribution functions,” *Journal of High Energy Physics*, vol. 2009, no. 4, article 065, 2009.
- [50] M. Cacciari, M. Greco, and P. Nason, “The p_T spectrum in heavy-flavour hadroproduction,” *Journal of High Energy Physics*, vol. 1998, no. 5, article 007, 1998.
- [51] A. Adare, S. Afanasiev, C. Aidala et al., “ J/ψ production versus centrality, transverse momentum, and rapidity in Au+Au collisions at $\sqrt{s_{NN}} = 200$ GeV,” *Physical Review Letters*, vol. 98, Article ID 232301, 2007.
- [52] T. Sjöstrand, P. Edén, C. Friberg et al., “High-energy-physics event generation with PYTHIA 6.1,” *Computer Physics Communications*, vol. 135, no. 2, pp. 238–259, 2001.
- [53] A. Adare, C. Aidala, N. N. Ajitanand et al., “ J/ψ suppression at forward rapidity in Au + Au collisions at $\sqrt{s_{NN}} = 39$ and 62.4 GeV,” *Physical Review C*, vol. 86, Article ID 064901, 2012.
- [54] K. Zhou, N. Xu, Z. Xu, and P. Zhuang, “Medium effects on charmonium production at ultrarelativistic energies available at the CERN Large Hadron Collider,” *Physical Review C*, vol. 89, Article ID 054911, 2014.
- [55] M. C. Abreu, B. Alessandro, C. Alexa et al., “Scaling of charged particle multiplicity in Pb-Pb collisions at SPS energies,” *Physics Letters B*, vol. 530, no. 1-4, pp. 43–55, 2002.
- [56] A. D. Frawley, T. Ullrich, and R. Vogt, “Heavy flavor in heavy-ion collisions at RHIC and RHIC II,” *Physics Reports*, vol. 462, no. 4-6, pp. 125–175, 2008.
- [57] E. Ferreira, F. Fleuret, J. Lansberg, and A. Rakotozafindrabe, “Cold nuclear matter effects on J/ψ production: intrinsic and extrinsic transverse momentum effects,” *Physics Letters B*, vol. 680, pp. 50–55, 2009.

Review Article

Quarkonium Production and Proposal of the New Experiments on Fixed Target at the LHC

A. B. Kurepin and N. S. Topilskaya

Institute for Nuclear Research, RAS, 60th October Anniversary Prospect 7a, Moscow 117312, Russia

Correspondence should be addressed to N. S. Topilskaya; topilskaya@inr.ru

Received 20 March 2015; Revised 26 May 2015; Accepted 28 June 2015

Academic Editor: Jibo He

Copyright © 2015 A. B. Kurepin and N. S. Topilskaya. This is an open access article distributed under the Creative Commons Attribution License, which permits unrestricted use, distribution, and reproduction in any medium, provided the original work is properly cited. The publication of this article was funded by SCOAP³.

The brief review of the experimental data on quarkonium productions measured at the CERN SPS, at the Brookhaven Collider RHIC, and at the LHC is presented. The dissociation of quarkonium resonances produced in heavy ion collisions was suggested as a possible signal of the Quark-Gluon Plasma formation. At the CERN SPS, the anomalous suppression of the J/ψ production was observed in central Pb-Pb collisions by the NA50 collaboration. However, the effects of J/ψ suppression on cold nuclear matter, feed-down production from higher charmonium states, and regeneration processes should be taken into account. If proton and ion beams at the LHC will be used with fixed targets, the energy interval between the SPS energy and the nominal RHIC energy (200 GeV) could be investigated. The high statistics data on quarkonium productions at these energies will give the possibility of clarifying the mechanism of charmonium productions to investigate the importance of the recombination process, since the probability of recombination decreases with decreasing the energy of collisions.

1. Introduction

The existence of the Quark-Gluon Plasma (QGP) is predicted by lattice QCD at high temperature and large energy density. Quarkonia are important probes to study the properties of the deconfined matter. The dissociation of heavy-quark resonances by color screening in a deconfined medium was suggested by Matsui and Satz as a possible signal of the Quark-Gluon Plasma formation in ultrarelativistic heavy ion collisions [1].

Quarkonium productions have been previously studied at the CERN SPS by NA38 [2], NA50 [3–7], and NA60 [8, 9] experiments, at the FNAL [10], and by fixed target p-A experiments at the HERA-B [11]. In 1997, the NA50 experiment has observed an “anomalous” suppression of the J/ψ production in central Pb-Pb collisions [3]. However, the cold nuclear matter (CNM) effects and feed-down production of J/ψ from higher charmonium states, which affect the extraction of hot and dense matter effects, should be carefully measured. In spite of many experimental results already

obtained on the J/ψ production in p-A collisions, they are still not well understood, especially at small Bjorken x_B and large Feynman x_F , where the CNM effects are expected to be large. Quarkonium productions have been studied in the Brookhaven National Laboratory at RHIC by PHENIX [12–16] and STAR experiments [17–19]. It was shown that the J/ψ suppression measured by PHENIX experiment at $\sqrt{s} = 200$ GeV is of the same order as the suppression at the SPS energies for Pb-Pb collisions [13, 20]. In order to get better agreement between theoretical description of the RHIC and the SPS experimental results the models that include the regeneration of J/ψ were developed [21–24]. The quarkonium productions have been measured at significantly higher energies at the LHC by ALICE [25, 26], CMS [27, 28], ATLAS [29, 30], and LHCb [31, 32] experiments. At the LHC energies the contribution of B-decay should be taken into account [27, 29, 31–33]. The high statistics measurements at the LHC could investigate the properties of matter at high energy density and temperature. However, the quarkonium study at energies below the LHC energy is also very important

in order to investigate the mechanism of production, the medium effects, and conditions for the Quark-Gluon Plasma formation. If it would be possible to use the proton and ion beams at the LHC with fixed targets, the data in the energy interval between maximum energy of the SPS ($\sqrt{s} \sim 29$ GeV) and the nominal RHIC energy ($\sqrt{s} = 200$ GeV) in p-A and A-A collisions could be obtained. For 0.45 TeV proton beam, the energy in N-N centre-of-mass system is $\sqrt{s_{NN}} = 29.1$ GeV, for 7 TeV proton beam $\sqrt{s_{NN}} = 114.6$ GeV and for 2.75 TeV Pb beam $\sqrt{s_{NN}} = 71.8$ GeV. The high statistics data on quarkonium production at these energies will give the possibility of clarifying the mechanism of charmonium production to investigate the importance of recombination process, since the probability of recombination decreases with decreasing the energy of collisions.

2. Charmonium Production at the CERN SPS

The productions of J/ψ and $\psi(2S)$ have been studied at the CERN SPS by the NA50 experiment. Data have been taken for Pb-Pb collisions at 158 GeV per nucleon [3, 7] and for p-A collisions at 450 [4, 5] and 400 GeV [6]. The nuclear suppression of the J/ψ production in proton-nucleus reactions and an anomalous suppression in central lead-lead collisions were observed [3, 7]. In the NA60 experiment, the J/ψ production was measured in In-In collisions at 158 GeV per nucleon [8] and in p-A collisions at 400 and 158 GeV [9]. The NA60 results in p-A collisions at 400 GeV confirm the NA50 values of absorption cross section at the same energy. On the other hand, the NA60 158 GeV p-A data give higher values of absorption. Rather strong energy dependence of the absorption cross section was observed. However, the older NA3 J/ψ results at 200 GeV [34] are in partial contradiction with these observations and give values of absorption cross section similar to those obtained at the higher energy. This difference has not yet been satisfactorily explained by theoretical models. Therefore, it is important to measure the charmonium production cross sections in p-p, p-A, and A-A collisions at the same energy and in the same kinematic domain.

The heavy-quark pair can interact with the nuclear matter and eventually break up. It is the effect of nuclear absorption. The cold nuclear matter (CNM) effect in suppression of the J/ψ production includes not only nuclear absorption, but also the shadowing effect, that is, the modification of the parton distribution function in nuclear matter compared to the free nucleon. If shadowing is taken into account, the amount of the anomalous J/ψ suppression is reduced. Also, it is necessary to consider the energy loss of partons in nuclear matter. The charmonium can also interact with surrounding comovers and lose energy or even break up.

For In-In collisions at 158 GeV per nucleon after adjustment for the effects of cold nuclear matter, the additional suppression becomes quite small. But the value of the anomalous suppression in the most central Pb-Pb collisions is of the order of 20–30%. So, to extract the effects of hot and dense nuclear matter in the J/ψ production at the SPS energies, the CNM effects and feed-down production from higher charmonium states must be taken into account.

3. Charmonium Production at the Relativistic Heavy Ion Collider RHIC

At the RHIC, the production of J/ψ was measured in p-p, d-Au, Au-Au, and Cu-Cu collisions by the PHENIX experiment at $\sqrt{s_{NN}} = 200$ GeV energy in the N-N centre-of-mass [12–16]. To quantify the suppression of the J/ψ production in heavy ion collisions, the nuclear modification factor R_{AA} was introduced:

$$R_{AA} \equiv \frac{dN_{AA}/dy}{(dN_{pp}/dy \cdot \langle N_{coll} \rangle)}, \quad (1)$$

which is the ratio of the J/ψ yield in A-A collisions, normalized to the number of binary collisions, N_{coll} , to the J/ψ yield in p-p collisions. The nuclear modification factor has been measured as a function of several parameters: the centrality of collisions, the multiplicity, the transverse momentum, and the number of participants (N_{part}).

The suppression of the J/ψ production in Au-Au collisions is considerably stronger at forward rapidity range $1.2 < |y| < 2.2$ than at midrapidity $|y| < 0.35$. The PHENIX data for Au-Au and d-Au collisions were analyzed simultaneously for estimation of the CNM contribution. The nuclear modification factor for cold nuclear matter $R_{AA}(CNM)$ was obtained in Au-Au collisions at the measured rapidity ranges [20]. The ratio $R_{AA}/R_{AA}(CNM)$ estimates the value of additional suppression of the J/ψ production in the hot and dense nuclear matter produced in relativistic heavy ions collisions. The $R_{AA}/R_{AA}(CNM)$ ratio at $\sqrt{s_{NN}} = 200$ GeV is similar to the forward rapidity and midrapidity and reaches about 50% for the most central events.

Comparison of the $R_{AA}/R_{AA}(CNM)$ ratio estimated for NA50, NA60, and PHENIX data versus $dN/d\eta$ at pseudorapidity $\eta = 0$, which is proportional to the energy density, shows that at RHIC energy anomalous suppression of J/ψ for colliding nuclei is the same as at SPS energy [20] (Figure 1).

The nuclear modification factor for cold matter $R_{AA}(CNM)$ was obtained under the assumption that in p-p, p-A, and d-Au collisions at SPS and RHIC energies the hot and dense nuclear matter is not formed. There are some indications that the hot matter effects could present in d-Au collisions at the RHIC energies [35]. These effects may contribute to p-p and p-A collisions at higher energies.

The production of J/ψ in p-p, Au-Au, and Cu-Cu collisions was measured also by STAR experiment at the RHIC at midrapidity $|y| < 1$ for low $p_T < 5$ GeV/c [17] and for high $p_T > 5$ GeV/c [18, 19]. The value of R_{AA} in Au-Au collisions shows strong suppression at low transverse momentum but the suppression decreases significantly with increasing momentum. The J/ψ suppression in Au-Au collisions at low $p_T < 5$ GeV/c and at midrapidity is compatible to that measured by PHENIX. It was found that the results are consistent with models that include color screening and regeneration [36, 37]. The data from PHENIX show a significant suppression in midcentral and central Cu-Cu collisions [15]. The STAR Cu-Cu data [19] exhibit no suppression, but the precision is limited by the available statistics.

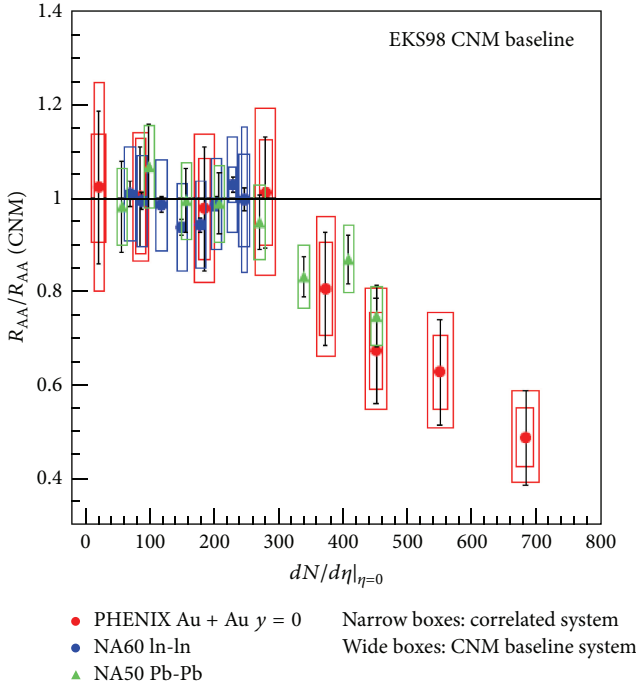


FIGURE 1: Comparison of the $R_{AA}/R_{AA}(\text{CNM})$ ratio obtained at the SPS and PHENIX versus $dN/d\eta|_{\eta=0}$.

The production of J/ψ in asymmetric Cu-Au heavy ion collisions was measured also at the RHIC at $\sqrt{s_{NN}} = 200$ GeV for both forward (Cu-going direction) and backward (Au-going direction) rapidity [38]. The suppression in the Au-going direction is found to be consistent with the suppression measured in Au-Au collisions. In the Cu-going direction, the J/ψ suppression is stronger. The difference may be due to the CNM effects which are different at forward and backward rapidity.

Recently at the RHIC, the J/ψ production in U-U collisions was measured at $\sqrt{s_{NN}} = 193$ GeV [39, 40]. The nuclear modification factor for J/ψ in U-U collisions for forward rapidity is very close to the Au-Au data with a hint of a slightly weaker suppression in central U-U collisions.

The RHIC experimental data could be described by theoretical models based on the regeneration of J/ψ . Additional J/ψ mesons are expected to be produced from deconfined charm quarks by kinetic recombination in the QGP [21, 22, 36, 37] or by statistical hadronization at the phase boundary [23, 24].

Bottomonium productions were also studied at the RHIC in p-p, d-Au, and Au-Au collisions [16, 39]. The suppression of total $\Upsilon(1S + 2S + 3S)$ yield measured by PHENIX is consistent with measurements made by STAR. The regeneration of bottomonia is expected to be small as compared to the J/ψ . But the energy resolution at RHIC was insufficient to separate the contributions of individual states.

The nuclear modification factor R_{AA} for the J/ψ production measured in Au-Au collisions at lower energies 62.4 and 39 GeV reveals approximately the same J/ψ suppression as at 200 GeV but has large statistical errors due to low luminosity

and large systematical errors because of lack of p-p collisions at the same energies [41]. At the RHIC, the luminosity strongly decreases with decreasing the energy of collisions. The investigations at lower energy with high statistics are very important for understanding the mechanism of charmonium production, for investigation the contribution of cold and hot nuclear matter effects. In addition, the contribution of recombination process decreases with decreasing the energy of collision.

The fixed target experiment at high luminosity LHC beams could provide measurements for p-p, p-A, and A-A collisions with the same equipment for different nuclei targets. The energy of collisions would be lower than the nominal RHIC energy (200 GeV). The charmonium production could be investigated with high statistics and low systematic errors and may provide reference from p-p data at these energies for RHIC.

4. Quarkonium Production at the CERN Large Hadron Collider LHC

At the LHC at CERN quarkonium productions were measured at the energy more than ten times higher than at RHIC. Five quarkonium states from two families are under study, charmonia: J/ψ and $\psi(2S)$ and bottomonia: $\Upsilon(1S)$, $\Upsilon(2S)$, and $\Upsilon(3S)$. In four experiments: ALICE [25, 26, 42–46], CMS [27, 28, 47–49], ATLAS [29, 30], and LHCb [31, 32, 50, 51], the quarkonium productions were measured in different energy, rapidity, and transverse momentum ranges. In all experiments p-p, p-Pb, and Pb-Pb collisions were measured, except for LHCb where there was no Pb-Pb program.

The quarkonium production in p-p collisions at $\sqrt{s_{NN}} = 2.76, 7$, and 8 TeV is useful for investigating the production mechanism, for comparison with different QCD model calculations and as a reference for understanding any additional effects in p-A and A-A collisions. The study of quarkonium production in p-Pb collisions at $\sqrt{s_{NN}} = 5.02$ TeV is important to distinguish the effects of Quark-Gluon Plasma from cold nuclear matter and to provide input to understanding of nucleus-nucleus collisions. The information about properties of hot and dense medium created in the collisions could be obtained from the measurements of Pb-Pb collisions at $\sqrt{s_{NN}} = 2.76$ TeV.

4.1. Charmonium Production at the LHC. At the LHC the charmonium J/ψ and $\psi(2S)$ productions were measured in p-p collisions at 2.76, 7, and 8 TeV and in Pb-Pb collisions at 2.76 TeV. Measurement of the J/ψ production in p-p collision at the same energy as in Pb-Pb collision provides the reference for extracting the nuclear modification factor R_{AA} . There is a good agreement for p-p collisions between the data obtained by ALICE [25], CMS [27], ATLAS [29], and LHCb [31] experiments in the same kinematic domains [52]. Comparison of charmonium J/ψ and $\psi(2S)$ production cross sections at forward rapidity in p-p collisions at 7 TeV [42], obtained by ALICE and LHCb experiments, is shown in Figure 2.

The mechanism of charmonium production was investigated by measuring the cross sections in p-p collisions

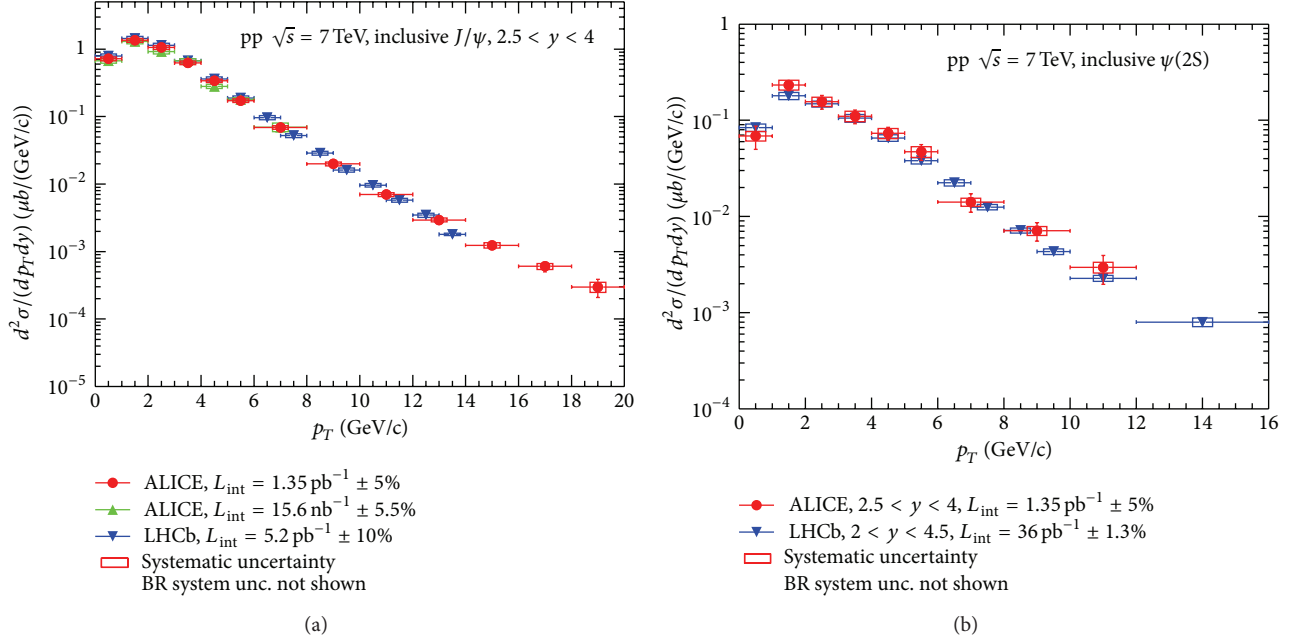


FIGURE 2: Comparison of charmonium production cross sections in p-p collisions at 7 TeV versus transverse momentum for ALICE and LHCb data for J/ψ (a) and $\psi(2S)$ (b).

as functions of energy, transverse momentum, and rapidity. Cross sections are compared to the theoretical models [42]. Unfortunately, none of the models, including NLO QCD, are able to describe simultaneously different aspects of quarkonium production. By increasing the energy of collisions, the mean transverse momentum and production cross section of J/ψ become larger. For forward rapidity, the cross section is smaller than at midrapidity. The contribution of B-decay to J/ψ production cross section was measured. This contribution depends on rapidity, increases with growing of J/ψ transverse momentum, and is of the order of 10% for transverse momentum about 1.5 GeV/c [27, 29, 33].

ALICE [26, 43], CMS [28], and ATLAS [30] experiments have measured charmonium productions in Pb-Pb collisions at $\sqrt{s_{\text{NN}}} = 2.76$ TeV. In the ALICE experiment, J/ψ mesons were detected in rapidity range $|y| < 0.9$ (for J/ψ decay into two electrons) and $2.5 < y < 4$ (for muon channel) with transverse momentum values from about zero up to 8 GeV/c . In ATLAS and CMS experiments, the J/ψ production was measured in the rapidity range $|y| < 2.4$, but the range of transverse momentum values depends on the rapidity. In ATLAS experiment, only the data for J/ψ mesons production with large transverse momentum $p_T > 6.5$ GeV/c were obtained. The comparison of PHENIX and ALICE nuclear modification factors R_{AA} for inclusive J/ψ production [13, 26] is shown in Figure 3.

Smaller suppression in the ALICE measurements of the inclusive J/ψ production in Pb-Pb collisions at $\sqrt{s_{\text{NN}}} = 2.76$ TeV [26, 43] compared to PHENIX results in Au-Au collisions at $\sqrt{s_{\text{NN}}} = 0.2$ TeV [13] was found. These measurements are compatible with a regeneration mechanism. This additional hot nuclear matter effect works in an opposite

direction to the suppression by color screening. At the LHC energy, the charm quark density produced in the collisions is larger than at SPS and RHIC energies. The probability of $c\bar{c}$ recombination increases with increasing the energy of collision and at the LHC energies may become dominant. In particular, this mechanism predicts an increase of R_{AA} from forward rapidity to midrapidity, where the density of charm quarks is higher. Moreover, in order to recombine, two charm quarks need to be close enough in phase space, so the effect will be larger at low p_T of J/ψ in agreement with experimental data [36, 37].

At the LHC, charmonium productions were measured in p-Pb collisions at the energy $\sqrt{s_{\text{NN}}} = 5.02$ TeV by ALICE [44, 45] and LHCb [50] experiments. The inclusive J/ψ production has been studied by ALICE [44]. The measurement is performed down to zero transverse momentum in the center of mass rapidity domains $2.03 < y < 3.53$ and $-4.46 < y < -2.96$ in muon channel. In p-Pb collisions, the J/ψ production was also measured in electron channel in rapidity domain $-1.37 < y < 0.43$ [44]. Since p-p collisions data at $\sqrt{s_{\text{NN}}} = 5.02$ TeV for determination of R_{pPb} are not available, the reference $\sigma_{\text{pp}}(J/\psi)$ has been obtained by an interpolation procedure, based on p-p collisions results at $\sqrt{s_{\text{NN}}} = 2.76$ TeV and 7 TeV obtained by the ALICE experiment. At forward rapidity, corresponding to the proton beam direction, a suppression of the J/ψ yield with respect to binary-scaled p-p collisions is observed, but in the backward region no suppression is found. The experimental results and comparison with theoretical predictions [44] are shown in Figure 4.

The Color Glass Condensate (CGC) model [53] could not describe the data. Theoretical calculations based on

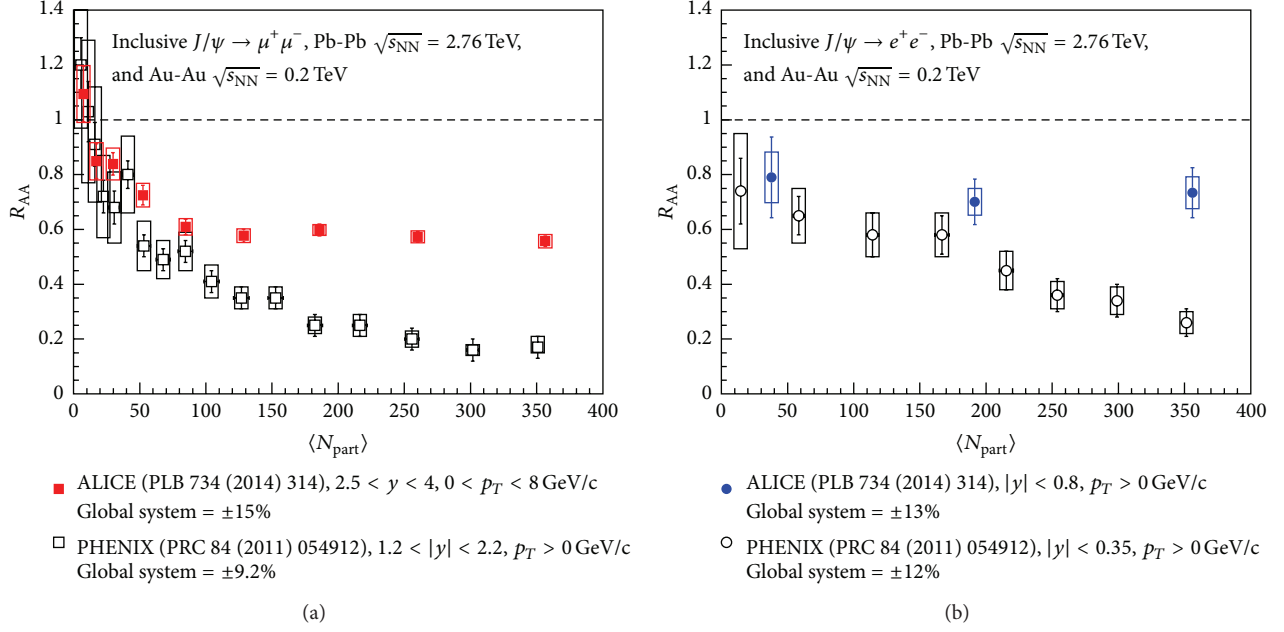


FIGURE 3: Comparison of R_{AA} results, obtained by PHENIX and ALICE experiments. The two panels show the data at forward rapidity (a) and midrapidity (b).

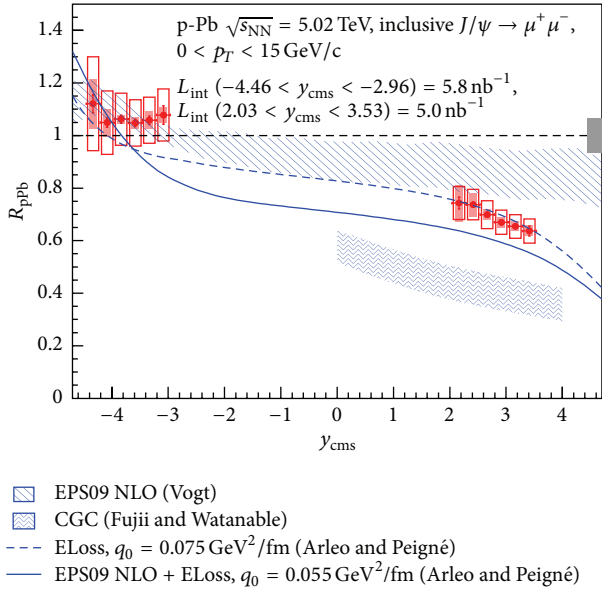


FIGURE 4: Comparison of ALICE R_{pPb} results for inclusive J/ψ with theoretical predictions.

nuclear shadowing [54] as well as on the models including, in addition, a contribution from partonic energy loss [55, 56] are in better agreement with the experimental results (Figure 4).

The ALICE results are in agreement with results for inclusive J/ψ mesons presented by LHCb collaboration [57]. Nuclear modification factors are determined separately for prompt J/ψ mesons and for J/ψ from B-hadron decays by

LHCb experiment. The suppression of prompt J/ψ mesons in p-Pb collisions with respect to p-p collisions at large rapidity is observed, while the production from B-hadron decays is less suppressed.

The $\psi(2S)$ production was measured in p-Pb collisions by ALICE [45]. The nuclear modification factor for inclusive $\psi(2S)$ is evaluated. A significantly larger suppression of the $\psi(2S)$ compared to the inclusive J/ψ was obtained. Theoretical models predictions, which include parton shadowing and coherent energy loss mechanism, reproduce J/ψ suppression but could not describe $\psi(2S)$ data [56]. The models underestimate the $\psi(2S)$ suppression. A comparison with theoretical predictions is shown in Figure 5. Additional effects should be considered for interpretation of the results.

4.2. Bottomonium Production at the LHC. In p-p collisions at $\sqrt{s_{NN}} = 7$ TeV, the inclusive production cross sections of $\Upsilon(1S)$ and $\Upsilon(2S)$ have been measured as a function of p_T and rapidity by ALICE [42]. There is a good agreement of ALICE data with measurements from LHCb experiment [31, 58] in the similar p_T and rapidity ranges. The data are complemented to CMS measurements at midrapidity [47, 59]. The results could be described by NLO NRQCD calculations.

The CMS Collaboration at the LHC has observed the sequential suppression of $\Upsilon(1S)$, $\Upsilon(2S)$, and $\Upsilon(3S)$ bottomonium states in Pb-Pb collisions at $\sqrt{s_{NN}} = 2.76$ TeV [48, 49]. The $\Upsilon(1S)$ yield is suppressed by approximately a factor of two with respect to the expectation from p-p collisions obtained by scaling with the number of binary nucleon-nucleon collisions. The $\Upsilon(2S)$ and the $\Upsilon(3S)$ are strongly suppressed. Due to the lower production cross section of

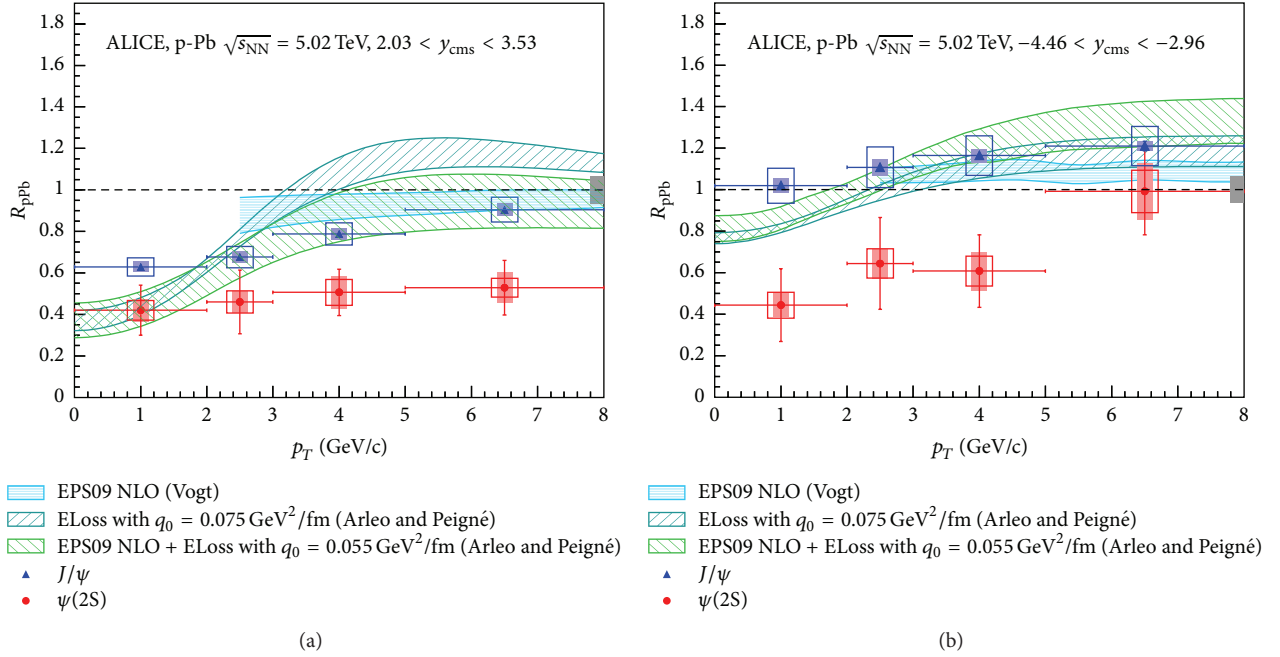


FIGURE 5: Comparison of ALICE R_{pPb} results for J/ψ and $\psi(2S)$ at forward (a) and backward (b) rapidity with theoretical predictions.

$b\bar{b}$ pairs compared to $c\bar{c}$ pairs, the regeneration of $Y(1S)$ is expected to be smaller than that of J/ψ [60]. On the other hand, the CNM effects can also modify the production of bottomonia in nucleus-nucleus collisions.

The inclusive $Y(1S)$ production in Pb-Pb collisions was measured by ALICE at forward rapidity in muon channel down to zero transverse momentum [61]. A strong suppression was observed with respect to p-p collisions scaled by the number of nucleon-nucleon collisions. The ALICE results are compared with CMS data ($|y| < 2.4$) [48]. The observed suppression is stronger at forward rapidity than at midrapidity. The transport model [60] predicts a nearly constant R_{AA} as a function of rapidity and could not reproduce ALICE and CMS data. The transport model includes both suppression and regeneration effects. CNM effects were estimated by using the effective absorption cross section. The transport model clearly underestimates the observed suppression, but the shape of the centrality dependence is quite well reproduced. Another transport model [62] also includes suppression and small regeneration component and CNM effect with shadowing. The model reproduces the CMS data but underestimates the ALICE data at forward rapidity. Both transport models [60, 62] predict stronger suppression for central events in agreement with centrality dependence of ALICE data. The comparison of the data with transport model calculations [60] is shown in Figure 6.

The inclusive $Y(1S)$ and $Y(2S)$ productions were measured also by ALICE [46] and LHCb [57] in p-Pb collisions at $\sqrt{s_{NN}} = 5.02$ TeV. At forward rapidity suppression of the inclusive $Y(1S)$ yield in p-Pb collisions with respect to the yield from p-p collisions scaled by the number of binary

nucleon-nucleon collisions is observed. But at backward rapidity the suppression is less (Figure 7).

The results are compared with several theoretical model calculations [54, 55] including partonic energy loss effects with and without nuclear shadowing. Only models with energy loss plus shadowing could describe the data at forward rapidity but these models underestimate the suppression at backward rapidity.

The production of charmonia and bottomonia is the object of intense theoretical and experimental investigations. Their production mechanism in p-p collisions is described by models based on Quantum Chromodynamics (QCD) and gives reference for comparison with p-A and A-A data. At the LHC in Pb-Pb collisions, the evidence for additional J/ψ production from regeneration at low p_T and strong J/ψ suppression at large transverse momentum was obtained. For p-Pb collisions theoretical models including nuclear suppression, parton shadowing, and coherent energy loss effects could reproduce J/ψ production but fail to describe additional suppression of $\psi(2S)$ and underestimate the observed $Y(1S)$ suppression at forward rapidity.

At the LHC and RHIC the collective and hot nuclear matter effects may also be present in p-Pb at 5.02 TeV and in d-Au collisions at 200 GeV [35]. Therefore, the measurement of nuclear effects at lower energies and assuming the absence of the QGP formation in p-p and p-A collisions could give a reference for the study of hot nuclear matter effects. Moreover, the contribution of recombination process is small at low energies. The RHIC heavy flavor program with the energy scan can perform this investigation but, unfortunately, the luminosity at RHIC strongly decreases with decreasing the energy of collision.

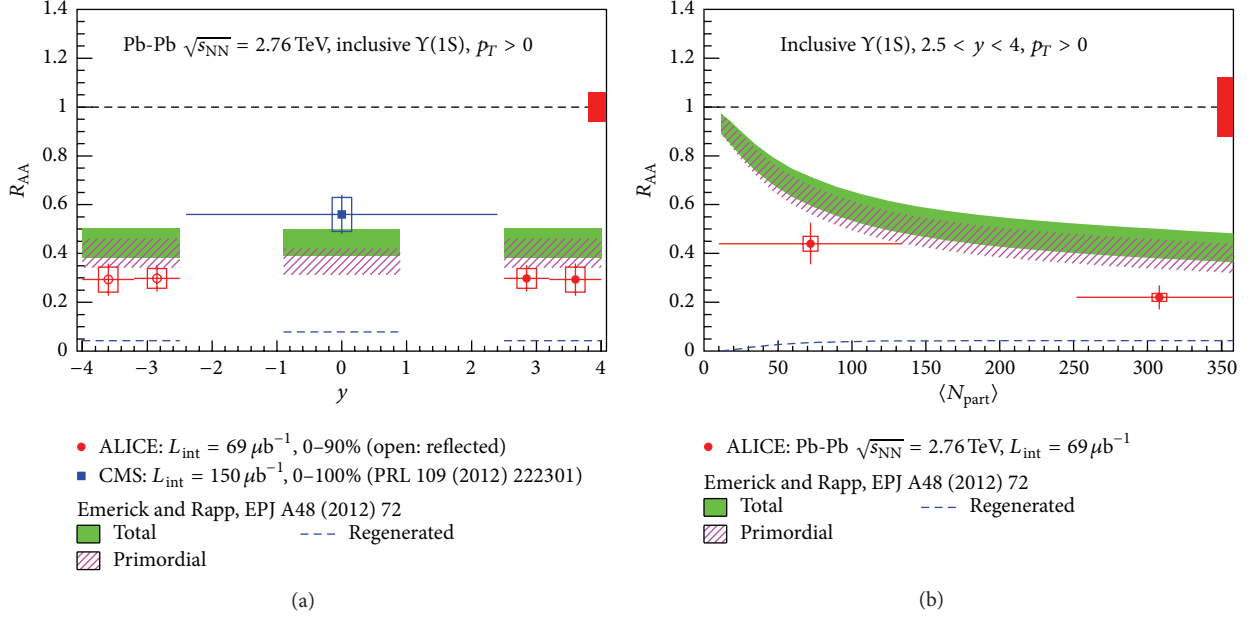


FIGURE 6: Comparison with theoretical predictions ALICE and CMS R_{pPb} results for $Y(1S)$ versus rapidity (a) and ALICE results versus N_{part} (b).

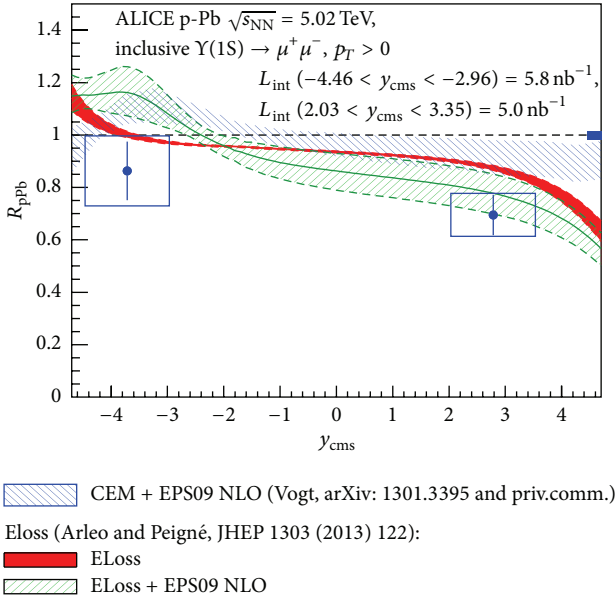


FIGURE 7: Comparison of ALICE R_{pPb} results for $Y(1S)$ versus rapidity with theoretical predictions.

5. Quarkonium Production at Fixed Target at the LHC Beams

The energy intervals between the SPS, the RHIC, and the LHC are very important to study the mechanism of quarkonium production and suppression and for the investigation of the medium effects and conditions of the Quark-Gluon Plasma formation. Investigation of the cold nuclear matter effect and understanding the properties of matter require systematic

and high statistics measurements of quarkonium production also in the low energy region. To clarify the CNM effects it will be possible to study the mechanism of quarkonium production and suppression with high statistics at low energies up to 35 GeV/per nucleon in the CBM experiment at FAIR [63] and in the MPD experiment at NICA collider in Dubna [64]. At the CERN SPS, the fixed target experiment CHIC (Charm in Heavy Ion Collisions) for charmonium study at energy up to $\sqrt{s_{NN}} \sim 20$ GeV is under preparation [65]. The Beam Energy Scan (BES-I) program at RHIC was performed by STAR and PHENIX collaborations. At STAR there is an ongoing fixed target program, with data already taken in the gold target test during 14.5 GeV Au-Au run in 2014 with $\sqrt{s_{NN}} = 3.9$ GeV [66].

If the LHC proton and ion beams would be used with fixed targets, the energy below the nominal RHIC energy (200 GeV) in p-A and A-A collisions could be investigated. For 7 TeV proton beam, the energy in N-N c.m. is $\sqrt{s_{NN}} = 114.6$ GeV, and for Pb beam at 2.75 TeV it is $\sqrt{s_{NN}} = 71.8$ GeV. By using the LHC beams with reduced energy, the data could be taken in the range 30–100 GeV. QCD phase diagram may have interesting features probed by 10–100 GeV beams on fixed target. Search for signature of the phase transition and location of the critical point is the main goal of energy scan. Moreover, this is a possibility of investigating the mechanism of charmonium, J/ψ , and $\psi(2S)$ productions. It will be possible to separate the mechanism of hard production and then suppression by hadronic dissociation in QGP from secondary production with recombination, since the probability of recombination could decrease with decreasing energy of collision like in thermal model [67].

The existing system to inject the gas target for the luminosity measurement (SMOG) at LHCb experiment could be used for fixed target physics [68]. There are some testing measurements of p-Ne and Pb-Ne collisions, but, for

the moment, there are no precise measurements of the gas density and pressure.

The main parameter for quarkonium production measurement in the fixed target experiment is the acceptance. In order to study the feasibility of using the fixed target at the LHC for charmonium production, the geometrical acceptances for J/ψ production on fixed target by means of AliRoot-FAST simulations were obtained. The detailed description of the calculation was given in [69]. For the model of quarkonium production the phenomenological Color Octet Model (COM) was used [70, 71]. For prompt J/ψ production the rapidity and transverse momentum distributions are obtained, respectively, as a parameterization of the COM predictions and by extrapolating to LHC energies the J/ψ transverse momentum (p_T) distribution, measured at midrapidity by the CDF experiment at energy $\sqrt{s_{NN}} = 1.8$ TeV. The geometrical acceptances of the J/ψ production for PHENIX at RHIC and fixed target experiments NA50 at SPS and HERA-B were also calculated for comparison [69].

5.1. Geometrical Acceptances for Fixed Target Pb-Pb Collisions at the Energy $T = 2.75$ TeV per Nucleon, $\sqrt{s_{NN}} = 71.8$ GeV. The geometrical acceptance for the J/ψ production at ALICE dimuon spectrometer was calculated by the beam axis at the interaction point $z = 0$, at the points $z = +50$ cm (in the direction to the dimuon spectrometer) and $z = -50$ cm (outside the ITS) and at point $z = +350$ cm. The transverse momentum distribution for J/ψ was generated using p_T spectra in the CDF form, the same as for HERA and PHENIX, consistent with COM:

$$\frac{dN}{dp_T} \sim p_T \left[1 + \left(\frac{35\pi p_T}{256 \langle p_T \rangle} \right)^2 \right]^{-6}. \quad (2)$$

For rapidity distribution the Gaussian spectra were used. The parameters of distribution were energy scaled. For Pb-Pb collisions p_T spectra with the value $\langle p_T \rangle = 1.4$ and Gaussian rapidity distribution with mean values $y_{cm} = 0$ and $\sigma = 1.1$ were used. The acceptances at $z = +50$ cm and $z = -50$ cm are approximately the same, but at point $z = +350$ cm the geometrical acceptance is much less. The results were shown in [69].

In Figure 8, the Pb-Pb results for $z = 0$ and $z = +50$ cm are plotted. The J/ψ are accepted in the rapidity range $-2.5 < \eta < -4.0$ ($-2.97 < \eta < -4.09$) for J/ψ production at the point $z = 0$ ($z = +50$ cm). The geometrical acceptances, I , are equal to $(12.0 \pm 0.2)\%$ for J/ψ production at $z = 0$ point and $(8.0 \pm 0.2)\%$ at $z = +50$ cm.

5.2. Geometrical Acceptances for Fixed Target p-p and p-A Collisions at the Energy $T = 7$ TeV, Corresponding to $\sqrt{s_{NN}} = 114.6$ GeV. The J/ψ productions in p-p and p-Pb collisions are generated using p_T spectra in the same form as for Pb-Pb collision, but with the energy scaled parameter:

$$\frac{dN}{dp_T} \sim p_T \left[1 + \left(\frac{35\pi p_T}{256 \langle p_T \rangle} \right)^2 \right]^{-6}, \quad (3)$$

where $\langle p_T \rangle = 1.6$. For rapidity distribution the Gaussian spectra were used with mean value being equal to $y_{cm} = 0$ and $\sigma = 1.25$. Geometrical acceptances for J/ψ production were calculated at points $z = 0$, $z = +50$ cm, and $z = -50$ cm (outside the ITS) and at point $z = +350$ cm. The results were shown in [69]. The acceptances at $z = +50$ cm and $z = -50$ cm are roughly the same, but at point $z = +350$ cm the geometrical acceptance is much less. In Figure 9, the results for $z = 0$ and $z = +50$ cm are plotted.

The geometrical acceptances, I , are equal to $(8.5 \pm 0.2)\%$ for J/ψ production at $z = 0$ point and $(6.0 \pm 0.3)\%$ at $z = +50$ cm. We have calculated also the geometrical acceptances for J/ψ with the cut on transverse momentum of the single muon $p_T > 1$ GeV/c. The calculated geometrical acceptances for fixed target measurements are of the same order and even larger than geometrical acceptances for colliding nuclei in ALICE [69].

5.3. Luminosity, Cross Sections, and Counting Rates for p-p, p-A, and Pb-Pb Collisions. The target in the form of thin ribbon could be placed around the main orbit of the LHC, as it was already used for the experiment on collider with a fixed target at HERA-B [72]. The life time of the beam is determined by the beam-beam and beam-gas interactions. Therefore, after some time the particles will leave the main orbit and interact with the target ribbon. So for fixed target measurements only halo of the beam will be used. Therefore, no deterioration of the main beam will be introduced. The experiments at other interaction points will not feel any presence of the fixed target. Since the target ribbon should not interfere during the beam formation and acceleration process it should be lifted in the working position after the tuning of the beam.

In the ALICE measurements in 2011 in p-p run it was $1.2 \cdot 10^{11}$ protons per bunch, 1380 bunches and life time of 14.5 hours. From these parameters one can estimate the particle loss of $1.1 \cdot 10^{13}$ protons during one hour ($3.1 \cdot 10^9$ protons/s) and mean luminosity about $3 \cdot 10^{30} \text{ cm}^{-2} \text{ s}^{-1}$ for 500-micron lead ribbon. For Pb beam it was $1 \cdot 10^8$ ions per bunch, 358 bunches and life time of 6.5 hours. The particle loss is about $5.1 \cdot 10^9$ ions during one hour ($1.4 \cdot 10^6$ ions/s). The mean luminosity is about $1.7 \cdot 10^{27} \text{ cm}^{-2} \text{ s}^{-1}$ for 500-micron lead ribbon. The luminosity estimates are shown in Table 1. The value of the nucleon-nucleon charmonium total production cross section shown in Table 1 for 14 TeV was calculated by CEM (Color Evaporation Model) [73] with MRST HO PDF. The cross sections for lower energies were obtained by interpolation of proton-proton cross sections measured at RHIC at $\sqrt{s_{NN}} = 200$ GeV and at SPS in the NA51 experiment at 450 GeV per nucleon ($\sqrt{s_{NN}} = 29.1$ GeV), and were extracted from the data of the NA50 experiment at $\sqrt{s_{NN}} = 27.4$ GeV for proton-lead collisions.

The high statistics results could be obtained by fixed target experiments on J/ψ production in p-Pb and Pb-Pb collisions with the counting rate values presented in Table 1. For Pb-Pb collisions, luminosity is smaller but the production cross section is larger. The measurement of $\psi(2S)$ production is also feasible with better statistical accuracy than at RHIC collider.

The fixed target experiment AFTER using the LHC beams extracted by a bent crystal was proposed [74]. The experiment

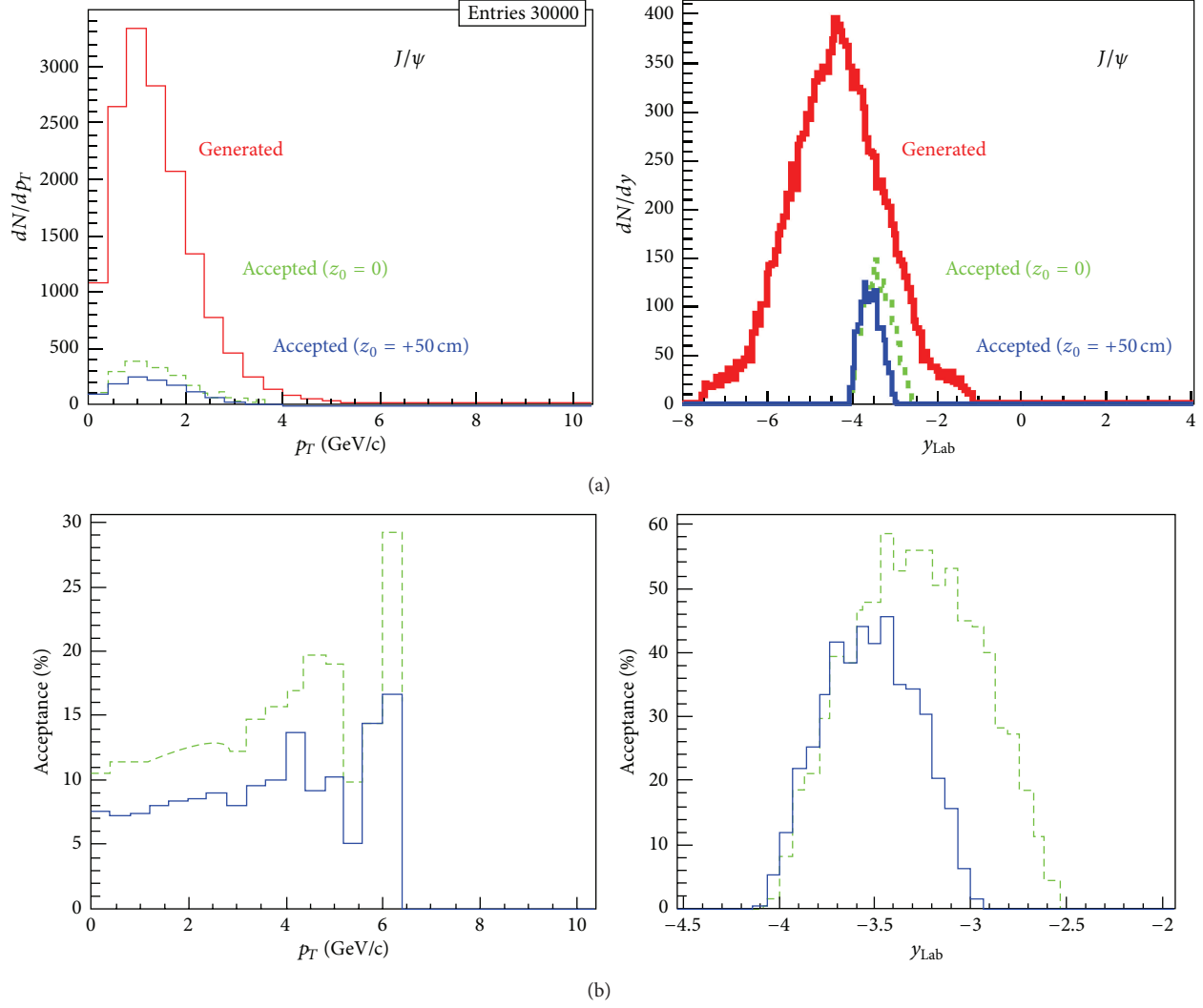


FIGURE 8: Transverse momentum and rapidity distributions for J/ψ events, produced at $z = +50$ cm (solid lines) and $z = 0$ (dashed lines) in fixed target Pb-Pb collisions at $\sqrt{s} = 71.8$ GeV per nucleon pair (a) and corresponding acceptances (b).

TABLE 1: Luminosity, cross sections ($x_F > 0$), and counting rates.

System	\sqrt{s} , TeV	σ_{NN} , μb	σ_{pA} , μb ($A^{0.92} \sigma_{NN}$)	I , %	IB σ_{pA} , μb	L , $cm^{-2}s^{-1}$	Rate, h^{-1}
pp	14	54.1	54.1	4.7	0.150	$3 \cdot 10^{30}$	1620
pp _{RHIC}	0.200	2.7	2.7	3.6	0.0057	$1 \cdot 10^{31}$	205
pPb _{NA50}	0.0274	0.19	25.7	14.0	0.212	$7 \cdot 10^{29}$	535
pPb _{fixed}	0.1146	0.65	80.2	6.0	0.310	$3 \cdot 10^{30*}$	3360
pPb _{fixed}	0.0718	0.55	74.6	8.0	0.349	$3 \cdot 10^{30*}$	3780
PbPb _{fixed}	0.0718	0.55	11970	8.0	42.9	$1.7 \cdot 10^{27**}$	292

* pPb_{fixed}, 500 μ wire, $3.1 \cdot 10^9$ protons/s.

** PbPb_{fixed}, 500 μ wire, $1.4 \cdot 10^6$ ions/s.

AFTER has a wide physical program and gives possibility of using different targets with high thickness, so it gets higher luminosity (20 times more for 1 cm target versus 500 μm). But the experiment AFTER demands a lot of space for installation and has high cost.

Fixed target experiment with the target in the form of thin ribbon may be placed at the existing experimental installation (e.g., LHCb). The target could be lifted in the working position with the aid of rotation system only after beam tuning. This experiment will use only halo of the beam

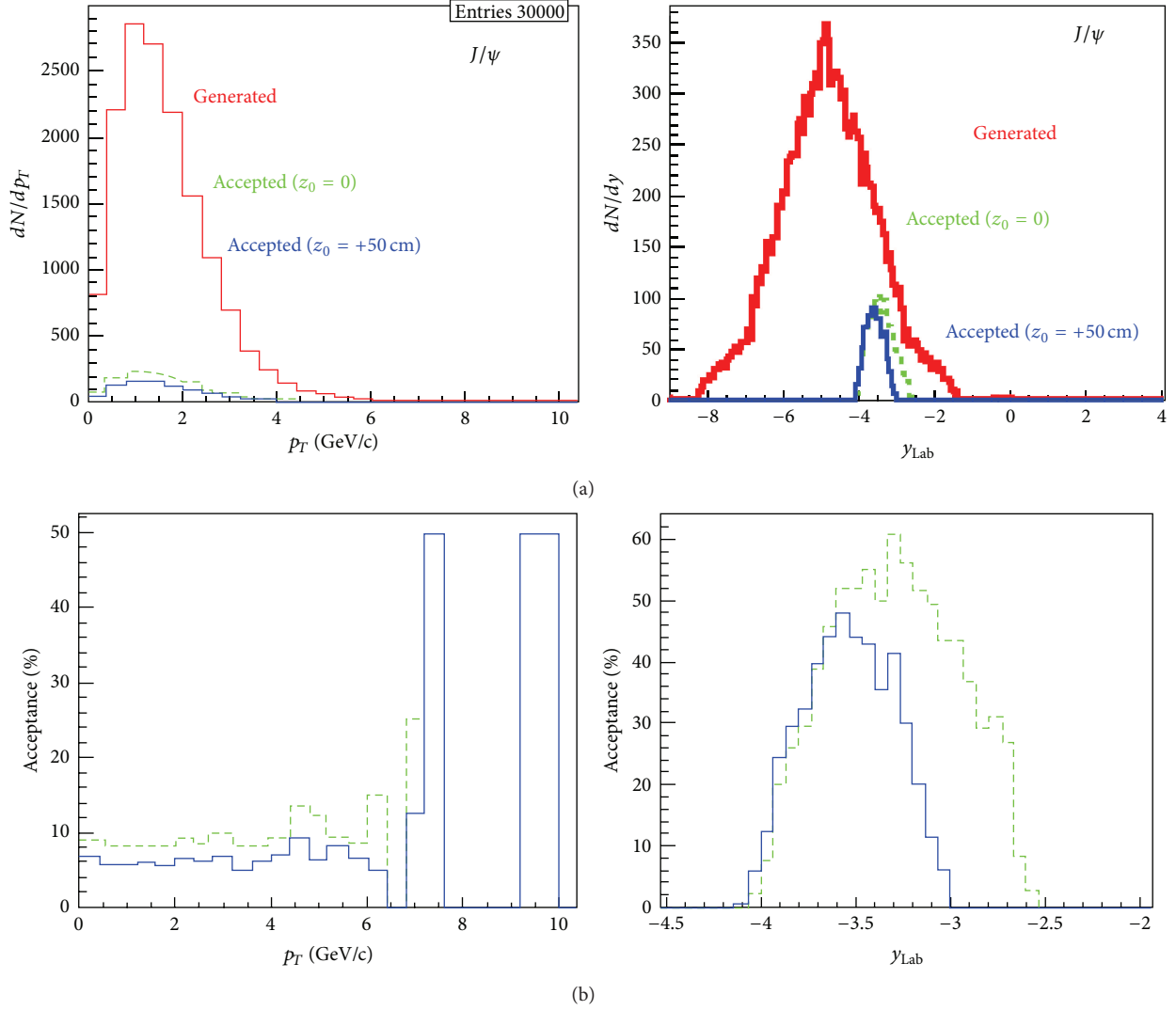


FIGURE 9: Transverse momentum and rapidity distributions for J/ψ events, produced at $z = +50$ cm (solid line) and at $z = 0$ (dashed line) in fixed target p-A collisions at $\sqrt{s_{NN}} = 114.6$ GeV per nucleon pair (a) and corresponding acceptances (b).

(the target could be used as extra collimator). This fixed target experiment with the target in the form of thin ribbon looks like a first stage of more complicated experiment AFTER.

6. Conclusion

The fixed target experiment at LHC will give possibility for precise quarkonium studies at energies below nominal RHIC energy (200 GeV). It has advantage of high luminosity compared to collider experiments. The use of fixed target at LHC could provide in a short time the data for different targets and maybe for different projectile nuclei with high statistics. By using the LHC beams the data could be taken in the range $\sqrt{s_{NN}} = 29$ –115 GeV. Search for signature of the phase transition and location of the critical point is the main goal of energy scan. Moreover, this is a possibility of investigating the mechanism of charmonium, J/ψ , and $\psi(2S)$

productions to separate the possibilities of hard production and then suppression by hadronic dissociation in QGP or secondary production with recombination. Additional J/ψ mesons are expected to be produced from deconfined charm quarks by kinetic recombination in the QGP or by statistical hadronization at the phase boundary. The probability of recombination decreases with decreasing energy of collision. Therefore, the important information about mechanism of charmonium production and possible QGP formation could be obtained. The experiment with the fixed target in the form of thin ribbon looks like a first stage of more complicated experiment AFTER on the LHC beams.

Conflict of Interests

The authors declare that there is no conflict of interests regarding the publication of this paper.

References

- [1] T. Matsui and H. Satz, “ J/ψ suppression by quark-gluon plasma formation,” *Physics Letters B*, vol. 178, no. 4, pp. 416–422, 1986.
- [2] M. C. Abreu, J. Astruc, C. Baglin et al., “ J/ψ and ψ' production in p, O and S induced reactions at SPS energies,” *Physics Letters B*, vol. 466, no. 2–4, pp. 408–414, 1999.
- [3] M. C. Abreu, B. Alessandro, C. Alexa et al., “Anomalous J/ψ suppression in Pb-Pb interactions at 158 GeV/c per nucleon,” *Physics Letters B*, vol. 410, no. 2–4, pp. 337–343, 1997.
- [4] B. Alessandro, C. Alexa, R. Arnaldi et al., “A new measurement of J/ψ suppression in Pb-Pb collisions at 158 GeV per nucleon,” *The European Physical Journal C*, vol. 39, pp. 335–345, 2005.
- [5] B. Alessandro, C. Alexa, R. Arnaldi et al., “Charmonia and Drell-Yan production in proton-nucleus collisions at the CERN SPS,” *Physics Letters B*, vol. 553, pp. 167–178, 2003.
- [6] B. Alessandro, C. Alexa, R. Arnaldi et al., “ J/ψ and ψ' production and their normal nuclear absorption in proton-nucleus collisions at 400 GeV,” *The European Physical Journal C*, vol. 48, no. 2, pp. 329–341, 2006.
- [7] B. Alessandro, C. Alexa, R. Arnaldi et al., “ ψ' production in Pb-Pb collisions at 158 GeV/nucleon,” *The European Physical Journal C*, vol. 49, no. 2, pp. 559–567, 2007.
- [8] R. Arnaldi and The NA60 Collaboration, “ J/ψ production in p-A and A-A collisions at fixed target experiments,” *Nuclear Physics A*, vol. 830, no. 1–4, pp. 345c–352c, 2009.
- [9] B. Alessandro, C. Alexa, R. Arnaldi et al., “ J/ψ production in proton-nucleus collisions at 158 and 400 GeV,” *Physics Letters B*, vol. 706, no. 4–5, pp. 263–267, 2012.
- [10] I. Abt, M. Adams, M. Agari et al., “Kinematic distributions and nuclear effects of J/ψ production in 920 GeV fixed-target proton-nucleus collisions,” *The European Physical Journal C*, vol. 60, no. 4, pp. 525–542, 2009.
- [11] M. J. Leitch, W. M. Lee, M. E. Beddo et al., “Measurement of differences between J/ψ and ψ' suppression in p-A collisions,” *Physical Review Letters*, vol. 84, no. 15, pp. 3256–3260, 2000.
- [12] A. Adare, S. Afanasiev, C. Aidala et al., “ J/ψ Production versus centrality, transverse momentum, and rapidity in Au + Au collisions at $\sqrt{s_{NN}} = 200$ GeV,” *Physical Review Letters*, vol. 98, Article ID 232301, 2007.
- [13] A. Adare, S. Afanasiev, C. Aidala et al., “ J/ψ suppression at forward rapidity in Au + Au collisions at $\sqrt{s_{NN}} = 200$ GeV,” *Physical Review C*, vol. 84, Article ID 054912, 2011.
- [14] A. Adare, S. Afanasiev, C. Aidala et al., “Ground and excited state charmonium production in p + p collisions at $\sqrt{s} = 200$ GeV,” *Physical Review D*, vol. 85, no. 9, Article ID 092004, 27 pages, 2012.
- [15] A. Adare, S. Afanasiev, C. Aidala et al., “ J/ψ production in $\sqrt{s_{NN}} = 200$ GeV Cu + Cu collisions,” *Physical Review Letters*, vol. 101, Article ID 122301, 2008.
- [16] A. Adare, S. Afanasiev, C. Aidala et al., “Cold nuclear matter effects on J/ψ yields as a function of rapidity and nuclear geometry in d+A collisions at $\sqrt{s_{NN}} = 200$ GeV,” *Physical Review Letters*, vol. 107, Article ID 142301, 2011.
- [17] L. Adamczyk, J. K. Adkins, G. Agakishiev et al., “ J/ψ production at low p_T in Au+Au and Cu+Cu collisions at $\sqrt{s_{NN}} = 200$ GeV with the STAR detector,” *Physical Review C*, vol. 90, no. 2, Article ID 24906, 13 pages, 2014.
- [18] J. Adams, C. Adler, M. M. Aggarwal et al., “ J/ψ production at high transverse momenta in p+p and Au + Au collisions at $\sqrt{s_{NN}} = 200$ GeV,” *Physics Letters B*, vol. 722, pp. 55–62, 2013.
- [19] B. I. Abelev, M. Aggarwal, Z. Ahammed, and et al., “ J/ψ production at high transverse momenta in p + p and Cu + Cu collisions at $\sqrt{s_{NN}} = 200$ GeV,” *Physical Review C*, vol. 80, Article ID 041902(R), 2009.
- [20] H. Brambilla, S. Eidelman, B. K. Heltsley et al., “Heavy quarkonium: progress, puzzles, and opportunities,” *The European Physical Journal C*, vol. 71, article 1534, 2011.
- [21] R. L. Thews, “Quarkonium formation in statistical and kinetic models,” *The European Physical Journal C*, vol. 43, no. 1–4, pp. 97–102, 2005.
- [22] R. L. Thews and M. L. Mangano, “Momentum spectra of charmonium produced in a quark-gluon plasma,” *Physical Review C*, vol. 73, no. 1, Article ID 014904, 2006.
- [23] A. Andronic, P. Braun-Munzinger, K. Redlich, and J. Stachel, “Charmonium and open charm production in nuclear collisions at SPS/FAIR energies and the possible influence of a hot hadronic medium,” *Physics Letters B*, vol. 659, no. 1–2, pp. 149–155, 2008.
- [24] P. Braun-Munzinger and J. Stachel, “(Non)thermal aspects of charmonium production and a new look at J/ψ suppression,” *Physics Letters B*, vol. 490, no. 3–4, pp. 196–202, 2000.
- [25] K. Aamodt, A. Abrahantes Quintana, D. Adamová et al., “Erratum to ‘Rapidity and transverse momentum dependence of inclusive J/ψ production in pp collisions at $\sqrt{s} = 7$ TeV,’” *Physics Letters B*, vol. 704, no. 5, p. 442, 2011, *Physics Letters B*, vol. 718, no. 2, pp. 692–698, 2012.
- [26] B. Abelev, J. Adam, D. Adamova et al., “Centrality, rapidity and transverse momentum dependence of J/ψ suppression in Pb-Pb collisions at $\sqrt{s_{NN}} = 2.76$,” *Physics Letters B*, vol. 734, pp. 314–327, 2014.
- [27] S. Chatrchyan, V. Khachatryan, A. M. Sirunyan et al., “ J/ψ and ψ (2S) production in pp collisions at $\sqrt{s} = 7$ TeV,” *Journal of High Energy Physics*, vol. 2012, article 11, 2012.
- [28] S. Chatrchyan, V. Khachatryan, A. M. Sirunyan et al., “Suppression of non-prompt J/ψ , prompt J/ψ , and Υ (1S) in PbPb collisions at $\sqrt{s_{NN}} = 2.76$ TeV,” *Journal of High Energy Physics*, vol. 2012, no. 5, article 63, 2012.
- [29] G. Aad, B. Abbott, J. Abdallah et al., “Measurement of the differential cross-sections of inclusive, prompt and non-prompt J/ψ production in proton-proton collisions at $\sqrt{s} = 7$ TeV,” *Nuclear Physics B*, vol. 850, no. 3, pp. 387–444, 2011.
- [30] G. Aad, B. Abbott, J. Abdallah et al., “Measurement of the centrality dependence of J/ψ yields and observation of Z production in lead-lead collisions with the ATLAS detector at the LHC,” *Physics Letters B*, vol. 697, no. 4, pp. 294–312, 2011.
- [31] R. Aaij, B. Adeva, M. Adinolfi et al., “Measurement of J/ψ production in pp collisions at $\sqrt{s} = 7$ TeV,” *The European Physical Journal C*, vol. 71, article 1645, 2011.
- [32] R. Aaij, C. A. Beteta, A. Adametz et al., “Measurement of J/ψ production in pp collisions at $\sqrt{s} = 2.76$ TeV,” *Journal of High Energy Physics*, vol. 2013, no. 02, article 041, 2013.
- [33] B. Abelev, J. Adam, D. Adamova et al., “Measurement of prompt J/ψ and beauty hadron production cross sections at mid-rapidity in pp collisions at $\sqrt{s} = 7$ TeV,” *Journal of High Energy Physics*, vol. 2012, no. 11, article 065, 2012.
- [34] J. Badier, J. Boucrot, J. Bourotte et al., “Experimental J/ψ hadronic production from 150 to 280 GeV/c,” *Zeitschrift für Physik C*, vol. 20, no. 2, pp. 101–106, 1983.
- [35] A. D. Frawley, “PHENIX charmonia: what have we learned from d+Au collisions?” *Nuclear Physics A*, vol. 932, pp. 105–110, 2014.

- [36] X. Zhao and R. Rapp, “Charmonium in medium: from correlators to experiment,” *Physical Review C*, vol. 82, Article ID 064905, 2010.
- [37] Y. Liu, Z. Qu, N. Xu, and P. Zhuang, “ J/ψ transverse momentum distribution in high energy nuclear collisions,” *Physics Letters B*, vol. 678, no. 1, pp. 72–76, 2009.
- [38] A. Adare, C. Aidala, N. N. Ajitanand et al., “Nuclear matter effects on J/ψ production in asymmetric Cu + Au collisions at $\sqrt{s_{NN}} = 200$ GeV,” *Physical Review C*, vol. 90, Article ID 064908, 2014.
- [39] A. Iordnava, “Nuclear matter effects on J/ψ production in Cu+Au and U+U collisions in PHENIX,” in *Proceedings of the International Workshop on Deep-Inelastic Scattering and Related Subjects (DIS '14)*, p. 191, 2014.
- [40] W. Zha, “Recent measurements of quarkonium production in p + p and A + A collisions from the STAR experiment,” *Nuclear Physics A*, vol. 931, pp. 596–600, 2014.
- [41] A. Adare, C. Aidala, N. N. Ajitanand et al., “ J/ψ suppression at forward rapidity in Au+Au collisions at $\sqrt{s_{NN}} = 39$ and 62.4 GeV,” *Physical Review C*, vol. 86, no. 6, Article ID 064901, 10 pages, 2012.
- [42] B. Abelev, J. Adam, D. Adamová et al., “Measurement of quarkonium production at forward rapidity in pp collisions at $\sqrt{s} = 7$ TeV,” *The European Physical Journal C*, vol. 74, article 2974, 2014.
- [43] B. Abelev, J. Adam, D. Adamová et al., “ J/ψ suppression at forward rapidity in Pb-Pb collisions at $\sqrt{s_{NN}} = 2.76$ TeV,” *Physical Review Letters*, vol. 109, Article ID 072301, 2012.
- [44] B. Abelev, J. Adam, D. Adamová et al., “ J/ψ production and nuclear effects in p-Pb collisions at $\sqrt{s_{NN}} = 5.2$ TeV,” *Journal of High Energy Physics*, vol. 2014, no. 2, article 73, 2014.
- [45] B. Abelev, J. Adam, D. Adamová et al., “ J/ψ Production and nuclear effects in p-Pb collisions at $\sqrt{s_{NN}} = 5.02$ TeV,” *Journal of High Energy Physics*, vol. 2014, no. 12, article 73, 2014.
- [46] B. Abelev and ALICE Collaboration, “Production of inclusive $\Upsilon(1S)$ and $\Upsilon(2S)$ in p-Pb collisions at $\sqrt{s_{NN}} = 5.02$ TeV,” *Physics Letters B*, vol. 740, pp. 105–117, 2015.
- [47] CMS Collaboration, “Measurement of the $\Upsilon(1S)$, $\Upsilon(2S)$, and $\Upsilon(3S)$ cross sections in pp collisions at $\sqrt{s} = 7$ TeV,” *Physics Letters B*, vol. 727, no. 1–3, pp. 101–125, 2013.
- [48] S. Chatrchyan, V. Khachatryan, A. M. Sirunyan et al., “Observation of sequential Υ suppression in PbPb collisions,” *Physical Review Letters*, vol. 109, no. 22, Article ID 222301, 15 pages, 2012.
- [49] S. Chatrchyan, V. Khachatryan, A. M. Sirunyan et al., “Indications of suppression of excited Υ states in Pb-Pb collisions at $\sqrt{s_{NN}} = 2.76$ TeV,” *Physical Review Letters*, vol. 107, Article ID 052302, 2011.
- [50] R. Aaij, B. Adeva, M. Adinolfi et al., “Study of J/ψ production and cold nuclear matter effects in p Pb collisions at $\sqrt{s_{NN}} = 5$ TeV,” *Journal of High Energy Physics*, vol. 2014, no. 2, article 72, 2014.
- [51] R. Aaij, B. Adeva, M. Adinolfi et al., “Study of Υ production and cold nuclear matter effects in pPb collisions at $\sqrt{s_{NN}} = 5$ TeV,” *Journal of High Energy Physics*, vol. 2014, no. 7, article 094, 2014.
- [52] B. Abelev, J. Adam, D. Adamová et al., “ J/ψ production as a function of charged particle multiplicity in pp collisions at $\sqrt{s} = 7$ TeV,” *Physics Letters B*, vol. 712, no. 3, pp. 165–175, 2012.
- [53] H. Fujii and K. Watanabe, “Heavy quark pair production in high-energy pA collisions: quarkonium,” *Nuclear Physics A*, vol. 915, pp. 1–23, 2013.
- [54] J. L. Abbacete, N. Armesto, R. Baier et al., “Predictions for p+Pb collisions at $\sqrt{s_{NN}} = 5$ TeV,” *International Journal of Modern Physics E*, vol. 22, Article ID 1330007, 2013.
- [55] F. Arleo and S. Peigné, “Heavy-quarkonium suppression in p-A collisions from parton energy loss in cold QCD matter,” *Journal of High Energy Physics*, vol. 2013, no. 3, article 122, 2013.
- [56] F. Arleo, R. Kolevati, S. Peigne, and M. Rustamova, “Centrality and p_{\perp} dependence of J/ψ suppression in proton-nucleus collisions from parton energy loss,” *Journal of High Energy Physics*, vol. 2013, no. 5, article 155, 2013.
- [57] R. Aaij, B. Adeva, M. Adinolfi et al., “Study of Υ production and cold nuclear matter effects in p Pb collisions at $\sqrt{s_{NN}} = 5$ TeV,” *Journal of High Energy Physics*, vol. 2014, no. 7, article 94, 2014.
- [58] R. Aaij, C. A. Beteta, B. Adeva et al., “Measurement of Υ production in pp collisions at $\sqrt{s} = 7$ TeV,” *The European Physical Journal C*, vol. 72, article 2025, 2012.
- [59] V. Khachatryan, A. M. Sirunyan, A. Tumasyan et al., “Upsilon production cross section in pp collisions at $\sqrt{s} = 7$ TeV,” *Physical Review D*, vol. 83, no. 11, Article ID 112004, 27 pages, 2011.
- [60] A. Emerick, X. Zhao, and R. Rapp, “Bottomonia in the quark-gluon plasma and their production at RHIC and LHC,” *The European Physical Journal A*, vol. 48, article 72, 2012.
- [61] B. Abelev, J. Adam, D. Adamová et al., “Suppression of $\Upsilon(1S)$ at forward rapidity in Pb-Pb collisions at $\sqrt{s_{NN}} = 2.76$ TeV,” *Physics Letters B*, vol. 738, pp. 361–372, 2014.
- [62] A. Zhou, N. Xu, Z. Xu, and P. Zhuang, “Medium effects on charmonium production at ultrarelativistic energies available at the CERN Large Hadron Collider,” *Physical Review C*, vol. 89, Article ID 054911, 2014.
- [63] C. Hohne, “Measurement of dileptons with the CBM experiment at FAIR,” *Nuclear Physics A*, vol. 931, pp. 735–739, 2014.
- [64] A. Sissakian, A. Sorin, I. Meshkov et al., “Design and construction of Nuclotron-based Ion Collider fAcility (NICA),” Conceptual Design Report, JINR, Dubna, Russia, 2008.
- [65] F. Fleuret, F. Arleo, E. G. Ferreira, P.-B. Gossiauxd, and S. Peigné, “Expression of Interest for an experiment to study charm production with proton and heavy ion beams (CHIC: Charm in Heavy Ion Collisions),” CERN-SPSC-2012-031/IPC-EOI-008, 2012.
- [66] B. Haag, O. Hajkova, A. Hamed et al., “A fixed-target program for STAR: extending the low energy reach of the RHIC beam energy scan,” QM2014, Quark Matter Poster, 2014.
- [67] R. Hagedorn, “Multiplicities, p_T distributions and the expected hadron-quark-gluon phase transition,” *La Rivista del Nuovo Cimento*, vol. 6, pp. 1–50, 1983.
- [68] M. Ferro-Luzzi, “Luminosity and luminous region shape for pure Gaussian bunches,” Tech. Rep. CERN-LHCb-PUB-2012-016, 2012.
- [69] A. B. Kurepin, N. S. Topilskaya, and M. B. Golubeva, “Charmonium production in fixed-target experiments with SPS and LHC beams at CERN,” *Physics of Atomic Nuclei*, vol. 74, no. 3, pp. 446–452, 2011.
- [70] M. Kramer, “Quarkonium production at high-energy colliders,” *Progress in Particle and Nuclear Physics*, vol. 47, no. 1, pp. 141–201, 2001.
- [71] E. Braaten, S. Fleming, and A. K. Leibovich, “Nonrelativistic QCD analysis of bottomonium production at the Fermilab Tevatron,” *Physical Review D*, vol. 63, no. 9, Article ID 094006, 2001.

- [72] K. Ehret, “Commissioning of the HERA-B internal target: using the HERA proton ring as a B-factory,” *Nuclear Instruments and Methods in Physics Research A*, vol. 446, no. 1-2, pp. 190–198, 2000.
- [73] V. D. Barger, W. Y. Keung, and R. J. Phillips, “On ψ and Y production via gluons,” *Physics Letters B*, vol. 91, no. 2, pp. 253–258, 1980.
- [74] S. J. Brodsky, F. Fleuret, C. Hadjidakis, and J. P. Lansberg, “Physics opportunities of a fixed-target experiment using LHC beams,” *Physics Reports*, vol. 522, no. 4, pp. 239–255, 2013.

Research Article

Quarkonium Suppression from Coherent Energy Loss in Fixed-Target Experiments Using LHC Beams

François Arleo¹ and Stéphane Peigné²

¹Laboratoire Leprince-Ringuet (LLR), École Polytechnique, CNRS/IN2P3, 91128 Palaiseau, France

²SUBATECH, UMR 6457, Université de Nantes, Ecole des Mines de Nantes, IN2P3/CNRS, 4 rue Alfred Kastler, 44307 Nantes Cedex 3, France

Correspondence should be addressed to François Arleo; francois.arleo@cern.ch

Received 3 May 2015; Accepted 26 July 2015

Academic Editor: Cédric Lorcé

Copyright © 2015 F. Arleo and S. Peigné. This is an open access article distributed under the Creative Commons Attribution License, which permits unrestricted use, distribution, and reproduction in any medium, provided the original work is properly cited. The publication of this article was funded by SCOAP³.

Quarkonium production in proton-nucleus collisions is a powerful tool to disentangle cold nuclear matter effects. A model based on coherent energy loss is able to explain the available quarkonium suppression data in a broad range of rapidities, from fixed-target to collider energies, suggesting coherent energy loss in cold nuclear matter to be the dominant effect in quarkonium suppression in p-A collisions. This could be further tested in a high-energy fixed-target experiment using a proton or nucleus beam. The nuclear modification factors of J/ψ and Υ as a function of rapidity are computed in p-A collisions at $\sqrt{s} = 114.6$ GeV, and in p-Pb and Pb-Pb collisions at $\sqrt{s} = 7.2$ TeV. These center-of-mass energies correspond to the collision on fixed-target nuclei of 7 TeV protons and 2.76 TeV (per nucleon) lead nuclei available at the LHC.

1. Introduction

Understanding the physical origin of quarkonium (J/ψ , Υ) suppression in proton-nucleus (p-A) collisions has been a challenge for the past thirty years. This would of course be a prerequisite in order to perform reliable *baseline* predictions in heavy-ion collisions, where quarkonia are expected to be dissociated due to Debye screening of the heavy-quark potential at finite temperature [1]. Perhaps even more importantly, the wealth of data (especially for J/ψ and Υ) available in p-A collisions could help to understand generic features of hard QCD processes in a nuclear environment.

In everyday language, we often make the distinction between “fixed-target” and “collider” experiments when it comes to quarkonium production. This separation might look a bit artificial but not entirely:

- (i) In fixed-target experiments, luminosities are often high, leading to abundant yields and consequently reduced statistical uncertainties. Moreover, thanks to the boost of the center-of-mass frame of the collision, the rapidity coverage of such experiments can extend

up to larger *negative* values of rapidity (we follow the usual convention where positive (negative) rapidities correspond to the proton (nucleus) fragmentation region) or Feynman- x , $x_F \approx 2M_{\perp}/\sqrt{s} \times \sinh y$, where M_{\perp} is the quarkonium transverse mass. The highest energies ever reached are of course rather modest, $\sqrt{s} = 38.7$ GeV and $\sqrt{s} = 41.6$ GeV, using, respectively, 800 GeV and 920 GeV proton beams at the Tevatron and at HERA. This, however, allows for probing also larger *positive* values of x_F than in collider experiments.

- (ii) At collider energies—RHIC and LHC, to quote only the facilities accelerating heavy ions—unprecedented energies can be reached, respectively, $\sqrt{s} = 200$ GeV and $\sqrt{s} = 5.02$ TeV, for instance, making the production of Υ states, marginally measured in fixed-target experiments, easier. In terms of acceptance, quarkonia are detected in a narrow window in x_F , centered around $x_F = 0$.

Let us illustrate this with a few examples, starting with one of the first experiments which measured J/ψ suppression in

p-A collisions. The NA3 spectrometer at the CERN SPS collected 1.5 million J/ψ events (!) in hadron-nucleus collisions [2], allowing for precise measurements close to the kinematic edge of phase-space, $x_F \lesssim 0.75$ (on the contrary, the coverage at RHIC and LHC is, resp., $|x_F| \lesssim 0.2$ and $|x_F| \lesssim 0.02$ for J/ψ production). It is remarkable that these data, taken in the early 1980s, prove to be as competitive as the most recent LHC results when it comes to understanding J/ψ suppression in nuclei. More than a decade after NA3, the FNAL E866 experiment reported on high-statistics measurements of J/ψ (3×10^6 events) and ψ' (10^5) production on several nuclear targets in the range $-0.2 \lesssim x_F \lesssim 0.9$ [3]. Other important measurements were reported by experiments at the SPS (NA38 [4], NA50 [5], and NA60 [6]) and HERA (HERA-B [7]), yet on a more restricted x_F range.

These data are nicely supplemented by those carried out in d-Au collisions at RHIC (PHENIX [8, 9] and STAR [10]) and in p-Pb collisions at LHC (ALICE [11] and LHCb [12]). At LHC, the relative suppression of Υ excited states (2S, 3S) with respect to 1S states has been performed by CMS [13], not to mention open heavy-flavor data (D mesons in ALICE [14], B mesons in CMS [15], and nonprompt J/ψ coming from B decays in ALICE [16] and LHCb [12]).

Several cold nuclear matter (CNM) effects could in principle affect quarkonium yields in proton-nucleus collisions. Without being comprehensive, let us mention the following ones:

- (i) Quarkonia may interact inelastically with the surrounding nucleons they may encounter while propagating through the nucleus. Such *nuclear absorption* may happen when the quarkonium formation time (in the rest frame of the nucleus) is comparable or less than the medium length L , $\tau_f \times \cosh y_{\text{lab}} \lesssim L$, where τ_f is the *proper* formation time ($\tau_f \approx 0.3$ fm for both J/ψ and Υ) and y_{lab} is the quarkonium rapidity in the nucleus rest frame. Note that y_{lab} is directly related to the momentum fraction x_2 carried by the target parton, $\cosh y_{\text{lab}} = M_\perp / (2m_p x_2)$, where m_p is the proton mass.
- (ii) Parton distribution functions (PDF) are known to be different in a proton and in a nucleus at all values of x . Such nuclear PDF (nPDF) effects could either suppress or enhance quarkonium yields in p-A collisions (with respect to p-p collisions) depending on the value of the momentum fraction x_2 . When x_2 is small (typically when the time for the hard process to occur is large in the nucleus rest frame, $t_h \approx (1/M_\perp) \times \cosh y_{\text{lab}} = 1/(2m_p x_2) \gtrsim L$, using $L = 10$ fm, this would correspond to $x_2 \lesssim 10^{-2}$), the nucleons in the nucleus act coherently leading to a reduction of the quarkonium yield in a nucleus—called *shadowing* [17], or *saturation* [18] to use a more modern language—as compared to the incoherent sum over A independent nucleons.
- (iii) Nuclear transverse momentum broadening of the heavy-quark pair induces coherent gluon radiation, arising from the interference between emission

amplitudes off the initial projectile parton and the final color octet quark pair. This coherent medium-induced radiation leads to an average induced energy loss proportional to the quarkonium energy [19]. The consequences of coherent energy loss are quarkonium suppression (resp., enhancement) at large positive (resp., large negative) values of the rapidity and at all center-of-mass energies of the p-A collision.

Although each of these CNM effects is plausible, it does not necessarily mean that all play a role in the nuclear dependence of quarkonium production; in particular, the strength of each CNM effect is usually unknown *a priori*. A sound strategy is to investigate each of these effects separately, through a systematic and quantitative comparison to all available data, while keeping the smallest number of assumptions and free parameters.

Quarkonium suppression reported at forward rapidities cannot be reproduced by either nuclear absorption or nPDF effects, nor by a mixture of both. Although the comparison to RHIC and LHC data only may still give the impression that strong nPDF effects could explain J/ψ data [11] (for examples of nPDF effects on quarkonium production in p-Pb collisions at LHC, see [20, 21]), the significant suppression measured by the fixed-target experiments (NA3 and E866) on a wider x_F range is clearly incompatible with the predictions of these two effects. An elegant way to be persuaded is to plot J/ψ suppression data as a function of $x_2 = M_\perp / \sqrt{s} \exp(-y)$ [22]. The suppression from either nuclear absorption or nPDF effects is expected to be a function of x_2 only, independent of \sqrt{s} . This is in strong disagreement with the accumulated data from fixed-target and RHIC experiments (see [3, 23]). Without a doubt, the world data indicate that at least another cold nuclear matter effect is at play.

Contrary to nuclear absorption or nPDF effects, the sole effect of coherent energy loss is able to reproduce the data on quarkonium suppression, from fixed-target to collider energies [24–26]. Detailed comparisons were published elsewhere, so let us only highlight the phenomenological successes of this approach:

- (i) The x_F (or y) dependence of J/ψ suppression is well reproduced on a very large domain (up to large values of $x_F \lesssim 0.8$, when data are available) and at all center-of-mass energies, from $\sqrt{s} \approx 20$ GeV to $\sqrt{s} = 5$ TeV.
- (ii) The p_\perp dependence is well-reproduced too, either at a fixed-target experiment (E866) or at colliders (RHIC, LHC), although the p_\perp dependence seems slightly more abrupt in the model than in collider data. The centrality dependence measured by PHENIX at RHIC is also nicely described.
- (iii) Υ measurements in p-A collisions are compatible with the expected mass dependence of coherent energy loss, although the present experimental uncertainties are still fairly large.
- (iv) Finally, an original prediction of coherent energy loss is a different magnitude of quarkonium suppression in p-A and π -A collisions (in contrast with nuclear absorption effects, which should be independent of

the projectile hadron), in agreement with the measurements of NA3.

The strength of coherent energy loss depends on a single free parameter, namely, the magnitude of the cold nuclear matter transport coefficient, $\hat{q}_0 = 0.075 \text{ GeV}^2/\text{fm}$ at $x = 10^{-2}$, obtained from a fit of the precise E866 measurements in p-W collisions.

We find it appealing that the variety of quarkonium measurements in p-A collisions can be described using a *single* CNM effect. Of course, by no means does this imply that no other CNM effects could play a role too, yet these clearly appear to be subleading when the quarkonium is produced at “large enough” rapidity. Both nPDF and coherent energy loss effects could in principle be incorporated consistently in the picture. As a matter of fact, attempts have been made in [25]. However, given the large theoretical uncertainties on nuclear parton distributions, due to the lack of small- x measurements in nuclear collisions (in this respect a high-energy electron-ion collider would be highly beneficial for the community. Let us mention in passing that no coherent energy loss effects are expected in deep-inelastic scattering experiments as the incoming projectile particle is color neutral [19]), especially for gluon densities at small x , we prefer to focus on the single (but in our opinion, leading) effect of coherent energy loss for which rather precise calculation can be performed.

An exciting possibility to further constrain cold nuclear matter effects (on quarkonium production, but not only) would be to smash the LHC proton and lead beams on a collection of fixed nuclear targets [27]. We believe that this proposal would combine the above-discussed advantages of fixed-target *and* collider experiments.

In this paper, the predictions for quarkonium suppression due to coherent energy loss in p-A collisions at $\sqrt{s} = 114.6 \text{ GeV}$ (corresponding to the nominal 7 TeV proton beam energy at the LHC) and Pb-A collisions at $\sqrt{s} = 72 \text{ GeV}$ (corresponding to the 2.76 TeV lead beam) are given. Before this, we recall in the next section the main ingredients of our approach.

2. Coherent Energy Loss Model in a Nutshell

2.1. Formulation. We briefly detail in this section the basics of the model based on coherent energy loss used to describe ψ (denoting J/ψ or Υ) suppression measured in proton-nucleus collisions. (The model can also be formulated in heavy-ion (A-B) collision; see [28] for details.) The single differential p-A production cross section as a function of the ψ energy reads [25]

$$\frac{1}{A} \frac{d\sigma_{pA}^{\psi}}{dE}(E) = \int_0^{\varepsilon^{\max}} d\varepsilon \mathcal{P}(\varepsilon, E, \ell_A^2) \frac{d\sigma_{pp}^{\psi}}{dE}(E + \varepsilon), \quad (1)$$

where E (resp., ε) is the energy (resp., energy loss) of the $Q\bar{Q}$ pair in the rest frame of the nucleus A. The upper limit on the energy loss is $\varepsilon^{\max} = \min(E, E_p - E)$, where E_p is the beam energy in that frame. \mathcal{P} denotes the energy loss probability distribution, or *quenching weight*.

The quenching weight is related to the medium-induced, coherent radiation spectrum $dI/d\varepsilon$ given in [25] (and earlier

TABLE 1: Values of L used in p, Ca, Cu, and Pb targets.

Nucleus	p	Ca	Cu	Pb
Atomic mass	1	40	63	208
L (fm)	1.5	5.69	6.67	10.11

in [19]), which is a very good approximation to the exact spectrum computed to all orders in the opacity expansion [29]. It depends on the accumulated transverse momentum transfer $\ell_A = \sqrt{\hat{q}L}$ (assumed to satisfy $\ell_A \ll M_{\perp}$) due to soft rescatterings in the nucleus, where L is the medium path-length and \hat{q} is the transport coefficient in cold nuclear matter (in our picture, the relevant transverse broadening $\sqrt{\hat{q}L}$ is that of the compact color octet crossing the nucleus, and L is thus the path-length from the “front” surface to the “back” surface of the nucleus for a given impact parameter. Note that, in nuclear absorption models, the relevant length is that from the hard production vertex to the “back” surface of the nucleus, that is, a factor ~ 2 smaller than the medium length L used here and quoted in Table 1). More precisely [25],

$$\begin{aligned} \hat{q} &\equiv \hat{q}_0 \left[\frac{10^{-2}}{\min(x_0, x_2)} \right]^{0.3}; \\ x_0 &\equiv \frac{1}{2m_p L}; \\ x_2 &\equiv \frac{M_{\perp}}{\sqrt{s}} e^{-y}, \end{aligned} \quad (2)$$

where y is the quarkonium rapidity in the center-of-mass frame of the proton-nucleon collision.

Using the fact that the quenching weight is a scaling function of the variable ε/E , namely, $E\mathcal{P}(\varepsilon, E, \ell^2) = \widehat{\mathcal{P}}(\varepsilon/E, \ell^2)$, we can rewrite (1) as [28]

$$\begin{aligned} \frac{1}{A} \frac{d\sigma_{pA}^{\psi}}{dy}(y, \sqrt{s}) &= \int_0^{\delta y^{\max}(y)} d\delta y \widehat{\mathcal{P}}(e^{\delta y} - 1, \hat{q}(y)L) \\ &\cdot \frac{d\sigma_{pp}^{\psi}}{dy}(y + \delta y, \sqrt{s}). \end{aligned} \quad (3)$$

Here, $\delta y^{\max}(y) = \min(\ln 2, y_{\max} - y)$, with $y_{\max} = \ln(\sqrt{s}/M_{\perp})$ the maximal ψ rapidity (in the proton-nucleon c.m. frame) allowed by kinematics. Using (3), we can determine the nuclear modification factor in p-A collision:

$$R_{pA}^{\psi}(y, \sqrt{s}) = \frac{(1/A) (d\sigma_{pA}^{\psi}/dy)(y, \sqrt{s})}{(d\sigma_{pp}^{\psi}/dy)(y, \sqrt{s})}. \quad (4)$$

As mentioned in the introduction, quarkonium may suffer inelastic interaction with the surrounding nucleons while escaping the nucleus. Although we do not aim to include such an effect in the present predictions, we nevertheless indicate the critical rapidity y^{crit} :

$$y^{\text{crit}}(\sqrt{s}, L) \equiv \ln \left(\frac{L}{\tau_f} \cdot \frac{2m_p}{\sqrt{s}} \right), \quad (5)$$

below which nuclear absorption might come into play.

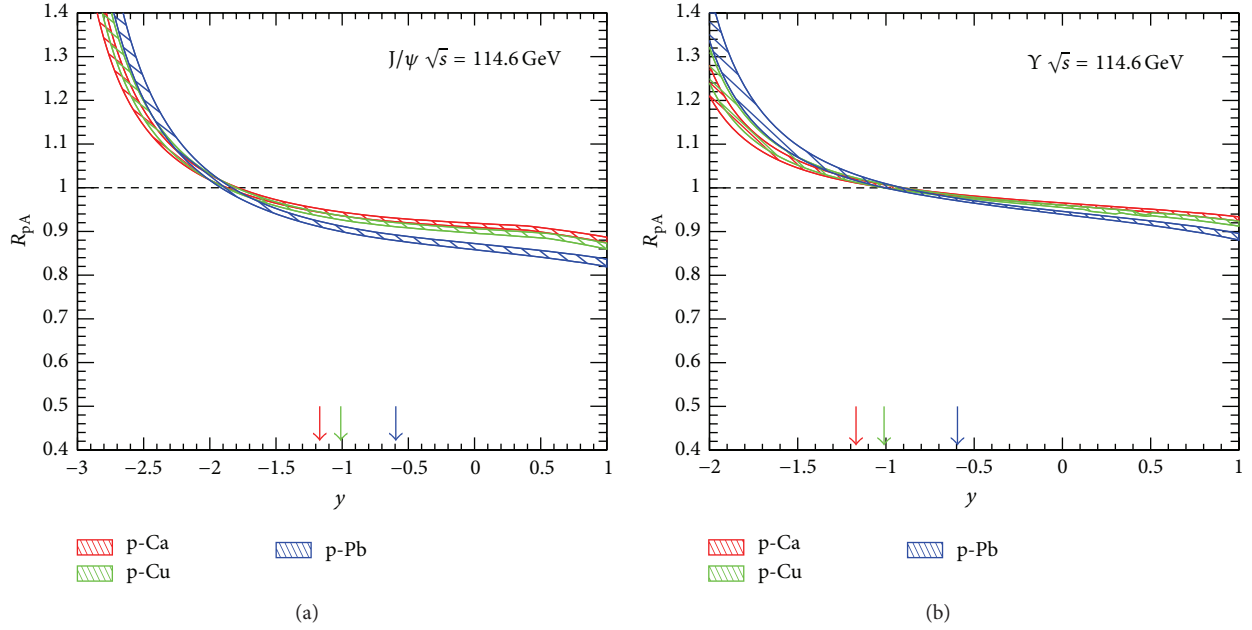


FIGURE 1: J/ψ (a) and Υ (b) suppression in p-Ca, p-Cu, and p-Pb collisions at $\sqrt{s} = 114.6$ GeV.

2.2. Ingredients. The medium length L is obtained from a Glauber model calculation using realistic nuclear densities. The values are given in [25] and reproduced in Table 1 for the nuclei of interest in the present paper. In addition, (3) requires the knowledge of the p-p cross section. It is given by a simple parameterization $d\sigma_{pp}^W/dy \propto (1 - (2M_{\perp}/\sqrt{s})\cosh y)^{n(\sqrt{s})}$, where the exponent n is obtained from a fit to p-p measurements. Lacking p-p data at the energies of interest ($\sqrt{s} = 114.6$ GeV in p-A and $\sqrt{s} = 72$ GeV in Pb-A collisions), an interpolation between the values obtained at FNAL ($\sqrt{s} = 38.7$ GeV) and RHIC ($\sqrt{s} = 200$ GeV) energies has been performed. The exponents used in the present paper are given in Table 2. Note that the normalization of the p-p cross section is irrelevant here as it cancels out when computing (4).

The transport coefficient \hat{q}_0 is the only free parameter of the model. It is determined by fitting the J/ψ suppression measured by E866 [3] in p-W over p-Be collisions ($\sqrt{s} = 38.7$ GeV); see [25]. The obtained value is $\hat{q}_0 = 0.075_{-0.005}^{+0.015}$ GeV²/fm.

3. Results

3.1. p-A Mode. The predictions for J/ψ and Υ suppression in p-Ca, p-Cu, and p-Pb collisions at $\sqrt{s} = 114.6$ GeV are shown in Figure 1. The rapidity range is chosen to match the acceptance of detectors like LHCb [30]. In terms of Feynman- x , the range $-3 < y < 1$ (resp., $-2 < y < 1$) corresponds to $-0.54 < x_F < 0.06$ (resp., $-0.60 < x_F < 0.19$) for J/ψ (resp., Υ (because of the more restricted phase-space from its larger mass, the rapidity acceptance is smaller for Υ than for J/ψ)).

The J/ψ suppression is rather moderate, less than 20%, and does not vary too strongly with rapidity except at

TABLE 2: Values of n used at $\sqrt{s} = 72$ GeV and $\sqrt{s} = 114.6$ GeV for J/ψ and Υ .

Mode	Pb-A	p-A
\sqrt{s} (GeV)	72	114.6
$n_{J/\psi}$	5.1 ± 0.2	6.0 ± 0.3
n_{Υ}	4.1 ± 0.3	5.0 ± 0.4

very negative rapidity values, $y < y_0 \approx -2$, where J/ψ enhancement ($R_{pA} > 1$) can be seen. In this rapidity region, however, nuclear absorption may come into play as can be seen from the vertical arrows indicating the values of y^{crit} ($y^{\text{crit}} \approx -1$) for each target. The suppression depends on the atomic mass number of the target (Ca, Cu, and Pb), yet this nuclear dependence is tempered somehow by the slow dependence of the coherent energy loss scale, $\hat{\omega}$, on the medium length, $\hat{\omega} \propto \sqrt{L}$ [25].

The shape of Υ suppression is similar. The value of the rapidity at which $R_{pA}(y_0) = 1$ is $y_0 \approx -1$, that is, one more unit than in the J/ψ channel. This can be understood from the approximate x_F scaling present in the model [25] (at a given rapidity y , the corresponding value of x_F is larger for Υ than for J/ψ due to the larger transverse mass, $x_F \propto M_{\perp}$) which would predict the difference between these two “crossing points” to be $y_0^{\Upsilon} - y_0^{J/\psi} \sim \ln(M^{\Upsilon}/M^{J/\psi}) \approx 1.1$. Once more, nuclear absorption may affect Υ suppression, though maybe not as much as the J/ψ because of its smaller radius.

3.2. A-p Mode. Let us move now to calculations corresponding to an incoming 2.76 TeV Pb beam on a proton and a Pb target, shown in Figure 2. This configuration allows for probing more easily quarkonium suppression in the

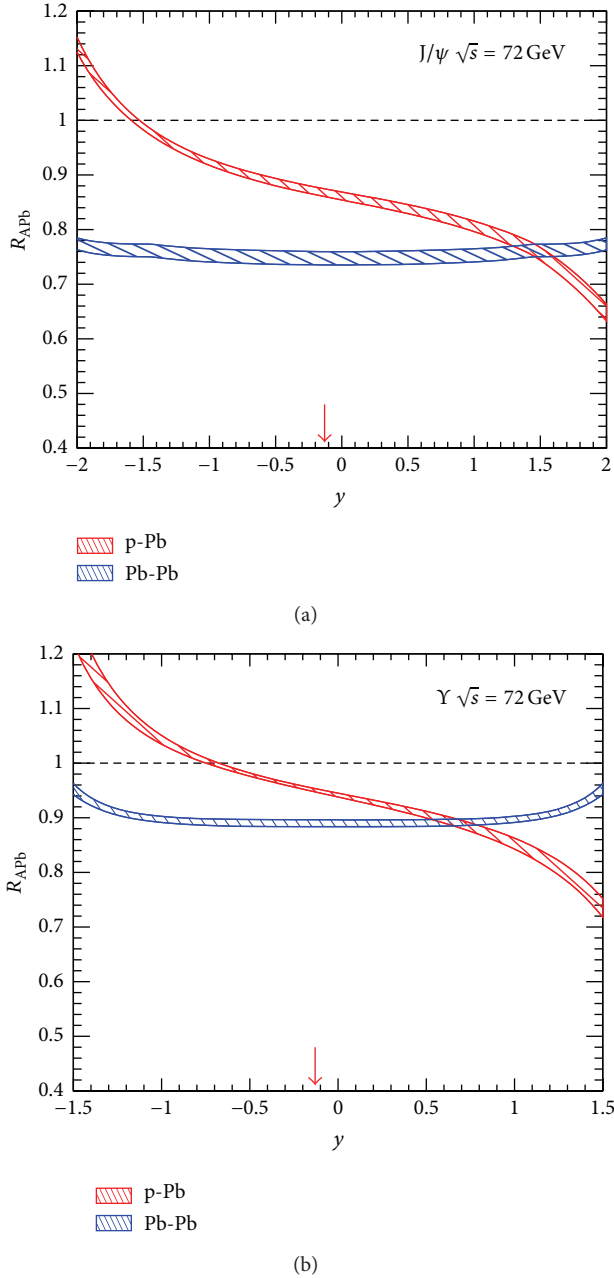


FIGURE 2: J/ψ (a) and Υ (b) suppression in p-Pb and Pb-Pb collisions at $\sqrt{s} = 72$ GeV.

proton fragmentation, that is, at positive rapidities. (Although the Pb nucleus collides with a proton, we will keep the convention that positive values of y correspond to the proton fragmentation region.) The chosen rapidity range $-2 < y < 2$ (resp., $-1.5 < y < 1.5$) corresponds to $-0.31 < x_F < 0.31$ ($-0.56 < x_F < 0.56$) for J/ψ (Υ). The lower center-of-mass energy however shifts y^{crit} in p-Pb collisions towards larger values, possibly leading to more pronounced nuclear absorption.

In Pb-Pb collisions, the suppression is naturally an even function of y . In such collisions, one expects a hot medium to be formed leading to extra quarkonium suppression. Therefore, the results should rather be seen as baseline calculations

than genuine predictions. Moreover, in A-A collisions, the condition for hadronization taking place outside *both* nuclei reads $y^{\text{crit}} < y < -y^{\text{crit}}$. This condition is only met in Pb-Pb collisions at $\sqrt{s} = 72$ GeV around midrapidity, $|y| \leq 0.1$. At larger $|y|$, the quarkonium state will be fully formed in one of the two nuclei and thus possibly sensitive to nuclear absorption.

Conflict of Interests

The authors declare that there is no conflict of interests regarding the publication of this paper.

References

- [1] T. Matsui and H. Satz, “ J/ψ suppression by quark-gluon plasma formation,” *Physics Letters B*, vol. 178, pp. 416–422, 1986.
- [2] J. Badier, J. Boucrot, J. Bourotte et al., “Experimental J/ψ hadronic production from 150 to 280 GeV/c,” *Zeitschrift für Physik C*, vol. 20, pp. 101–116, 1983.
- [3] M. J. Leitch, W. M. Lee, M. E. Beddo et al., “Measurement of differences between J/ψ and ψ' suppression in p – A collisions,” *Physical Review Letters*, vol. 84, no. 15, pp. 3256–3260, 2000.
- [4] M. C. Abreu, C. Baglin, A. Baldit et al., “Charmonia production in 450 GeV/c proton induced reactions,” *Physics Letters B*, vol. 444, pp. 516–522, 1998.
- [5] B. Alessandro, C. Alexa, R. Arnaldi et al., “ J/ψ and ψ' production and their normal nuclear absorption in proton-nucleus collisions at 400 GeV,” *The European Physical Journal C*, vol. 48, no. 2, pp. 329–341, 2006.
- [6] R. Arnaldi, K. Banicz, J. Castor et al., “ J/ψ production in proton-nucleus collisions at 158 and 400 GeV,” *Physics Letters B*, vol. 706, no. 4–5, pp. 263–267, 2012.
- [7] I. Abt, M. Adams, M. Agari et al., “Kinematic distributions and nuclear effects of J/ψ production in 920 GeV fixed-target proton-nucleus collisions,” *The European Physical Journal C*, vol. 60, no. 4, pp. 525–542, 2009.
- [8] A. Adare, S. Afanasiev, C. Aidala et al., “Cold nuclear matter effects on J/ψ yields as a function of rapidity and nuclear geometry in $d + A$ collisions at $\sqrt{s_{NN}} = 200$ GeV,” *Physical Review Letters*, vol. 107, Article ID 142301, 2011.
- [9] A. Adare, S. Afanasiev, C. Aidala et al., “Transverse-momentum dependence of the J/ψ nuclear modification in $d + \text{Au}$ collisions at $\sqrt{s_{NN}} = 200$ GeV,” *Physical Review C*, vol. 87, Article ID 034904, 2013.
- [10] L. Adamczyk, J. K. Adkins, G. Agakishiev et al., “Suppression of Υ production in $d + \text{Au}$ and $\text{Au} + \text{Au}$ collisions at $\sqrt{s_{NN}} = 200$ GeV,” *Physics Letters B*, vol. 735, pp. 127–137, 2014.
- [11] B. B. Abelev, J. Adam, D. Adamová et al., “ J/ψ production and nuclear effects in p-Pb collisions at $\sqrt{s_{NN}} = 5.02$ TeV,” *Journal of High Energy Physics*, vol. 2014, no. 2, article 073, 2014.
- [12] R. Aaij, B. Adeva, M. Adinolfi et al., “Study of J/ψ production and cold nuclear matter effects in p Pb collisions at $\sqrt{s_{NN}} = 5$ TeV,” *Journal of High Energy Physics*, vol. 2014, no. 2, article 072, 2014.
- [13] S. Chatrchyan, V. Khachatryan, A. M. Sirunyan et al., “Event activity dependence of $Y(\text{nS})$ production in $\sqrt{s_{NN}} = 5.02$ TeV pPb and $\sqrt{s} = 2.76$ TeV pp collisions,” *Journal of High Energy Physics*, vol. 2014, no. 4, article 103, 2014.

- [14] B. B. Abelev, J. Adam, M. M. Aggarwal et al., “Measurement of prompt D -meson production in p -Pb Collisions at $\sqrt{s_{NN}} = 5.02$ TeV,” *Physical Review Letters*, vol. 113, no. 23, Article ID 232301, 11 pages, 2014.
- [15] CMS Collaboration, “Measurements of the B^+ , B^0 and B_s^0 production cross sections in pPb collisions at $\sqrt{s_{NN}} = 5.02$ TeV,” Tech. Rep. CMS-PAS-HIN-14-004, CERN, 2014.
- [16] J. Adam, D. Adamova, M. M. Aggarwal et al., “Inclusive, prompt and non-prompt J/ψ production at mid-rapidity in Pb-Pb collisions at $\sqrt{s_{NN}} = 2.76$ TeV,” *Journal of High Energy Physics*, vol. 2015, no. 7, article 051, 2015.
- [17] N. Armesto, “Nuclear shadowing,” *Journal of Physics G: Nuclear and Particle Physics*, vol. 32, no. 11, p. R367, 2006.
- [18] F. Gelis, E. Iancu, J. Jalilian-Marian, and R. Venugopalan, “The color glass condensate,” *Annual Review of Nuclear and Particle Science*, vol. 60, pp. 463–489, 2010.
- [19] F. Arleo, S. Peigné, and T. Sami, “Revisiting scaling properties of medium-induced gluon radiation,” *Physical Review D*, vol. 83, Article ID 114036, 2011.
- [20] J. Albacete, N. Armesto, R. Baier et al. et al., “Predictions for p +Pb collisions at $\sqrt{s_{NN}} = 5$ TeV,” *International Journal of Modern Physics E*, vol. 22, Article ID 1330007, 2013.
- [21] E. Ferreira, F. Fleuret, J. Lansberg, and A. Rakotozafindrabe, “Impact of the nuclear modification of the gluon densities on J/ψ production in p Pb collisions at $\sqrt{s_{NN}} = 5$ TeV,” *Physical Review C*, vol. 88, Article ID 047901, 2013.
- [22] P. Hoyer, M. Vanttinen, and U. Sukhatme, “Violation of factorization in charm hadroproduction,” *Physics Letters B*, vol. 246, no. 1-2, pp. 217–220, 1990.
- [23] M. J. Leitch, “Overview of charm physics at RHIC,” *AIP Conference Proceedings*, vol. 892, no. 1, pp. 404–409, 2007.
- [24] F. Arleo and S. Peigné, “ J/ψ suppression in p -A collisions from parton energy loss in cold QCD matter,” *Physical Review Letters*, vol. 10, no. 12, Article ID 122301, 5 pages, 2012.
- [25] F. Arleo and S. Peigné, “Heavy-quarkonium suppression in p -A collisions from parton energy loss in cold QCD matter,” *Journal of High Energy Physics*, vol. 2013, no. 3, article 122, 2013.
- [26] F. Arleo, R. Kolevato, S. Peigné, and M. Rustamova, “Centrality and p_{\perp} dependence of J/ψ suppression in proton-nucleus collisions from parton energy loss,” *Journal of High Energy Physics*, vol. 2013, no. 5, article 155, 2013.
- [27] S. J. Brodsky, F. Fleuret, C. Hadjidakis, and J. P. Lansberg, “Physics opportunities of a fixed-target experiment using LHC beams,” *Physics Reports*, vol. 522, no. 4, pp. 239–255, 2013.
- [28] F. Arleo and S. Peigné, “Quarkonium suppression in heavy-ion collisions from coherent energy loss in cold nuclear matter,” *Journal of High Energy Physics*, vol. 2014, no. 10, article 73, 2014.
- [29] S. Peigné, F. Arleo, and R. Kolevato, “Medium-induced gluon radiation: an update,” <http://arxiv.org/abs/1402.1671>.
- [30] L. Massacrier, B. Trzeciak, F. Fleuret et al., “Feasibility studies for quarkonium production at a fixed-target experiment using the LHC proton and lead beams (AFTER@LHC),” <http://arxiv.org/abs/1504.05145>.

Research Article

Transverse Single-Spin Asymmetries in Proton-Proton Collisions at the AFTER@LHC Experiment in a TMD Factorisation Scheme

M. Anselmino,^{1,2} U. D'Alesio,^{3,4} and S. Melis¹

¹*Dipartimento di Fisica, Università di Torino, Via P. Giuria 1, 10125 Torino, Italy*

²*INFN, Sezione di Torino, Via P. Giuria 1, 10125 Torino, Italy*

³*Dipartimento di Fisica, Università di Cagliari, Cittadella Universitaria, 09042 Monserrato, Italy*

⁴*INFN, Sezione di Cagliari, CP 170, 09042 Monserrato, Italy*

Correspondence should be addressed to M. Anselmino; mauro.anselmino@to.infn.it

Received 14 April 2015; Accepted 15 June 2015

Academic Editor: Jibo He

Copyright © 2015 M. Anselmino et al. This is an open access article distributed under the Creative Commons Attribution License, which permits unrestricted use, distribution, and reproduction in any medium, provided the original work is properly cited. The publication of this article was funded by SCOAP³.

The inclusive large- p_T production of a single pion, jet or direct photon, and Drell-Yan processes, are considered for proton-proton collisions in the kinematical range expected for the fixed-target experiment AFTER, proposed at LHC. For all these processes, predictions are given for the transverse single-spin asymmetry, A_N , computed according to a Generalised Parton Model previously discussed in the literature and based on TMD factorisation. Comparisons with the results of a collinear twist-3 approach, recently presented, are made and discussed.

1. Introduction and Formalism

Transverse Single-Spin Asymmetries (TSSAs) have been abundantly observed in several inclusive proton-proton experiments for a long time; when reaching large enough energies and p_T values, their understanding from basic quark-gluon QCD interactions is a difficult and fascinating task, which has always been one of the major challenges for QCD.

In fact, large TSSAs cannot be generated by the hard elementary processes, because of helicity conservation (in the massless limit) typical of QED and QCD interactions; indeed, such asymmetries were expected to vanish at high energies. Their persisting must be related to nonperturbative properties of the nucleon structure, such as parton intrinsic and orbital motion. A true understanding of the origin of TSSAs would allow a deeper understanding of the nucleon structure.

Since the 1990s two different, despite being somewhat related, approaches have attempted to tackle the problem. One is based on the collinear QCD factorisation scheme and involves as basic quantities, which can generate single-spin

dependences, higher-twist quark-gluon-quark correlations in the nucleon as well as higher-twist fragmentation correlators. The second approach is based on a physical, although unproven, generalisation of the parton model, with the inclusion, in the factorisation scheme, of transverse momentum dependent partonic distribution and fragmentation functions (TMDs), which also can generate single-spin dependences. The twist-3 correlations are related to moments of some TMDs. We refer to [1–9], and references therein, for more detailed account of the two approaches and possible variations, with all relevant citations. Following [10], we denote by CT-3 the first approach while the second one is, as usual, denoted by GPM.

In this paper we consider TSSAs at the proposed AFTER@LHC experiment, in which high-energy protons extracted from the LHC beam would collide on a (polarised) fixed target of protons, with high luminosity. For a description of the physics potentiality of this experiment see [11] and for the latest technical details and importance for TMD studies see, for example, [12]. Due to its features the AFTER@LHC is an ideal experiment to study and understand the origin of

SSAs and, in general, the role of QCD interactions in high-energy hadronic collisions; AFTER@LHC would be a polarised fixed-target experiment with unprecedented high luminosity.

We recall our formalism by considering the Transverse Single-Spin Asymmetry A_N , measured in $pp^\uparrow \rightarrow hX$ inclusive reactions and defined as

$$A_N = \frac{d\sigma^\uparrow - d\sigma^\downarrow}{d\sigma^\uparrow + d\sigma^\downarrow} \quad \text{with } d\sigma^{\uparrow,\downarrow} \equiv \frac{E_h d\sigma^{pp^{\uparrow,\downarrow} \rightarrow hX}}{d^3\mathbf{p}_h}, \quad (1)$$

where \uparrow, \downarrow are opposite spin orientations perpendicular to the x - z scattering plane, in the pp^\uparrow c.m. frame. We define the \uparrow direction as the $+\hat{y}$ -axis and the unpolarised proton is moving along the $+\hat{z}$ -direction. In such a process the only large scale is the transverse momentum $p_T = |(\mathbf{p}_h)_x|$ of the final hadron.

In the GPM A_N originates mainly from two spin and transverse momentum effects, one introduced by Sivers in the partonic distributions [13, 14] and one by Collins in the parton fragmentation process [15], being all the other effects strongly suppressed by azimuthal phase integrations [16]. According to the Sivers effect the number density of unpolarised quarks q (or gluons) with intrinsic transverse momentum \mathbf{k}_\perp inside a transversely polarised proton p^\uparrow , with three-momentum \mathbf{P} and spin polarisation vector \mathbf{S} , can be written as

$$\begin{aligned} \hat{f}_{q/p^\uparrow}(x, \mathbf{k}_\perp) &= f_{q/p}(x, k_\perp) \\ &+ \frac{1}{2} \Delta^N f_{q/p^\uparrow}(x, k_\perp) (\mathbf{S} \cdot (\hat{\mathbf{P}} \times \hat{\mathbf{k}}_\perp)), \end{aligned} \quad (2)$$

where x is the proton light-cone momentum fraction carried by the quark, $f_{q/p}(x, k_\perp)$ is the unpolarised TMD ($k_\perp = |\mathbf{k}_\perp|$), and $\Delta^N f_{q/p^\uparrow}(x, k_\perp)$ is the Sivers function. $\hat{\mathbf{P}} = \mathbf{P}/|\mathbf{P}|$ and $\hat{\mathbf{k}}_\perp = \mathbf{k}_\perp/k_\perp$ are unit vectors. Notice that the Sivers function is most often denoted as $f_{1T}^{\perp q}(x, k_\perp)$ [17]; this notation is related to ours by [18]

$$\Delta^N f_{q/p^\uparrow}(x, k_\perp) = -\frac{2k_\perp}{m_p} f_{1T}^{\perp q}(x, k_\perp), \quad (3)$$

where m_p is the proton mass.

Similarly, according to the Collins effect the number density of unpolarised hadrons h with transverse momentum \mathbf{p}_\perp resulting in the fragmentation of a transversely polarised quark q^\uparrow , with three-momentum \mathbf{q} and spin polarisation vector \mathbf{S}_q , can be written as

$$\begin{aligned} \hat{D}_{q^\uparrow/h}(z, \mathbf{p}_\perp) &= D_{h/q}(z, p_\perp) \\ &+ \frac{1}{2} \Delta^N D_{q^\uparrow/h}(z, p_\perp) (\mathbf{S}_q \cdot (\hat{\mathbf{q}} \times \hat{\mathbf{p}}_\perp)), \end{aligned} \quad (4)$$

where z is the parton light-cone momentum fraction carried by the hadron, $D_{h/q}(z, p_\perp)$ is the unpolarised TMD ($p_\perp = |\mathbf{p}_\perp|$), and $\Delta^N D_{q^\uparrow/h}(z, p_\perp)$ is the Collins function. $\hat{\mathbf{q}} = \mathbf{q}/|\mathbf{q}|$ and $\hat{\mathbf{p}}_\perp = \mathbf{p}_\perp/p_\perp$ are unit vectors. Notice that the Collins function is most often denoted as $H_1^{\perp q}(z, p_\perp)$ [17]; this notation is related to ours by [18]

$$\Delta^N D_{h/q^\uparrow}(z, p_\perp) = \frac{2p_\perp}{z M_h} H_1^{\perp q}(z, p_\perp), \quad (5)$$

where M_h is the hadron mass.

According to the GPM formalism [1, 2, 16], A_N can then be written as

$$A_N = \frac{[d\sigma^\uparrow - d\sigma^\downarrow]_{\text{Sivers}} + [d\sigma^\uparrow - d\sigma^\downarrow]_{\text{Collins}}}{d\sigma^\uparrow + d\sigma^\downarrow}. \quad (6)$$

The Collins and Sivers contributions were recently studied, respectively, in [1] and [2], and are given by

$$\begin{aligned} [d\sigma^\uparrow - d\sigma^\downarrow]_{\text{Sivers}} &= \sum_{a,b,c,d} \int \frac{dx_a dx_b dz}{16\pi^2 x_a x_b z^2 s} d^2\mathbf{k}_{\perp a} d^2\mathbf{k}_{\perp b} d^3\mathbf{p}_\perp \delta(\mathbf{p}_\perp \cdot \hat{\mathbf{p}}_c) \\ &\cdot J(p_\perp) \delta(\hat{s} + \hat{t} + \hat{u}) \Delta^N f_{a/p^\uparrow}(x_a, k_{\perp a}) \cos(\phi_a) \\ &\cdot f_{b/p}(x_b, k_{\perp b}) \frac{1}{2} \left[|\widehat{M}_1^0|^2 + |\widehat{M}_2^0|^2 + |\widehat{M}_3^0|^2 \right]_{ab \rightarrow cd} \\ &\cdot D_{h/c}(z, p_\perp), \\ [d\sigma^\uparrow - d\sigma^\downarrow]_{\text{Collins}} &= \sum_{q_a, b, q_c, d} \int \frac{dx_a dx_b dz}{16\pi^2 x_a x_b z^2 s} d^2\mathbf{k}_{\perp a} d^2\mathbf{k}_{\perp b} d^3\mathbf{p}_\perp \delta(\mathbf{p}_\perp \cdot \hat{\mathbf{p}}_c) \\ &\cdot J(p_\perp) \delta(\hat{s} + \hat{t} + \hat{u}) \Delta_T q_a(x_a, k_{\perp a}) \cos(\phi_a + \varphi_1) \\ &- \varphi_2 + \phi_\pi^H) f_{b/p}(x_b, k_{\perp b}) \left[\widehat{M}_1^0 \widehat{M}_2^0 \right]_{q_a b \rightarrow q_c d} \\ &\cdot \Delta^N D_{h/q_c^\uparrow}(z, p_\perp). \end{aligned} \quad (7)$$

For details and full explanation of the notations in the above equations we refer to [16] (where \mathbf{p}_\perp is denoted as $\mathbf{k}_{\perp C}$). It suffices to notice here that $J(p_\perp)$ is a kinematical factor, which at $\mathcal{O}(p_\perp/E_h)$ equals 1. The phase factor $\cos(\phi_a)$ in (7) originates directly from the \mathbf{k}_\perp dependence of the Sivers distribution $[\mathbf{S} \cdot (\hat{\mathbf{P}} \times \hat{\mathbf{k}}_\perp), (2)]$. The (suppressing) phase factor $\cos(\phi_a + \varphi_1 - \varphi_2 + \phi_\pi^H)$ in (8) originates from the \mathbf{k}_\perp dependence of the unintegrated transversity distribution $\Delta_T q$, the polarized elementary interaction, and the spin- \mathbf{p}_\perp correlation in the Collins function. The explicit expressions of φ_1 , φ_2 , and ϕ_π^H in terms of the integration variables can be found via (60)–(63) in [16] and (35)–(42) in [19].

The \widehat{M}_i^0 's are the three independent hard scattering helicity amplitudes describing the lowest order QCD interactions. The sum of their moduli squared is related to the elementary unpolarised cross section $d\hat{\sigma}^{ab \rightarrow cd}$; that is,

$$\frac{d\hat{\sigma}^{ab \rightarrow cd}}{d\hat{t}} = \frac{1}{16\pi\hat{s}^2} \frac{1}{2} \sum_{i=1}^3 |\widehat{M}_i^0|^2. \quad (9)$$

The explicit expressions of the combinations of \widehat{M}_i^0 's which give the QCD dynamics in (7) and (8), can be found, for all possible elementary interactions, in [16] (see also [1] for a

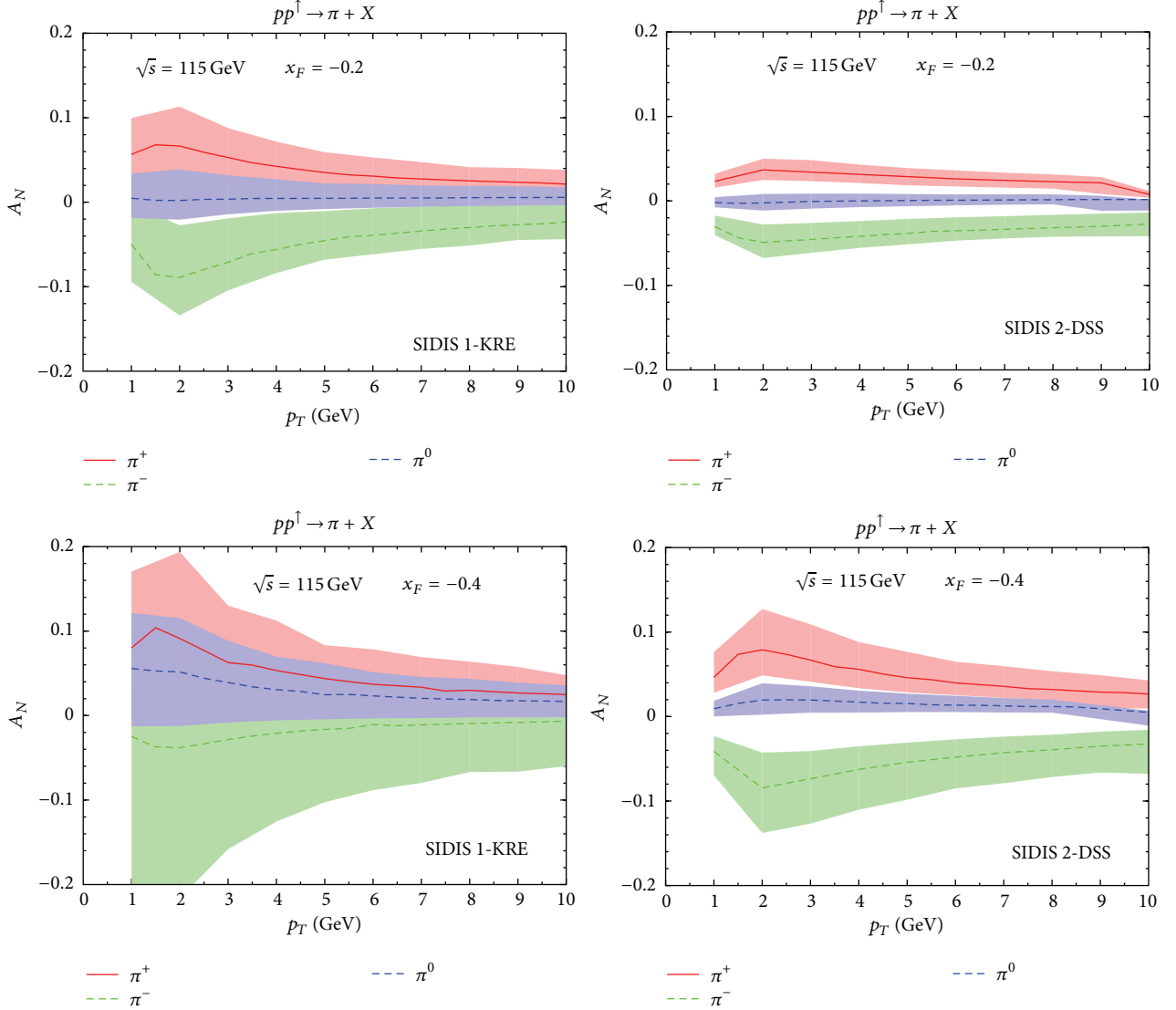


FIGURE 1: Our theoretical estimates for A_N versus p_T at $\sqrt{s} = 115$ GeV, $x_F = -0.2$ (upper plots), and $x_F = -0.4$ (lower plots) for inclusive π^+ and π^0 production in $pp^\dagger \rightarrow \pi X$ processes, computed according to (6)–(8) of the text. The contributions from the Siverts and the Collins effects are added together. The computation is performed adopting the Siverts and Collins functions of [20, 22] (SIDIS 1-KRE, left panels) and of [21, 23] (SIDIS 2-DSS, right panels). The overall statistical uncertainty band, also shown, is the envelope of the two independent statistical uncertainty bands obtained following the procedure described in Appendix A of [21].

correction to one of the product of amplitudes). The QCD scale is chosen as $Q = p_T$.

The denominator of (1) or (6) is twice the unpolarised cross section and is given in our TMD factorisation by the same expression as in (7), where one simply replaces the factor $\Delta^N f_{a/p^\dagger} \cos(\phi_a)$ with $2f_{a/p}$.

2. A_N for Single Pion, Jet, and Direct Photon Production

We present here our results for A_N , (1), based on our GPM scheme, (6), (7), and (8). The TMDs which enter in these equations are those extracted from the analysis of Semi-Inclusive Deep Inelastic (SIDIS) and e^+e^- data [20–23], adopting simple factorised forms, which we recall here.

For the unpolarised TMD partonic distributions and fragmentation functions we have, respectively,

$$f_{q/p}(x, k_\perp) = f_{q/p}(x) \frac{e^{-k_\perp^2/\langle k_\perp^2 \rangle}}{\pi \langle k_\perp^2 \rangle} \quad (10)$$

$$\langle k_\perp^2 \rangle = 0.25 \text{ GeV}^2,$$

$$D_{h/q}(z, p_\perp) = D_{h/q}(z) \frac{e^{-p_\perp^2/\langle p_\perp^2 \rangle}}{\pi \langle p_\perp^2 \rangle} \quad (11)$$

$$\langle p_\perp^2 \rangle = 0.20 \text{ GeV}^2.$$

The Siverts function is parameterised as

$$\Delta^N f_{q/p^\dagger}(x, k_\perp) = 2\mathcal{N}_q^S(x) f_{q/p}(x) h(k_\perp) \frac{e^{-k_\perp^2/\langle k_\perp^2 \rangle}}{\pi \langle k_\perp^2 \rangle}, \quad (12)$$

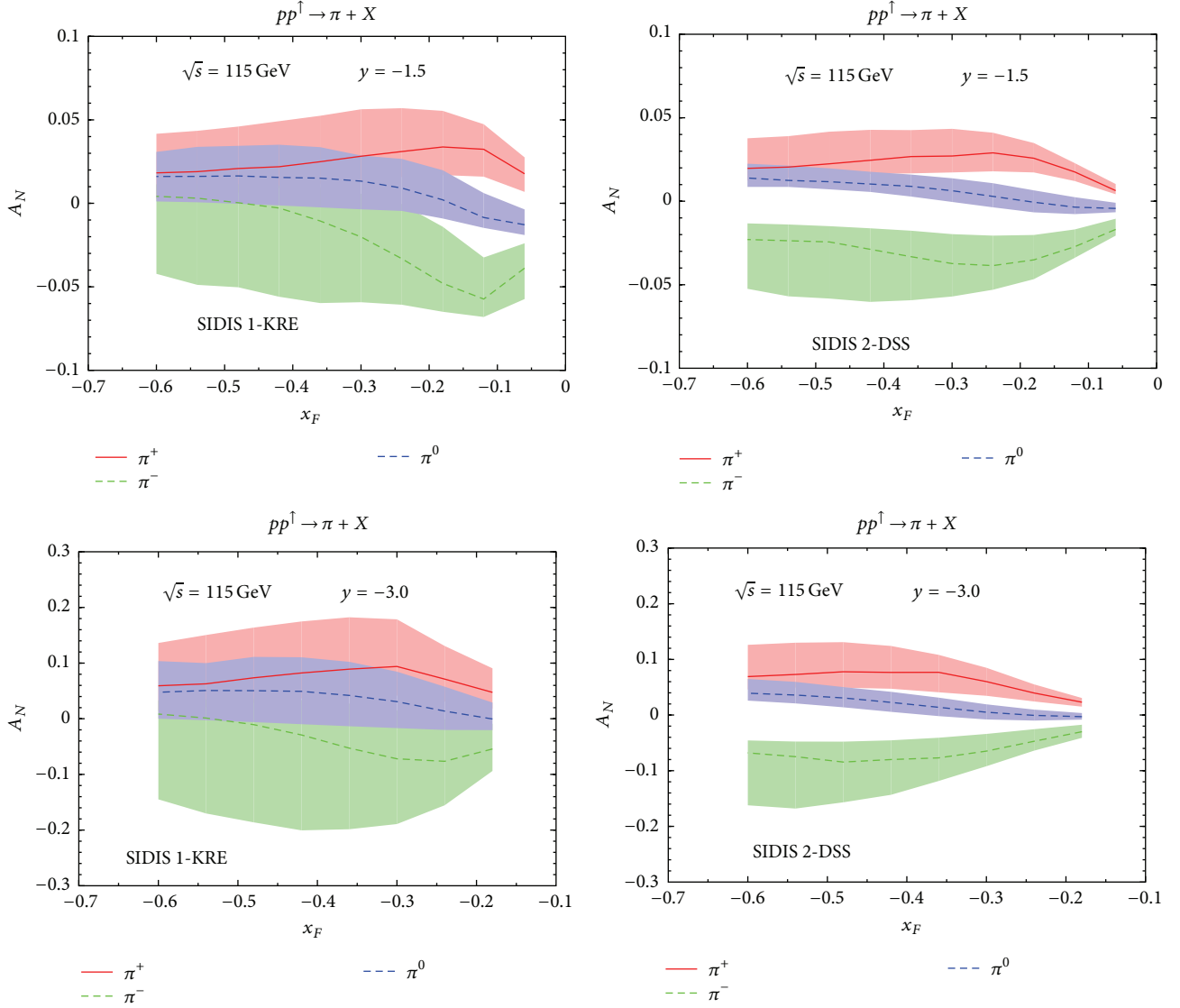


FIGURE 2: Our theoretical estimates for A_N versus x_F at $\sqrt{s} = 115$ GeV, $y = -1.5$ (upper plots), and $y = -3.0$ (lower plots) for inclusive π^+ and π^0 production in $pp^\dagger \rightarrow \pi X$ processes, computed according to (6)–(8) of the text. The contributions from the Siverson and the Collins effects are added together. The computation is performed adopting the Siverson and Collins functions of [20, 22] (SIDIS 1-KRE, left panels) and of [21, 23] (SIDIS 2-DSS, right panels). The overall statistical uncertainty band, also shown, is the envelope of the two independent statistical uncertainty bands obtained following the procedure described in Appendix A of [21].

where

$$\mathcal{N}_q^S(x) = N_q^S x^{\alpha_q} (1-x)^{\beta_q} \frac{(\alpha_q + \beta_q)^{(\alpha_q + \beta_q)}}{\alpha_q^{\alpha_q} \beta_q^{\beta_q}}, \quad (13)$$

with $|N_q^S| \leq 1$, and

$$h(k_\perp) = \sqrt{2} e^{-\frac{k_\perp^2}{M^2}}. \quad (14)$$

Similarly, the quark transversity distribution, $\Delta_T q(x, k_\perp)$, and the Collins fragmentation function, $\Delta^N D_{h/q^\dagger}(z, p_\perp)$, have been parametrized as follows:

$$\Delta_T q(x, k_\perp) = \frac{1}{2} \mathcal{N}_q^T(x) [f_{q/p}(x) + \Delta q(x)] \frac{e^{-k_\perp^2/(k_\perp^2)}}{\pi \langle k_\perp^2 \rangle},$$

$$\Delta^N D_{h/q^\dagger}(z, p_\perp) = 2 \mathcal{N}_q^C(z) D_{h/q}(z) h(p_\perp) \frac{e^{-p_\perp^2/\langle p_\perp^2 \rangle}}{\pi \langle p_\perp^2 \rangle}, \quad (15)$$

where $\Delta q(x)$ is the usual collinear quark helicity distribution,

$$\begin{aligned} \mathcal{N}_q^T(x) &= N_q^T x^{\alpha_q} (1-x)^{\beta_q} \frac{(a_q + b_q)^{(\alpha_q + \beta_q)}}{a_q^{\alpha_q} b_q^{\beta_q}}, \\ \mathcal{N}_q^C(z) &= N_q^C z^{\gamma_q} (1-z)^{\delta_q} \frac{(\gamma_q + \delta_q)^{(\gamma_q + \delta_q)}}{\gamma_q^{\gamma_q} \delta_q^{\delta_q}}, \end{aligned} \quad (16)$$

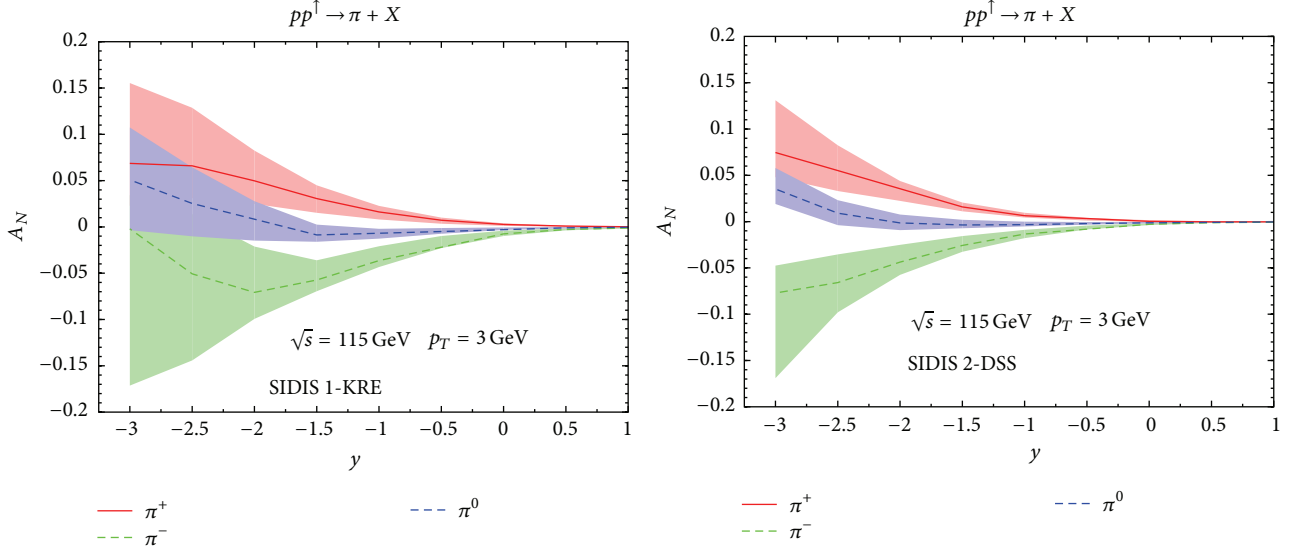


FIGURE 3: Our theoretical estimates for A_N versus y at $\sqrt{s} = 115$ GeV and $p_T = 3$ GeV, for inclusive π^\pm and π^0 production in $pp^\uparrow \rightarrow \pi X$ processes, computed according to (6)–(8) of the text. The contributions from the Siverts and the Collins effects are added together. The computation is performed adopting the Siverts and Collins functions of [20, 22] (SIDIS 1-KRE, left panel) and of [21, 23] (SIDIS 2-DSS, right panel). The overall statistical uncertainty band, also shown, is the envelope of the two independent statistical uncertainty bands obtained following the procedure described in Appendix A of [21].

with $|N_q^{T(C)}| \leq 1$, and

$$h(p_\perp) = \sqrt{2} e^{\frac{p_\perp}{M_c}} e^{-p_\perp^2/M_c^2}. \quad (17)$$

All details concerning the motivations for such a choice, the values of the parameters, and their derivation can be found in [20–23]. We do not repeat them here, but in the caption of each figure we will give the corresponding references which allow fixing all necessary values.

We present our results on A_N for the process $pp^\uparrow \rightarrow \pi X$ at the expected AFTER@LHC energy ($\sqrt{s} = 115$ GeV) in Figures 1–3. Following [1, 2], our results are given for two possible choices of the SIDIS TMDs and are shown as function of p_T at two fixed x_F values (Figure 1), as function of x_F at two fixed rapidity y values (Figure 2) and as function of rapidity at one fixed p_T value (Figure 3). x_F is the usual Feynman variable defined as $x_F = 2p_L/\sqrt{s}$ where $p_L = (\mathbf{p}_h)_z$ is the z -component of the final hadron momentum. Notice that, in our chosen reference frame, a forward production, with respect to the polarised proton, means negative values of x_F . The uncertainty bands reflect the uncertainty in the determinations of the TMDs and are computed according to the procedure explained in the appendix of [21]. More information can be found in the figure captions.

Notice that, for both our choices of the Siverts functions, the gluon Siverts distributions are taken to be vanishing, as suggested by data [21, 24]. Gluon channels contribute instead to the unpolarised cross sections, in the denominator of (1) or (6). For the unpolarised partonic distributions we adopt the GRV98LO PDF set [25] and for the fragmentation functions the DSS set from [26] and the Kretzer (KRE) set from [27].

The analogous results for the single direct photon are shown in Figures 4–6 (where $x_F = 2(\mathbf{p}_{\text{jet}})_z/\sqrt{s}$) and those for the single jet production in Figures 7–9 ($x_F = 2(\mathbf{p}_y)_z/\sqrt{s}$). In these cases, obviously, there is no fragmentation process and only the Siverts effect contributes to A_N , with $D_{h/c}(z, p_\perp)$ simply replaced by $\delta(z-1)\delta^2(\mathbf{p}_\perp)$ in (7) (see [2] for further details). In our leading order treatment the jet coincides with a single final parton. Notice that for a jet production we have all the same QCD subprocesses which contribute to hadron production, while for a direct photon production the basic partonic subprocesses are the Compton scattering $gq(\bar{q}) \rightarrow \gamma q(\bar{q})$ and the annihilation process $q\bar{q} \rightarrow \gamma g$ [28].

3. A_N for Drell-Yan Processes

Drell-Yan (D-Y) processes are expected to play a crucial role in our understanding of the origin, at the partonic level, of TSSAs. For such processes, like for SIDIS processes and contrary to single hadron production, the TMD factorisation has been proven to hold, so that there is a general consensus that the Siverts effect should be visible via TSSAs in D-Y [29–32]. The widely accepted interpretation of the QCD origin of TSSAs as final or initial state interactions of the scattering partons [33] leads to the conclusion that the Siverts function has opposite signs in SIDIS and D-Y processes [34], which remains to be seen.

Predictions for Siverts A_N in D-Y and at different possible experiments were given in [35], which we follow here.

In [35] predictions were given for the $p^\uparrow p \rightarrow \ell^+ \ell^- X$ D-Y process in the $p^\uparrow - p$ c.m. frame, in which one observes the four-momentum q of the final $\ell^+ \ell^-$ pair. Notice that $q^2 = M^2$ is the large scale in the process, while $q_T = |\mathbf{q}_T|$

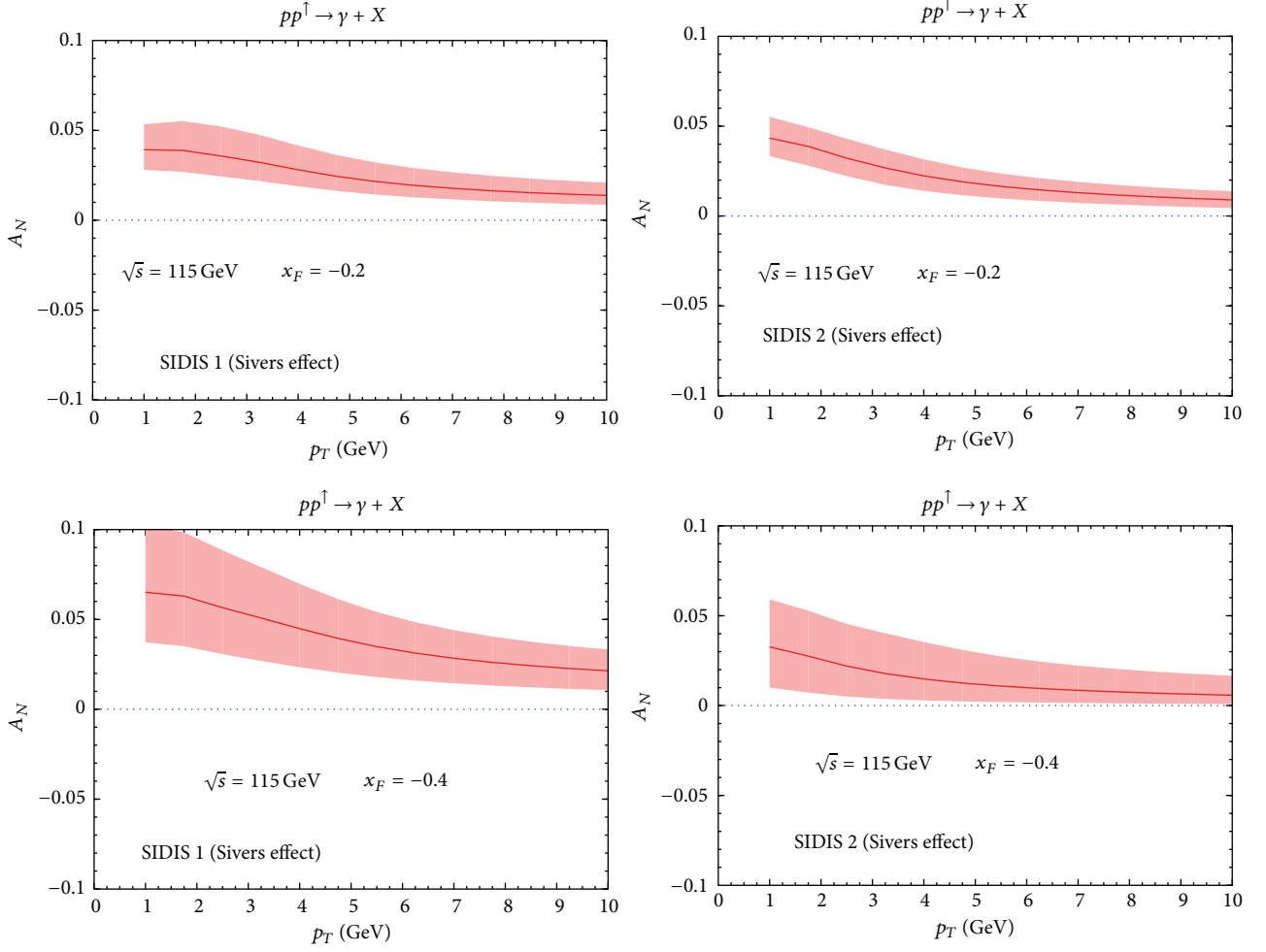


FIGURE 4: Our theoretical estimates for A_N versus p_T at $\sqrt{s} = 115$ GeV, $x_F = -0.2$ (upper plots), and $x_F = -0.4$ (lower plots) for inclusive photon production in $pp^\uparrow \rightarrow \gamma X$ processes, computed according to (6) and (7) of the text. Only the Sivers effect contributes. The computation is performed adopting the Sivers functions of [20] (SIDIS 1, left panels) and of [21] (SIDIS 2, right panels). The overall statistical uncertainty band, also shown, is obtained following the procedure described in Appendix A of [21].

the small one. In order to collect data at all azimuthal angles, one defines the weighted spin asymmetry:

$$A_N^{\sin(\phi_\gamma - \phi_S)} \equiv \frac{\int_0^{2\pi} d\phi_\gamma [d\sigma^\uparrow - d\sigma^\downarrow] \sin(\phi_\gamma - \phi_S)}{(1/2) \int_0^{2\pi} d\phi_\gamma [d\sigma^\uparrow + d\sigma^\downarrow]}, \quad (18)$$

$$= \frac{\int d\phi_\gamma \left[\sum_q e_q^2 \int d^2\mathbf{k}_{\perp 1} d^2\mathbf{k}_{\perp 2} \delta^2(\mathbf{k}_{\perp 1} + \mathbf{k}_{\perp 2} - \mathbf{q}_T) \Delta^N f_{q/p^\uparrow}(x_1, \mathbf{k}_{\perp 1}) f_{\bar{q}/p}(x_2, \mathbf{k}_{\perp 2}) \right] \sin(\phi_\gamma - \phi_S)}{\int d\phi_\gamma \left[\sum_q e_q^2 \int d^2\mathbf{k}_{\perp 1} d^2\mathbf{k}_{\perp 2} \delta^2(\mathbf{k}_{\perp 1} + \mathbf{k}_{\perp 2} - \mathbf{q}_T) f_{q/p}(x_1, \mathbf{k}_{\perp 1}) f_{\bar{q}/p}(x_2, \mathbf{k}_{\perp 2}) \right]}, \quad (19)$$

where ϕ_γ and ϕ_S are, respectively, the azimuthal angle of the $\ell^+ \ell^-$ pair and of the proton transverse spin and we have defined (see (2))

$$\begin{aligned} \Delta^N f_{q/p^\uparrow}(x, \mathbf{k}_\perp) &\equiv \Delta^N f_{q/p^\uparrow}(x, \mathbf{k}_\perp) \mathbf{S} \cdot (\hat{\mathbf{P}} \times \hat{\mathbf{k}}_\perp) \\ &= \hat{f}_{q/p^\uparrow}(x, \mathbf{k}_\perp) - \hat{f}_{q/p^\downarrow}(x, \mathbf{k}_\perp). \end{aligned} \quad (20)$$

Adopting for the unpolarised TMD and the Sivers function the same expressions as in (10) and (12)–(14) allows, at $\mathcal{O}(k_\perp/M)$, an analytical integration of the numerator and denominator of (19), resulting in a simple expression for the asymmetry $A_N^{\sin(\phi_\gamma - \phi_S)}$ [35].

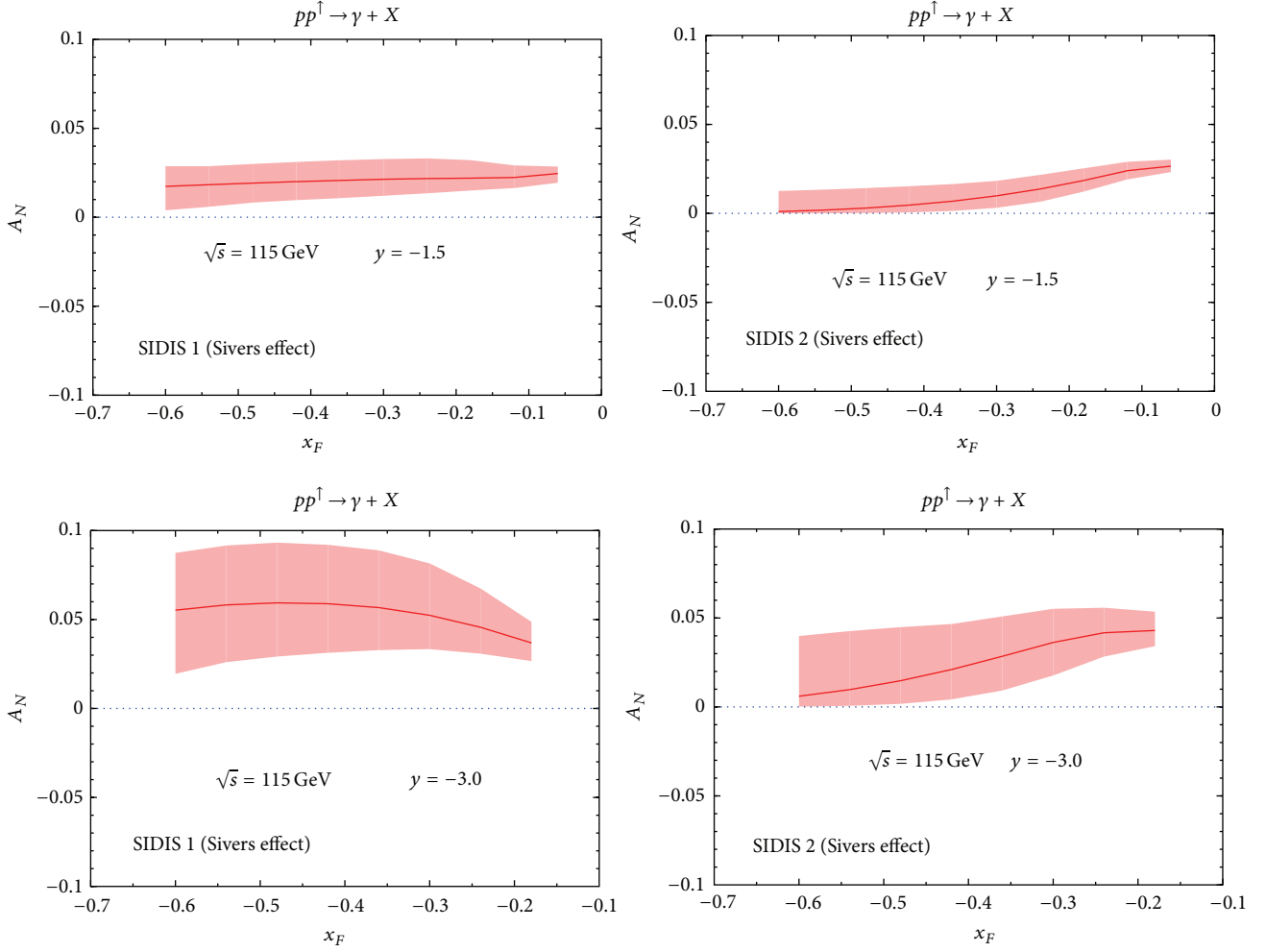


FIGURE 5: Our theoretical estimates for A_N versus x_F at $\sqrt{s} = 115$ GeV, $y = -1.5$ (upper plots), and $y = -3.0$ (lower plots) for inclusive photon production in $pp^\dagger \rightarrow \gamma X$ processes, computed according to (6) and (7) of the text. Only the Sivers effect contributes. The computation is performed adopting the Sivers functions of [20] (SIDIS 1, left panels) and of [21] (SIDIS 2, right panels). The overall statistical uncertainty band, also shown, is obtained following the procedure described in Appendix A of [21].

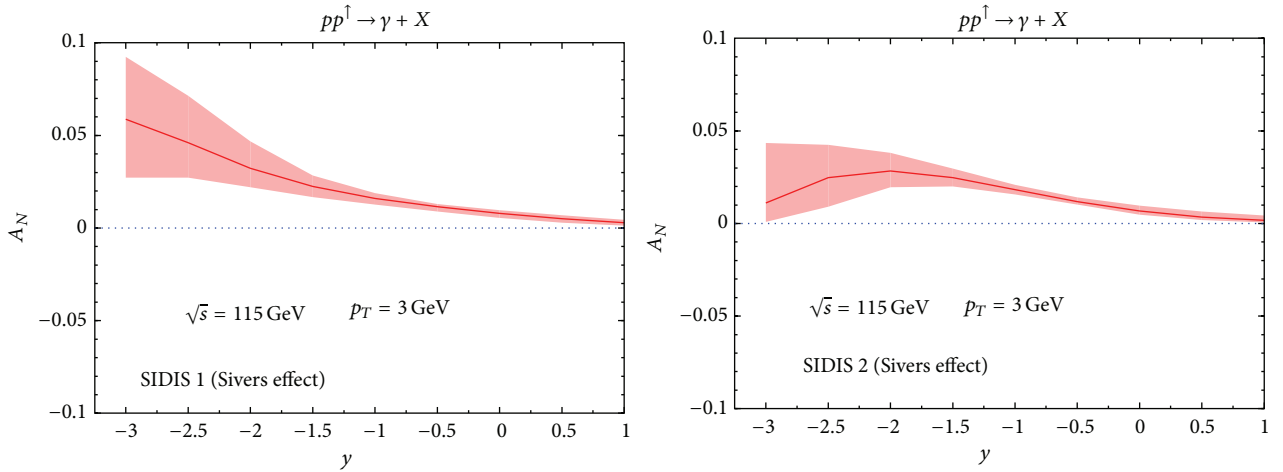


FIGURE 6: Our theoretical estimates for A_N versus y at $\sqrt{s} = 115$ GeV and $p_T = 3$ GeV, for inclusive photon production in $pp^\dagger \rightarrow \gamma X$ processes, computed according to (6)–(8) of the text. Only the Sivers effects contributes. The computation is performed adopting the Sivers functions of [20] (SIDIS 1, left panel) and of [21] (SIDIS 2, right panel). The overall statistical uncertainty band, also shown, is the envelope of the two independent statistical uncertainty bands obtained following the procedure described in Appendix A of [21].

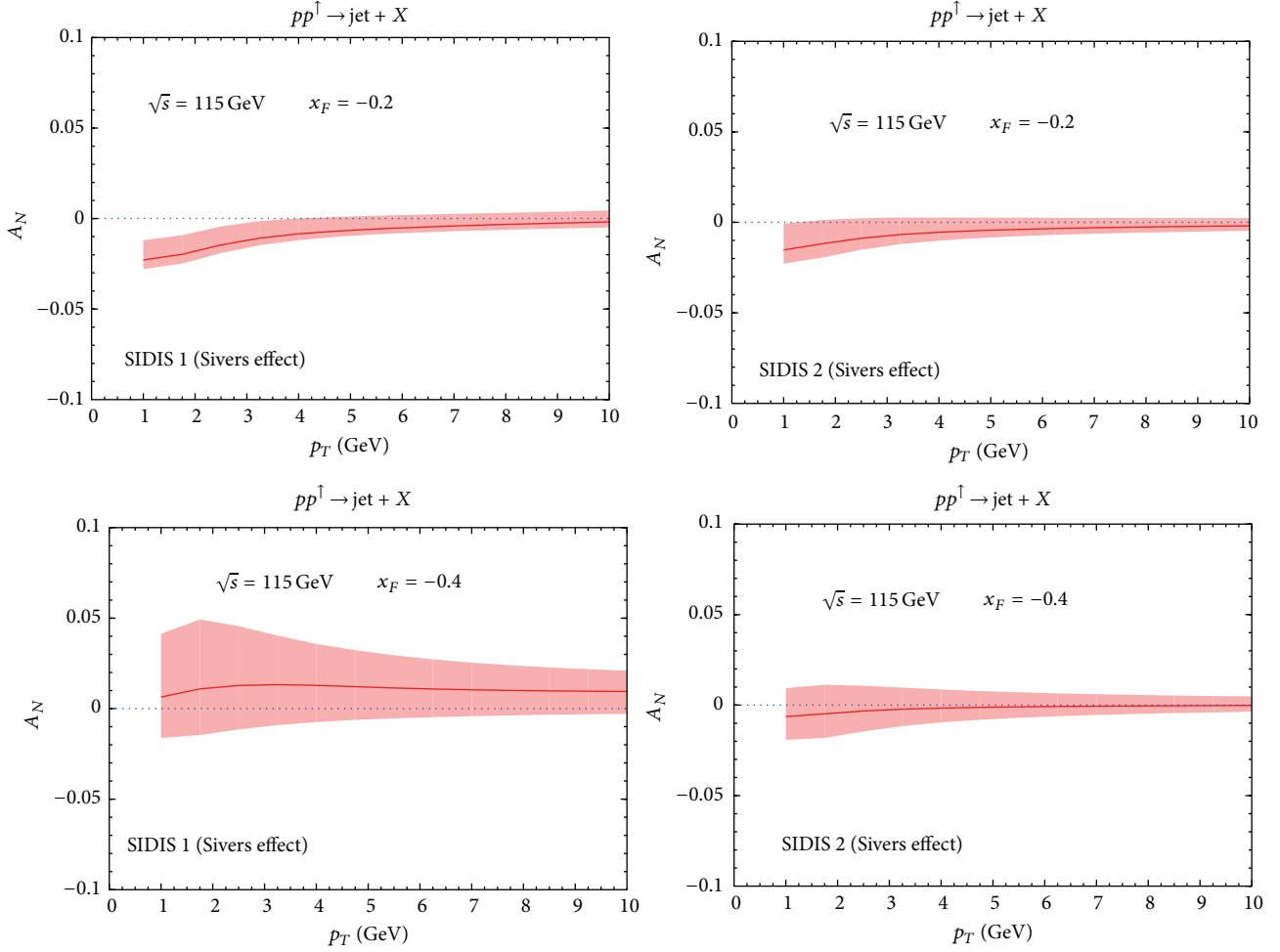


FIGURE 7: Our theoretical estimates for A_N versus x_F at $\sqrt{s} = 115$ GeV, $x_F = -0.2$ (upper plots), and $x_F = -0.4$ (lower plots) for inclusive single jet production in $pp^\uparrow \rightarrow \text{jet } X$ processes, computed according to (6) and (7) of the text. Only the Sivers effect contributes. The computation is performed adopting the Sivers functions of [20] (SIDIS 1, left panels) and of [21] (SIDIS 2, right panels). The overall statistical uncertainty band, also shown, is obtained following the procedure described in Appendix A of [21].

Notice that we consider here the $pp^\uparrow \rightarrow \ell^+ \ell^- X$ D-Y process in the $p - p^\uparrow$ c.m. frame. For such a process the TSSA is given by [35]

$$\begin{aligned} A_N^{\sin(\phi_\gamma - \phi_S)}(pp^\uparrow \rightarrow \gamma^* X; x_F, M, q_T) \\ = -A_N^{\sin(\phi_\gamma - \phi_S)}(p^\uparrow p \rightarrow \gamma^* X; -x_F, M, q_T). \end{aligned} \quad (21)$$

Our results for the Sivers asymmetry $A_N^{\sin(\phi_\gamma - \phi_S)}$ at AFTER@LHC, obtained following [35], (21) and using the SIDIS extracted Sivers function *reversed in sign*, are shown in Figure 10. Further details can be found in the captions of these figures.

4. Comments and Conclusions

Some final comments and further details might help in understanding the importance of the measurements of the TSSAs at AFTER@LHC:

- (i) Most predictions given show clear asymmetries, sufficiently large as to be easily measurable, given the expected performance of AFTER@LHC [11]. The uncertainty bands reflect the uncertainty in the extraction of the Sivers and transversity functions from SIDIS data, which are focused on small and intermediate x values ($x \leq 0.3$); in fact the bands grow larger at larger values of $|x_F|$.
- (ii) The values of A_N found for pion production can be as large as 10% for π^\pm , while they are smaller for π^0 . They result from the sum of the Sivers and the Collins effects. The relative importance of the two contributions varies according to the kinematical regions and the set of distributions and fragmentation functions adopted. As a tendency, the contribution from the Sivers effect is larger than the Collins contribution with the SIDIS 1-KRE set, while the opposite is true for the SIDIS 2-DSS set.

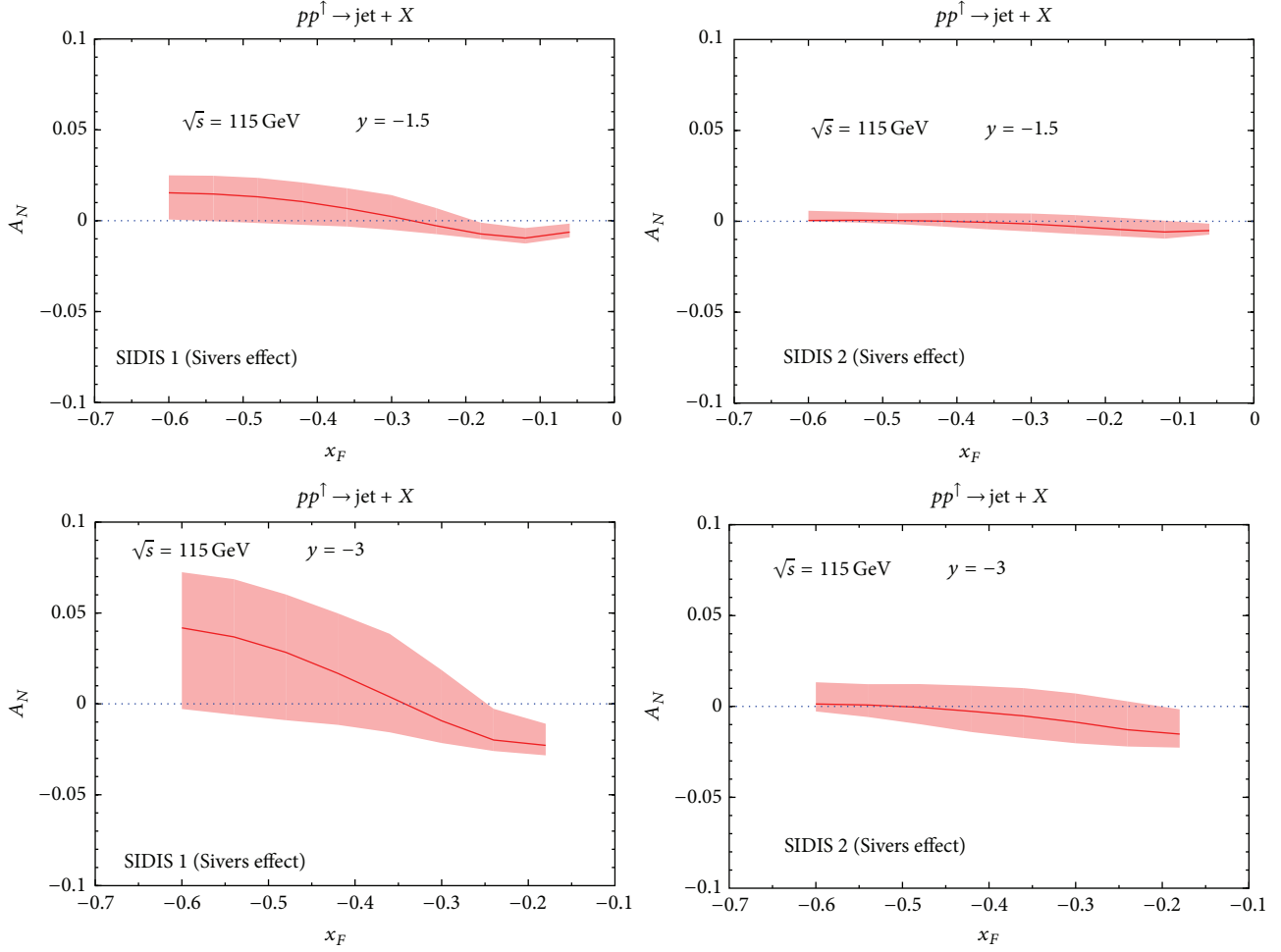


FIGURE 8: Our theoretical estimates for A_N versus x_F at $\sqrt{s} = 115$ GeV, $y = -1.5$ (upper plots), and $y = -3.0$ (lower plots) for inclusive single jet production in $pp^\uparrow \rightarrow \text{jet } X$ processes, computed according to (6) and (7) of the text. Only the Sivers effect contributes. The computation is performed adopting the Sivers functions of [20] (SIDIS 1, left panels) and of [21] (SIDIS 2, right panels). The overall statistical uncertainty band, also shown, is obtained following the procedure described in Appendix A of [21].

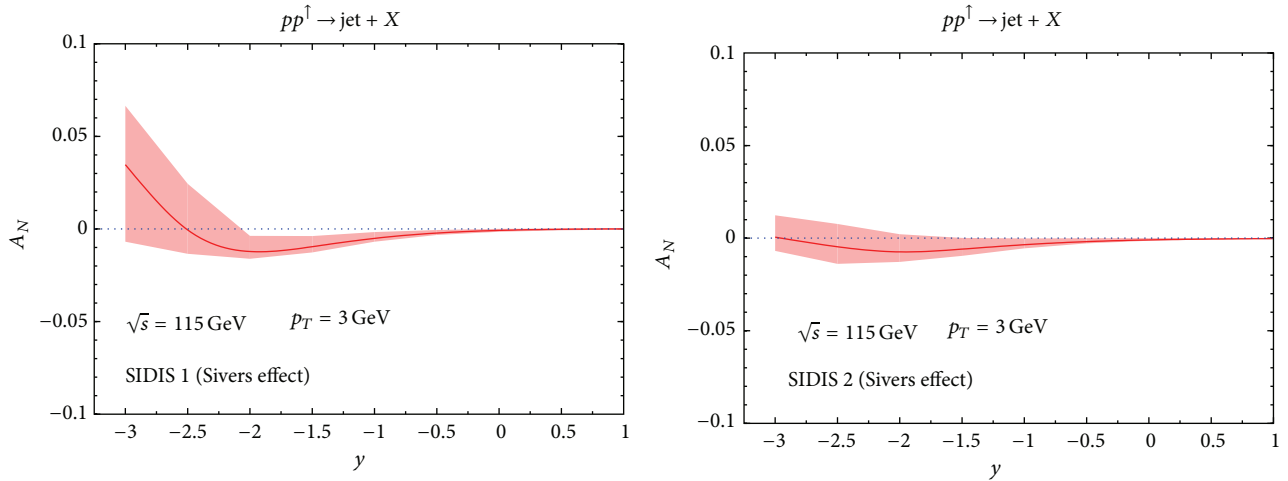


FIGURE 9: Our theoretical estimates for A_N versus y at $\sqrt{s} = 115$ GeV and $p_T = 3$ GeV, for inclusive single jet production in $pp^\uparrow \rightarrow \text{jet } X$ processes, computed according to (6)–(8) of the text. Only the Sivers effect contributes. The computation is performed adopting the Sivers functions of [20] (SIDIS 1, left panel) and of [21] (SIDIS 2, right panel). The overall statistical uncertainty band, also shown, is the envelope of the two independent statistical uncertainty bands obtained following the procedure described in Appendix A of [21].

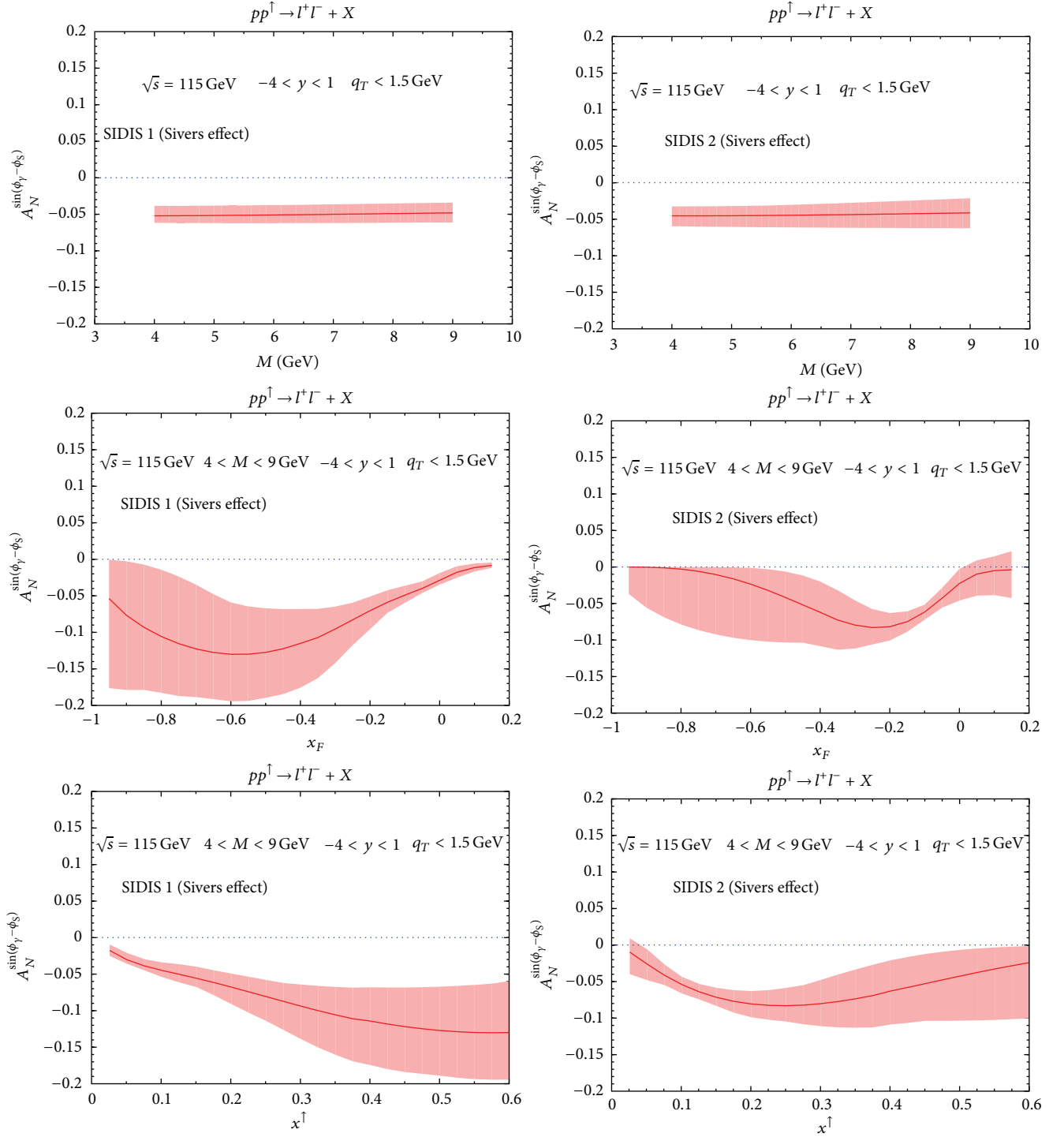


FIGURE 10: Our theoretical estimates for $A_N^{(\phi_\gamma - \phi_S)}$ in D-Y processes as expected at AFTER@LHC. Our results are presented as function of M (upper plots), x_F (middle plots), and x^\uparrow of the quark inside the polarised proton, x^\uparrow (lower plots). The other kinematical variables are either fixed or integrated, as indicated in each figure. They are computed according to [35] and (21), adopting the Sivers functions of [20] (SIDIS 1, left panels) and of [21] (SIDIS 2, right panels), *reversed in sign*. The overall statistical uncertainty band, also shown, is obtained following the procedure described in Appendix A of [21].

The values found here are in agreement, both in sign and qualitative magnitude, with the values found in [10] within the collinear twist-3 (CT-3) approach.

- (iii) The results for single photon production are interesting; they isolate the Sivers effect and our predictions show that they can reach values of about 5%, with a reduced uncertainty band. We find positive values of A_N as the relative weight of the quark charges leads to a dominance of the u quark and the Sivers functions $\Delta^N f_{u/p^\uparrow}$ which is positive [20, 21].

Our results, obtained within the GPM, have a similar magnitude to those obtained in [3, 10], within the CT-3 approach, but have an *opposite sign*. Thus, a measurement of A_N for a single photon production, despite being difficult, would clearly discriminate between the two approaches.

- (iv) The values of A_N for single jet production, which might be interesting as they also have no contribution from the Collins effect, turn out to be very small and compatible with zero, due to a strong cancellation between the u and d quark contributions. The same result is found in [10].
- (v) A measurement of $A_N^{\sin(\phi_\gamma - \phi_S)}$ in D-Y processes at AFTER@LHC is the most interesting one. In such a case the TMD factorisation has been shown to be valid and the Sivers asymmetry should show the expected sign change with respect to SIDIS processes [33, 34]. Our computations, Figure 10, predict a clear asymmetry, which can be as sizeable as 10%, with a definite sign, even within the uncertainty band.

Both the results of [10] and the results of this paper obtain solid non negligible values for the TSSA A_N measurable at the AFTER@LHC experiment. The two sets of results are based on different approaches, respectively, the CT-3 and the GPM factorisation schemes. While the magnitude of A_N is very similar in the two cases, the signs can be different, in particular, the TSSA for a direct photon production, $pp^\uparrow \rightarrow \gamma X$, has opposite signs in the two schemes.

In this paper we have also considered azimuthal asymmetries in polarised D-Y processes, related to the Sivers effect. As explained above, in this case, due to the presence of a large and a small scale, like in SIDIS, the TMD factorisation is valid, with the expectation of an opposite sign of the Sivers function in SIDIS and D-Y processes. Also this prediction can be checked at AFTER@LHC.

Conflict of Interests

The authors declare that there is no conflict of interests regarding the publication of this paper.

Acknowledgments

M. Anselmino and S. Melis acknowledge support from the “Progetto di Ricerca di Ateneo/CSP” (code TO-Call3-2012-0103). U. D'Alesio is grateful to the Department of Theoretical

Physics II of the Universidad Complutense of Madrid for the kind hospitality extended to him during the completion of this work.

References

- [1] M. Anselmino, M. Boglione, U. D'Alesio et al., “Role of Collins effect in the single spin asymmetry A_N in $p^\uparrow p \rightarrow hX$ processes,” *Physical Review D*, vol. 86, Article ID 074032, 2012.
- [2] M. Anselmino, M. Boglione, U. D'Alesio, S. Melis, F. Murgia, and A. Prokudin, “Sivers effect and the single spin asymmetry A_N in $p^\uparrow p \rightarrow hX$ processes,” *Physical Review D*, vol. 88, no. 5, Article ID 054023, 12 pages, 2013.
- [3] K. Kanazawa, Y. Koike, A. Metz, and D. Pitonyak, “Transverse single-spin asymmetries in $p^\uparrow p \rightarrow \gamma X$ from quark-gluon-quark correlations in the proton,” *Physical Review D*, vol. 91, Article ID 014013, 2015.
- [4] K. Kanazawa, Y. Koike, A. Metz, and D. Pitonyak, “Towards an explanation of transverse single-spin asymmetries in proton-proton collisions: the role of fragmentation in collinear factorization,” *Physical Review D*, vol. 89, no. 11, Article ID 111501, 5 pages, 2014.
- [5] J.-W. Qiu and G. F. Sterman, “Single transverse spin asymmetries in direct photon production,” *Nuclear Physics B*, vol. 378, no. 1-2, pp. 52–78, 1992.
- [6] J.-W. Qiu and G. F. Sterman, “Single transverse-spin asymmetries in hadronic pion production,” *Physical Review D*, vol. 59, Article ID 014004, 1999.
- [7] C. Kouvaris, J.-W. Qiu, W. Vogelsang, and F. Yuan, “Single transverse-spin asymmetry in high transverse momentum pion production in pp collisions,” *Physical Review D*, vol. 74, no. 11, Article ID 114013, 15 pages, 2006.
- [8] X. Ji, J.-W. Qiu, W. Vogelsang, and F. Yuan, “Single transverse-spin asymmetry in Drell-Yan production at large and moderate transverse momentum,” *Physical Review D*, vol. 73, Article ID 094017, 2006.
- [9] U. D'Alesio and F. Murgia, “Azimuthal and single spin asymmetries in hard scattering processes,” *Progress in Particle and Nuclear Physics*, vol. 61, no. 2, pp. 394–454, 2008.
- [10] K. Kanazawa, Y. Koike, A. Metz, and D. Pitonyak, “Transverse single-spin asymmetries in proton-proton collisions at the AFTER@LHC experiment,” <http://arxiv.org/abs/1502.04021>.
- [11] S. J. Brodsky, F. Fleuret, C. Hadjidakis, and J. P. Lansberg, “Physics opportunities of a fixed-target experiment using LHC beams,” *Physics Reports*, vol. 522, no. 4, pp. 239–255, 2013.
- [12] L. Massacrier, M. Anselmino, R. Arnaldi et al., “Studies of transverse-momentum-dependent distributions with a fixed-target experiment using the LHC beams (AFTER@LHC),” <http://arxiv.org/abs/1502.00984>.
- [13] D. W. Sivers, “Single-spin production asymmetries from the hard scattering of pointlike constituents,” *Physical Review D*, vol. 41, pp. 83–90, 1990.
- [14] D. W. Sivers, “Hard-scattering scaling laws for single-spin production asymmetries,” *Physical Review D*, vol. 43, no. 1, pp. 261–263, 1991.
- [15] J. C. Collins, “Fragmentation of transversely polarized quarks probed in transverse momentum distributions,” *Nuclear Physics B*, vol. 396, no. 1, pp. 161–182, 1993.
- [16] M. Anselmino, M. Boglione, U. D'Alesio, E. Leader, S. Melis, and F. Murgia, “General partonic structure for hadronic spin

- asymmetries,” *Physical Review D*, vol. 73, Article ID 014020, 2006.
- [17] P. J. Mulders and R. D. Tangerman, “The complete tree-level result up to order $1/Q$ for polarized deep-inelastic lepton production,” *Nuclear Physics B*, vol. 461, no. 1-2, pp. 197–237, 1996.
 - [18] A. Bacchetta, U. D’Alesio, M. Diehl, and C. A. Miller, “Single-spin asymmetries: the Trento conventions,” *Physical Review D*, vol. 70, no. 11, Article ID 117504, 2004.
 - [19] M. Anselmino, M. Boglione, U. D’Alesio, E. Leader, and F. Murgia, “Parton intrinsic motion: suppression of the Collins mechanism for transverse single spin asymmetries in $p^\uparrow p \rightarrow \pi X$,” *Physical Review D*, vol. 71, Article ID 014002, 2005.
 - [20] M. Anselmino, M. Boglione, U. D’Alesio, A. Kotzinian, F. Murgia, and A. Prokudin, “Extracting the Sivers function from polarized semi-inclusive deep inelastic scattering data and making predictions,” *Physical Review D*, vol. 72, no. 9, Article ID 094007, 9 pages, 2005.
 - [21] M. Anselmino, M. Boglione, U. D’Alesio et al., “Sivers effect for pion and kaon production in semi-inclusive deep inelastic scattering,” *The European Physical Journal A*, vol. 39, no. 1, pp. 89–100, 2009.
 - [22] M. Anselmino, M. Boglione, U. D’Alesio et al., “Transversity and Collins functions from SIDIS and e^+e^- data,” *Physical Review D*, vol. 75, Article ID 054032, 2007.
 - [23] M. Anselmino, M. Boglione, U. D’Alesio et al., “Update on transversity and Collins functions from SIDIS and e^+e^- data,” *Nuclear Physics B—Proceedings Supplements*, vol. 191, pp. 98–107, 2009.
 - [24] M. Anselmino, U. D’Alesio, S. Melis, and F. Murgia, “Constraints on the gluon Sivers distribution via transverse single spin asymmetries at midrapidity in $p^\uparrow p \rightarrow \pi^0 X$ processes at BNL RHIC,” *Physical Review D*, vol. 74, no. 9, Article ID 094011, 7 pages, 2006.
 - [25] M. Gluck, E. Reya, and A. Vogt, “Dynamical parton distributions revisited,” *The European Physical Journal C*, vol. 5, no. 3, pp. 461–470, 1998.
 - [26] D. de Florian, R. Sassot, and M. Stratmann, “Global analysis of fragmentation functions for pions and kaons and their uncertainties,” *Physical Review D*, vol. 75, Article ID 114010, 2007.
 - [27] S. Kretzer, “Fragmentation functions from flavor-inclusive and flavor-tagged e^+e^- annihilations,” *Physical Review D*, vol. 62, Article ID 054001, 2000.
 - [28] U. D’Alesio and F. Murgia, “Parton intrinsic motion in inclusive particle production: unpolarized cross sections, single spin asymmetries, and the Sivers effect,” *Physical Review D*, vol. 70, no. 7, Article ID 074009, 22 pages, 2004.
 - [29] J. C. Collins, D. E. Soper, and G. F. Sterman, “Transverse momentum distribution in Drell-Yan pair and W and Z boson production,” *Nuclear Physics B*, vol. 250, no. 1–4, pp. 199–224, 1985.
 - [30] X.-D. Ji, J.-P. Ma, and F. Yuan, “QCD factorization for spin-dependent cross sections in DIS and Drell-Yan processes at low transverse momentum,” *Physics Letters B*, vol. 597, no. 3–4, pp. 299–308, 2004.
 - [31] J. Collins, *Foundations of Perturbative QCD*, vol. 32 of *Cambridge Monographs on Particle Physics, Nuclear Physics and Cosmology*, Cambridge University Press, Cambridge, UK, 2011.
 - [32] M. G. Echevarria, A. Idilbi, and I. Scimemi, “Factorization theorem for Drell-Yan at low q_T and transverse-momentum distributions on-the-light-cone,” *Journal of High Energy Physics*, vol. 2012, article 2, 2012.
 - [33] S. J. Brodsky, D. S. Hwang, and I. Schmidt, “Final-state interactions and single-spin asymmetries in semi-inclusive deep inelastic scattering,” *Physics Letters B*, vol. 530, no. 1–4, pp. 99–107, 2002.
 - [34] J. C. Collins, “Leading-twist single-transverse-spin asymmetries: Drell-Yan and deep-inelastic scattering,” *Physics Letters B*, vol. 536, no. 1–2, pp. 43–48, 2002.
 - [35] M. Anselmino, M. Boglione, U. D’Alesio, S. Melis, F. Murgia, and A. Prokudin, “Sivers effect in Drell-Yan processes,” *Physical Review D*, vol. 79, Article ID 054010, 2009.

Research Article

Transverse Single-Spin Asymmetries in Proton-Proton Collisions at the AFTER@LHC Experiment

K. Kanazawa,¹ Y. Koike,² A. Metz,¹ and D. Pitonyak³

¹Department of Physics, SERC, Temple University, Philadelphia, PA 19122, USA

²Department of Physics, Niigata University, Ikarashi, Niigata 950-2181, Japan

³RIKEN BNL Research Center, Brookhaven National Laboratory, Upton, NY 11973, USA

Correspondence should be addressed to D. Pitonyak; dpitonyak@quark.phy.bnl.gov

Received 9 March 2015; Accepted 24 April 2015

Academic Editor: Jean-Philippe Lansberg

Copyright © 2015 K. Kanazawa et al. This is an open access article distributed under the Creative Commons Attribution License, which permits unrestricted use, distribution, and reproduction in any medium, provided the original work is properly cited. The publication of this article was funded by SCOAP³.

We present results for transverse single-spin asymmetries in proton-proton collisions at kinematics relevant for AFTER, a proposed fixed-target experiment at the Large Hadron Collider. These include predictions for pion, jet, and direct photon production from analytical formulas already available in the literature. We also discuss specific measurements that will benefit from the higher luminosity of AFTER, which could help resolve an almost 40-year puzzle of what causes transverse single-spin asymmetries in proton-proton collisions.

1. Introduction

Transverse single-spin asymmetries (TSSAs), denoted by A_N , have been a fundamental observable since the mid-1970s to test perturbative quantum chromodynamics (pQCD). Such measurements were first conducted at FermiLab, where large effects were found in $pBe \rightarrow \Lambda^+ X$ [1]. These results contradicted the naïve collinear parton model, which said that A_N should be extremely small [2], and doubts were raised as to whether pQCD can actually describe these reactions [2]. However, in the 1980s it was shown that if one went beyond the parton model and included collinear twist-3 (CT3) quark-gluon-quark correlations in the nucleon, substantial TSSAs could be generated [3, 4]. In the 1990s this CT3 approach was worked out in more detail for proton-proton collisions, first for direct photon production [5–7] and then for pion production [8]. Over the last decade, several other analyses furthered the development of this formalism; see [9–19] and references therein. During the same time, another mechanism was also put forth to explain TSSAs in proton-proton collisions. This approach involves the Sivers [20, 21], Collins [22], and Boer-Mulders [23, 24] transverse momentum dependent (TMD) functions and became known as the Generalized Parton Model (GPM); see [25–29]

and references therein. (We mention that since most likely a rigorous factorization formula involving TMD functions does not hold for single-inclusive processes (which have only one scale), the GPM can only be considered a phenomenological model.) In addition to all of this theoretical work, many experimental measurements of A_N have been performed at proton-(anti)proton accelerators [30–42]. Most of the experimental data in the more negative x_F region has come in the form of light-hadron asymmetries A_N^h , for example, $h = \pi, K, \eta$, with the exception of the jet asymmetry A_N^{jet} measured a few years ago at the Relativistic Heavy Ion Collider (RHIC) by the A_N DY Collaboration [40]. (Throughout the paper we will use the convention $x_F = 2l_z/\sqrt{s}$, where l is the momentum of the outgoing particle, and the transversely polarized proton moves along the $-z$ -axis. That is, $x_F \rightarrow -1$ means large momentum fractions x^\uparrow of the parton probed inside the transversely polarized proton. This setup causes x_F to be opposite in sign to the one used in collider experiments (like those at RHIC).) Plans are also in place to measure the direct photon asymmetry A_N^γ at RHIC by both the PHENIX Collaboration and the STAR Collaboration [43–45].

Although much progress has been made in understanding TSSAs, there is not a definitive answer on what their

origin might be. In the CT3 approach it was assumed for many years that a soft-gluon pole (SGP) chiral-even quark-gluon-quark (qgq) matrix element called the Qiu-Sterman (QS) function $T_F(x, x)$ was the main cause of A_N^π [8, 11]. However, this led to a so-called “sign-mismatch” between the QS function and the TMD Sivvers function f_{1T}^\perp extracted from semi-inclusive deep-inelastic scattering (SIDIS) [46]. This issue could not be resolved through more flexible parameterizations of the Sivvers function [47]. Moreover, the authors of [48] argued, by looking at A_N data on the target TSSA in inclusive DIS [49, 50], that $T_F(x, x)$ cannot be the main source of A_N^π . This observation led us last year in [51] to analyze A_N^π by including not only the QS function but also the fragmentation mechanism, whose analytical formula was first fully derived in [18] (the so-called “derivative term” was first computed in [52]) (see also [17, 53, 54] for fragmentation terms in other processes). We found in this situation for the first time in pQCD that one can fit all RHIC high transverse momentum pion data very well without any sign-mismatch issue. Furthermore, we showed that a simultaneous description of TSSAs in $p^\dagger p \rightarrow \pi X$, SIDIS, and $e^+e^- \rightarrow h_1 h_2 X$ is possible. Nevertheless, more work must be done to confirm/refute this explanation and its predictions. We mention that, in the GPM, one cannot draw a definitive conclusion as to whether the Sivvers or Collins mechanism is the main cause of A_N^π [28, 29]. (In principle the Boer-Mulders function and gluon Sivvers function can also contribute to the GPM formalism, but these pieces have not been analyzed in the literature.) This is due to the theoretical error bands being too large, since the associated TMD functions are mostly unconstrained in the large- x^\dagger regime covered by the data [28, 29]. For a detailed discussion of the GPM formalism and its predictions for the AFTER experiment, see [55].

In addition, in order to have a complete knowledge of TSSAs, it is important to have a “clean” extraction of the QS function from observables like A_N^{jet} and A_N^γ that do not have any fragmentation contributions. (We will ignore photons coming from fragmentation [56], which can be largely suppressed by using isolation cuts.) (For recent analyses of A_N^γ in $p^\dagger A$ collisions, see [57, 58].) This is necessary in order to help resolve the sign-mismatch issue and better understand the role of rescattering effects in the nucleon. The jet asymmetry has been studied in [11, 46, 59, 60] and the direct photon asymmetry has been investigated in [6, 11, 12, 56, 59–64]. It is important to point out that other contributions to A_N^{jet} and A_N^γ exist besides the one from the (SGP qgq chiral-even) QS function. These other pieces include (i) soft-fermion pole (SFP) chiral-even qgq functions, (ii) SGP and SFP qgq chiral-odd functions, and (iii) SGP trigluon functions. For A_N^γ the numerical analyses in [59, 64] show that (i) is negligible for $x_F < 0$ while the study in [64] draws a similar conclusion for (ii) as does the work in [62] for (iii). That is, for A_N^γ , the QS function dominates the asymmetry. We mention that, at present in the GPM, A_N^γ is predicted to have the *opposite sign* to that from the CT3 approach [29]. Therefore, as was emphasized in [64], this observable could allow us for the first time to clearly distinguish between the two frameworks as well as learn about the process dependence of the Sivvers

function [65], which is a feature of this nonperturbative object that is crucial to our current understanding of TMD functions.

For A_N^{jet} the conclusions as to which piece dominates are not as clear. The study in [66, 67] provides evidence that (ii) should be small in the whole x_F -region. The work in [59] shows that the same is most likely true for (i) but that analysis suffers from the sign-mismatch issue. Also, in [19] there is an indication that (iii) could be significant. Therefore, it will be necessary to reassess the impact of (i) and (iii) on A_N^{jet} . Nevertheless, one can gain insight into these other terms by looking at the contribution from the QS function and comparing it with data.

Given the open issues that still remain, it is an opportune time for the Large Hadron Collider (LHC) to produce data on TSSAs in proton-proton collisions via the AFTER experiment. These measurements will not only add to the data from FermiLab, AGS, and RHIC but also, through the high luminosity of the experiment [68, 69], probe certain features that remain ambiguous. For example, the behavior of A_N^π at large pion transverse momentum l_T appears to fall off very slowly (or is even flat), a feature which the theory says should persist to high l_T [29, 51, 55, 59] (see also [70] in the context of Λ^\dagger production). However, the data from RHIC [71] has too large error bars (or not enough statistics) in this high- l_T region to ascertain whether or not this is true. Also, A_N^{jet} measured by $A_N \text{DY}$ [40] has large error bars as x_F becomes more negative, which makes it difficult to determine whether or not the QS function alone can describe that data. Moreover, as previously mentioned, A_N^γ has never been measured before, yet it could be a tremendous opportunity to learn about the process dependence of the Sivvers function and distinguish between the CT3 and GPM frameworks. Already, PHENIX and STAR plan to carry out such experiments [43–45].

Therefore, in this paper we give predictions within the CT3 formalism for A_N^π , A_N^{jet} , and A_N^γ at AFTER@LHC kinematics. (For related work on charmonium and bottomonium production we refer to [72, 73].) Since the relevant analytical formulas already exist within the literature, in Section 2 we focus on the phenomenology and refer the reader to the appropriate papers on the underlying theory. These numerical results are summarized in Section 3, and there we highlight again how AFTER can offer unique insight into TSSAs in proton-proton collisions, which is a truly fundamental observable to test pQCD at higher twist.

2. Pion, Photon, and Jet TSSAs at AFTER

We start first with A_N^π , where we follow our numerical work in [51]. (We also refer the reader to [11, 13, 18] for more formal discussions of the relevant analytical formulas.) There we took into account the contribution from the QS function and the fragmentation term. The former has a model-independent relation to the Sivvers function [74], while the latter involves three nonperturbative CT3 fragmentation functions (FFs): \hat{H} , $\hat{H}_{FU}^\mathfrak{S}$, and H . Of these, \hat{H} has a model-independent connection to the Collins function [18, 52]

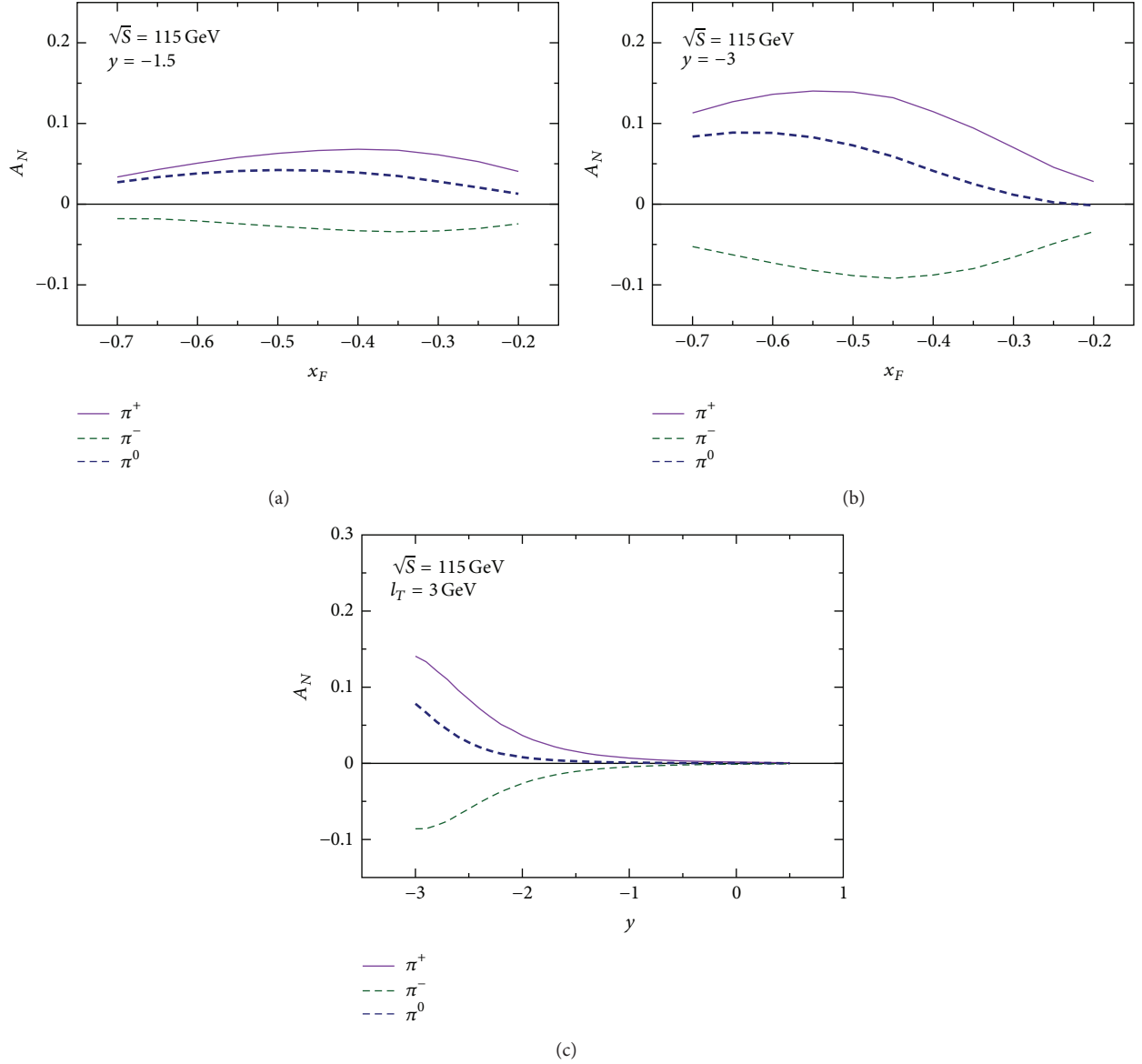


FIGURE 1: A_N^π versus x_F at fixed $y = -1.5$ (a) and $y = -3$ (b) and A_N^π versus y at fixed $l_T = 3$ GeV (c). All plots are at $\sqrt{S} = 115$ GeV for pion production at AFTER.

and H can be written in terms of the other two through a QCD equation-of-motion relation [18]. In Figures 1 and 2 we provide predictions for neutral and charged pion production at AFTER based on our fit in [51]. One sees in Figure 1 from A_N^π versus x_F that the magnitude of the asymmetry can be anywhere from ~ 5 –10% and from A_N^π versus y that it increases with more negative (center-of-mass) rapidity y . (Recall the relation between x_F , y , and l_T : $x_F = 2 l_T \sinh(y) / \sqrt{S}$, so A_N versus x_F (A_N versus y) at fixed y (l_T) implies a running in l_T (x_F).) One also notices that A_N^π turns over at more negative x_F values, which was also observed in some of the STAR data [33, 34, 39]. In Figure 2, where we show A_N^π versus l_T , one sees that the asymmetry is flat or falls off very slowly as l_T increases, a feature that had also been measured by STAR [71]. It will be important to establish with

more precision if this flatness persists at higher- l_T values, say 12–15 GeV, and AFTER, with its much higher luminosity, will be in a position to make such a measurement.

We next look at A_N^{jet} and A_N^γ , which do not receive contributions from FFs. As we discussed in Section 1, the former may receive nonnegligible contributions from terms other than the QS function, while for the latter we recently showed in [64] that the QS function is the dominant piece to that asymmetry. (All of the analytical expressions for A_N^γ can be found in [64] while those for A_N^{jet} are determined simply by setting $D_1(z)$ (the unpolarized FF) to $\delta(1-z)$ in the equations for A_N^π given in [11, 14, 19, 66, 67].) (We note the A_N^γ analytical formulas for the piece involving chiral-odd functions are new from [64], while those involving chiral-even functions were derived before in the literature, and the relevant references are

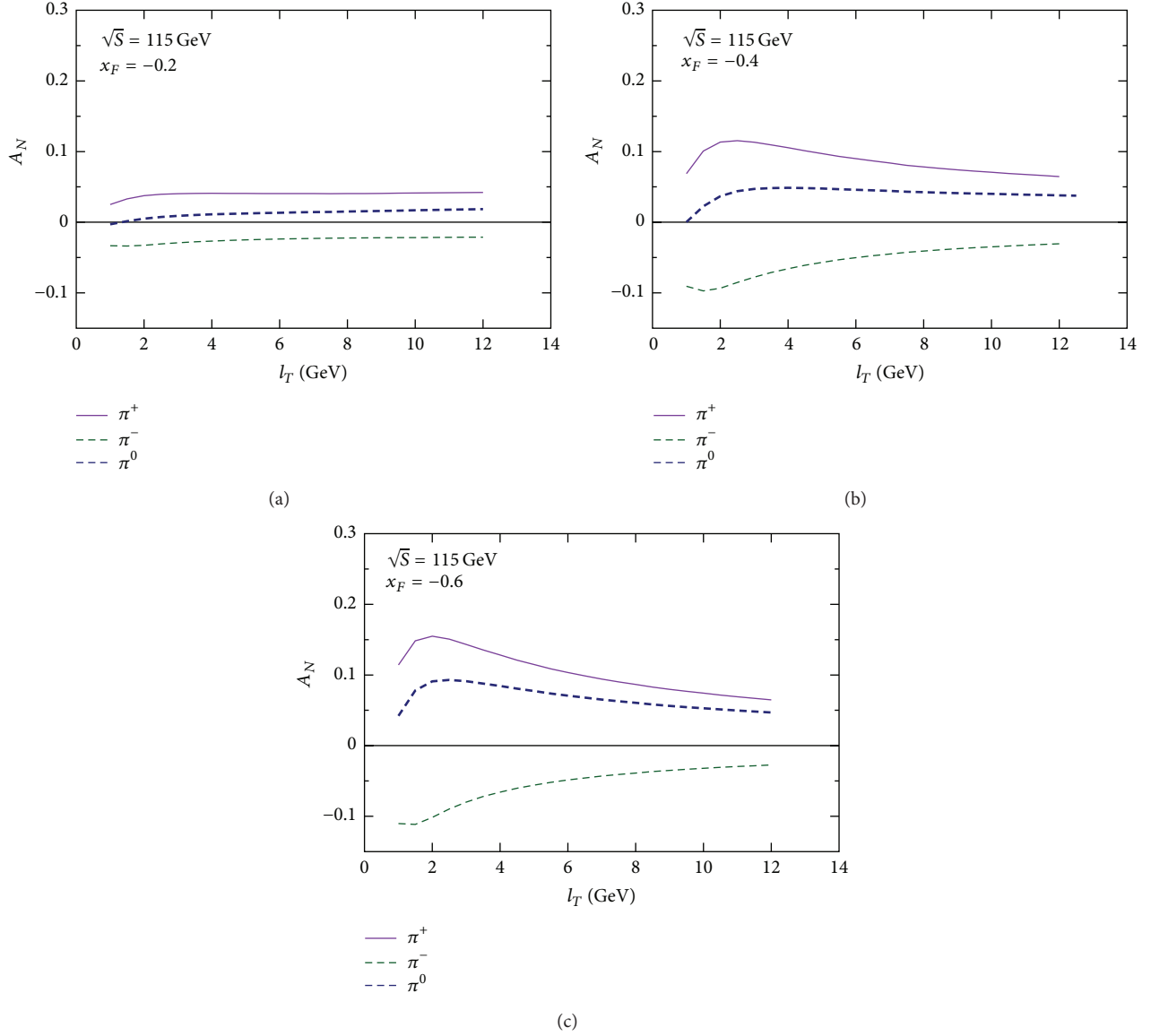


FIGURE 2: A_N^π versus l_T at fixed $x_F = -0.2$ (a), $x_F = -0.4$ (b), and $x_F = -0.6$ (c) at $\sqrt{s} = 115$ GeV for pion production at AFTER.

cited therein.) However, given that the other pieces for A_N^{jet} are not reliably known, for that asymmetry we will only look at the contribution from the QS function using its relation to the Siverts function, while for A_N^γ we adopt our work in [64]. In Figures 3 and 4 we show results for jet and photon production at AFTER. We see that A_N^{jet} is very small, although we caution the reader that the Siverts function (which we use as input for the QS function) is mostly unconstrained in the large- x^\uparrow region, and when this uncertainty is taken into account, one could obtain a measurable asymmetry [60]. Also, as we mentioned, there is the potential for (chiral-even) SFP and/or trigluon functions to make an impact. Therefore, in order to determine if the Siverts function alone can describe A_N^{jet} , along with the current data from A_N^{DY} , we need more precise data in the far backward region, which should be

possible at AFTER. (We note that STAR has preliminary data on electromagnetic “jets” that could also be helpful [75].)

Unlike the jet asymmetry, A_N^γ could be on the order of $\sim -5\%$ at less negative x_F and more negative y (see Figures 3(a) and 3(b)) or smaller l_T and less negative x_F (see Figure 4). Both of these observations are consistent with the behavior of A_N^γ as a function of rapidity (see Figure 3(c)), where the asymmetry peaks at $y \sim -2$ (with $l_T = 3$ GeV), which corresponds to $x_F \sim -0.2$. Since the QS function is the dominant source of the asymmetry, we can have “clean” access to it. We state again that the GPM framework at present predicts A_N^γ to be *positive* [29]. Therefore, a clear nonzero signal for this observable would help to distinguish between the CT3 and GPM formalisms. However, we emphasize that should data contradict the predictions of the GPM, this does not invalidate the results obtained for TMD observables that

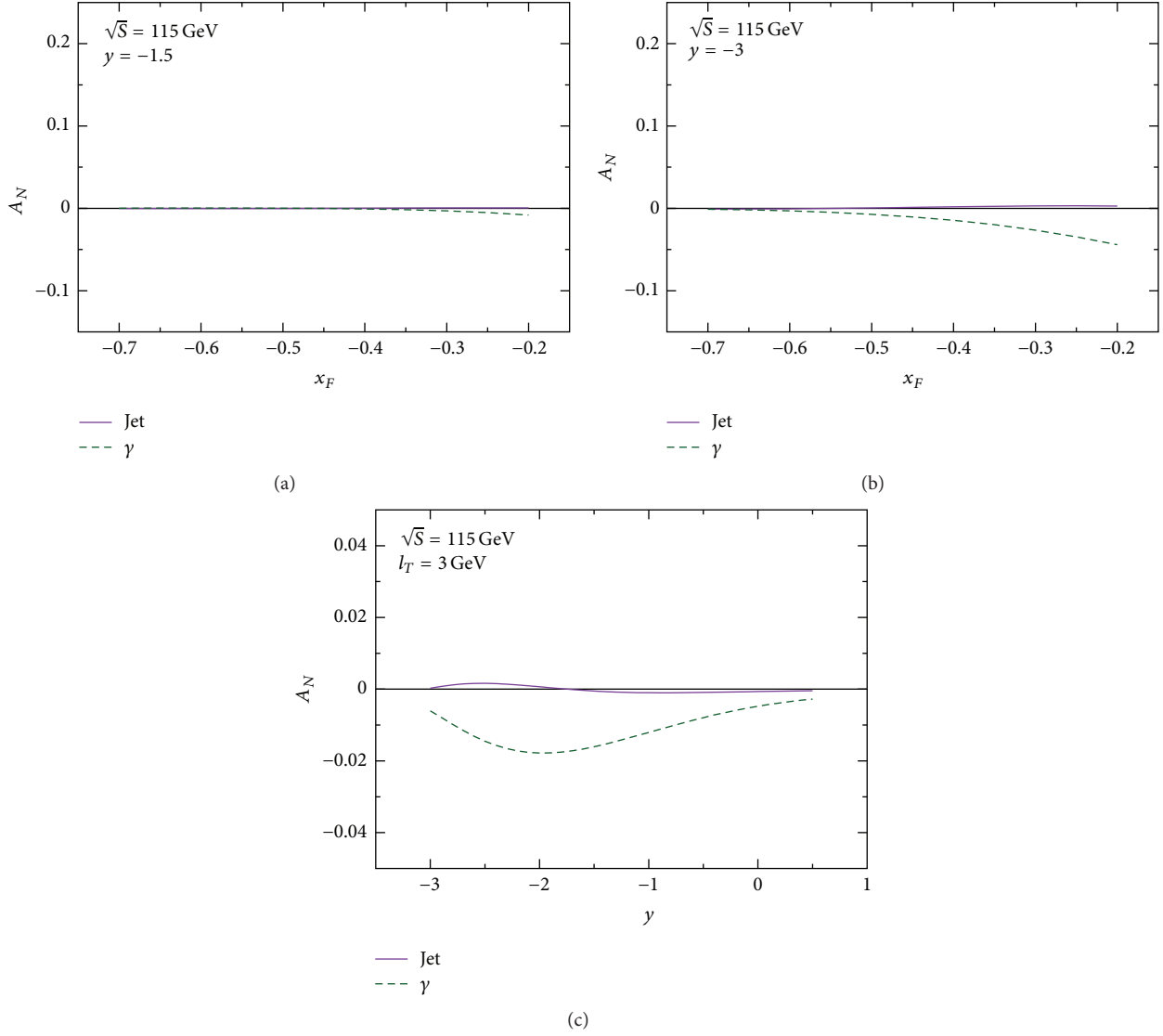


FIGURE 3: A_N versus x_F at fixed $y = -1.5$ (a) and $y = -3$ (b) and A_N versus y at fixed $l_T = 3$ GeV (c). All plots are at $\sqrt{S} = 115$ GeV for jet/photon production at AFTER.

are based on rigorous TMD factorization proofs. Also, since we use the Siverts function from SIDIS as our input for the QS function, we can learn about the predicted process dependence of the Siverts function.

3. Summary and Outlook

In this paper we have discussed TSSAs in single-inclusive pion, jet, and photon production from proton-proton collisions, that is, $p^\dagger p \rightarrow \{\pi, \text{jet}, \gamma\} X$, at kinematics relevant for the proposed AFTER@LHC experiment. These asymmetries have been fundamental observables to test pQCD at higher twist for close to 40 years, and much work has been performed on both the theoretical and experimental sides. Nevertheless, issues still remain as to the origin of these TSSAs, which makes a measurement of A_N at the LHC via the AFTER experiment timely. For A_N^{π} we have found

that AFTER should expect (absolute) asymmetries on the order of 5–10% as a function of x_F and increasing as the rapidity becomes more negative. Also, the l_T dependence of A_N^{π} still falls off slowly and flattens out at high l_T . For A_N^{jet} we predict a very small asymmetry, but we must remember that uncertainties in the Siverts function could allow for a measurable observable [60] and also that other contributions (like chiral-even SFP and trigluon) could make an impact. Lastly, for A_N^{γ} we expect asymmetries on the order of $\sim -5\%$ and decreasing with more negative x_F and increasing l_T . These are opposite in sign to the ones predicted from the GPM [29].

Even though these observables have been (or are planned to be) measured at RHIC, AFTER has the ability, through its much higher luminosity, to not only supplement the RHIC data but also provide important information on still unknown issues. For example, it will be key to determine

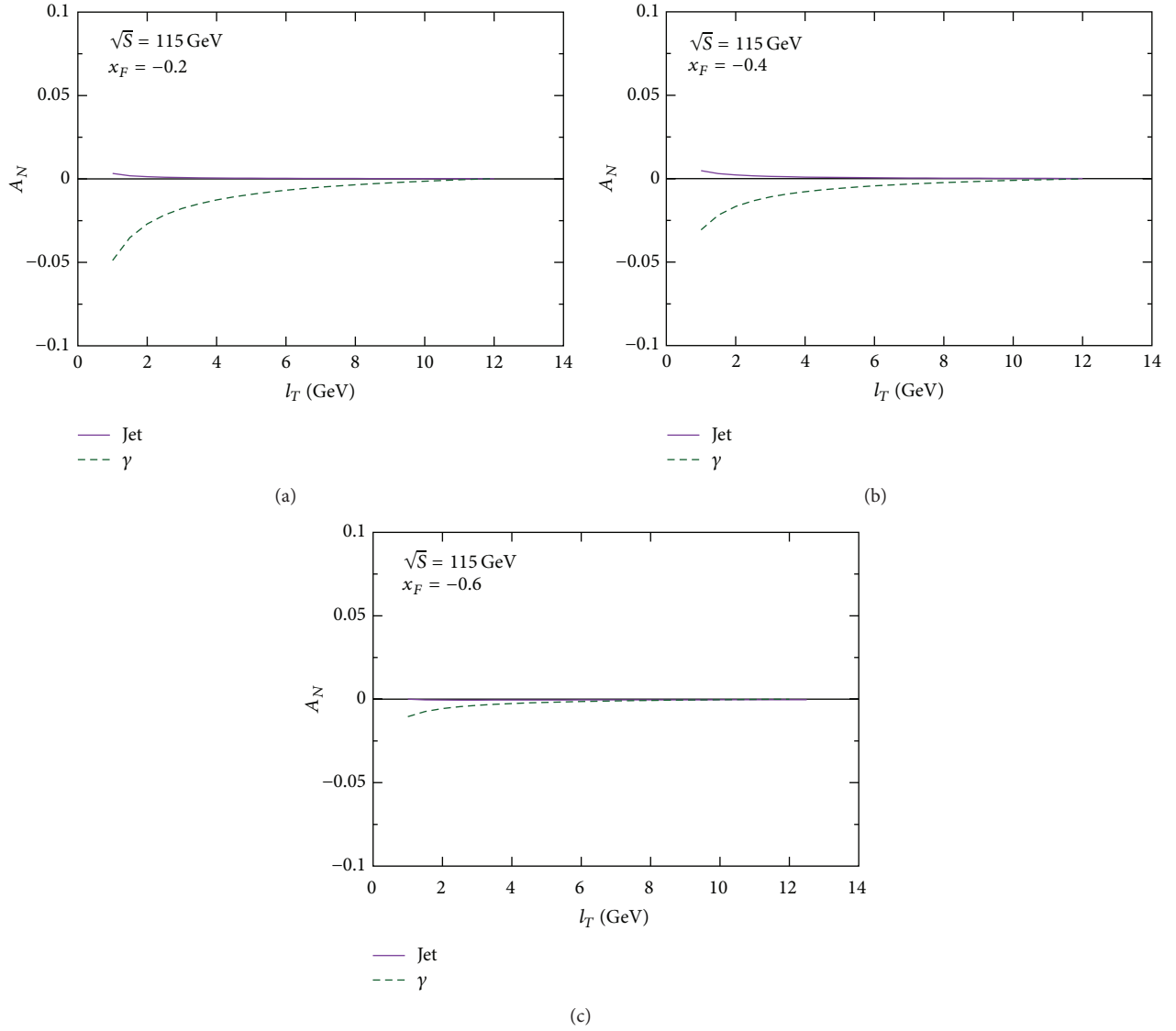


FIGURE 4: A_N versus l_T at fixed $x_F = -0.2$ (a), $x_F = -0.4$ (b), and $x_F = -0.6$ (c) at $\sqrt{S} = 115$ GeV for jet/photon production at AFTER.

if A_N^π stays flat at higher- l_T , say to 12–15 GeV, like theory predicts [29, 51, 55, 59, 70] and STAR has evidence for [71]. Also, higher statistics should allow for more precise measurements of A_N^{jet} at more negative x_F , which will be necessary to determine if the QS function is the sole source of that asymmetry. Moreover, A_N^γ has never been measured before and provides the opportunity to clearly distinguish between the CT3 and GPM frameworks and learn about the process dependence of the Siverson function. Given the questions that remain as to the origin of TSSAs, which has been unresolved for almost 40 years, AFTER could provide valuable data on these observables.

Conflict of Interests

The authors declare that there is no conflict of interests regarding the publication of this paper.

Acknowledgments

This work has been supported by the Grant-in-Aid for Scientific Research from the Japanese Society of Promotion of Science under Contract no. 26287040 (Y. Koike), the National Science Foundation under Contract no. PHY-1205942 (K. Kanazawa and A. Metz), and the RIKEN BNL Research Center (D. Pitonyak).

References

- [1] G. Bunce, R. Handler, R. March et al., “ Λ^0 hyperon polarization in inclusive production by 300-gev protons on beryllium,” *Physical Review Letters*, vol. 36, no. 19, pp. 1113–1116, 1976.
- [2] G. L. Kane, J. Pumplin, and W. Repko, “Transverse quark polarization in large- p_T reactions, e^+e^- jets, and lepton production: a test of quantum chromodynamics,” *Physical Review Letters*, vol. 41, p. 1689, 1978.

- [3] A. V. Efremov and O. V. Teryaev, "On spin effects in quantum chromodynamics," *Soviet Journal of Nuclear Physics*, vol. 36, p. 140, 1982, English translation to *Yadernaya fizika*, vol. 36, p. 242, 1982.
- [4] A. V. Efremov and O. V. Teryaev, "QCD asymmetry and polarized hadron structure function measurement," *Physics Letters B*, vol. 150, no. 5, pp. 383–386, 1985.
- [5] J.-W. Qiu and G. F. Sterman, "Single transverse spin asymmetries," *Physical Review Letters*, vol. 67, no. 17, pp. 2264–2267, 1991.
- [6] J.-W. Qiu and G. F. Sterman, "Single transverse spin asymmetries in direct photon production," *Nuclear Physics B*, vol. 378, pp. 52–78, 1992.
- [7] V. M. Korotkiyan and O. V. Teryaev, "Compton twist-three subprocesses for pp single spin asymmetries," *Physical Review D*, vol. 52, no. 9, pp. R4775–R4779, 1995.
- [8] J.-W. Qiu and G. F. Sterman, "Single transverse-spin asymmetries in hadronic pion production," *Physical Review D*, vol. 59, Article ID 014004, 1999.
- [9] H. Eguchi, Y. Koike, and K. Tanaka, "Single transverse spin asymmetry for large- p_T pion production in semi-inclusive deep inelastic scattering," *Nuclear Physics B*, vol. 752, no. 1-2, pp. 1–17, 2006.
- [10] H. Eguchi, Y. Koike, and K. Tanaka, "Twist-3 formalism for single transverse spin asymmetry reexamined: semi-inclusive deep inelastic scattering," *Nuclear Physics B*, vol. 763, no. 1-2, pp. 198–227, 2007.
- [11] C. Kouvaris, J. W. Qiu, W. Vogelsang, and F. Yuan, "Single transverse-spin asymmetry in high transverse momentum pion production in pp collisions," *Physical Review D*, vol. 74, Article ID 114013, 2006.
- [12] Y. Koike and K. Tanaka, "Master formula for twist-3 soft-gluon-pole mechanism to single transverse-spin asymmetry," *Physics Letters B*, vol. 646, no. 5-6, pp. 232–241, 2007, Erratum in: *Physics Letters B*, vol. 668, no. 5, pp. 458–459, 2008.
- [13] Y. Koike and K. Tanaka, "Universal structure of twist-3 soft-gluon-pole cross sections for single transverse-spin asymmetry," *Physical Review D*, vol. 76, no. 1, Article ID 011502(R), 5 pages, 2007.
- [14] Y. Koike and T. Tomita, "Soft-fermion-pole contribution to single-spin asymmetry for pion production in pp collisions," *Physics Letters B*, vol. 675, no. 2, pp. 181–189, 2009.
- [15] K. Kanazawa and Y. Koike, "New analysis of the single transverse-spin asymmetry for hadron production at RHIC," *Physical Review D*, vol. 82, Article ID 034009, 2010.
- [16] K. Kanazawa and Y. Koike, "A phenomenological study of single transverse-spin asymmetry for inclusive light-hadron productions at RHIC," *Physical Review D*, vol. 83, no. 11, Article ID 114024, 8 pages, 2011.
- [17] K. Kanazawa and Y. Koike, "Contribution of the twist-3 fragmentation function to the single transverse-spin asymmetry in semi-inclusive deep inelastic scattering," *Physical Review D*, vol. 88, no. 7, Article ID 074022, 15 pages, 2013.
- [18] A. Metz and D. Pitonyak, "Fragmentation contribution to the transverse single-spin asymmetry in proton-proton collisions," *Physics Letters B*, vol. 723, no. 4-5, pp. 365–370, 2013.
- [19] H. Beppu, K. Kanazawa, Y. Koike, and S. Yoshida, "Three-gluon contribution to the single spin asymmetry for light hadron production in pp collision," *Physical Review D*, vol. 89, Article ID 034029, 2014.
- [20] D. W. Sivers, "Single-spin production asymmetries from the hard scattering of pointlike constituents," *Physical Review D*, vol. 41, no. 1, pp. 83–90, 1990.
- [21] D. Sivers, "Hard-scattering scaling laws for single-spin production asymmetries," *Physical Review D*, vol. 43, no. 1, pp. 261–263, 1991.
- [22] J. Collins, "Fragmentation of transversely polarized quarks probed in transverse momentum distributions," *Nuclear Physics B*, vol. 396, no. 1, pp. 161–182, 1993.
- [23] D. Boer and P. J. Mulders, "Time-reversal odd distribution functions in leptonproduction," *Physical Review D*, vol. 57, pp. 5780–5786, 1998.
- [24] D. Boer and P. J. Mulders, "Investigating the origins of transverse spin asymmetries at BNL RHIC," *Physical Review D*, vol. 60, Article ID 014012, 1999.
- [25] M. Anselmino, M. Boglione, and F. Murgia, "Single spin asymmetry for $p \uparrow p \rightarrow \pi X$ in perturbative QCD," *Physics Letters B*, vol. 362, no. 1-4, pp. 164–172, 1995.
- [26] M. Anselmino and F. Murgia, "Single spin asymmetries in $p^\uparrow p$ and $\bar{p}^\uparrow p$ inclusive processes," *Physics Letters B*, vol. 442, no. 1-4, pp. 470–478, 1998.
- [27] M. Anselmino, M. Boglione, U. D'Alesio, E. Leader, S. Melis, and F. Murgia, "General partonic structure for hadronic spin asymmetries," *Physical Review D*, vol. 73, Article ID 014020, 2006.
- [28] M. Anselmino, M. Boglione, U. D'Alesio et al., "Role of Collins effect in the single spin asymmetry A_N in $p^\uparrow p \rightarrow hX$ processes," *Physical Review D*, vol. 86, Article ID 074032, 2012.
- [29] M. Anselmino, M. Boglione, U. D'Alesio, S. Melis, F. Murgia, and A. Prokudin, "Sivers effect and the single spin asymmetry A_N in $p^\uparrow p \rightarrow hX$ processes," *Physical Review D*, vol. 88, Article ID 054023, 2013.
- [30] D. L. Adams, N. Akchurin, N. I. Belikov et al., "Comparison of spin asymmetries and cross sections in π^0 production by 200 GeV polarized antiprotons and protons," *Physics Letters B*, vol. 261, no. 1-2, pp. 201–206, 1991.
- [31] D. L. Adams, N. Akchurin, N. I. Belikov et al., "Analyzing power in inclusive π^+ and π^- production at high x_F with a 200 GeV polarized proton beam," *Physics Letters B*, vol. 264, no. 3-4, pp. 462–466, 1991.
- [32] K. Krueger, C. Allgower, T. Kasprzyk et al., "Large analyzing power in inclusive π^\pm production at high x_F with a 22-GeV/c polarized proton beam," *Physics Letters B*, vol. 459, pp. 412–416, 1999.
- [33] J. Adams, C. Adler, M. M. Aggarwal et al., "Cross sections and transverse single-spin asymmetries in forward neutral-pion production from proton collisions at $\sqrt{s} = 200$ GeV," *Physical Review Letters*, vol. 92, Article ID 171801, 2004.
- [34] B. I. Abelev, M. M. Aggarwal, Z. Ahammed et al., "Forward neutral-pion transverse single-spin asymmetries in $p + p$ collisions at $\sqrt{s} = 200$ GeV," *Physical Review Letters*, vol. 101, Article ID 222001, 2008.
- [35] S. S. Adler, S. Afanasiev, C. Aidala et al., "Measurement of transverse single-spin asymmetries for midrapidity production of neutral pions and charged hadrons in polarized $p + p$ collisions at $\sqrt{s} = 200$ GeV," *Physical Review Letters*, vol. 95, Article ID 202001, 2005.
- [36] J. H. Lee, F. Videbæk, E. McBreen et al., "Single Spin Asymmetries of Identified Hadrons in Polarized p+p at $\sqrt{s} = 62.4$ and 200 GeV," *AIP Conference Proceedings*, vol. 915, p. 533, 2007.
- [37] I. Arsene, I. G. Bearden, D. Beavis et al., "Single-transverse-spin asymmetries of identified charged hadrons in polarized pp collisions at $\sqrt{s} = 62.4$ GeV," *Physical Review Letters*, vol. 101, Article ID 042001, 2008.

- [38] L. Adamczyk, G. Agakishiev, M. M. Aggarwal et al., “Longitudinal and transverse spin asymmetries for inclusive jet production at mid-rapidity in polarized $p + p$ collisions at $\sqrt{s} = 200$ GeV,” *Physical Review D*, vol. 86, Article ID 032006, 2012.
- [39] L. Adamczyk, G. Agakishiev, M. M. Aggarwal et al., “Transverse single-spin asymmetry and cross section for π^0 and η mesons at large Feynman x in $p^\dagger + p$ collisions at $\sqrt{s} = 200$ GeV,” *Physical Review D*, vol. 86, Article ID 051101, 2012.
- [40] L. C. Bland, E. Brash, H. J. Crawford et al., “Cross sections and transverse single-spin asymmetries in forward jet production from proton collisions at $\sqrt{s} = 500$ GeV,” <http://arxiv.org/abs/1304.1454>.
- [41] A. Adare, S. Afanasiev, C. Aidala et al., “Measurement of transverse-single-spin asymmetries for midrapidity and forward-rapidity production of hadrons in polarized $p + p$ collisions at $\sqrt{s} = 200$ and 62.4 GeV,” *Physical Review D*, vol. 90, Article ID 012006, 2014.
- [42] A. Adare, C. Aidala, N. N. Ajitanand et al., “Cross section and transverse single-spin asymmetry of η mesons in $p^\dagger + p$ collisions at $\sqrt{s} = 200$ GeV at forward rapidity,” *Physical Review D*, vol. 90, Article ID 072008, 2014.
- [43] J. Nagle, *PHENIX Beam Use Proposal: Run-15 and Run-16*, University of New Mexico, 2014.
- [44] The STAR Collaboration, “RHIC Beam Use Request for Runs 15 and 16,” June 2014.
- [45] E.-C. Aschenauer, A. Bazilevsky, M. Diehl et al., “The RHIC SPIN program: achievements and future opportunities,” <http://arxiv.org/abs/1501.01220>.
- [46] Z.-B. Kang, J.-W. Qiu, W. Vogelsang, and F. Yuan, “Observation concerning the process dependence of the Sivers functions,” *Physical Review D*, vol. 83, Article ID 094001, 2011.
- [47] Z.-B. Kang and A. Prokudin, “Global fitting of single spin asymmetry: an attempt,” *Physical Review D*, vol. 85, Article ID 074008, 2012.
- [48] A. Metz, D. Pitonyak, A. Schafer, M. Schlegel, W. Vogelsang, and J. Zhou, “Single-spin asymmetries in inclusive deep inelastic scattering and multiparton correlations in the nucleon,” *Physical Review D*, vol. 86, Article ID 094039, 2012.
- [49] A. Airapetian, N. Akopov, Z. Akopov et al., “Search for a two-photon exchange contribution to inclusive deep-inelastic scattering,” *Physics Letters B*, vol. 682, pp. 351–354, 2010.
- [50] J. Katich, X. Qian, Y. X. Zhao et al., “Measurement of the target-normal single-spin asymmetry in deep-inelastic scattering from the reaction $^3\text{He}^\dagger(e, e')X$,” *Physical Review Letters*, vol. 113, Article ID 022502, 2014.
- [51] K. Kanazawa, Y. Koike, A. Metz, and D. Pitonyak, “Towards an explanation of transverse single-spin asymmetries in proton-proton collisions: the role of fragmentation in collinear factorization,” *Physical Review D*, vol. 89, Article ID 111501, 2014.
- [52] Z. B. Kang, F. Yuan, and J. Zhou, “Twist-three fragmentation function contribution to the single spin asymmetry in pp collisions,” *Physics Letters B*, vol. 691, pp. 243–248, 2010.
- [53] L. Gamberg, Z. B. Kang, A. Metz, D. Pitonyak, and A. Prokudin, “Left-right spin asymmetry in $\ell N^\dagger \rightarrow hX$,” *Physical Review D*, vol. 90, Article ID 074012, 2014.
- [54] K. Kanazawa, A. Metz, D. Pitonyak, and M. Schlegel, “Longitudinal-transverse double-spin asymmetries in single-inclusive lepton production of hadrons,” *Physics Letters B*, vol. 742, pp. 340–346, 2015.
- [55] M. Anselmino, U. D’Alesio, and S. Melis, “Transverse single-spin asymmetries in proton-proton collisions at the AFTER@LHC experiment in a TMD factorisation scheme,” <http://arxiv.org/abs/1504.03791>.
- [56] L. Gamberg and Z. B. Kang, “Single transverse spin asymmetry of prompt photon production,” *Physics Letters B*, vol. 718, no. 1, pp. 181–188, 2012.
- [57] Y. V. Kovchegov and M. D. Sievert, “New mechanism for generating a single transverse spin asymmetry,” *Physical Review D*, vol. 86, Article ID 034028, 2012, Erratum in: new mechanism for generating a single transverse spin asymmetry, *Physical Review D*, vol. 86, Article ID 079906, 2012.
- [58] A. Schafer and J. Zhou, “Transverse single spin asymmetry in direct photon production in polarized pA collisions,” *Physical Review D*, vol. 90, Article ID 034016, 2014.
- [59] K. Kanazawa and Y. Koike, “Single transverse-spin asymmetry for direct-photon and single-jet productions at RHIC,” *Physics Letters B*, vol. 720, pp. 161–165, 2013.
- [60] L. Gamberg, Z. B. Kang, and A. Prokudin, “Indication on the process dependence of the sivers effect,” *Physical Review Letters*, vol. 110, Article ID 232301, 2013.
- [61] X. Ji, J. W. Qiu, W. Vogelsang, and F. Yuan, “Single transverse-spin asymmetry in Drell-Yan production at large and moderate transverse momentum,” *Physical Review D*, vol. 73, Article ID 094017, 2006.
- [62] Y. Koike and S. Yoshida, “Three-gluon contribution to the single spin asymmetry in Drell-Yan and direct-photon processes,” *Physical Review D*, vol. 85, Article ID 034030, 2012.
- [63] K. Kanazawa and Y. Koike, “Hard- and soft-fermion-pole contributions to single transverse-spin asymmetry for Drell-Yan process,” *Physics Letters B*, vol. 701, pp. 576–580, 2011.
- [64] K. Kanazawa, Y. Koike, A. Metz, and D. Pitonyak, “Transverse single-spin asymmetries in $p^\dagger p \rightarrow \gamma X$ from quark-gluon-quark correlations in the proton,” *Physical Review D*, vol. 91, Article ID 014013, 2015.
- [65] J. C. Collins, “Leading-twist single-transverse-spin asymmetries: Drell-Yan and deep-inelastic scattering,” *Physics Letters B*, vol. 536, no. 1-2, pp. 43–48, 2002.
- [66] Y. Kanazawa and Y. Koike, “Chiral-odd contribution to single-transverse spin asymmetry in hadronic pion production,” *Physics Letters B*, vol. 478, pp. 121–126, 2000.
- [67] Y. Kanazawa and Y. Koike, “Estimate of a chiral-odd contribution to single transverse-spin asymmetry in hadronic pion production,” *Physics Letters B*, vol. 490, pp. 99–105, 2000.
- [68] S. J. Brodsky, F. Fleuret, C. Hadjidakis, and J. P. Lansberg, “Physics opportunities of a fixed-target experiment using LHC beams,” *Physics Reports*, vol. 522, no. 4, pp. 239–255, 2013.
- [69] J. P. Lansberg, M. Anselmino, R. Arnaldi et al., “Spin physics and TMD studies at a fixed-target experiment at the LHC (AFTER@LHC),” *EPJ Web of Conferences*, vol. 85, Article ID 02038, 2015.
- [70] M. Anselmino, D. Boer, U. D’Alesio, and F. Murgia, “A polarization from unpolarized quark fragmentation,” *Physical Review D*, vol. 63, Article ID 054029, 2001.
- [71] S. Heppelmann, *PoS DIS*, vol. 2013, p. 240, 2013.
- [72] D. Boer and C. Pisano, “Polarized gluon studies with charmonium and bottomonium at LHCb and AFTER,” *Physical Review D*, vol. 86, Article ID 094007, 2012.
- [73] A. Schäfer and J. Zhou, “Transverse single spin asymmetry in hadronic $\eta_{c,b}$ production,” *Physical Review D*, vol. 88, no. 1, Article ID 014008, 2013.

- [74] D. Boer, P. J. Mulders, and F. Pijlman, “Universality of T-odd effects in single spin and azimuthal asymmetries,” *Nuclear Physics B*, vol. 667, pp. 201–241, 2003.
- [75] M. M. Mondal et al., “Measurement of the transverse single-spin asymmetries for π^0 and jet-like events at forward rapidities at STAR in $p + p$ Collisions at $\sqrt{s} = 500$ GeV,” *Proceedings of Science*, vol. DIS2014, p. 216, 2014, <http://arxiv.org/abs/1407.3715>.

Research Article

Feasibility Studies for Quarkonium Production at a Fixed-Target Experiment Using the LHC Proton and Lead Beams (AFTER@LHC)

L. Massacrier,^{1,2} B. Trzeciak,³ F. Fleuret,⁴ C. Hadjidakis,² D. Kikola,⁵
J. P. Lansberg,² and H.-S. Shao⁶

¹LAL, Université Paris-Sud, CNRS/IN2P3, 91406 Orsay, France

²IPNO, Université Paris-Sud, CNRS/IN2P3, 91406 Orsay, France

³FNSPE, Czech Technical University, Prague, Czech Republic

⁴Laboratoire Leprince Ringuet, École Polytechnique, CNRS/IN2P3, 91128 Palaiseau, France

⁵Faculty of Physics, Warsaw University of Technology, Ulica Koszykowa 75, 00-662 Warsaw, Poland

⁶PH Department, Theory Unit, CERN, CH-1211, Geneva 23, Switzerland

Correspondence should be addressed to B. Trzeciak; trzebar@fjfi.cvut.cz

Received 17 April 2015; Accepted 16 June 2015

Academic Editor: Michal Kreps

Copyright © 2015 L. Massacrier et al. This is an open access article distributed under the Creative Commons Attribution License, which permits unrestricted use, distribution, and reproduction in any medium, provided the original work is properly cited. The publication of this article was funded by SCOAP³.

Being used in the fixed-target mode, the multi-TeV LHC proton and lead beams allow for studies of heavy-flavour hadroproduction with unprecedented precision at backward rapidities, far negative Feynman- x , using conventional detection techniques. At the nominal LHC energies, quarkonia can be studied in detail in $p + p$, $p + d$, and $p + A$ collisions at $\sqrt{s_{NN}} \approx 115$ GeV and in Pb + p and Pb + A collisions at $\sqrt{s_{NN}} \approx 72$ GeV with luminosities roughly equivalent to that of the collider mode that is up to $20 \text{ fb}^{-1} \text{ yr}^{-1}$ in $p + p$ and $p + d$ collisions, up to $0.6 \text{ fb}^{-1} \text{ yr}^{-1}$ in $p + A$ collisions, and up to $10 \text{ nb}^{-1} \text{ yr}^{-1}$ in Pb + A collisions. In this paper, we assess the feasibility of such studies by performing fast simulations using the performance of a LHCb-like detector.

1. Introduction

Since its start-up, the large hadron collider (LHC), the most energetic hadron collider ever built so far, has already made the demonstration of its outstanding capabilities. These can greatly be complemented by the addition of a fixed-target physics program. Its multi-TeV beams indeed allow one to study $p + p$, $p + d$, and $p + A$ collisions at a center-of-mass (c.m.s.) energy $\sqrt{s_{NN}} \approx 115$ GeV as well as Pb + p and Pb + A collisions at $\sqrt{s_{NN}} \approx 72$ GeV, with the high precision typical of the fixed-target mode. In this context, the proposal of a fixed-target experiment at the LHC [1], referred to as AFTER@LHC, has been promoted [1] in order to complement the existing collider experiments such as the Relativistic Heavy Ion Collider (RHIC) or the future Electron-Ion Collider (EIC) project in a similar energy range. The idea

underlying the AFTER@LHC proposal is a multipurpose detector allowing for the study of a multitude of probes.

Various technological ways to perform fixed-target experiment at the LHC exist. On the one hand, the beam can be extracted by means of a bent crystal. This technology [2, 3] is currently developed as a smart beam-collimation solution and is studied by the UA9/LUA9 collaboration, respectively, at SPS and LHC. A bent crystal installed in the halo of the LHC beam would deflect the particles of the halo onto a target, with a flux of 5×10^8 proton/s without any impact on the LHC performances [3–5].

On the other hand, the LHC beam can go through an internal-gas-target system in an existing (or new) LHC experiment. Such a system is already tested at low gas pressure by the LHCb collaboration to monitor the luminosity of the beam [6–8]. Data were taken at a center-of-mass energy of

TABLE 1: Expected luminosities obtained for a 7 (2.76) TeV proton beam (Pb) extracted by means of a bent crystal or obtained with an internal-gas-target system.

Beam	Target	Thickness (cm)	ρ (g·cm ⁻³)	\mathcal{L} ($\mu\text{b}^{-1}\cdot\text{s}^{-1}$)	$\int \mathcal{L}$ (pb ⁻¹ ·y ⁻¹)
p	Liquid H	100	0.068	2000	20000
p	Liquid D	100	0.16	2400	24000
p	Pb	1	11.35	16	160
Pb	Liquid H	100	0.068	0.8	0.8
Pb	Liquid D	100	0.16	1	1
Pb	Pb	1	11.35	0.007	0.007
Beam	Target	Usable gas zone (cm)	Pressure (Bar)	\mathcal{L} ($\mu\text{b}^{-1}\cdot\text{s}^{-1}$)	$\int \mathcal{L}$ (pb ⁻¹ ·y ⁻¹)
p	Perfect gas	100	10 ⁻⁹	10	100
Pb	Perfect gas	100	10 ⁻⁹	0.001	0.001

$\sqrt{s_{\text{NN}}} = 87$ (54) GeV with $p + \text{Ne}$ (Pb + Ne) collisions during pilot runs in 2012 and 2013. Although this system, called SMOG, was tested during only few hours in a row, no decrease of the LHC performances was observed.

In the bent crystal case, the luminosity achievable with AFTER@LHC would surpass that of RHIC by 3 orders of magnitudes [1]. We have reported in Table 1 the instantaneous and yearly integrated luminosities expected with the proton and Pb beams on various target species of various thicknesses, for the bent crystal as well as internal-gas-target options. Integrated luminosities as large as 20 fb⁻¹ can be delivered during a one-year run of $p + \text{H}$ collisions with a bent crystal. Besides, it is worth mentioning that both technologies allow one to polarise the target, which is an important requirement to lead an extensive spin physics programme [1, 11].

Overall, thanks to the large luminosity expected, AFTER@LHC would become a quarkonium [12], prompt photon, and heavy-flavour observatory [1, 13] in $p + p$ and $p + A$ collisions where, by instrumenting the target-rapidity region, gluon and heavy-quark distributions of the proton, the neutron and the nuclei can be accessed at large x and even at x larger than unity in the nuclear case [14]. In addition, the fixed-target mode allows for single-target-spin-asymmetry measurements over the full backward rapidity domain up to $x_F \approx -1$ [15, 16]. Also, the versatility in the target choices offer a unique opportunity to study the nuclear matter versus the hot and dense matter formed in heavy ion collisions which can be studied during the one-month lead run. In the latter case, modern detection technology (such as high granularity calorimeter) should allow for extensive studies of quarkonium excited states, from $\psi(2S)$ to χ_c and χ_b resonances thanks to the boost of the fixed-target mode [17].

In this paper, we report on a feasibility study of quarkonium production at a fixed-target experiment using LHC beams. In Section 2, we outline the simulation framework which was used. In Section 3, we describe how a fast simulation of a detector response has been implemented, following a LHCb-like detector setup. In Section 4, we present the charmonium and bottomonium family studies performed with the $p + \text{H}$ simulations at $\sqrt{s} = 115$ GeV. In Section 5, we

present multiplicity studies in $p + A$ and $A + p$ collisions as well as the expected nuclear modification factors for J/ψ and Υ in $p + \text{Pb}$ collisions at $\sqrt{s_{\text{NN}}} = 115$ GeV. Finally in Section 6 some prospects for Pb + A measurement at $\sqrt{s_{\text{NN}}} = 72$ GeV are given. Section 7 gathers our conclusions.

2. Simulation Inputs

In order to get the most realistic minimum bias simulations at AFTER@LHC energy for quarkonium studies in the dimuon decay channels, we have simulated the quarkonium signal and all the background sources separately to have under control the transverse momentum and rapidity input distributions as well as the normalisation of the different sources.

The simulation has been performed for $p + p$ collisions at $\sqrt{s} = 115$ GeV. On the one hand, the quarkonium signal and the correlated background (Drell-Yan, $c\bar{c}$, $b\bar{b}$) were simulated with HELAC-ONIA [18] which produces outputs following the format of Les Houches Event Files [19]. The outputs were then processed with PYTHIA (PYTHIA 8.185 [20]) to perform the hadronisation, the initial/final-state radiations, and the decay of the resonances. On the other hand, the uncorrelated background was obtained from minimum bias $p + p$ collisions generated with PYTHIA.

The relative normalisation of the signal and background sources was performed according to the production cross section of the process (taking into account initial phase space cuts, if any). Values of the cross section and the number of simulated events N_{sim} , not to be confused with the expected events for a specific luminosity, are reported in Table 2. The cross section values are integrated over rapidity and p_T .

2.1. Signal and Correlated Background

2.1.1. Quarkonium Signal. J/ψ , $\psi(2S)$, $\Upsilon(1S)$, $\Upsilon(2S)$, and $\Upsilon(3S)$ were simulated in a data-driven way. The amplitude of $gg \rightarrow \mathcal{Q} + X$ (where \mathcal{Q} is the quarkonium) is expressed in an empirical functional form [21]:

$$\overline{|\mathcal{A}_{gg \rightarrow \mathcal{Q}+X}|^2} = \begin{cases} K \exp\left(-\kappa \frac{p_T^2}{M_{\mathcal{Q}}^2}\right) & \text{when } p_T \leq \langle p_T \rangle \\ K \exp\left(-\kappa \frac{\langle p_T \rangle^2}{M_{\mathcal{Q}}^2}\right) \left(1 + \frac{\kappa}{n} \frac{p_T^2 - \langle p_T \rangle^2}{M_{\mathcal{Q}}^2}\right)^{-n} & \text{when } p_T > \langle p_T \rangle, \end{cases} \quad (1)$$

where $K = \lambda^2 \kappa \hat{s} / M_{\mathcal{Q}}^2$ with \hat{s} the partonic center-of-mass energy and $M_{\mathcal{Q}}$ the mass of the quarkonium \mathcal{Q} taken from the PDG table [22].

The parameters κ , λ , n , and $\langle p_T \rangle$ were determined by fitting the differential cross section $d^2\sigma/dp_T dy$ to the experimental data. The dedicated codes used to perform the fit and to generate unweighted events for quarkonium production have been implemented in HELAC-ONIA [18] and we used MSTW2008NLO PDF set [23] provided in LHAPDF5 [24] and the factorisation scale $\mu_F = \sqrt{M_{\mathcal{Q}}^2 + p_T^2}$. In order to constrain the nontrivial energy dependence of quarkonium production, we used the differential measurements of charmonium production performed by the

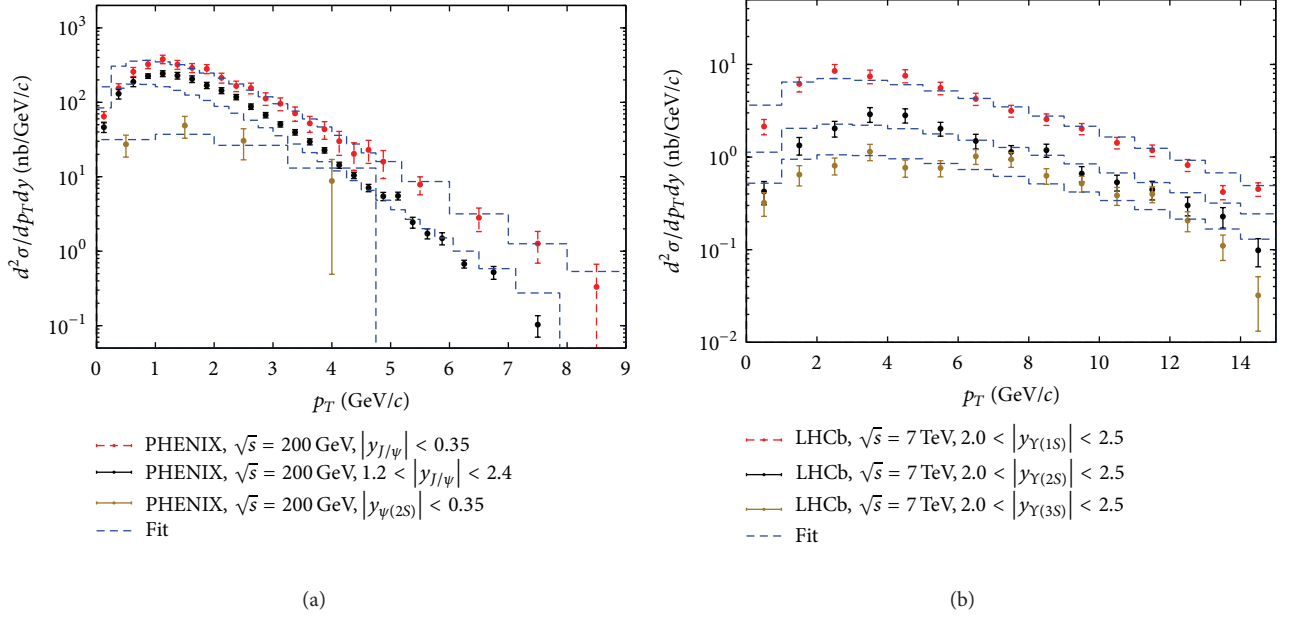


FIGURE 1: Some illustrative comparisons between fits and the PHENIX data [9] for charmonium production (a) and LHCb data [10] for bottomonium production (b).

TABLE 2: Total cross section for different processes in $p + p$ collisions at $\sqrt{s} = 115$ GeV and number of simulated events N_{sim} .

	σ_{tot} (mb)	N_{sim}
J/ψ	1.30×10^{-3}	1.47×10^6
$\psi(2S)$	1.61×10^{-4}	1.12×10^6
$Y(1S)$	4.30×10^{-7}	1.46×10^6
$Y(2S)$	1.22×10^{-7}	1.49×10^6
$Y(3S)$	5.28×10^{-8}	1.48×10^6
Drell-Yan ($M > 2.5 \text{ GeV}/c^2$)	2.52×10^{-6}	4.3×10^5
Drell-Yan ($M > 7 \text{ GeV}/c^2$)	1.49×10^{-7}	2.0×10^6
$c\bar{c}$	2.29×10^{-1}	81.5×10^6
$b\bar{b}$	4.86×10^{-4} ($gg \rightarrow b\bar{b}$)	32.3×10^6 ($gg \rightarrow b\bar{b}$)
	1.49×10^{-4} ($q\bar{q} \rightarrow b\bar{b}$)	85.7×10^6 ($q\bar{q} \rightarrow b\bar{b}$)
Minimum bias	26.68	11.0×10^8

PHENIX collaboration at RHIC, in $p + p$ collisions at $\sqrt{s} = 200$ GeV [9] to predict the corresponding yields at $\sqrt{s} = 115$ GeV. Given the lack of such measurements for Y at RHIC, we performed a combined fit to CDF [25], ATLAS [26], CMS [27], and LHCb [10, 28] data on Y production. The values of the fitted parameters are listed in Table 3. For illustration, the comparison between fits and the selected experimental data is shown in Figure 1.

In order to increase the statistics of the simulated data sample, the decay of the quarkonium in PYTHIA is forced into the dimuon decay channel. The simulated yields are then weighted by the cross section for this process multiplied by the Branching Ratio (BR).

2.1.2. Open Charm. Open charm production was simulated with the process $gg \rightarrow c\bar{c}$ in HELAC-ONIA. In order to avoid the huge theoretical uncertainties in the state-of-the-art perturbative calculations, open charm yields at $\sqrt{s} =$

TABLE 3: Fit parameters obtained after a combined fit of $d^2\sigma/dp_T dy$ to the PHENIX data [9] for charmonium production and to CDF [25], ATLAS [26], CMS [27], and LHCb [10, 28] data for bottomonium production. We have fixed $n = 2$ and $\langle p_T \rangle = 4.5$ (13.5) GeV/ c for charmonium (bottomonium) production. The number of fitted data points is also reported.

	κ	λ	Number of data points	χ^2
J/ψ	0.674	0.380	51	422
$\psi(2S)$	0.154	0.351	4	1.12
$Y(1S)$	0.707	0.0837	288	1883
$Y(2S)$	0.604	0.0563	205	856
$Y(3S)$	0.591	0.0411	197	886

115 GeV are also computed in a data-driven way following the method described in the previous section. Similarly, the matrix element of $gg \rightarrow c\bar{c}$ is determined using (1).

The parameters are obtained from a fit to the p_T -differential $c\bar{c}$ cross section measured by the STAR experiment [29] in $p + p$ collisions at $\sqrt{s} = 200$ GeV (see Figure 3). We obtained $\kappa = 0.437$, $\lambda = 3.04$, and $\langle p_T \rangle = 2.86$ GeV/ c when $n = 2$ by using CTEQ6L1 [30] and by fixing the c quark mass to $m_c = 1.5$ GeV/ c^2 and the factorisation scale to $\mu_F = \sqrt{m_c^2 + p_T^2}$. The χ^2 of the fit is equal to 4.39 with 10 experimental data points. The tuned result is shown in Figure 2. The evolution of the cross section with the energy down to $\sqrt{s} = 115$ GeV is then given by HELAC-ONIA.

After embedding the Les Houches Event File into PYTHIA, muons from the underlying PYTHIA event can be produced on top of muons from the initial $c\bar{c}$ pair. The combination of those additional muons with a muon from the initial $c\bar{c}$ pair is not included in our definition of open charm correlated background. We have however checked that this contribution is negligible. In order to increase the statistics, D^0 , \bar{D}^0 , $D^{+/-}$, and $D_s^{+/-}$ were forced to decay into muons and only those decay muons were considered as correlated background. $\mu^+\mu^-$ pairs coming from all possible combinations, $D^0\bar{D}^0$, D^+D^- , $D_s^+D_s^-$, $D^0D^{+/-}$, $D^0D_s^{+/-}$, and $D^{+/-}D_s^{+/-}$, are considered. The simulated events are weighted by the production cross section times the pair Branching Ratio times the fraction of c quark fragmenting to D^0 , \bar{D}^0 , $D^{+/-}$, or $D_s^{+/-}$. This fraction is obtained from PYTHIA and found to be 95%.

2.1.3. Open Beauty. The theoretical uncertainty on open beauty production is relatively smaller than the one on open charm production. We therefore calculated open beauty production yields with a Leading Order (LO) matrix element which was normalised to the Next-To-Leading-Order (NLO) K factor. The NLO cross section with the same setup was calculated by MADGRAPH5_AMC@NLO [31]. We used CTEQ6L1 (CTEQ6M) for the LO (NLO) calculation. The K factor is found to be 1.83. The renormalisation and factorisation scale is $\mu_R = \mu_F = \sqrt{m_b^2 + p_T^2}$ with the mass of the b quark taken as $m_b = 4.5$ GeV/ c^2 . We have adopted a similar definition for the open beauty correlated background as the one of open charm (see the previous section).

2.1.4. Drell-Yan. Drell-Yan (DY) correlated background was simulated with the process $q\bar{q} \rightarrow \gamma^*/Z \rightarrow \mu^+\mu^-$ at LO where $q\bar{q}$ is a pair of the same flavour light quarks. The LO calculation was done with the CTEQ6L1 pdf set and the renormalisation and factorisation scale was set to $\mu_R = \mu_F = Q/2$. In order to have enough statistics in the J/ψ and $\psi(2S)$ mass window, a phase space cut requesting that the invariant mass of the dimuons (M) is greater than 2.5 GeV/ c^2 was applied. For the simulation of the DY background under the Υ family peaks, a phase space cut $M > 7$ GeV/ c^2 was applied. The DY cross section obtained with HELAC-ONIA at $\sqrt{s} = 38.8$ GeV is compared to the existing E866 data at the same energy [32]. A K factor 1.2 is needed to match the data and therefore it was also applied at $\sqrt{s} = 115$ GeV. Such a K factor is known to approximately account for the higher-order QCD corrections.

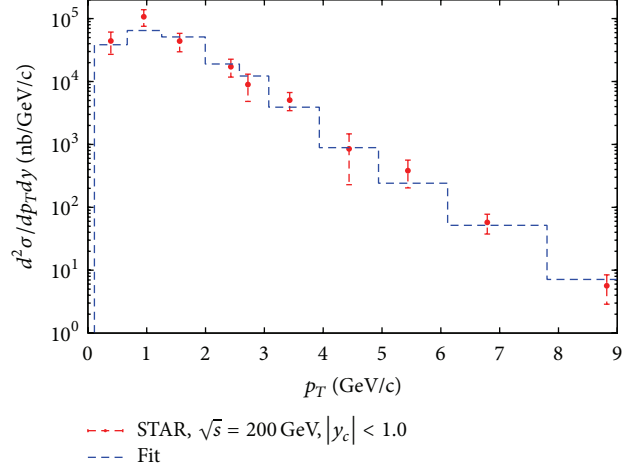


FIGURE 2: A comparison between fit and the STAR data [29] in $p + p$ collisions at $\sqrt{s} = 200$ GeV, for $c\bar{c}$ production.

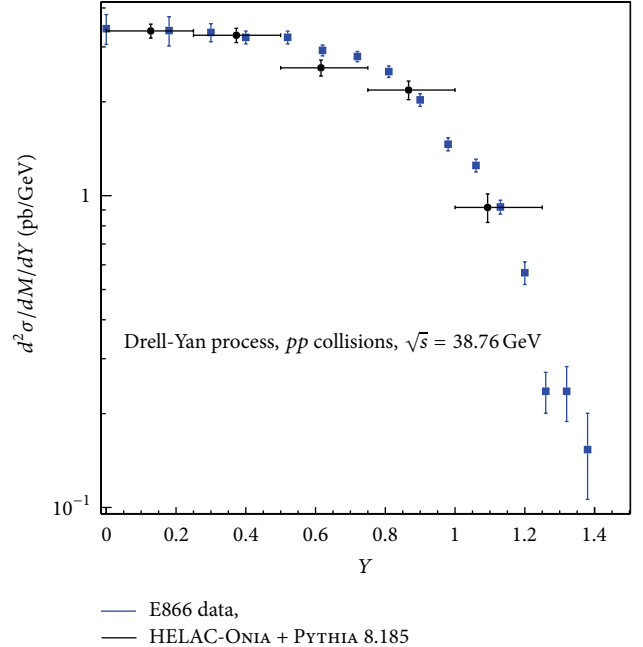


FIGURE 3: Drell-Yan cross section as a function of the rapidity in the center-of-mass frame obtained with HELAC-ONIA + PYTHIA at $\sqrt{s} = 38.76$ GeV and rescaled by a factor 1.2, together with E866 data extracted from [33]. The invariant mass range considered is $7.2 < M < 8.7$ GeV/ c^2 .

2.2. Uncorrelated Background. The uncorrelated background was obtained from a minimum bias PYTHIA $p + p$ simulation at $\sqrt{s} = 115$ GeV using the process `SoftQCD:nonDiffractive` with the MRSTMCaLHgrid LHAPDF (6.1.4) set [34]. By comparing our simulation of open charm with a low statistic pure minimum bias PYTHIA simulation, we have checked that the contribution of dimuons originating from a muon from charm/beauty and a muon from π/K is negligible.

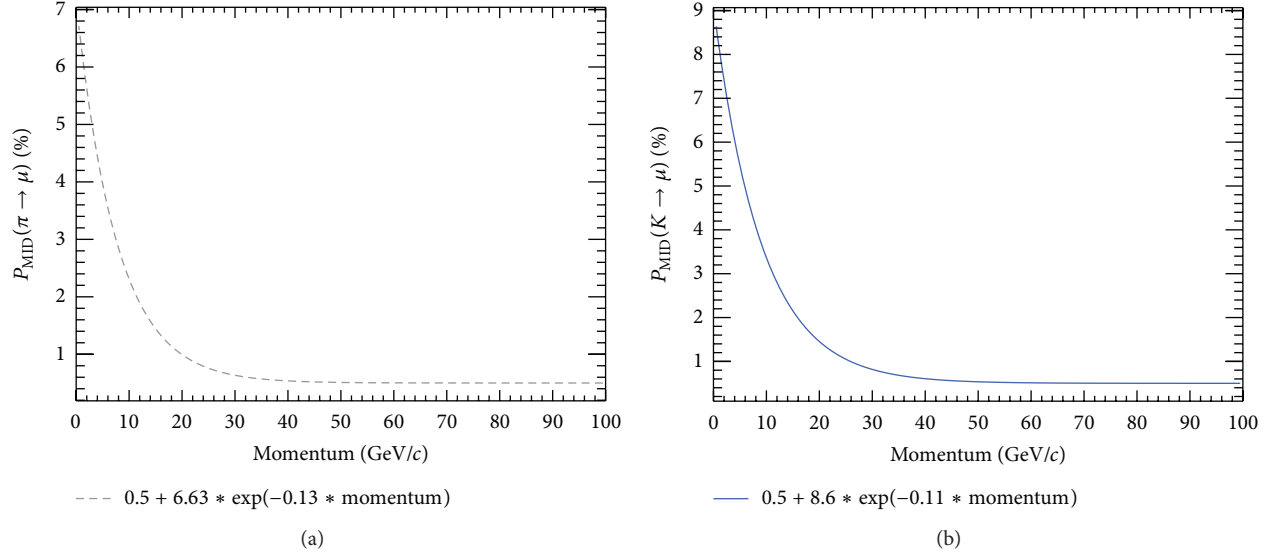


FIGURE 4: Misidentification probability of π (a) and K (b) as muon candidates as a function of momentum, $P_{\text{MID}}(\pi \rightarrow \mu)$ and $P_{\text{MID}}(K \rightarrow \mu)$, respectively.

The dominant source of uncorrelated opposite-sign muon pairs is the simultaneous semimuonic decay of uncorrelated π and/or K . In order to avoid possible double counting of signal and correlated background processes, the following hard processes have been switched off from the minimum bias simulations: `HardQCD:hardccbar`, `HardQCD:hardbbbar`, `WeakSingleBoson:ffbar2gmZ` (in order to avoid Drell-Yan pair production.), `Charmonium:all` and `Bottomonium:all`.

3. Fast Simulation of the Response of a LHCb-Like Detector

The HELAC-ONIA and PYTHIA generators provide the opposite-sign muon pairs from quarkonium decays, correlated and uncorrelated backgrounds sources, as defined in the previous section. In order to account for the detector resolution and the particle identification capabilities of a given detector and to investigate the feasibility of the quarkonium studies in $p + p$ collisions at $\sqrt{s} \approx 115$ GeV, the detector response needs to be simulated. For this purpose, we have chosen a detector setup similar to the LHCb detector [35]. A forward detector is very well suited as a fixed-target experiment setup as well, with a good tracking and particle identification capabilities.

According to LHCb analysis cuts, muons in our simulations are required to have their transverse momentum satisfying $p_T > 0.7$ GeV/c [36] and their pseudorapidity in the laboratory frame satisfying $2 < \eta < 5$. The η cut range corresponds to the LHCb detector coverage. Since the momentum resolution reported by LHCb is $\delta p/p \sim 0.4$ (0.6)% for a momentum of 3 (100) GeV/c [37], we consider a momentum resolution of $\delta p/p = 0.5\%$. The single μ identification efficiency is taken to be $\epsilon_p = 98\%$, which is an average efficiency obtained by LHCb for muons coming from J/ψ decays, for $p > 3$ GeV/c and $p_T > 0.8$ GeV/c [37].

These cuts and the abovementioned detector response on the muons are applied to simulate the quarkonium states and all the background sources.

In the case of uncorrelated background, as discussed in Section 2, most of the μ originate from $\pi^{+/-}$ or $K^{+/-}$ decays. If a π or K decays to a μ before 12 m along the z axis, the μ is rejected by the tracking system and it is not considered in the simulation. 12 m corresponds to the distance where the calorimeters, followed by the muon stations, are placed in the LHCb detector setup. If the μ is produced beyond 12 m or if a π/K is misidentified with μ in the muon stations, a π/K misidentification probability is applied. The misidentification probabilities depend on the total particle momentum and were reported by the LHCb collaboration in [38]. These probabilities are parameterised with the following functions: $P_{\text{MID}}(\pi \rightarrow \mu)(p) = (0.5 + 6.63 \exp(-0.13p))\%$ and $P_{\text{MID}}(K \rightarrow \mu)(p) = (0.5 + 8.6 \exp(-0.11p))\%$, and they are shown in Figures 4(a) and 4(b), for π and K , respectively. Based on the single μ identification efficiency $\epsilon_{\mu^{+/-}}$, the dimuon, $\mu^+\mu^-$, efficiency is calculated as a product of the single efficiencies: $\epsilon_{\mu^+\mu^-} = \epsilon_{\mu^+} \times \epsilon_{\mu^-}$. For muons coming from π^+ or $K^{+/-}$ decays, misidentification probabilities are used: $\epsilon_{\mu^{+/-}} = P_{\text{MID}}(\pi \rightarrow \mu)(p)$ or $\epsilon_{\mu^{+/-}} = P_{\text{MID}}(K \rightarrow \mu)(p)$, respectively, for π and K , and for prompt muons $\epsilon_{\mu^{+/-}} = \epsilon_p = 0.98$.

The pair efficiency is extracted in each kinematic phase space point and is shown as a function of the dimuon invariant mass, transverse momentum, and rapidity in Figure 5. This efficiency is used to correct dimuon spectra obtained with the uncorrelated background PYTHIA simulations.

4. Quarkonium Production Studies in $p + \text{H}$ Collisions at $\sqrt{s} = 115$ GeV

In this section, we show results on the quarkonium production studies in the dimuon decay channels, with

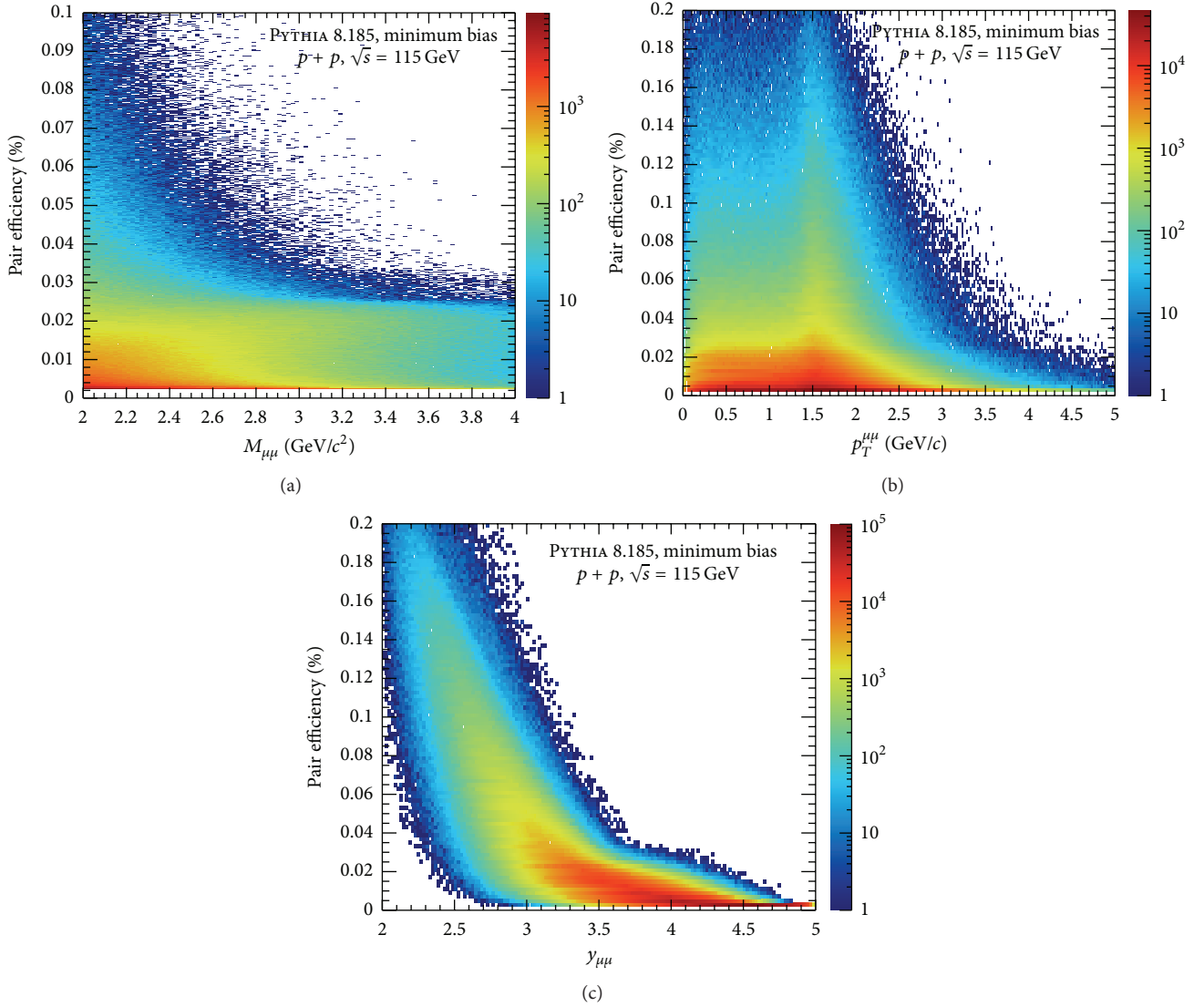


FIGURE 5: Muon pair, $\mu^+\mu^-$, identification efficiency as a function of the pair invariant mass (a), transverse momentum (b), and rapidity (c) for uncorrelated muon background. The efficiency takes into account the identification efficiency of the prompt muons and the π and K misidentification probability, $P_{\text{MID}}(\pi \rightarrow \mu)$ and $P_{\text{MID}}(K \rightarrow \mu)$.

the dominant background sources. Simulations have been performed for a 7 TeV proton beam on a hydrogen target ($p + p$), which gives $\sqrt{s} = 115$ GeV. We consider an integrated luminosity of 10 fb^{-1} which is expected to be obtained after half of a LHC year with the crystal mode, as described in Section 1 and Table 1.

4.1. Background Studies. These simulations allow us to quantify the background sources in the quarkonium studies in the dimuon decay channel, which could potentially make the quarkonium signal extraction more difficult or even prevent from obtaining a clear signal. In particular, this may be critical for the excited states. We present here simulations of invariant mass of opposite-sign muon pairs, $\mu^+\mu^-$, from the quarkonia and from the dominant background sources, in two mass ranges; see Figure 6. The first range corresponds to the J/ψ

and $\psi(2S)$ invariant mass windows and the second one to the mass range of the $\Upsilon(1S)$, $\Upsilon(2S)$, and $\Upsilon(3S)$. The invariant mass distributions are integrated over the whole transverse momentum and rapidity ranges. The plots show the simulated quarkonium signals and the background, separately from the different sources, and the black solid line is a sum of all contributions. The background sources correspond to an integrated luminosity of 10 fb^{-1} .

In the J/ψ and $\psi(2S)$ invariant mass window, the dominant background source is from uncorrelated $\mu^+\mu^-$ pairs, mostly from $\pi^{+/-}$ and $K^{+/-}$ decays. The contributions from Drell-Yan and $b\bar{b}$ continuum are very small. In the case of $\Upsilon(nS)$ states, the Drell-Yan contribution is the dominant one. Under the $\Upsilon(nS)$ peak, the contribution from the $c\bar{c}$ continuum is negligible, and it is not considered here.

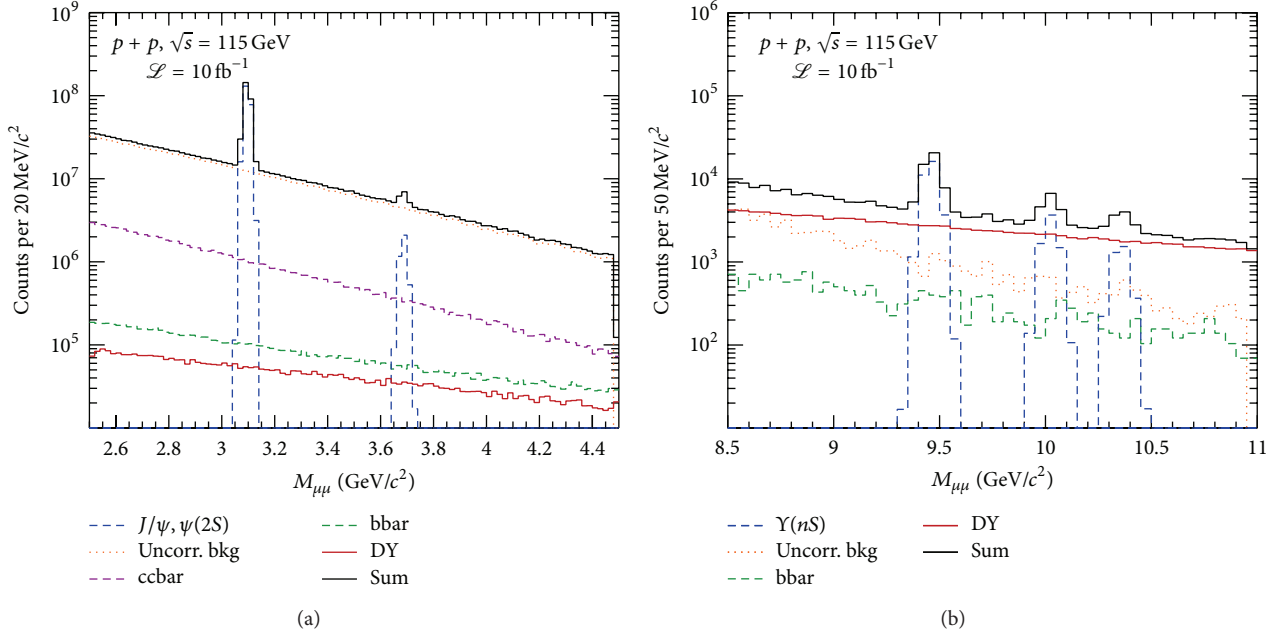


FIGURE 6: Dimuon invariant mass distributions for J/ψ and $\psi(2S)$ (a) and $\Upsilon(nS)$ (b) with different background sources.

The significance ($\text{sig} = S/\sqrt{(S+B)}$, where S is the number of signal counts and B is the number of background counts, in the invariant mass range $M_Q \pm 3\sigma_Q$) and the signal to background ratio (S/B) of each quarkonium state are given in the following:

- (i) $\text{sig}_{J/\psi} = 134.6 \cdot 10^2 \sigma$, $S/B_{J/\psi} = 4.21$,
- (ii) $\text{sig}_{\psi(2S)} = 735.2 \sigma$, $S/B_{\psi(2S)} = 0.16$,
- (iii) $\text{sig}_{\Upsilon(1S)} = 140.73 \sigma$, $S/B_{\Upsilon(1S)} = 1.75$,
- (iv) $\text{sig}_{\Upsilon(2S)} = 45.29 \sigma$, $S/B_{\Upsilon(2S)} = 0.48$,
- (v) $\text{sig}_{\Upsilon(3S)} = 25.75 \sigma$, $S/B_{\Upsilon(3S)} = 0.28$,

for J/ψ , $\psi(2S)$, $\Upsilon(1S)$, $\Upsilon(2S)$, and $\Upsilon(3S)$, respectively.

Transverse momentum and rapidity distributions for the quarkonium signals and for each background source were also studied. As an example, the p_T and y distributions in the J/ψ mass range, $3.063 < M_{\mu^+\mu^-} < 3.129 \text{ GeV}/c^2$ (corresponding to $M_{J/\psi} \pm 3\sigma_{J/\psi}$), are shown in Figure 7. It is visible that the distributions for the J/ψ and different backgrounds differ. In more backward or forward rapidity regions, the signal to background ratio increases. This can also be seen in Figure 8, where the dimuon invariant mass distributions in J/ψ and $\psi(2S)$ mass window are shown in three rapidity ranges. In terms of transverse momentum, one can obtain a very clean signal when going to higher p_T . Above $\sim 4 \text{ GeV}/c$, the uncorrelated background starts to vanish. Since $c\bar{c}$, $b\bar{b}$, and Drell-Yan simulations are LO simulations, the p_T spectra of these correlated background sources are not shown here.

4.2. Quarkonium Simulations. We have also studied the p_T and rapidity coverage reach of the quarkonium signals. The transverse momentum distributions are shown in

Figure 9(a), for J/ψ , $\psi(2S)$, $\Upsilon(1S)$, $\Upsilon(2S)$, and $\Upsilon(3S)$, from the top to the bottom distribution. Similarly, Figure 9(b) shows the rapidity distribution for each quarkonium state. With an integrated luminosity of 10 fb^{-1} the quarkonium studies can be carried out in a wide rapidity and p_T range. It should be possible to study $\Upsilon(nS)$ signals up to $p_T \approx 10 \text{ GeV}/c$, and J/ψ and $\psi(2S)$ could be studied even up to $p_T \approx 15 \text{ GeV}/c$. All the quarkonium states can be measured down to $p_T = 0 \text{ GeV}/c$.

This study is limited by the rapidity range of $2 < y < 5$, in the laboratory frame, due to the pseudorapidity cuts on the decay μ . The red x -axis on the top of Figure 9(b) denotes the rapidity in the center-of-mass frame. The rapidity shift for a 7 TeV proton beam on a fixed-target is -4.8 ; that is, $y_{\text{CM}} = 0 \rightarrow y_{\text{lab}} = 4.8$. J/ψ and $\psi(2S)$ signals can be studied in the whole mentioned rapidity range, while the lowest rapidity reach for $\Upsilon(nS)$ is ~ 2.5 – 3 .

5. Quarkonium Measurements in $p + A$ Collisions at $\sqrt{s} = 115 \text{ GeV}$ and Pb + H Collisions at $\sqrt{s} = 72 \text{ GeV}$

5.1. Multiplicity in Proton-Nucleus Collisions. In proton-nucleus collisions, the high track multiplicity may induce a high detector occupancy and lead to a reduction of the detector capabilities. Since LHCb has successfully measured the J/ψ and Υ production in $p + \text{Pb}$ collisions at $\sqrt{s_{\text{NN}}} = 5 \text{ TeV}$ [39, 40], one would expect a good capability of such detector under similar particle multiplicity environment. In the following, the charged particle multiplicity has been generated with the EPOS generator [41, 42] in different configurations: $p + \text{Pb}$ collisions at $\sqrt{s_{\text{NN}}} = 5 \text{ TeV}$ in collider mode (the lead goes in the detector direction), $p + \text{Pb}$ collisions at $\sqrt{s_{\text{NN}}} = 115 \text{ GeV}$, and Pb + H collisions at

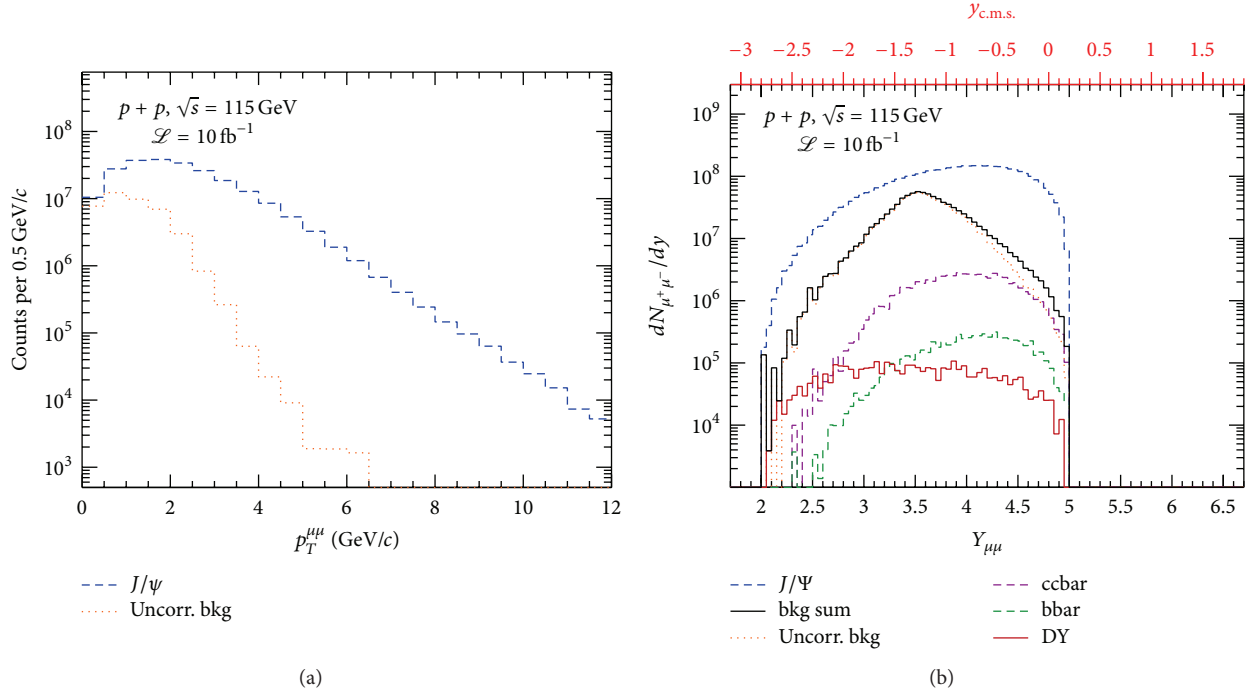


FIGURE 7: p_T (a) and y (b) spectra of J/ψ signal and different background sources in the J/ψ mass range.

$\sqrt{s_{\text{NN}}} = 72 \text{ GeV}$ in fixed-target mode. The charged particle multiplicity is dominated by the π multiplicity. By comparing these three distributions as a function of the pseudorapidity of the particle in the laboratory frame as shown in Figure 10, one can conclude that the charged particle multiplicity in a fixed-target mode never exceeds the one obtained in $p + \text{Pb}$ collisions at $\sqrt{s_{\text{NN}}} = 5 \text{ TeV}$ in the collider mode in the full pseudorapidity range: a detector with the LHCb capabilities will be able to run in such conditions.

5.2. Prospects for the Measurements of the Nuclear Modification Factors for J/ψ and Υ in $p + \text{Pb}$ Collisions at $\sqrt{s_{\text{NN}}} = 115 \text{ GeV}$. To illustrate the potential offered by AFTER@LHC in $p + \text{Pb}$ collisions at $\sqrt{s_{\text{NN}}} = 115 \text{ GeV}$, we have evaluated, in this section, the impact of the nuclear modification of the gluon densities in nucleons within large nucleus, generically referred to as gluon shadowing, and its uncertainty as encoded in the nuclear PDF set EPS09. For that, we have used the probabilistic Glauber Monte-Carlo framework, JIN [43, 44], which allows us to encode different mechanisms for the partonic production and to interface these production processes with different cold nuclear matter effects, such as the aforementioned shadowing, in order to get the production cross sections for proton-nucleus and nucleus-nucleus collisions. JIN also straightforwardly computes any nuclear modification factor for minimum bias collisions or in specific centrality classes. In the case of proton-nucleus ($p + A$) collisions, it is the ratio of the yield per inelastic collision in $p + A$ collisions to the yield in pp collisions at the same energy

multiplied by the average number of binary collisions in a typical $p + p$ collision, $\langle N_{\text{coll}} \rangle$:

$$R_{pA} = \frac{dN_{pA}}{\langle N_{\text{coll}} \rangle dN_{pp}}. \quad (2)$$

In the presence of a net nuclear effect, R_{pA} is defined such that it differs from *unity*. In the simplest case of minimum bias collisions, one should have

$$R_{pA} = \frac{d\sigma_{pA}}{A d\sigma_{pp}}. \quad (3)$$

As in [45], we have used the central curve of EPS09 as well as four specific extreme curves (minimal/maximal shadowing, minimal/maximal EMC effect), which reproduce the envelope of the gluon nPDF uncertainty encoded in EPS09 LO [46].

In addition to the modification of the partonic densities, quarkonium production in $p + A$ collisions can be affected by other effects, for instance, by the nuclear absorption which depends much on the nature of the object traversing the nuclear medium. If the meson is already formed, it may be affected more than a smaller pre-resonant pair. To discuss such an effect, it is useful to introduce the concept of the formation time, t_f , based on the Heisenberg uncertainty principle and the time, in the rest frame of the meson, to discriminate between two S states, for instance, the J/ψ and the $\psi(2S)$. In fact, one finds [45, 47] that such a time is similar for the charmonium and bottomonium states and is on the order

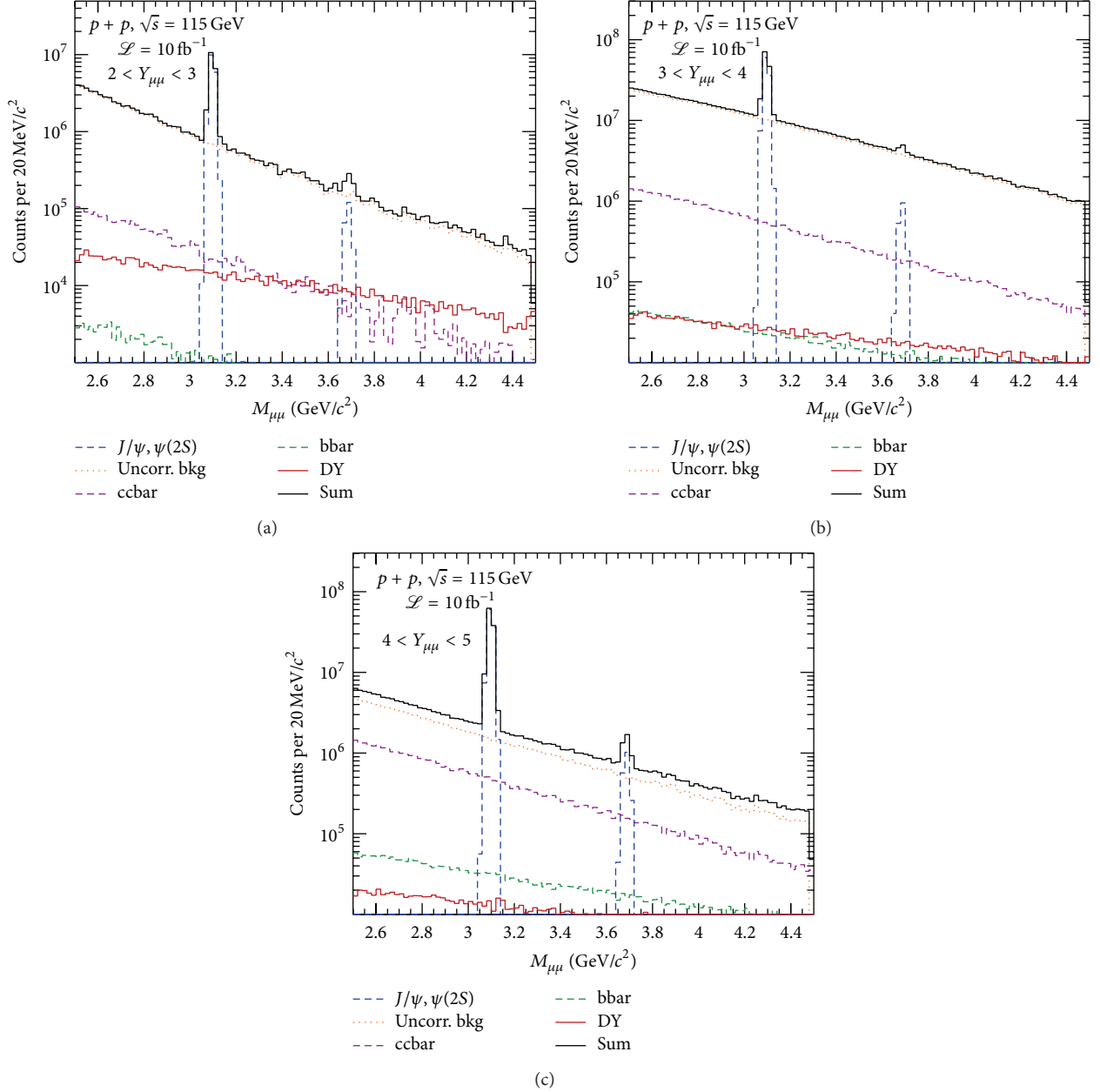


FIGURE 8: Dimuon invariant mass distributions for three rapidity bins in J/ψ and $\psi(2S)$ mass window. $2 < Y_{\mu^+\mu^-} < 3$, $3 < Y_{\mu^+\mu^-} < 4$, and $4 < Y_{\mu^+\mu^-} < 5$, shown on panels (a), (b), and (c), respectively.

of 0.3–0.4 fm. Obviously, this time has to be boosted in the frame where the nuclear matter sits. For t_f smaller than the nucleus radius, the quarkonium is formed before escaping it. In the fixed-target mode with a proton beam and a nuclear target, the boost factor is simply $\gamma(y_{\text{lab}}) = \cosh(y_{\text{lab}})$. We therefore obtain t_f as in Table 4.

One sees that looking at quarkonium production in p +Pb collisions at different backward rapidities allows one to look at quarkonia traversing the nuclear matter at very different stages of their evolution. This effect could theoretically be studied by giving an ad hoc rapidity dependence to the effective absorption cross section, $\sigma_{\text{abs}}^{\text{effective}}$. This is left for

TABLE 4: Boost and formation time in the (target) Pb rest frame of J/ψ and Y as a function of its c.m.s. rapidity at $\sqrt{s_{\text{NN}}} = 115$ GeV.

$y_{\text{c.m.s.}}$	y_{lab}	$\gamma(y_{\text{lab}})$	$t_f^{J/\psi,Y}(y)$	$y_{\text{c.m.s.}}$	y_{lab}	$\gamma(y_{\text{lab}})$	$t_f^{J/\psi,Y}(y)$
-2.5	2.3	5	1.75 fm	-0.5	4.3	37	13 fm
-1.5	3.3	14	5 fm	0.0	4.8	61	21 fm
-1.0	3.8	22	8 fm	0.5	5.3	100	35 fm

a future study since, here, we wish to consider only the nPDF effects and the expected statistics. Other effects to be considered are the coherent energy loss [48] (expected to

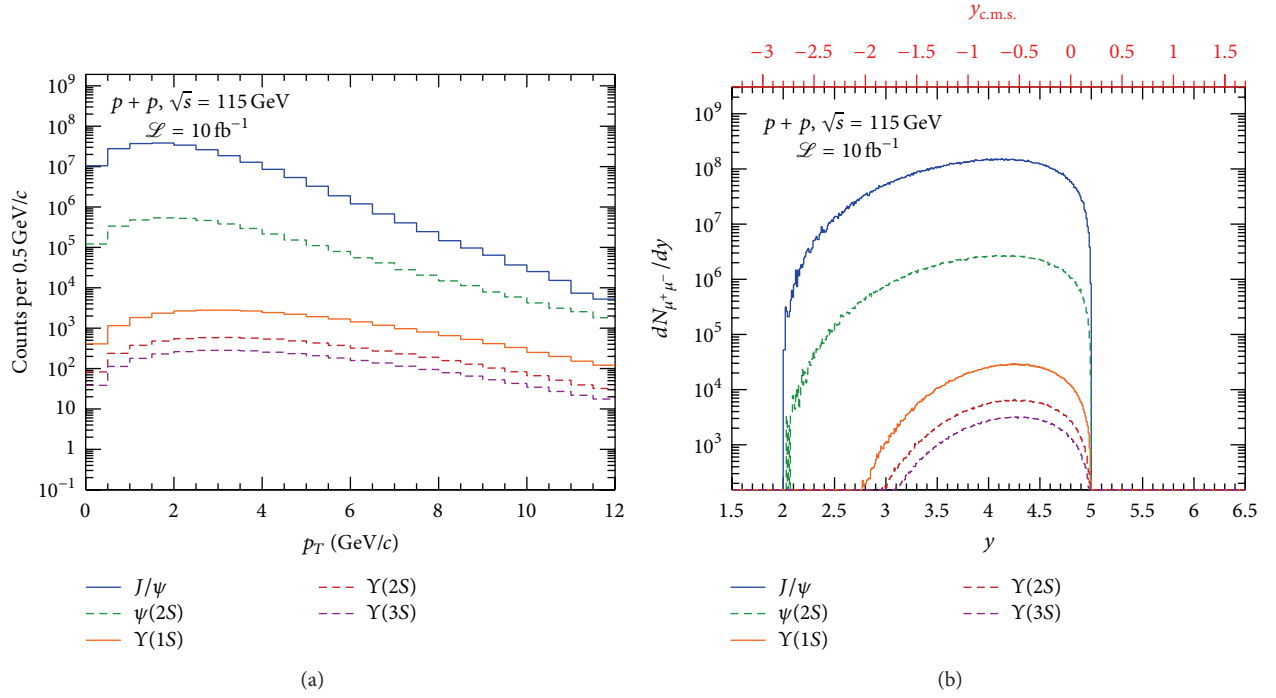


FIGURE 9: Transverse momentum (a) and rapidity (b) distributions for J/ψ , $\psi(2S)$, $Y(1S)$, $Y(2S)$, and $Y(3S)$ from the top to the bottom distribution.

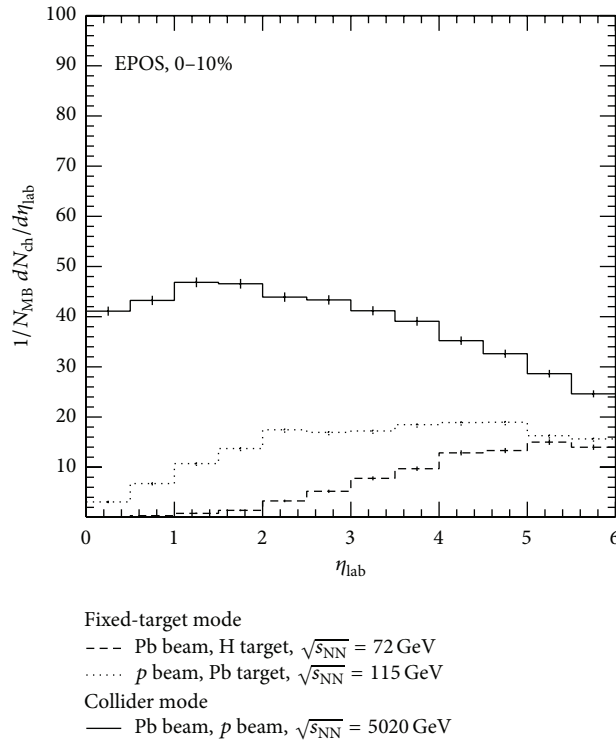


FIGURE 10: Averaged number of charged particles in $p + A$ collisions as a function of the pseudorapidity in the laboratory frame.

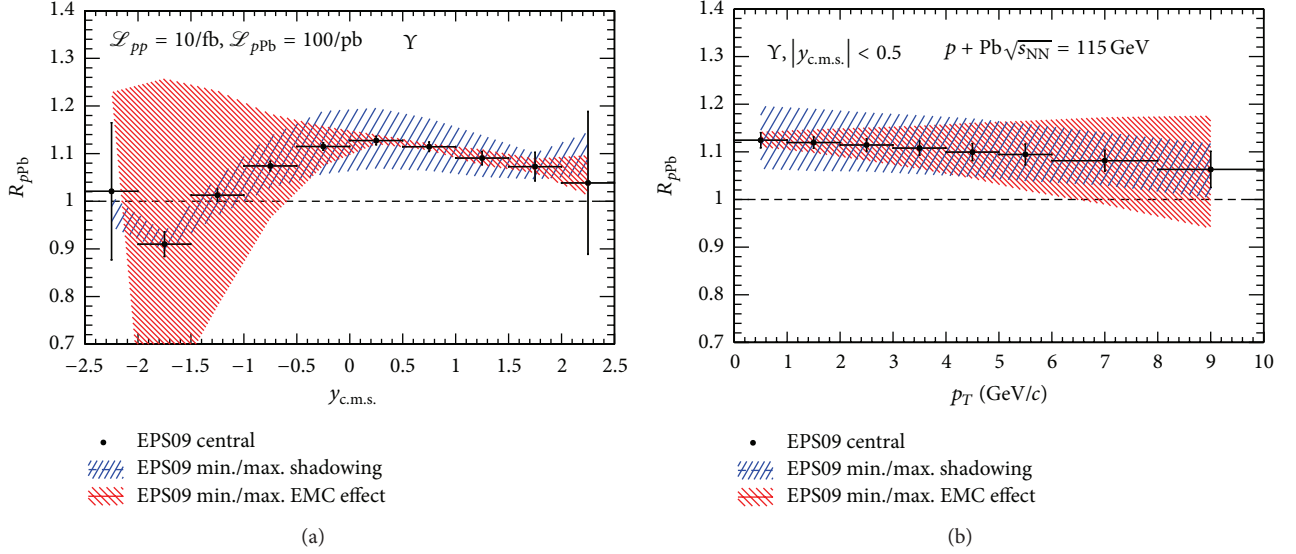


FIGURE 11: Nuclear modification factor for Υ as a function of (a) y_{CM} and (b) p_T in $p + Pb$ collisions at $\sqrt{s_{NN}} = 115$ GeV. The uncertainties attached to the central points are derived from the statistics to be collected with $\mathcal{L}_{p+p} = 10 \text{ fb}^{-1}$ and $\mathcal{L}_{p+Pb} = 100 \text{ pb}^{-1}$.

grow in the forward region) and the rescattering by comovers [49] (expected to grow with the multiplicity along the J/ψ direction).

Since we wish to assess the discriminating power of the possible data to be taken with AFTER@LHC, we attribute to the EPS09 central values statistical uncertainties which directly follow from the differential yields, respectively, expected in $p + p$ and $p + Pb$ collisions. For that we take an integrated luminosity of 10 fb^{-1} for the $p + p$ runs and 100 pb^{-1} for the $p + Pb$ runs, in accordance with the luminosities discussed above (see Table 1). As this stage, we do not consider additional systematical uncertainties. This simplifying assumption could be lifted in a more detailed study which would also take into account a possible detector acceptance (and related efficiencies) as done in the previous section. In particular, we do not expect that the rapidity region for $y_{CM} > 1.5$ would be easily accessible.

In Figure 11, we show the rapidity dependence of R_{pPb} for Υ and its p_T dependence near $y = 0$. The only million of Υ to be collected per year allows for the measurement of a R_{pPb} with a much better precision than the gluon nPDF, nearly up to $x \rightarrow 1$. In addition, one notes that the nuclear modification factor is certainly measurable up to $p_T \approx 10 \text{ GeV}/c$.

In Figure 12, we also show the rapidity dependence of R_{pPb} for J/ψ and its p_T dependence near $y = 0$. In both cases, the luminosity to be taken in a year at AFTER@LHC yields to statistical uncertainties which are largely negligible as compared to the nPDF uncertainties; the statistical uncertainties are not even visible in Figure 12. We expect this to hold also for the $\psi(2S)$ although its yields are down by a factor of 100.

As aforementioned, the nPDFs do not account for all the expected nuclear matter effects. However, it is clear that combining the measurements of Υ , J/ψ , and $\psi(2S)$ for

$-3 < y_{CM} < 0$ (as a LHCb-like detector would do) will allow one to pin down the existence of a possible gluon EMC and antishadowing effect. We also stress that the complications induced by a rapidity dependence of $\sigma_{abs}^{effective}$ could be avoided by the parallel measurement of R_{pPb} for nonprompt J/ψ which can only be sensitive to the energy loss since the b quark decay (weakly) into the J/ψ , way outside the nucleus. Figure 13 shows that the trend is similar compared to Υ . Measuring the p_T dependence of R_{pPb} for prompt J/ψ and Υ should also avoid the sensitivity on formation time effects.

6. Prospects of Pb + A Measurements at $\sqrt{s} = 72 \text{ GeV}$

The charged particle multiplicity has been generated with the EPOS generator [41, 42] in different configurations: Pb + Pb at $\sqrt{s_{NN}} = 5.5 \text{ TeV}$ in collider mode, Pb + Ar, Pb + Xe, and Pb + Pb at $\sqrt{s_{NN}} = 72 \text{ GeV}$ in fixed-target mode. By comparing these three distributions in the pseudorapidity of the particle in the laboratory frame as shown in Figure 14, one can conclude that the charged particle multiplicity in a fixed-target mode never exceeds the one obtained in Pb + Pb collisions at $\sqrt{s_{NN}} = 5.5 \text{ TeV}$ obtained in a collider mode in the full pseudorapidity range: a detector with the ALICE MFT+Muon detector [50] capability will be able to run in such conditions. Detailed studies are needed to evaluate up to which multiplicity a detector such as LHCb would be able to take good quality data.

7. Conclusion

In summary, we have shown that in a fixed-target mode with an integrated luminosity of 10 fb^{-1} , using 7 TeV LHC proton beam on a hydrogen target, and with a detector setup and performances similar to the LHCb detector, quarkonium

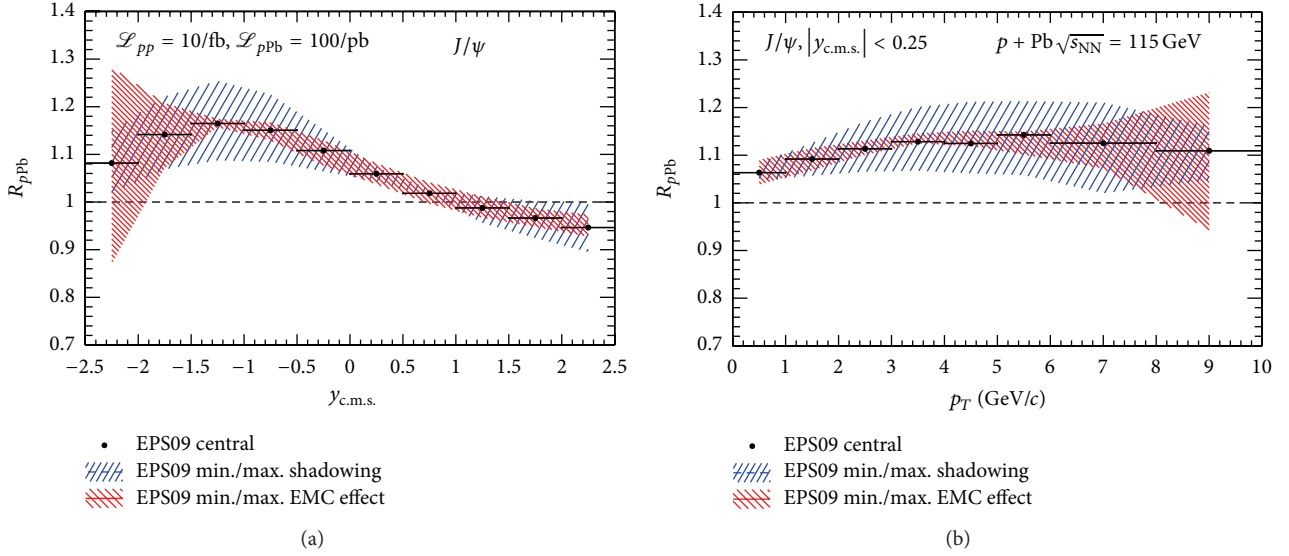


FIGURE 12: Nuclear modification factor for J/ψ as a function of (a) y_{CMS} and (b) p_T in $p + Pb$ collisions at $\sqrt{s_{NN}} = 115$ GeV. The uncertainties derived from the statistics to be collected with $\mathcal{L}_{p+p} = 10 \text{ fb}^{-1}$ and $\mathcal{L}_{p+Pb} = 100 \text{ pb}^{-1}$ are smaller than the point size.

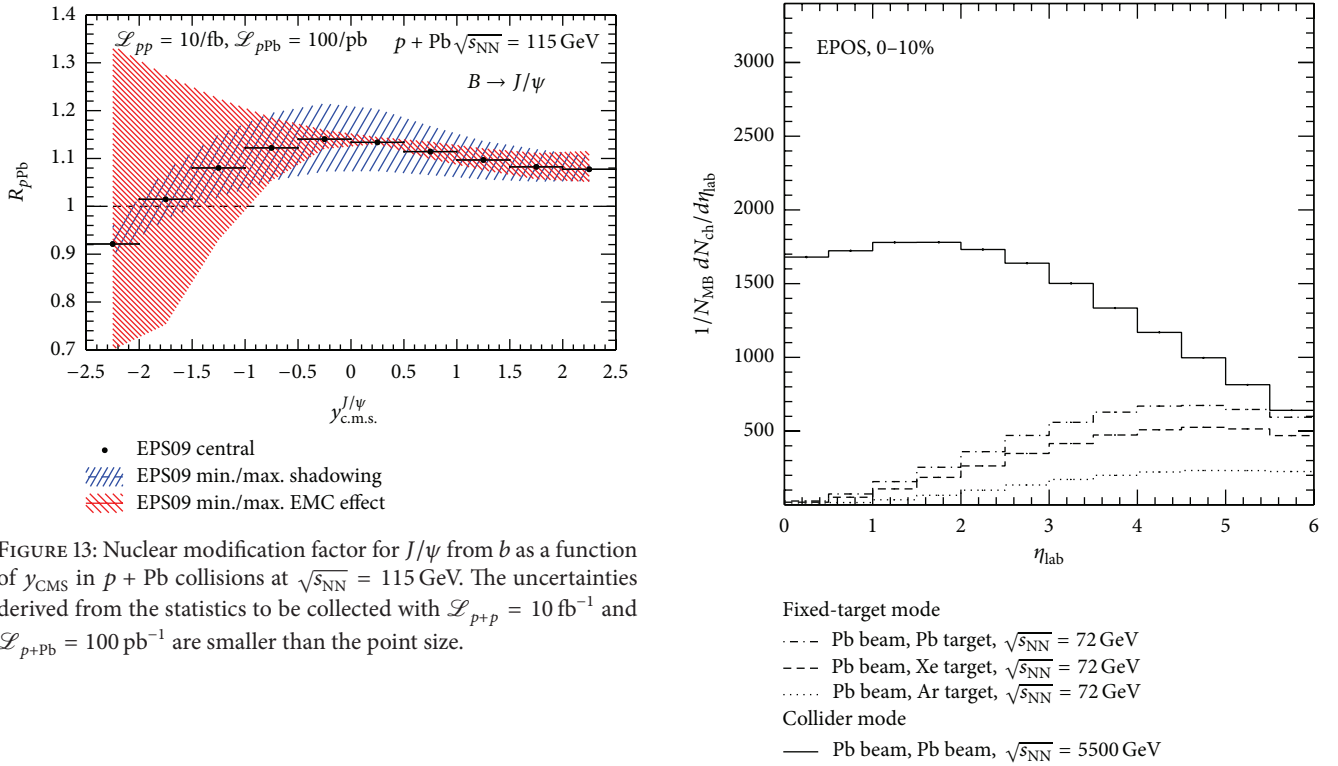


FIGURE 13: Nuclear modification factor for J/ψ from b as a function of y_{CMS} in $p + Pb$ collisions at $\sqrt{s_{NN}} = 115$ GeV. The uncertainties derived from the statistics to be collected with $\mathcal{L}_{p+p} = 10 \text{ fb}^{-1}$ and $\mathcal{L}_{p+Pb} = 100 \text{ pb}^{-1}$ are smaller than the point size.

studies in the dimuon decay channel can be performed over a wide transverse momentum range and rapidity in the center-of-mass from ~ -2.8 for J/ψ and $\psi(2S)$ and ~ -2 for Y states to ~ 0 . We have performed simulations of the dominant background sources contributing to the $\mu^+\mu^-$ invariant mass spectrum. The uncorrelated background was obtained using PYTHIA generator and dimuons from correlated background sources, $c\bar{c}$, $b\bar{b}$, and Drell-Yan, were simulated using both HELAC-ONIA and PYTHIA generators. The estimated background level allows for J/ψ , $\psi(2S)$, $Y(1S)$,

FIGURE 14: Averaged number of charged particles in $A + A$ collisions as a function of the pseudorapidity in the laboratory frame.

$Y(2S)$, and $Y(3S)$ measurements in the dimuon decay channel with good signal to background ratios.

These simulations set the stage for further ones including, on the one hand, the detection of photon from P wave or η_c decay or from the production of a $J/\psi + \gamma$ pair, whose studies

at low transverse momentum can provide important insight on the gluon transverse dynamics [51–54], and, on the other hand, the large combinatorial background typical of $p+A$ and $A+A$ collisions in which the study of excited quarkonium at AFTER@LHC energies is of paramount importance [1, 13]. We note that the DELPHES [55] framework seems particularly well suited to account for the photon detectability in such prospective studies.

Along our investigations, we have also noted that the main source of dimuons around the $Y(nS)$ masses is from the Drell-Yan process (see Figure 6(b)). This gives us great confidence that the corresponding cross section can easily be extracted in this mass region in $p+p$ collisions, a fortiori with a vertex detector allowing for tagging the heavy-flavour muons. We therefore consider that the single-spin asymmetries for Drell-Yan pair production can indeed be extracted using a light polarised target. Motivations for such studies are discussed in [15, 16, 56]. Quarkonium polarisation measurements are of course also possible, given the large statistical samples.

As regards the case of $p+A$ collisions, we have had a first look at the charged particle multiplicities as a function of the laboratory pseudorapidity. We have found out that, for all the possible fixed-target modes, $p+Pb$, $Pb+H$, and $Pb+Pb$, these are smaller than the ones reached in the collider modes, where the LHCb was used ($p+Pb$ and $Pb+p$ at 5 TeV). We therefore believe that a detector with similar characteristics as compared to LHCb can very well be used in the fixed-target mode (our observation is obviously supported by the preliminary analysis of the LHCb-SMOG data taken during the pilot run of p^+ beam (Pb beam) on a Neon gas target from 2012 (2013) at a c.m.s energy of $\sqrt{s_{NN}} = 87$ GeV (54 GeV) [57]).

In view of the above, we have evaluated the impact, and its uncertainty, on the nuclear modification of the gluon densities on prompt and nonprompt J/ψ and Y in the form of R_{p+Pb} . We have found that the measurements at backward rapidities allow one to search for the gluon antishadowing, the gluon EMC effect, and even the Fermi motion effect on the gluons with the unheard statistical precisions. The statistics are large enough to perform such measurement with the $\psi(2S)$ and probably also with $Y(2S)$ and $Y(3S)$ allowing for thorough investigations of the formation time effect of the meson propagating in the nuclear matter. Overall, our results confirm the great potential of AFTER@LHC for heavy-quark and quarkonium physics.

Conflict of Interests

The authors declare that there is no conflict of interests regarding the publication of this paper.

Acknowledgments

The authors thank C. Da Silva, D. d'Enterria, E. G. Ferreira, R. Mikkelsen, S. Porteboeuf-Houssais, A. Rakotozafindrabe, P. Robbe, M. Selvaggi, M. Schmelling, P. Skands, and Z. Yang for the important and stimulating discussions. This research was supported in part by the ERC Grant 291377

“LHCtheory: Theoretical predictions and analyses of LHC physics: advancing the precision frontier,” by the COPIN-IN2P3 Agreement, by the French P210 Excellence Laboratory, by the French CNRS via the grants PICS-06149 Torino-IPNO and FCPPL-Quarkonium4AFTER & PEPS4AFTER2, by the European Social Fund within the framework of realizing the project “Support of intersectoral mobility and quality enhancement of research teams at Czech Technical University in Prague,” CZ.1.07/2.3.00/30.0034, by Grant Agency of the Czech Republic, Grant no. 13-20841S, and by the Foundation for Polish Science Grant HOMING PLUS/2013-7/8.

References

- [1] S. J. Brodsky, F. Fleuret, C. Hadjidakis, and J. P. Lansberg, “Physics opportunities of a fixed-target experiment using LHC beams,” *Physics Reports*, vol. 522, no. 4, pp. 239–255, 2013.
- [2] G. Arduini, K. Elsener, G. Fidencaro et al., “On the energy dependence of proton beam extraction with a bent crystal,” *Physics Letters B*, vol. 422, no. 1–4, pp. 325–333, 1998.
- [3] W. Scandale, G. Arduini, R. Assmann et al., “Comparative results on collimation of the SPS beam of protons and Pb ions with bent crystals,” *Physics Letters B*, vol. 703, no. 5, pp. 547–551, 2011.
- [4] E. Uggerhoj and U. I. Uggerhoj, “Strong crystalline fields: a possibility for extraction from the LHC,” *Nuclear Instruments and Methods in Physics Research B*, vol. 234, pp. 31–39, 2005.
- [5] LHC Committee, “Minutes of 107th meeting,” Tech. Rep. CERN/LHC, 2011.
- [6] C. Barschel, *Precision luminosity measurement at LHCb with beam-gas imaging [Ph.D. thesis]*, RWTH Aachen University, 2013.
- [7] M. Ferro-Luzzi, “Proposal for an absolute luminosity determination in colliding beam experiments using vertex detection of beam-gas interactions,” *Nuclear Instruments and Methods in Physics Research A*, vol. 553, no. 3, pp. 388–399, 2005.
- [8] R. Aaij, B. Adeva, M. Adinolfi et al., “Precision luminosity measurements at LHCb,” *Journal of Instrumentation*, vol. 9, no. 12, Article ID P12005, 2014.
- [9] A. Adare, S. Afanasiev, C. Aidala et al., “Ground and excited state charmonium production in $p+p$ collisions at $\sqrt{s} = 200$ GeV,” *Physical Review D*, vol. 85, Article ID 092004, 2012.
- [10] R. Aaij, C. Abellan Beteta, B. Adeva et al., “Measurement of Y production in pp collisions at $\sqrt{s} = 7$ TeV,” *The European Physical Journal C*, vol. 72, article 2025, 2012.
- [11] A. Rakotozafindrabe, M. Anselmino, R. Arnaldi et al., “Spin physics at a fixed-target experiment at the LHC (AFTER@LHC),” *Physics of Particles and Nuclei*, vol. 45, no. 1, pp. 336–337, 2014.
- [12] N. Brambilla, S. Eidelman, B. K. Heltsley et al., “Heavy quarkonium: progress, puzzles, and opportunities,” *The European Physical Journal C*, vol. 71, article 1534, 2011.
- [13] J. P. Lansberg, S. J. Brodsky, F. Fleuret, and C. Hadjidakis, “Quarkonium physics at a fixed-target experiment using the LHC beams,” *Few-Body Systems*, vol. 53, no. 1–2, pp. 11–25, 2012.
- [14] J. P. Lansberg, R. Arnaldi, S. J. Brodsky et al., “AFTER@LHC: a precision machine to study the interface between particle and nuclear physics,” *EPJ Web of Conferences*, vol. 66, Article ID 11023, 2014.
- [15] T. Liu and B.-Q. Ma, “Azimuthal asymmetries in lepton-pair production at a fixed-target experiment using the LHC beams

- (AFTER)," *The European Physical Journal C*, vol. 72, article 2037, 2012.
- [16] K. Kanazawa, Y. Koike, A. Metz, and D. Pitonyak, "Transverse single-spin asymmetries in proton-proton collisions at the AFTER@LHC experiment," *Advances in High Energy Physics*. Accepted.
 - [17] A. Rakotozafindrabe, R. Arnaldi, S. J. Brodsky et al., "Ultra-relativistic heavy-ion physics with AFTER@LHC," *Nuclear Physics A*, vol. 904-905, pp. 957c-960c, 2013.
 - [18] H.-S. Shao, "HELAC-Onia: an automatic matrix element generator for heavy quarkonium physics," *Computer Physics Communications*, vol. 184, no. 11, pp. 2562-2570, 2013.
 - [19] J. Alwall, A. Ballestrero, P. Bartalini et al., "A standard format for Les Houches event files," *Computer Physics Communications*, vol. 176, no. 4, pp. 300-304, 2007.
 - [20] T. Sjöstrand, S. Mrenna, and P. Skands, "A brief introduction to PYTHIA 8.1," *Computer Physics Communications*, vol. 178, no. 11, pp. 852-867, 2008.
 - [21] C. H. Kom, A. Kulesza, and W. J. Stirling, "Pair production of J/ψ as a probe of double parton scattering at LHCb," *Physical Review Letters*, vol. 107, no. 8, Article ID 082002, 2011.
 - [22] K. Olive, K. Agashe, C. Amsler et al., "Review of particle physics," *Chinese Physics C*, vol. 38, Article ID 090001, 2014.
 - [23] A. D. Martin, W. J. Stirling, R. S. Thorne, and G. Watt, "Parton distributions for the LHC," *The European Physical Journal C*, vol. 63, no. 2, pp. 189-285, 2009.
 - [24] M. Whalley, D. Bourilkov, and R. Group, "The les Houches accord PDFs (LHAPDF) and LHAGLUE," <http://arxiv.org/abs/hep-ph/0508110>.
 - [25] D. Acosta, T. Affolder, H. Akimoto et al., "Y production and polarization in $p\bar{p}$ collisions at $\sqrt{s} = 1.8$ TeV," *Physical Review Letters*, vol. 88, Article ID 161802, 2002.
 - [26] G. Aad, B. Abbott, J. Abdallah et al., "Measurement of upsilon production in 7 TeV pp collisions at ATLAS," *Physical Review D*, vol. 87, no. 5, Article ID 052004, 2013.
 - [27] S. Chatrchyan, V. Khachatryan, A. M. Sirunyan et al., "Measurement of the $Y(1S)$, $Y(2S)$, and $Y(3S)$ cross sections in pp collisions at $\sqrt{s} = 7$ TeV," *Physics Letters B*, vol. 727, no. 1-3, pp. 101-125, 2013.
 - [28] R. Aaij, C. Abellan Beteta, B. Adeva et al., "Production of J/ψ and Y mesons in pp collisions at $\sqrt{s} = 8$ TeV," *Journal of High Energy Physics*, vol. 2013, no. 6, article 64, 2013.
 - [29] STAR Collaboration and Z. Ye, "Open charm hadron production in $p + p$, Au + Au and U + U collisions at STAR," *Nuclear Physics A*, vol. 931, pp. 520-524, 2014.
 - [30] J. Pumplin, D. R. Stump, J. Huston, H.-L. Lai, P. Nadolsky, and W.-K. Tung, "New generation of parton distributions with uncertainties from global QCD analysis," *Journal of High Energy Physics*, vol. 6, no. 7, pp. 325-371, 2002.
 - [31] J. Alwall, R. Frederix, S. Frixione et al., "The automated computation of tree-level and next-to-leading order differential cross sections, and their matching to parton shower simulations," *Journal of High Energy Physics*, vol. 2014, no. 7, article 079, 2014.
 - [32] J. C. Webb, T. C. Awes, M. L. Brooks et al., "Absolute Drell-Yan dimuon cross sections in 800 GeV/c pp and pd collisions," <http://arxiv.org/abs/hep-ex/0302019>.
 - [33] C. Anastasiou, L. J. Dixon, K. Melnikov, and F. Petriello, "Dilepton rapidity distribution in the Drell-Yan process at NNLO in QCD," *Physical Review Letters*, vol. 91, Article ID 182002, 2003.
 - [34] A. Buckley, J. Ferrando, S. Lloyd et al., "LHAPDF6: parton density access in the LHC precision era," *The European Physical Journal C*, vol. 75, no. 3, p. 132, 2015.
 - [35] A. Augusto Alves Jr., I. Andrade Filho, A. F. Barbosa et al., "The LHCb detector at the LHC," *Journal of Instrumentation*, vol. 3, Article ID S08005, 2008.
 - [36] R. Aaij, B. Adeva, M. Adinolfi et al., "Measurement of J/ψ production in pp collisions at $\sqrt{s} = 7$ TeV," *The European Physical Journal C*, vol. 71, article 1645, 2011.
 - [37] F. Archilli, W. Baldini, G. Bencivenni et al., "Performance of the Muon identification at LHCb," *Journal of Instrumentation*, vol. 8, Article ID P10020, 2013.
 - [38] R. Aaij, B. Adeva, M. Adinolfi et al., "LHCb detector performance," *International Journal of Modern Physics A*, vol. 30, no. 7, Article ID 1530022, 2015.
 - [39] R. Aaij, B. Adeva, M. Adinolfi et al., "Study of J/ψ production and cold nuclear matter effects in p Pb collisions at $\sqrt{s_{NN}} = 5$ TeV," *Journal of High Energy Physics*, vol. 2014, no. 2, article 72, 2014.
 - [40] R. Aaij, B. Adeva, M. Adinolfi et al., "Study of Y production and cold nuclear matter effects in p Pb collisions at $\sqrt{s_{NN}} = 5$ TeV," *Journal of High Energy Physics*, vol. 2014, no. 7, article 094, 2014.
 - [41] T. Pierog, I. Karpenko, J. Katzy, E. Yatsenko, and K. Werner, "EPOS LHC: test of collective hadronization with LHC data," <http://arxiv.org/abs/1306.0121>.
 - [42] K. Werner, F.-M. Liu, and T. Pierog, "Parton ladder splitting and the rapidity dependence of transverse momentum spectra in deuteron-gold collisions at the BNL Relativistic Heavy Ion Collider," *Physical Review C*, vol. 74, no. 4, Article ID 044902, 11 pages, 2006.
 - [43] E. Ferreira, F. Fleuret, and A. Rakotozafindrabe, "Transverse-momentum dependence of J/ψ shadowing effects," *The European Physical Journal C*, vol. 61, no. 4, pp. 859-864, 2009.
 - [44] E. G. Ferreira, F. Fleuret, J. P. Lansberg, and A. Rakotozafindrabe, "Cold nuclear matter effects on J/ψ production: intrinsic and extrinsic transverse momentum effects," *Physics Letters B*, vol. 680, no. 1, pp. 50-55, 2009.
 - [45] E. G. Ferreira, F. Fleuret, J. P. Lansberg, and A. Rakotozafindrabe, "Impact of the nuclear modification of the gluon densities on J/ψ production in pPb collisions at $\sqrt{s_{NN}} = 5$ TeV," *Physical Review C*, vol. 88, no. 4, Article ID 047901, 2013.
 - [46] K. Eskola, H. Paukkunen, and C. Salgado, "EPS09: a new generation of NLO and LO nuclear parton distribution functions," *Journal of High Energy Physics*, vol. 2009, no. 4, article 065, 2009.
 - [47] E. G. Ferreira, F. Fleuret, J. P. Lansberg, N. Matagne, and A. Rakotozafindrabe, "Y production in $p(d)A$ collisions at RHIC and the LHC," *The European Physical Journal C*, vol. 73, article 2427, 2013.
 - [48] F. Arleo and S. Peigné, " J/ψ suppression in p-A collisions from parton energy loss in cold QCD matter," *Physical Review Letters*, vol. 109, no. 12, Article ID 122301, 2012.
 - [49] E. Ferreira, " $\psi(2S)$ versus J/ψ suppression in the comover interaction approach," <http://arxiv.org/abs/1411.0549>.
 - [50] ALICE Collaboration, "Addendum of the letter of intent for the upgrade of the ALICE experiment: the Muon forward tracker," Tech. Rep. CERN-LHCC-2013-014. LHCC-I-022-ADD-1, CERN, Geneva, Switzerland, 2013, <https://cds.cern.ch/record/1592659>.
 - [51] D. Boer and C. Pisano, "Polarized gluon studies with charmonium and bottomonium at LHCb and after," *Physical Review D—Particles, Fields, Gravitation and Cosmology*, vol. 86, no. 9, Article ID 094007, 2012.

- [52] J. P. Ma, J. X. Wang, and S. Zhao, “Transverse momentum dependent factorization for quarkonium production at low transverse momentum,” *Physical Review D*, vol. 88, no. 1, Article ID 014027, 2013.
- [53] W. J. den Dunnen, J.-P. Lansberg, C. Pisano, and M. Schlegel, “Accessing the transverse dynamics and polarization of gluons inside the proton at the LHC,” *Physical Review Letters*, vol. 112, no. 21, Article ID 212001, 2014.
- [54] J. P. Lansberg, “Back-to-back isolated photon-quarkonium production at the LHC and the transverse-momentum-dependent distributions of the gluons in the proton,” <http://arxiv.org/abs/1502.02263>.
- [55] J. de Favereau, C. Delaere, P. Demin et al., “DELPHES 3: a modular framework for fast simulation of a generic collider experiment,” *Journal of High Energy Physics*, vol. 2014, no. 2, article 057, 2014.
- [56] M. Anselmino, U. D’Alesio, and S. Melis, “Transverse single-spin asymmetries in proton-proton collisions at the AFTER@LHC experiment in a TMD factorisation scheme,” <http://arxiv.org/abs/1504.03791>.
- [57] R. Aaij, J. de Miranda, A. Gomes et al., “First analysis of the $p\text{Pb}$ pilot run data with LHCb,” LHCb-CONF-2012-034, January 2013.

Research Article

Gluon Shadowing Effects on J/ψ and Υ Production in $p + \text{Pb}$ Collisions at $\sqrt{s_{NN}} = 115 \text{ GeV}$ and $\text{Pb} + p$ Collisions at $\sqrt{s_{NN}} = 72 \text{ GeV}$ at AFTER@LHC

R. Vogt^{1,2}

¹Nuclear and Chemical Sciences Division, Lawrence Livermore National Laboratory, Livermore, CA 94551, USA

²Physics Department, University of California at Davis, Davis, CA 95616, USA

Correspondence should be addressed to R. Vogt; rlvogt@lbl.gov

Received 19 March 2015; Accepted 21 May 2015

Academic Editor: Barbara Trzeciak

Copyright © 2015 R. Vogt. This is an open access article distributed under the Creative Commons Attribution License, which permits unrestricted use, distribution, and reproduction in any medium, provided the original work is properly cited. The publication of this article was funded by SCOAP³.

We explore the effects of shadowing on inclusive J/ψ and $\Upsilon(1S)$ production at AFTER@LHC. We also present the rates as a function of p_T and rapidity for $p + \text{Pb}$ and $\text{Pb} + p$ collisions in the proposed AFTER@LHC rapidity acceptance.

1. Introduction

The AFTER@LHC quarkonium program has the unique opportunity to study quarkonium production at large momentum fractions, x , in the target region [1]. The most favorable configuration for high rates at large x for the nucleus is a proton beam from the LHC on a heavy nuclear target. In this case, the nucleon-nucleon center of mass energy is more than half that of the RHIC collider, $\sqrt{s_{NN}} = 115 \text{ GeV}$, for the top LHC proton beam energy of 7 TeV. However, the fixed-target configuration is an advantage because of the higher intensity on target. The longer LHC proton runs give a luminosity over a 10^7 s LHC “year.” On a 1 cm thick Pb target, with $p + \text{Pb}$ collisions, $\mathcal{L} = 16 A \mu\text{b}^{-1} \text{ s}^{-1}$. When a lead beam is extracted, the run time is shorter and an LHC Pb “year” is 10^6 s . The lower Z/A ratio also results in a lower center of mass energy of $\sqrt{s_{NN}} = 72 \text{ GeV}$ for the top lead beam energy of 2.76 TeV. On a liquid H_2 target, for $\text{Pb} + p$ collisions, $\mathcal{L} = 8 A_{\text{Pb}} \text{ mb}^{-1} \text{ s}^{-1}$ per centimeter target length so that a 1 m target gives a luminosity of $\mathcal{L} = 800 A_{\text{Pb}} \text{ mb}^{-1} \text{ s}^{-1}$ [1].

Here, we will consider the inclusive J/ψ and $\Upsilon(1S)$ rates in $p + \text{Pb}$ collisions at $\sqrt{s_{NN}} = 115 \text{ GeV}$ and $\text{Pb} + p$ collisions at $\sqrt{s_{NN}} = 72 \text{ GeV}$. The results are presented as a function

of rapidity, y , and transverse momentum, p_T , of the quarkonium state. We choose to present the p_T results in a 0.5-unit wide rapidity bin in the backward region of the center of mass of the collision, $-2.5 < y_{\text{cms}} < -2.0$ for $\sqrt{s_{NN}} = 115 \text{ GeV}$ and $-1.9 < y_{\text{cms}} < -1.4$ for $\sqrt{s_{NN}} = 72 \text{ GeV}$. This is a region that has been virtually unexplored in previous quarkonium production measurements but, as we will show, can be studied by AFTER@LHC with relatively high statistics in most cases.

Our calculations are done in the next-to-leading order (NLO) color evaporation model (CEM) [2] and employ the EPS09 NLO parameterization [3] of the effects of modification of the parton distribution functions in the nucleus, referred to here as “shadowing.” Since this set also provides an uncertainty band, the results are representative of the range of shadowing parameterizations produced by other groups.

We also present the nuclear suppression factor ratios, $R_{p\text{Pb}}$ for $p + \text{Pb}$ collisions and $R_{\text{Pb}p}$ for $\text{Pb} + p$ collisions. These quantities are the ratio of the per nucleon cross sections in $p + \text{Pb}$ ($\text{Pb} + p$) collisions relative to the same cross section in $p + p$ collisions at the same center of mass energy. These ratios are also given as a function of p_T and y .

In Section 2, we will show the EPS09 NLO shadowing parameterizations at the appropriate factorization scale for J/ψ and Υ production as a function of x with emphasis on

the appropriate x regions for the AFTER@LHC kinematics. We present the ratios and rates obtained with the EPS09 NLO parameterization in Section 3. We conclude with some final remarks in Section 4.

2. Shadowing Parameterization

Our calculations employ the EPS09 shadowing parameterization [3]. At NLO, it is based on the CTEQ6M proton parton densities (PDFs) [4, 5]. In our calculations of quarkonium production [6, 7], we use the CT10 [8] proton PDFs with the EPS09 NLO parameterization. As long as both calculations are at NLO, the choice of proton PDFs used to calculate quarkonium production does not affect the shape or magnitude of the nuclear suppression factors [9].

One possibility for the AFTER@LHC experiment is to use the LHCb detector, either as is, with $2 < y_{\text{lab}} < 5$, or an improved LHCb (LHCb+), with $1 < y_{\text{lab}} < 5$.

In the fixed-target kinematics of AFTER@LHC, with a 7 TeV proton beam, the rapidity range is $\Delta y = 4.8$, corresponding to a center of mass rapidity coverage of $-2.8 < y_{\text{cms}} < 0.2$ for LHCb or $-3.8 < y_{\text{cms}} < 0.2$ for LHCb+ in p +Pb collisions at $\sqrt{s_{NN}} = 115$ GeV. In this case, the Pb nucleus is the target. If x_1 refers to the momentum fraction probed in the proton beam and x_2 is the momentum fraction probed in the lead target, in these kinematics, the negative rapidity means that x_2 is large, $x_2 > 0.1$. This x_2 range has not been explored since early nuclear deep-inelastic scattering (nDIS) measurements, such as the European Muon Collaboration [10, 11] and SLAC [12], and has never been explored by gluon-dominated processes such as quarkonium production. AFTER@LHC would be the first experiment to probe these kinematics since most fixed-target configurations studying quarkonium have placed the detectors downstream where $x_1 > x_2$, as the CERN SPS [13, 14] and the Fermilab Tevatron [15]. The only quarkonium experiment to measure part of this backward large x_2 region was HERA-B with its foils placed around the edges of the proton beam at HERA [16].

On the other hand, with a 2.76 TeV lead beam, the rapidity range is $\Delta y = 4.3$, corresponding to a center of mass rapidity coverage of $-2.3 < y_{\text{cms}} < 0.7$ for LHCb or $-3.3 < y_{\text{cms}} < 0.7$ for LHCb+ in Pb + p collisions at $\sqrt{s_{NN}} = 72$ GeV. In this case, the proton is the target, with x_2 , and the lead beam is assigned as x_1 . Thus, the nuclear momentum fractions probed are moderate, $x_1 \sim 0.01$. This x region has been well studied in nDIS experiments but, again, not for final states dominated by initial-state gluons.

Global fits to the nuclear parton densities (nPDFs), such as EPS09, typically include nuclear deep-inelastic scattering data (F_2 in $l + A$ and $dF_2/d\ln Q^2$), Drell-Yan data, and, more recently, RHIC data such as π^0 production [3]. The range over which DGLAP evolution can be applied ($Q^2 > 1 \text{ GeV}^2$) for fixed-target nDIS limits the minimum x values probed. In addition, such analyses do not take into account the possibility of any other cold nuclear matter effects so that the possibility of an effect such as initial-state energy loss in matter by quarks in Drell-Yan dilepton production is folded in with the global analysis of nuclear shadowing. Quarkonium production is particularly subject to other cold

nuclear matter effects such as energy loss in matter, breakup of the quarkonium state by nucleons (nuclear absorption), and interactions with comoving hadrons; see, for example, [17] for a discussion. Regarding the purposes of this paper, we focus only on the expected effects of shadowing.

Figure 1 shows the EPS09 NLO gluon shadowing parameterization as a function of momentum fraction, x . The scales at which the results are shown correspond to those used in the CEM for J/ψ (Figures 1(a) and 1(c)) and Υ (Figures 1(b) and 1(d)) production. Along with the central set, denoted by the solid curves, the dotted curves display the uncertainty band. EPS09 obtains 30 additional sets of shadowing ratios by varying each of the 15 parameters within one standard deviation of the mean. The differences are added in quadrature to produce the uncertainty band in the shadowing ratio S_g . (We note that the uncertainties in the corresponding LO set are larger while the central shadowing effect is greater at LO than at NLO. For more details concerning this set as well as differences between other available nPDF sets, see [9].)

The vertical blue line in Figure 1 shows the average x value for the final quarkonium states at each energy, $p + \text{Pb}$ on top and $\text{Pb} + p$ on the bottom. This is obtained by estimating the average x value from the simpler $2 \rightarrow 1$ kinematics of the LO CEM with $x_{1,2} = (2m/\sqrt{s_{NN}}) \exp(\pm y)$ and replacing m by $m_T = \sqrt{m^2 + p_T^2}$ with $p_T^2 = 0.5(p_{T_Q}^2 + p_{T_{\bar{Q}}}^2)$. The x value from the LO CEM represents a lower limit on x relative to the actual $2 \rightarrow 2$ and $2 \rightarrow 3$ kinematics of the LO and NLO contributions to the full NLO CEM calculation. The average center of mass rapidity, $\langle y_{\text{cms}} \rangle$, shown in Figure 1 is the approximate midpoint of our chosen rapidity interval in each case. The average p_T of ~ 2 GeV is near the peak of the p_T distributions. These values should not be thought of as having the most weight in the actual calculations which integrate over the rapidity interval for the p_T distributions and all p_T for the rapidity distributions. Indeed, since the rapidity distributions are steeply falling, the preponderance of the rate comes from the upper end of the range in each case. Thus, the vertical lines represent an estimate of the lower bound on the x range at the given value of p_T .

The $p + \text{Pb}$ kinematics emphasize high x in the nucleus (Figures 1(a) and 1(b)) and thus explore an x range rarely probed, especially by gluon-dominated processes. It is partly in the ‘‘EMC’’ region of the x range and also moves into the regime of ‘‘Fermi motion.’’ See a discussion of how the various x regions are parameterized by Eskola and collaborators in [18, 19]. Given the shortage of direct gluon-induced data in the global analyses, the gluon shadowing ratios are constrained by the momentum sum rule. The gluon shadowing ratios shown in Figures 1(a) and 1(b) are plotted on a linear scale to highlight the large x region. Here, the scale dependence is very weak, illustrated by the similarities in the results for the two quarkonium scales shown, while the uncertainties in the nPDF extraction are the largest. AFTER@LHC measurements could help narrow this uncertainty range.

On the other hand, the $\text{Pb} + p$ kinematics are in an x region where quark-dominated processes, as in nDIS, are well measured and the uncertainties can be expected to be relatively small, see Figures 1(c) and 1(d).

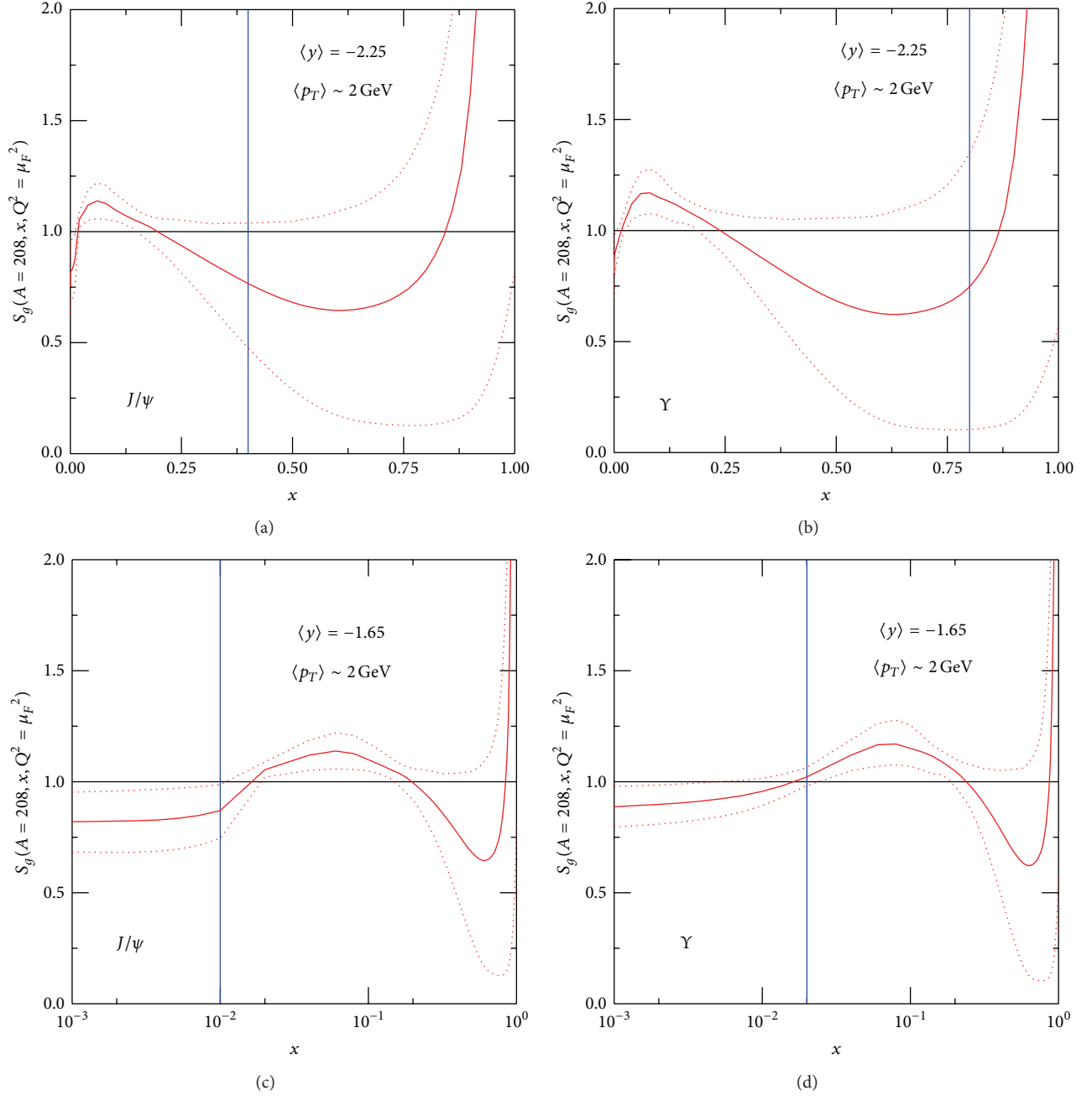


FIGURE 1: The EPS09 NLO shadowing ratios for J/ψ (a, c) and $\Upsilon(1S)$ (b, d) production. The solid curve in each plot is the central EPS09 NLO result, while the dotted curves outline the shadowing uncertainty band. (a, b) are on a linear scale to emphasize the large x region, while (c, d) are on a logarithmic scale to expand the low x region. The approximate kinematic area of interest is indicated by the vertical line in each case.

3. Cold Nuclear Matter Effects and Quarkonium Production Rates

There are other possible cold matter effects on J/ψ production in addition to those of shadowing: breakup of the quarkonium state due to inelastic interactions with nucleons (absorption) or produced hadrons (comovers) and energy loss in cold matter.

The quarkonium absorption cross section at midrapidity was seen to decrease with center of mass energy in [20], independent of whether shadowing effects were included or not. It was also seen that incorporating shadowing into the extraction of the absorption cross section required a larger effective cross section [20]. Extrapolating from the results of [20] to the energy range of AFTER@LHC, we can expect an effective absorption cross section of a few millibarns at

midrapidity. Away from midrapidity, the effective absorption cross section was seen to rise at forward Feynman x , x_F [20], which could be attributed to energy loss in matter [21, 22]. When a similar analysis was extended to the RHIC collider geometry, the effective absorption cross section was also seen to increase in the backward region [23]. Such behavior could be attributed to the quarkonium state being fully formed inside the nucleus. The $p + \text{Pb}$ kinematics of AFTER@LHC would be an ideal environment to study absorption in the target if other observables such as direct photon production can also probe shadowing effects to disentangle the two.

The shadowing results shown here are obtained in the color evaporation model (CEM) [24, 25] at next-to-leading order in the total cross section [2]. In the CEM, the quarkonium production cross section is some fraction, F_C , of all $Q\bar{Q}$ pairs below the $H\bar{H}$ threshold where H is the lowest mass heavy-flavor hadron:

$$\sigma_C^{\text{CEM}}(s) = F_C \sum_{ij} \int_{4m^2}^{4m_H^2} ds \int dx_1 dx_2 f_i^p(x_1, \mu_F^2) \cdot f_j^p(x_2, \mu_F^2) \hat{\sigma}_{ij}(\hat{s}, \mu_F^2, \mu_R^2), \quad (1)$$

where $ij = q\bar{q}$ or gg and $\hat{\sigma}_{ij}(\hat{s})$ are the $ij \rightarrow Q\bar{Q}$ subprocess cross section. The normalization factor F_C is fit to the forward (integrated over $x_F > 0$) J/ψ cross-sectional data and the combined $Y(nS)$ state data at midrapidity. We use the code of [26] with the mass cut implemented.

The same values of the central charm quark mass and scale parameters are employed as those found for open charm, $m_c = 1.27 \pm 0.09 \text{ GeV}$, $\mu_F/m_c = 2.10_{-0.85}^{+2.55}$, and $\mu_R/m_c = 1.60_{-0.12}^{+0.11}$ [6]. The normalization F_C is obtained for the central set, $(m_c, \mu_F/m_c, \mu_R/m_c) = (1.27 \text{ GeV}, 2.1, 1.6)$. The calculations for the extent of the mass and scale uncertainties are multiplied by the same value of F_C to obtain the extent of the J/ψ uncertainty band [6]. These values reproduce the energy dependence of J/ψ production from fixed target to collider energies. The resulting rapidity and p_T distributions also agree with the $p + p$ data from RHIC and the LHC at $\sqrt{s} = 200 \text{ GeV}$ and 7 TeV , respectively [6].

We calculate Y production in the same manner, with the central result obtained for $(m_b, \mu_F/m_b, \mu_R/m_b) = (4.65 \text{ GeV}, 1.4, 1.1)$ [7]. We have also found good agreement with \sqrt{s} and p_T distributions from previous measurements [7]. Unfortunately, the uncertainties from RHIC measurements are rather large and few data are available on the shape of the Y rapidity distributions.

To obtain the quarkonium p_T distributions at low p_T , intrinsic transverse momentum, k_T , smearing for quarkonium is included in the initial-state parton densities [27]. Since the MNR code cancels divergences numerically, instead of slowing the calculations by adding more integrations, the k_T kick is added in the final, rather than the initial, state [26]. The Gaussian function $g_p(k_T) = \pi \langle k_T^2 \rangle_p^{-1} \exp(-k_T^2 / \langle k_T^2 \rangle_p)$ [28] multiplies the parton distribution functions for both hadrons, assuming that x and k_T dependencies in the initial partons completely factorize. If factorization applies, it does not matter whether the k_T dependence appears in the initial

or final state if the kick is not too large. The effect of the intrinsic k_T on the shape of the J/ψ p_T distribution can be expected to decrease as \sqrt{s} increases because the average p_T of the J/ψ also increases with energy. However, the value of $\langle k_T^2 \rangle$ may increase with \sqrt{s} . We can check the energy dependence of $\langle k_T^2 \rangle$ by the shape of the J/ψ p_T distributions at central and forward rapidity at RHIC. We find that $\langle k_T^2 \rangle = 1 + (1/12) \ln(\sqrt{s}/20) \approx 1.19 \text{ GeV}^2$ at $\sqrt{s} = 200 \text{ GeV}$ agrees well with the J/ψ p_T distributions [6]. All the calculations are NLO in the total cross section and assume that the intrinsic k_T broadening is the same in $p + p$ as in $p + \text{Pb}$. While the broadening is expected to increase in collisions with nuclei as projectile, target, or both, the agreement of the J/ψ $p + \text{Pb}$ ratio $R_{p\text{Pb}}(p_T)$ with the LHC data is better without any additional broadening [9]. Therefore, we do not change the value here.

3.1. J/ψ and $Y(1S)$ Production in $p + \text{Pb}$ Collisions at $\sqrt{s_{NN}} = 115 \text{ GeV}$. In this section, the results for J/ψ and Y shadowing in $p + \text{Pb}$ collisions at $\sqrt{s_{NN}} = 115 \text{ GeV}$ are presented. Figure 2 shows the results for J/ψ while Figure 3 shows the Y results. In both cases, the left-hand side shows the ratios $R_{p\text{Pb}}$ as a function of y (Figures 2(a) and 3(a)) and p_T in the rapidity range $-2.5 < y_{\text{cms}} < -2$ (Figures 2(c) and 3(c)). The rates to dileptons in the rapidity acceptance, assuming a lead target, are shown in Figures 2(b), 2(d), 3(b), and 3(d).

In the kinematics of this configuration, the large x_2 in the nucleus puts the peak for Fermi motion at the most negative rapidities. (The full center of mass rapidity range for J/ψ 's produced at this energy is $|y_{\text{cms}}| = \ln(\sqrt{s}/m) < 3.8$ for the mass and scale parameters appropriate for the CEM calculation.) The EMC region is in the J/ψ rapidity acceptance. There is a steep drop in $R_{p\text{Pb}}(y_{\text{cms}})$ as y_{cms} decreases from -2 to -2.5 , changing the central value of $R_{p\text{Pb}}(y_{\text{cms}})$ by $\sim 30\%$ over the range. The decrease into the EMC region is more apparent as a function of p_T where the region is expanded for $p_T < 10 \text{ GeV}$. The large uncertainty in this x range, as emphasized in Figures 1(a) and 1(b), is enhanced here.

The rates as a function of rapidity for J/ψ and $Y(1S)$ decays to lepton pairs are shown in Table 1. While the rates are shown for the entire rapidity range, the broad LHCb+ center of mass rapidity acceptance ends at $y_{\text{cms}} \sim 1$. The rates are given in the bins of $\Delta y_{\text{cms}} = 0.5$ with the value of y_{cms} at the center of the bin shown in Table 1. The rates include the branching ratios to lepton pairs.

The J/ψ rates in $p + \text{Pb}$ collisions are very high. The rate is $BdN/dy \sim 2.7 \times 10^8$ in the chosen backward rapidity bin of $-2.5 < y_{\text{cms}} < -2$; see Figure 2(b). The cross section is rather high since $\sqrt{s_{NN}}$ is above the region where the production cross section is still increasing steeply with $\sqrt{s_{NN}}$. In addition, the J/ψ production range in rapidity is fully within the AFTER@LHC acceptance.

Finally, even though the rates fall off quickly with p_T , more than 100 events can be collected at $p_T \sim 9.5 \text{ GeV}$; see Figure 2(d) and the upper part of Table 2, which is likely enough to determine where $R_{p\text{Pb}}(p_T)$ lies within the EPS09 band.

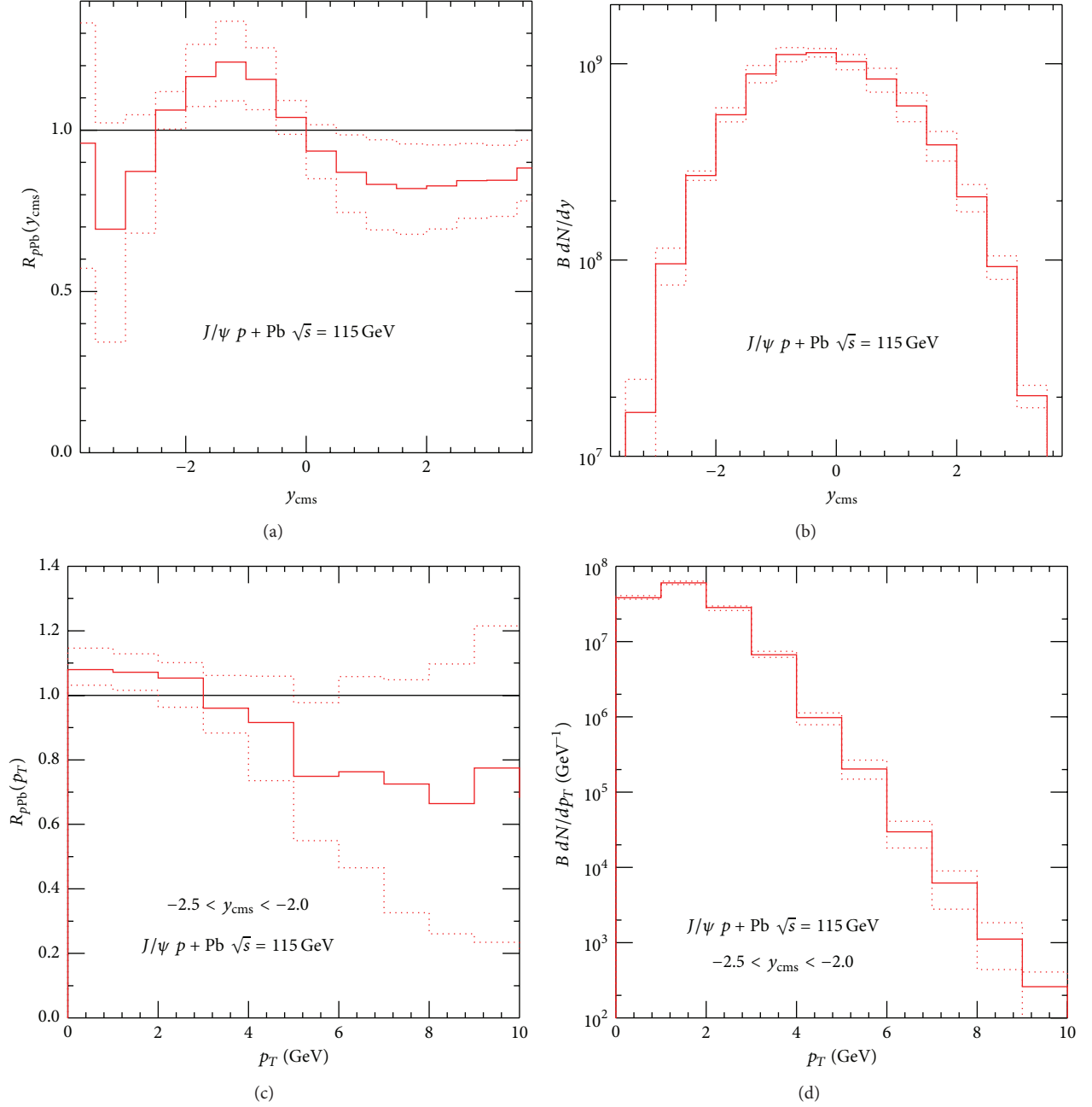


FIGURE 2: The predicted J/ψ shadowing ratios (a, c) and rates (b, d) as a function of center of mass rapidity (a, b) and p_T (c, d) for $p + \text{Pb}$ collisions at $\sqrt{s_{NN}} = 115 \text{ GeV}$. The solid curve in each plot is the central EPS09 NLO result, while the dotted curves outline the shadowing uncertainty band.

The $\Upsilon(1S)$ rates, shown in Figure 3, are significantly lower. At this energy, the production cross section is still increasing rapidly so that the available phase space for Υ production is $|y_{\text{cms}}| < 2.9$ in the CEM calculation. Thus, the AFTER@LHC acceptance is just inside the lower end of this range and the rate for Υ production in this region is relatively low. While the rates over all phase space can be quite high, with nearly 10^6 events at midrapidity, there are less than 10^4 events in the region $-2.5 < y_{\text{cms}} < -2$; see Table 1 and Figure 3(d).

As shown in Table 2, the Υ states that are produced in the AFTER@LHC acceptance are primarily at low p_T , $p_T \leq 3 \text{ GeV}$. Indeed, there are fewer than 10 events per year for $p_T > 6 \text{ GeV}$ so that any division into p_T bins for $p_T > 5 \text{ GeV}$ is unlikely to be feasible.

The AFTER@LHC rapidity bin is in the EMC region and touching on the Fermi motion region at $y_{\text{cms}} \sim -2.5$, as seen on Figure 3(a). The p_T -dependent ratio reflects the large uncertainty of the EMC region and is almost independent of

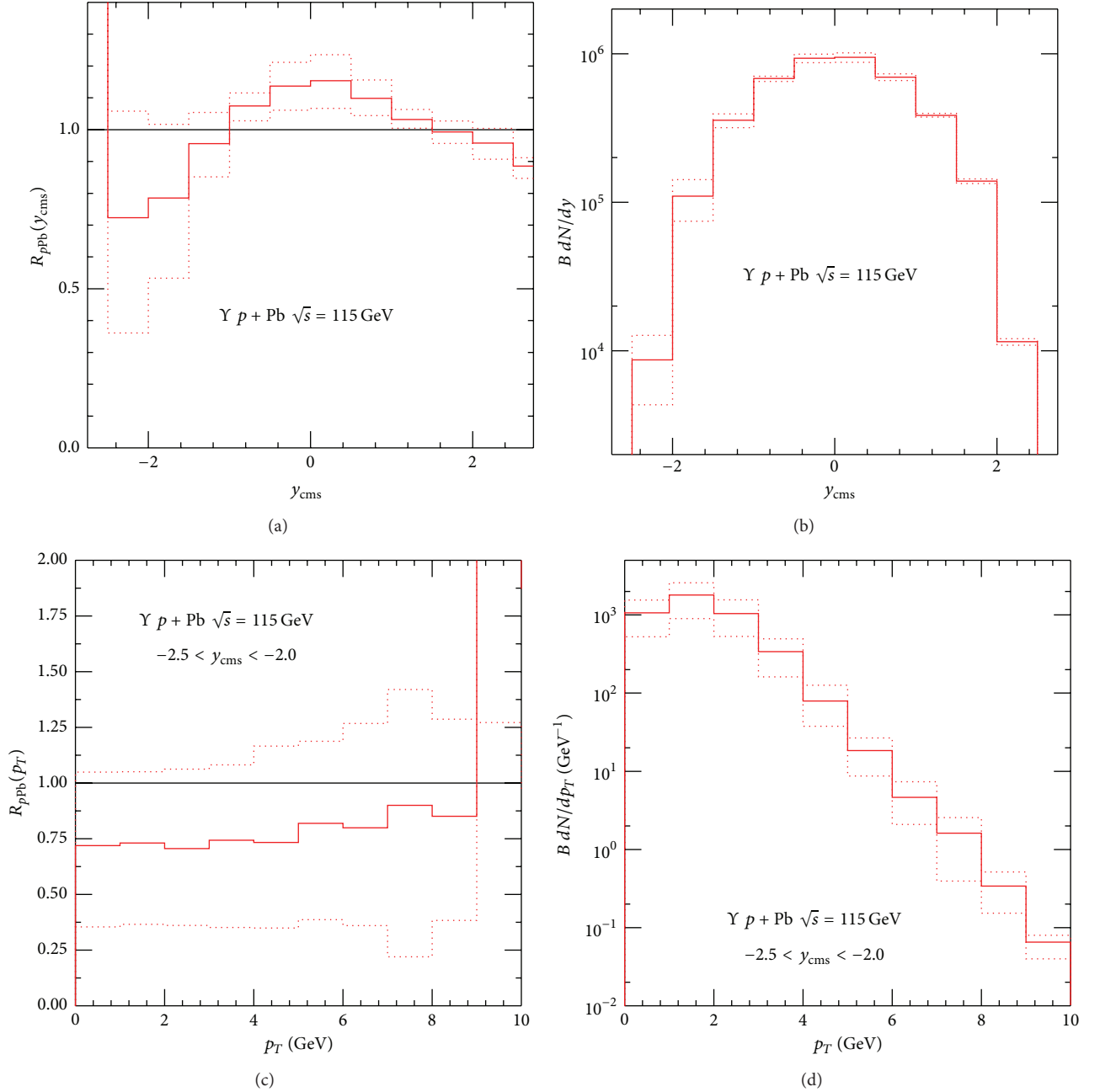


FIGURE 3: The predicted $\Upsilon(1S)$ shadowing ratios (a, c) and rates (b, d) as a function of center of mass rapidity (a, b) and p_T (c, d) for $p + \text{Pb}$ collisions at $\sqrt{s_{NN}} = 115$ GeV. The solid curve in each plot is the central EPS09 NLO result, while the dotted curves outline the shadowing uncertainty band.

p_T until $p_T \sim 9$ GeV in the EPS09 parameterization where it increases sharply. The low rate will make it difficult to study this interesting region in detail.

3.2. J/ψ and $\Upsilon(1S)$ Production in $\text{Pb} + p$ Collisions at $\sqrt{s_{NN}} = 72$ GeV. In this section, the results for J/ψ and Υ shadowing in $\text{Pb} + p$ collisions at $\sqrt{s_{NN}} = 72$ GeV are presented. Figure 4 shows the results for J/ψ while Figure 5 shows the Υ results. In both cases, Figures 5(a) and 5(c) shows the ratios $R_{p\text{Pb}}$ as

a function of y_{cms} (Figure 5(a)) and p_T in the $-1.9 < y_{\text{cms}} < -1.4$ rapidity bin (Figure 5(c)). The rates to dileptons in the rapidity acceptance, assuming a 1 m long liquid hydrogen target, are shown in Figures 4(b), 4(d), 5(b), and 5(d) and in the bottom parts of Tables 1 and 2. The lower cross sections at this reduced energy still result in rather high rates for the long liquid hydrogen target, at least at midrapidity.

In these kinematics, the rapidity bin $-1.9 < y_{\text{cms}} < -1.4$ now corresponds to the more typical fixed-target kinematics

TABLE 1: The rates per 0.5-unit rapidity for J/ψ and $Y(1S)$ in the two scenarios discussed in the text. The values are given for the EPS09 NLO central set.

System	y_{cms}	$N(J/\psi \rightarrow l^+l^-)$	$N(Y(1S) \rightarrow l^+l^-)$
$p + \text{Pb}$ $\sqrt{s_{NN}} = 115 \text{ GeV}$	-3.75	2.32×10^5	—
	-3.25	1.67×10^7	—
	-2.75	9.56×10^7	—
	-2.25	2.69×10^8	8.68×10^3
	-1.75	5.50×10^8	1.10×10^5
	-1.25	8.88×10^8	3.56×10^5
	-0.75	1.11×10^9	6.81×10^5
	-0.25	1.14×10^9	9.33×10^5
	0.25	1.02×10^9	9.47×10^5
	0.75	8.36×10^8	6.96×10^5
	1.25	6.10×10^8	3.85×10^5
	1.75	3.86×10^8	1.39×10^5
	2.25	2.10×10^8	1.15×10^4
	2.75	9.25×10^7	—
	3.25	2.04×10^7	—
	3.75	2.13×10^5	—
$\text{Pb} + p$ $\sqrt{s_{NN}} = 72 \text{ GeV}$	-3.25	1.54×10^3	—
	-2.75	1.05×10^5	—
	-2.25	4.36×10^5	—
	-1.75	9.67×10^5	5.36×10^1
	-1.25	1.78×10^6	5.10×10^2
	-0.75	2.79×10^6	1.20×10^3
	-0.25	3.72×10^6	1.66×10^3
	0.25	4.15×10^6	1.59×10^3
	0.75	3.64×10^6	1.03×10^3
	1.25	2.42×10^6	3.78×10^2
	1.75	1.24×10^6	3.77×10^1
	2.25	4.58×10^5	—
	2.75	8.68×10^4	—
	3.25	1.55×10^3	—

with the lead nucleus at the lower x_1 . Here, the ratio $R_{\text{Pb}p}(y_{\text{cms}})$ is reversed. The x range for the J/ψ is in the higher x end of the shadowing region while the Y is just entering the antishadowing region; recall Figure 1.

The antishadowing peak for J/ψ in Figure 4(a) is actually just at forward rapidity instead of being in the $y_{\text{cms}} < 0$ region. (The full center of mass rapidity range for J/ψ production at this energy is $|y_{\text{cms}}| < 3.3$.) Within the chosen rapidity bin, the p_T -dependent ratio has the largest uncertainty at the low p_T where there is still some shadowing. However, at $p_T > 5 \text{ GeV}$, the x values move somewhat into the antishadowing region (Figure 4(c)).

TABLE 2: The p_T -dependent rates per 1 GeV p_T bin for J/ψ and $Y(1S)$ in the two scenarios discussed in the text. The values are given for the EPS09 NLO central set.

System	$p_T \text{ (GeV)}$	$N(J/\psi \rightarrow l^+l^-)$	$N(Y(1S) \rightarrow l^+l^-)$
$p + \text{Pb}$ $\sqrt{s_{NN}} = 115 \text{ GeV}$	0.5	3.83×10^7	1.06×10^3
	1.5	6.62×10^7	1.79×10^3
	2.5	2.83×10^7	1.04×10^3
	3.5	6.69×10^6	3.40×10^2
	4.5	9.78×10^5	7.93×10^1
	5.5	2.03×10^5	1.84×10^1
	6.5	2.96×10^4	4.64×10^0
	7.5	6.20×10^3	1.62×10^0
	8.5	1.12×10^3	3.40×10^{-1}
	9.5	2.60×10^2	6.51×10^{-2}
$\text{Pb} + p$ $\sqrt{s_{NN}} = 72 \text{ GeV}$	10.5	3.96×10^1	1.03×10^{-2}
	0.5	1.38×10^5	1.39×10^1
	1.5	2.36×10^5	2.26×10^1
	2.5	1.33×10^5	1.20×10^1
	3.5	3.90×10^4	3.39×10^0
	4.5	7.69×10^3	7.44×10^{-1}
	5.5	1.16×10^3	1.71×10^{-1}
	6.5	2.11×10^2	4.69×10^{-2}
	7.5	4.15×10^1	1.28×10^{-2}
	8.5	8.62×10^0	3.25×10^{-3}
	9.5	1.89×10^0	6.72×10^{-4}
	10.5	3.39×10^{-1}	1.65×10^{-4}

The J/ψ rates for this system are still high; see the lower half of Table 1. Thanks to the length of the H_2 target, for the lead beam, the p_T -integrated rates in this configuration are still on the order of 10^6 in the AFTER@LHC acceptance. The p_T -dependent rates show that the statistics become poor for the J/ψ at $p_T > 7 \text{ GeV}$. The rates at this energy are helped somewhat since there is antishadowing for $p_T > 8 \text{ GeV}$ while there is strong shadowing at $\sqrt{s_{NN}} = 115 \text{ GeV}$; see Figure 2.

The situation with $Y(1S)$ is similar; see Figure 5 and Table 1. (The rapidity range for Y production is $|y_{\text{cms}}| < 2.4$ so that again the AFTER@LHC acceptance is on the edge of the Y range.) The shadowing (or antishadowing) effect is on the order of a few percent. While there are a few thousand Y in a year at midrapidity, the rate in the AFTER@LHC acceptance is rather low, under 100 per year, as shown in Figures 5(b) and 5(d) and in Table 2. Indeed, there is effectively no rate for the Y rate for $p_T > 4 \text{ GeV}$.

4. Conclusions

We have only presented a bare minimum of the rates for the breadth of quarkonium studies possible at AFTER@LHC.

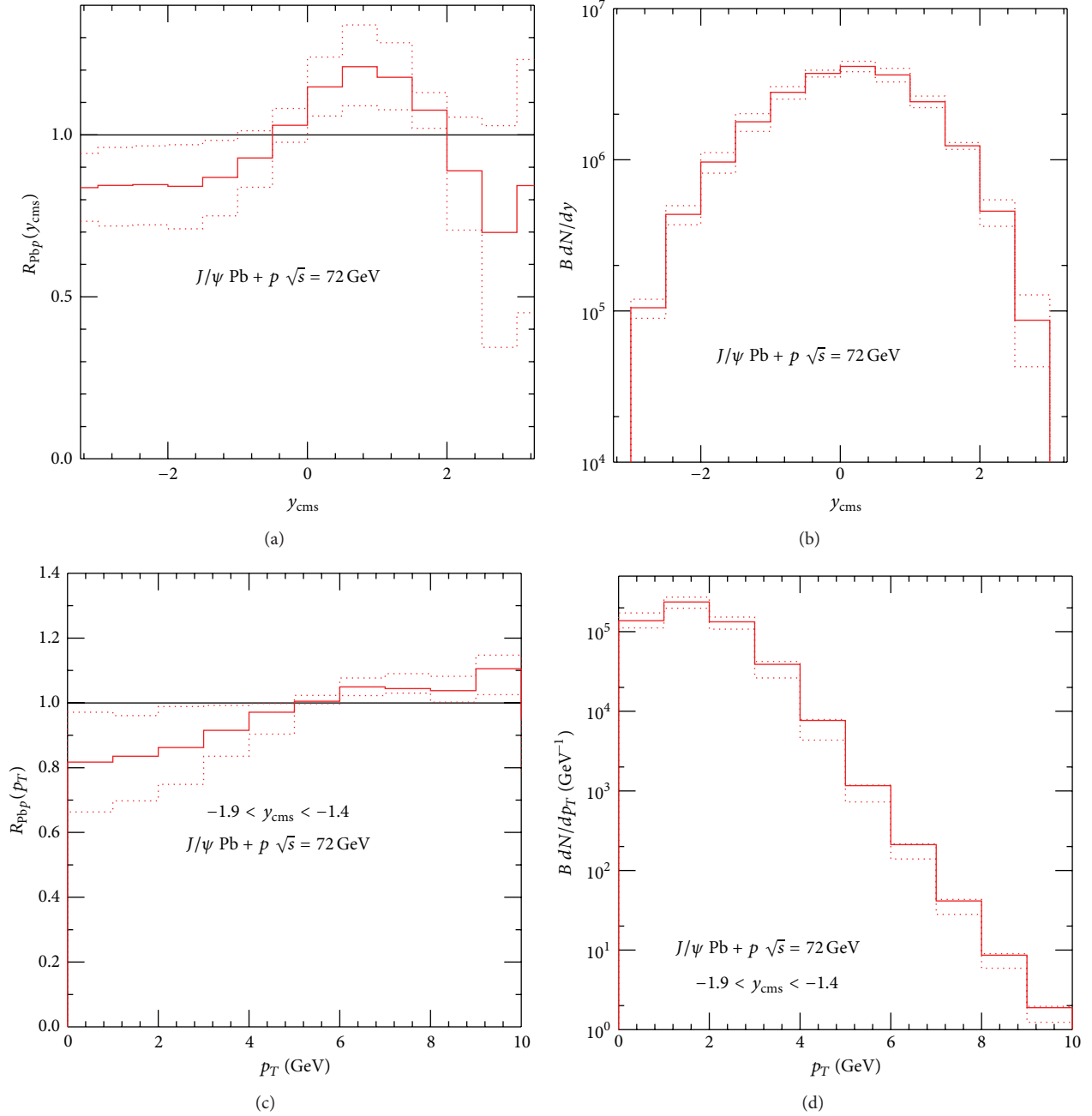


FIGURE 4: The predicted J/ψ shadowing ratios (a, c) and rates (b, d) as a function of center of mass rapidity (a, b) and p_T (c, d) for Pb + p collisions at $\sqrt{s_{NN}} = 72$ GeV. The solid curve in each plot is the central EPS09 NLO result, while the dotted curves outline the shadowing uncertainty band.

The fixed-target configuration, especially for long runs with the dedicated proton beam, allows detailed measurements with a range of nuclear targets. We have only shown the Pb results here because the larger nuclear mass number produces what is expected to be the maximum effect due to shadowing.

The large x region available for nuclear targets in the AFTER@LHC kinematics with a proton beam has the unique capability to make unprecedented studies of this heretofore

unexplored range. The AFTER@LHC measurements would bridge the gap between the dedicated fixed-target experiments in the range $17.2 \leq \sqrt{s_{NN}} \leq 41$ GeV and the d + Au and the upcoming $p + A$ collider experiments at RHIC, albeit in an x range never before studied.

In the AFTER@LHC configuration with a Pb beam, the rates are smaller, though still significant, and the more conventional x range is probed.

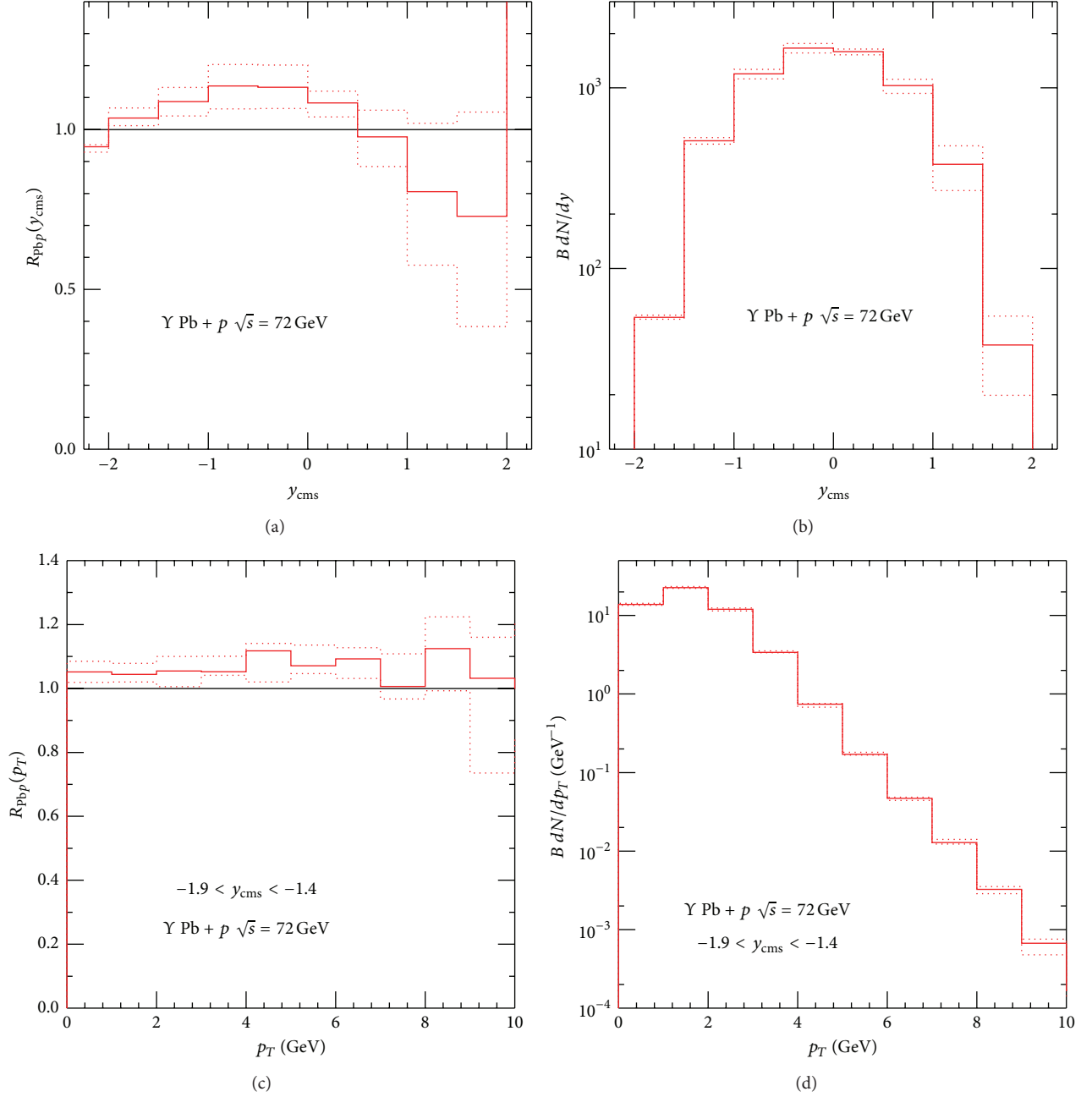


FIGURE 5: The predicted Y(1S) shadowing ratios (a, c) and rates (b, d) as a function of center of mass rapidity (a, b) and p_T (c, d) for Pb + p collisions at $\sqrt{s_{NN}} = 72$ GeV. The solid curve in each plot is the central EPS09 NLO result, while the dotted curves outline the shadowing uncertainty band.

Conflict of Interests

The author declares that there is no conflict of interests regarding the publication of this paper.

Acknowledgments

This work was performed under the auspices of the U.S. Department of Energy by Lawrence Livermore National Laboratory under Contract DE-AC52-07NA27344. The author

also thanks the Institute for Nuclear Theory at the University of Washington, where this work was initiated, for hospitality.

References

- [1] S. J. Brodsky, F. Fleuret, C. Hadjidakis, and J. P. Lansberg, "Physics opportunities of a fixed-target experiment using LHC beams," *Physics Reports*, vol. 522, no. 4, pp. 239–255, 2013.
- [2] R. Gavai, D. Kharzeev, H. Satz, G. A. Schuler, K. Sridhar, and R. Vogt, "Quarkonium production in hadronic collisions,"

- International Journal of Modern Physics A*, vol. 10, pp. 3043–3070, 1995.
- [3] K. J. Eskola, H. Paukkunen, and C. A. Salgado, “EPS09—a new generation of NLO and LO nuclear parton distribution functions,” *Journal of High Energy Physics*, vol. 2009, article 065, 2009.
 - [4] J. Pumplin, D. R. Stump, J. Huston, H. L. Lai, P. M. Nadolsky, and W. K. Tung, “New generation of parton distributions with uncertainties from global QCD analysis,” *Journal of High Energy Physics*, vol. 2002, no. 7, article 012, 2002.
 - [5] D. Stump, J. Huston, J. Pumplin et al., “Inclusive jet production, parton distributions, and the search for new physics,” *Journal of High Energy Physics*, vol. 2003, no. 10, p. 046, 2003.
 - [6] R. E. Nelson, R. Vogt, and A. D. Frawley, “Narrowing the uncertainty on the total charm cross section and its effect on the J/ψ cross section,” *Physical Review C*, vol. 87, no. 1, Article ID 014908, 17 pages, 2013.
 - [7] R. E. Nelson, R. Vogt, and A. D. Frawley, In preparation.
 - [8] H. L. Lai, M. Guzzi, J. Huston et al., “New parton distributions for collider physics,” *Physical Review D—Particles, Fields, Gravitation and Cosmology*, vol. 82, no. 7, Article ID 074024, 2010.
 - [9] R. Vogt, In preparation.
 - [10] M. Arneodo, A. Arvidson, J. J. Aubert et al., “Shadowing in deep inelastic muon scattering from nuclear targets,” *Physics Letters B*, vol. 211, no. 4, pp. 493–499, 1988.
 - [11] J. Ashman, B. Badelek, G. Baum et al., “Measurement of the ratios of deep inelastic muon-nucleus cross sections on various nuclei compared to deuterium,” *Physics Letters B*, vol. 202, no. 4, pp. 603–610, 1988.
 - [12] L. W. Whitlow, E. M. Riordan, S. Dasu, S. Rock, and A. Bodek, “Precise measurements of the proton and deuteron structure functions from a global analysis of the SLAC deep inelastic electron scattering cross sections,” *Physics Letters B*, vol. 282, no. 3–4, pp. 475–482, 1992.
 - [13] M. C. Abreu, C. Baglin, A. Baldit et al., “Charmonia production in 450 GeV/c proton induced reactions,” *Physics Letters B*, vol. 444, no. 3–4, pp. 516–522, 1998.
 - [14] B. Alessandro, C. Alexa, R. Arnaldi et al., “Charmonium production and nuclear absorption in p-A interactions at 450 GeV,” *The European Physical Journal C*, vol. 33, no. 1, pp. 31–40, 2004.
 - [15] M. J. Leitch, W. M. Lee, M. E. Beddo et al., “Measurement of differences between J/ψ and ψ' suppression in p–A collisions,” *Physical Review Letters*, vol. 84, no. 15, pp. 3256–3260, 2000.
 - [16] I. Abt, M. Adams, M. Agari et al., “Measurement of the J/ψ production cross section in 920 GeV/c fixed-target proton–nucleus interactions,” *Physics Letters B*, vol. 638, no. 5–6, pp. 407–414, 2006.
 - [17] R. Vogt, “ x_F dependence of ψ and Drell-Yan production,” *Physical Review C*, vol. 61, no. 3, Article ID 035203, 2000.
 - [18] K. J. Eskola, V. J. Kolhinen, and P. V. Ruuskanen, “Scale evolution of nuclear parton distributions,” *Nuclear Physics B*, vol. 535, no. 1–2, pp. 351–371, 1998.
 - [19] K. J. Eskola, V. J. Kolhinen, and C. A. Salgado, “The scale dependent nuclear effects in parton distributions for practical applications,” *European Physical Journal C*, vol. 9, no. 1, pp. 61–68, 1999.
 - [20] C. Lourenço, R. Vogt, and H. Wohri, “Energy dependence of J/ψ absorption in proton-nucleus collisions,” *Journal of High Energy Physics*, vol. 2009, no. 2, article 014, 2009.
 - [21] F. Arleo and S. Peigné, “Heavy-quarkonium suppression in p-A collisions from parton energy loss in cold QCD matter,” *Journal of High Energy Physics*, vol. 2013, no. 3, article 122, 2013.
 - [22] F. Arleo, R. Kolevatov, S. Peigné, and M. Rustamova, “Centrality and p_T dependence of J/ψ suppression in proton-nucleus collisions from parton energy loss,” *Journal of High Energy Physics*, vol. 2013, no. 5, article 155, 2013.
 - [23] D. C. McGlinchey, A. D. Frawley, and R. Vogt, “Impact-parameter dependence of the nuclear modification of J/ψ production in d+Au collisions at $\sqrt{s_{NN}} = 200$ GeV,” *Physical Review C*, vol. 87, no. 5, Article ID 054910, 10 pages, 2013.
 - [24] V. D. Barger, W. Y. Keung, and R. J. N. Phillips, “On ψ and Y production via gluons,” *Physics Letters B*, vol. 91, no. 2, pp. 253–258, 1980.
 - [25] V. Barger, W. Y. Keung, and R. J. N. Phillips, “Hadroproduction of ψ and Y ,” *Zeitschrift für Physik C*, vol. 6, no. 2, pp. 169–174, 1980.
 - [26] M. L. Mangano, P. Nason, and G. Ridolfi, “Heavy-quark correlations in hadron collisions at next-to-leading order,” *Nuclear Physics B*, vol. 373, no. 2, pp. 295–345, 1992.
 - [27] G. A. Schuler and R. Vogt, “Systematics of quarkonium production,” *Physics Letters B*, vol. 387, pp. 181–186, 1996.
 - [28] M. L. Mangano, P. Nason, and G. Ridolfi, “Fixed-target hadroproduction of heavy quarks,” *Nuclear Physics B*, vol. 405, no. 2–3, pp. 507–535, 1993.

Research Article

Prospects for Open Heavy Flavor Measurements in Heavy Ion and $p + A$ Collisions in a Fixed-Target Experiment at the LHC

Daniel Kikoła

Faculty of Physics, Warsaw University of Technology, Ulica Koszykowa 75, 00-662 Warsaw, Poland

Correspondence should be addressed to Daniel Kikoła; kikola@if.pw.edu.pl

Received 20 March 2015; Accepted 24 May 2015

Academic Editor: Cédric Lorcé

Copyright © 2015 Daniel Kikoła. This is an open access article distributed under the Creative Commons Attribution License, which permits unrestricted use, distribution, and reproduction in any medium, provided the original work is properly cited. The publication of this article was funded by SCOAP³.

High luminosity data in a fixed-target experiment allow studying interactions of heavy quarks with nuclear matter in the intermediate energy range with extremely high precision. We present a feasibility study for open charm and bottom production measurements in the energy range of a fixed-target experiment at the LHC (AFTER@LHC). We demonstrate, that high-precision data from AFTER will allow answering two open questions: if there is a collective behavior of charm quarks in $p + A$ collisions at RHIC energy and if charm production is suppressed in the energy range of $\sqrt{s_{NN}} = 60\text{--}80$ GeV. We argue that simultaneous measurement of D^0 suppression as a function of transverse momentum at midrapidity and forward rapidity can help to pin down the mechanism of charm energy loss in the hot and dense nuclear medium.

1. Introduction

Relativistic heavy ion collisions provide a unique opportunity for studying quark-gluon plasma (QGP), a new state of nuclear matter with properties determined by quark and gluon degrees of freedom. Its properties can be studied with heavy quarks: charm and bottom. They are produced very early in the collision, in the initial interactions with large momentum transfer. Their production and both total and differential cross sections are well described by perturbative QCD calculations. Moreover, due to large masses, they are expected to interact with the nuclear matter differently compared to light partons.

We can infer properties of the QGP by studying modification of heavy quarks production in the heavy ion collisions compared to proton-proton baseline (for details, see [1] and references therein). Energy loss and elliptic flow of open heavy flavor are sensitive to the dynamics of the medium; such measurements could be used to determine the fundamental properties of the QGP, for instance, transport coefficients. Elliptic flow of heavy quarks can give insights into degree of thermalization of the created nuclear matter and can help to discriminate between different models of heavy quark interactions with the QGP.

Heavy flavor production at RHIC (measured via D^0 and electrons from semileptonic decays of heavy flavor hadrons, e^{HF}) in Au + Au collisions at $\sqrt{s_{NN}} = 200$ GeV is suppressed at high transverse momentum (p_T) and e^{HF} have a significant elliptic flow v_2 (elliptic flow is defined as the second harmonic in the Fourier expansion of the particle azimuthal distribution with respect to the reaction plane [2]). These results suggest that charm quarks are strongly coupled with the medium: heavy quarks lose a large amount of energy and acquire a significant elliptic flow during interaction with matter created at top RHIC energy.

Beam energy scan (BES) program at RHIC was carried out recently to study the phase diagram of nuclear matter and search for a phase transition and a critical point. BES results show that elliptic flow of inclusive charged hadrons is approximately independent of beam energy (the difference is less than 10% for $0.5 < p_T < 3$ GeV/c) and light hadron production is suppressed at high p_T in the energy range of 39–200 GeV. In Au + Au collisions at $\sqrt{s_{NN}} = 62.4$ GeV, production of e^{HF} is not suppressed (within large uncertainties). Moreover, measurements of elliptic flow of e^{HF} in Au + Au collisions at $\sqrt{s_{NN}} = 62.4$ and 39 GeV [3] showed that v_2 of e^{HF} is consistent with zero. This is a different

TABLE 1: Average number of participants $\langle N_{\text{part}} \rangle$ and binary collisions $\langle N_{\text{bin}} \rangle$ in p -Pb collisions at $\sqrt{s_{NN}} = 115$ GeV for centrality classes defined as percentiles of the hadronic cross section. The mean values and the RMS are obtained with a Glauber Monte Carlo calculation.

Centrality	b_{min} [fm]	b_{max} [fm]	$\langle N_{\text{bin}} \rangle$	RMS(N_{bin})	$\langle N_{\text{part}} \rangle$	RMS(N_{part})
0–10%	0	2.41	8.0	2.7	9.0	2.7
10–20%	2.41	3.42	7.3	2.6	8.3	2.6
20–30%	3.42	4.19	6.6	2.4	7.6	2.4
30–40%	4.19	4.83	5.8	2.3	6.8	2.3
40–50%	4.83	5.41	4.9	2.1	5.9	2.1
50–60%	5.41	5.93	3.9	1.8	4.9	1.8
60–70%	5.93	6.43	2.9	1.5	3.9	1.5
70–80%	6.43	6.95	2.2	1.2	3.2	1.2
80–90%	6.95	7.60	1.6	0.8	2.6	0.8
90–100%	7.60	19.80	1.2	0.4	2.2	0.4

behavior than that for light hadrons, where a positive v_2 is observed and the difference between $\sqrt{s_{NN}} = 200$ GeV and 39 GeV is small. These results suggest that there is a difference in the interactions of the heavy quarks with the surrounding nuclear matter at 200 GeV compared to the two lower energies and there is already a change of the nuclear matter properties in the energy range of 62.4–200 GeV. High luminosity data of a proposed fixed-target experiment at the LHC ($\sqrt{s_{NN}} = 72$ GeV) together with a wide rapidity coverage could shed new light on the energy loss mechanism for charm quarks (which we discuss in Section 5) and give a precise answer if heavy flavor production is suppressed or not at high p_T .

For the interpretation of the results from heavy ion collisions, it is important to have a good handle on the so-called cold nuclear matter (CNM) effects. This category includes modifications of the particle yields not related to the QGP formation, such as a shadowing (modification of parton distributions in a nucleus) or a Cronin effect (an enhancement of transverse momentum in $p + A$ with respect to $p + p$ collisions). Experiments at RHIC and LHC recently reported collective behavior of light hadrons in high multiplicity $d + \text{Au}$ [4] and $p + \text{Pb}$ collisions [5], where these hadrons have significant elliptic flow with a characteristic mass-splitting pattern [6]. These observations triggered speculations that an enhancement of e^{HF} production in central and minimum bias $d + \text{Au}$ collisions at midrapidity at RHIC [7] could indicate a collective phenomenon (radial flow) of heavy quarks in $d + \text{Au}$ [8]. However, this enhancement could be also due to the CNM effects: it can be reproduced assuming Cronin effect for charm quarks [9]. A direct measurement of elliptic flow v_2 of D^0 will answer the question of heavy quark collectivity in $p + A$ collisions. High luminosity $p + A$ collisions at AFTER will allow quantifying the CNM effects and measuring v_2 with high precision to address these two issues.

In this paper we present estimates of the precision expected for open heavy flavor measurements at the proposed fixed target experiment at LHC (AFTER@LHC). We first describe the simulation setup we use and then present and discuss estimates for physical observables for open charm and open bottom in $p + A$ collisions at $\sqrt{s_{NN}} = 115$ GeV

and Pb + Pb collisions at $\sqrt{s_{NN}} = 72$ GeV. We argue that these measurements at AFTER will address open questions about heavy quark collectivity in $p + A$ collisions and energy dependence of the heavy quark interactions with a nuclear matter.

2. Centrality Estimation

We estimate centrality bins in $p + \text{Pb}$ collisions at $\sqrt{s_{NN}} = 115$ GeV and Pb + Pb at $\sqrt{s_{NN}} = 72$ GeV using Glauber Monte Carlo calculations with the PHOBOS Glauber Monte Carlo [10, 11] version 2.1. We assume that the nucleon-nucleon cross section $\sigma_{NN} = 37$ mb at $\sqrt{s_{NN}} = 72$ GeV and the nucleon-nucleon cross section $\sigma_{NN} = 39$ mb at $\sqrt{s_{NN}} = 115$ GeV, and the rest of parameters have the default values.

Centrality bins are defined as percentiles of hadronic cross sections. Figure 1 shows impact parameter distributions in p -Pb collisions at $\sqrt{s_{NN}} = 115$ GeV and (b) Pb-Pb collisions at $\sqrt{s_{NN}} = 72$ GeV. Tables 1 and 2 show the average number of participants $\langle N_{\text{part}} \rangle$ and binary collisions $\langle N_{\text{bin}} \rangle$ and their root mean square (RMS) values for those two systems for the centrality classes.

3. Simulation Setup

3.1. Detector Setup. We consider a detector with similar apparatus as the LHCb experiment [12]. We assume rapidity coverage in the laboratory frame of $2 < y_{\text{Lab}} < 5$ and similar particle detector capabilities and efficiencies (muon detection capability and precise microvertexing detector). The efficiencies reported by LHCb [13, 14] are used in our estimates (Figure 2). We consider two experimental techniques for open heavy flavor measurements: D^0 measurements via secondary vertex reconstruction and $B \rightarrow J/\psi$ determination via a pseudo-lifetime method.

Since both D^0 and J/ψ from B-hadron decays are measured at the forward rapidity in a laboratory frame with a precise vertex detector, a large boost will strongly suppress the background. Thus we neglect the background contribution to the statistical uncertainties in our estimations. The large boost also allows for D and B mesons and $B \rightarrow J/\psi$ measurements down to zero p_T via displaced vertex reconstruction.

TABLE 2: Average number of participants $\langle N_{\text{part}} \rangle$ and binary collisions $\langle N_{\text{bin}} \rangle$ in Pb-Pb collisions at $\sqrt{s_{NN}} = 72$ GeV for centrality classes defined as percentiles of the hadronic cross section. The mean values and the RMS are obtained with a Glauber Monte Carlo calculation.

Centrality	b_{min} [fm]	b_{max} [fm]	$\langle N_{\text{bin}} \rangle$	$\text{RMS}(N_{\text{bin}})$	$\langle N_{\text{part}} \rangle$	$\text{RMS}(N_{\text{part}})$
0–10%	0	4.80	884.0	128.0	338.5	34.0
10–20%	4.80	6.77	557.2	82.2	241.8	25.6
20–30%	6.77	8.30	346.5	58.9	170.8	20.8
30–40%	8.30	9.59	206.2	42.9	117.1	17.2
40–50%	9.59	10.72	115.4	30.6	76.7	14.6
50–60%	10.72	11.75	59.4	20.6	47.0	12.0
60–70%	11.75	12.69	28.0	13.0	26.6	9.5
70–80%	12.69	13.58	12.2	7.5	13.7	6.8
80–90%	13.58	14.55	5.2	4.0	6.8	4.2
90–100%	14.55	20.00	2.3	1.8	3.5	2.1

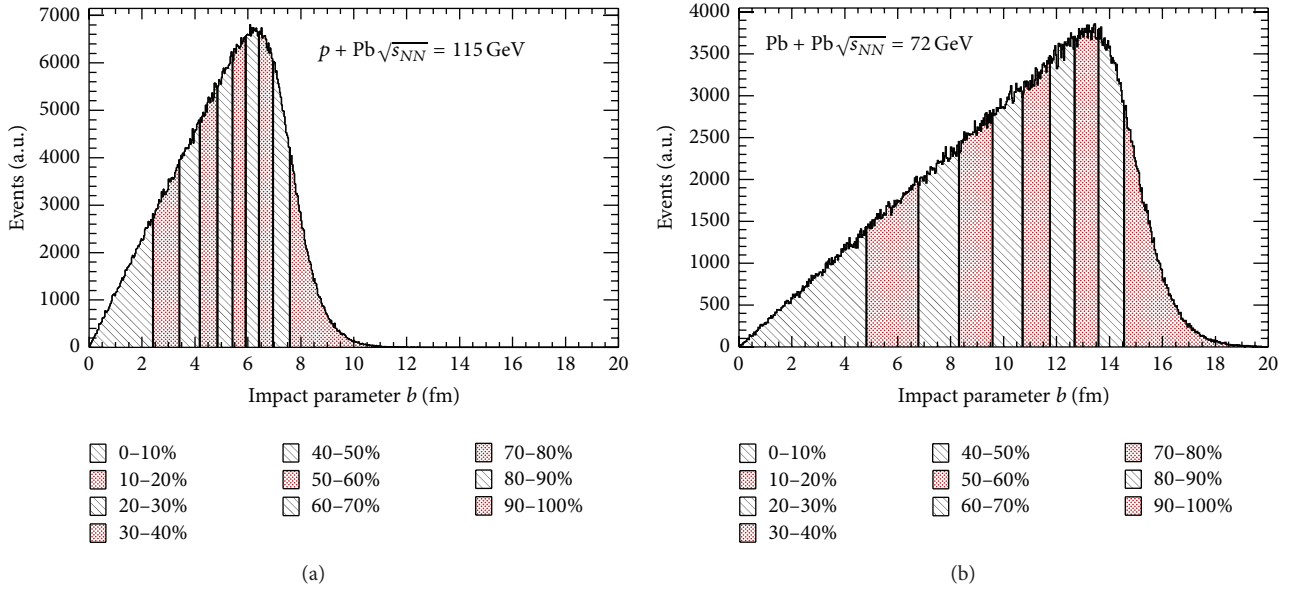


FIGURE 1: Impact parameter distribution for percentiles of the hadronic cross section obtained from a Glauber Monte Carlo calculation in (a) p -Pb collisions at $\sqrt{s_{NN}} = 115$ GeV and (b) Pb-Pb collisions at $\sqrt{s_{NN}} = 72$ GeV.

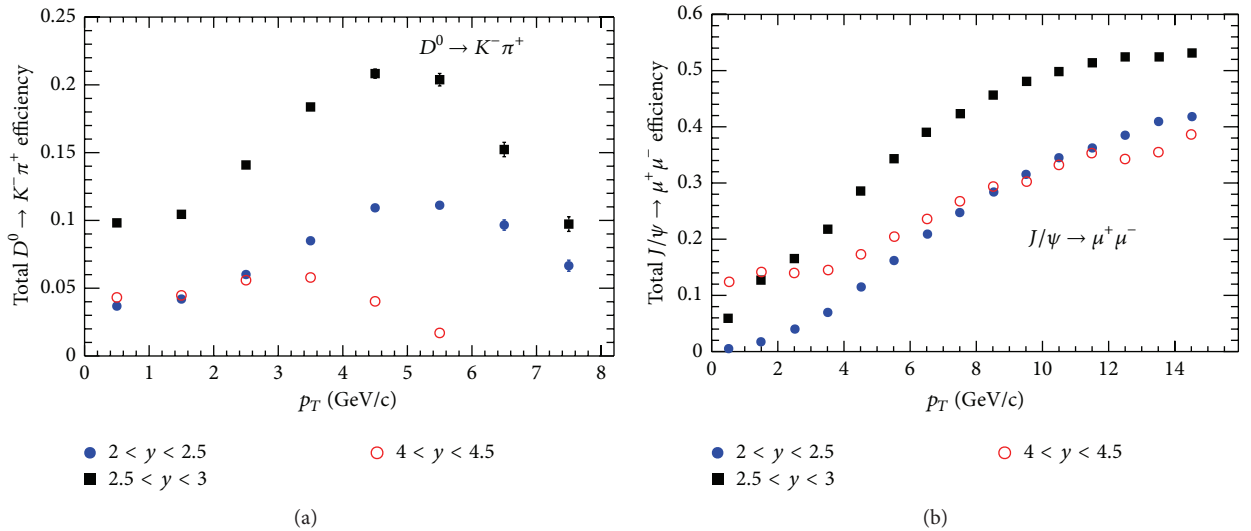


FIGURE 2: Total reconstruction efficiency for (a) D^0 [13] and (b) J/ψ [14] in the LHCb experiment.

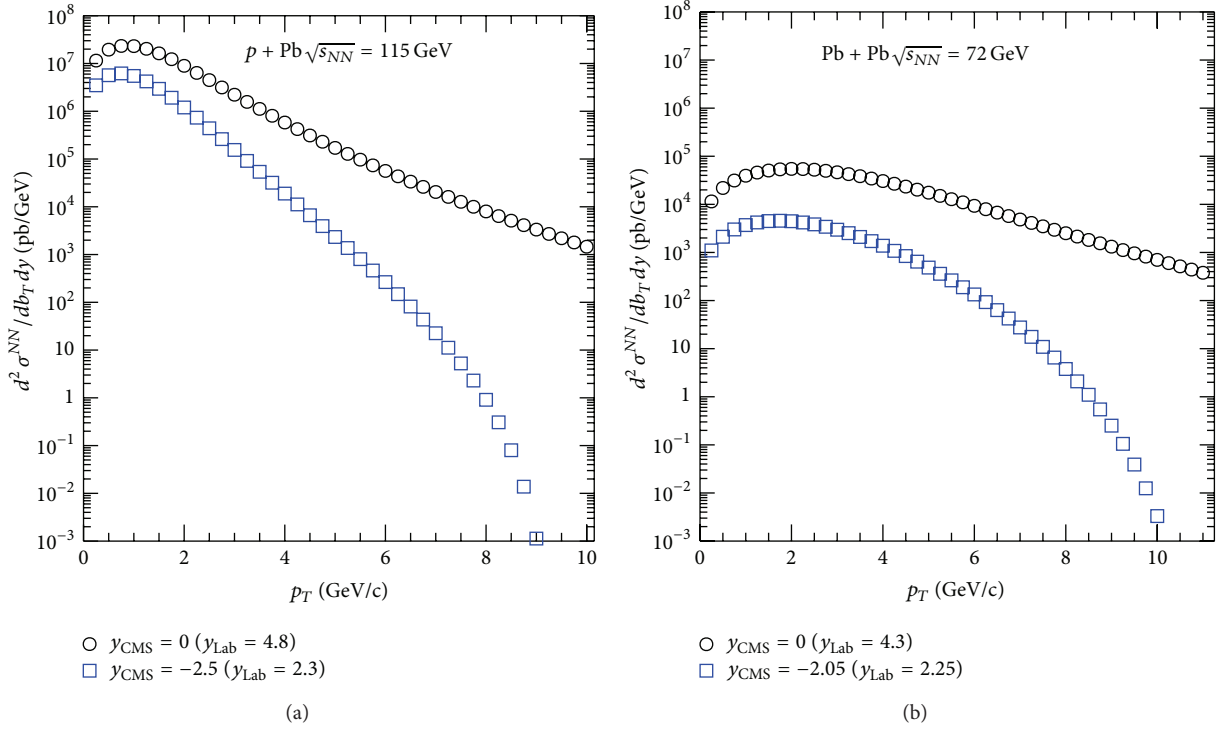


FIGURE 3: Charm quark differential cross section per nucleon-nucleon collision as a function of p_T in $p + \text{Pb}$ and $\text{Pb} + \text{Pb}$ collisions.

3.2. Heavy Quarks Production Cross Sections. We obtain charm and bottom quark production cross sections using FONLL (fixed-order plus next-to-leading logs) program [15, 16], version 1.3.3 [17]. We run the calculation assuming charm quark mass $m_c = 1.5 \text{ GeV}/c^2$ and bottom mass $m_b = 4.75 \text{ GeV}/c^2$ using CTEQ6.6 [18] parton distribution function convoluted with EPS09 [19] shadowing parametrization (central value). Other parameters (scales) have the default values.

Figures 3 and 4 show charm and bottom quarks differential cross section per nucleon-nucleon collision as a function of p_T in $p + \text{Pb}$ and $\text{Pb} + \text{Pb}$ collisions. Only central values from FONLL are shown. Since experimental data for heavy flavor production at RHIC energies are consistent with upper limit on the FONLL calculations [20, 21] we believe that the results in Figures 3 and 4 provide us with conservative estimates of heavy quark cross section for those energies.

3.3. Charmed and Bottom Mesons Production. In the experiments we measure the final-state particles (D^0 , B-meson or J/ψ from B-meson decays). In this study we made a few simplifications to estimate the expected yields based on charm and bottom cross sections. For D^0 meson, we assume that it has approximately the same p_T spectrum as charm quarks. Charm hadronization ratio to D^0 is 0.565 [22] and D^0 will be measured via $D^0 \rightarrow K^- \pi^+$ (branching ratio $\text{BR} = 3.8\%$) via secondary vertex reconstruction. We used TPythia8Decayer from the ROOT framework [23] to simulate $B \rightarrow J/\psi$ decays. For the input, we assumed that B^\pm , B_s , and B^0 have the same p_T spectrum as bottom quarks, rapidity has a uniform distribution in narrow bins we have used ($\Delta y = 0.5$), and the hadronization fraction to B meson

is $f(b \rightarrow B) = 0.764$ ($f(b \rightarrow B^0) = f(b \rightarrow B^\pm) = (33.7 \pm 2.2)\%$ and $f(b \rightarrow B_s) = (9.0 \pm 0.9)\%$ [24]). The branching ratio for $B \rightarrow J/\psi + X$ is taken as $\text{BR} = 1.16\%$. Figure 4(b) shows an input bottom quark spectrum and J/ψ from bottom meson decays for $|y| < 0.25$. At the energy of $\sqrt{s_{NN}} = 115$ GeV, we expect bottom quark production with p_T up to 11 GeV/c, which allows for $B \rightarrow J/\psi$ measurement with p_T up to 10 GeV/c.

To calculate the production rates, we take an integrated luminosity $\mathcal{L} = 160 \text{ pb}^{-1}$ for $p + \text{Pb}$ collisions at $\sqrt{s_{NN}} = 115$ GeV and $\mathcal{L} = 7 \text{ nb}^{-1}$ for $\text{Pb} + \text{Pb}$ collisions at $\sqrt{s_{NN}} = 72$ GeV [25]. Finally, we apply the charmed meson and J/ψ reconstruction efficiencies reported by LHCb (Figure 2) to the simulated D^0 and $B \rightarrow J/\psi$ distributions to estimate the yields and statistical uncertainties expected in the experiment.

3.4. Energy Loss of Charm Quarks. The suppression of open heavy flavor production observed at RHIC is comparable to that for light hadrons. This was a surprising result at the beginning because models which described well the light flavor data assuming gluon radiation (radiative energy loss, dE/dx_{rad}) predicted that the heavy quark production will be less suppressed than light partons [26]. This led to introduction of collisional energy loss dE/dx_{coll} due to binary interactions of partons with other objects in the QGP. One difficulty in modeling heavy quark energy loss is that the relative contributions of dE/dx_{coll} and dE/dx_{rad} are unknown. To understand better the interplay of these two processes, precise measurements of suppression of charm and bottom separately are necessary. We argue that measurements

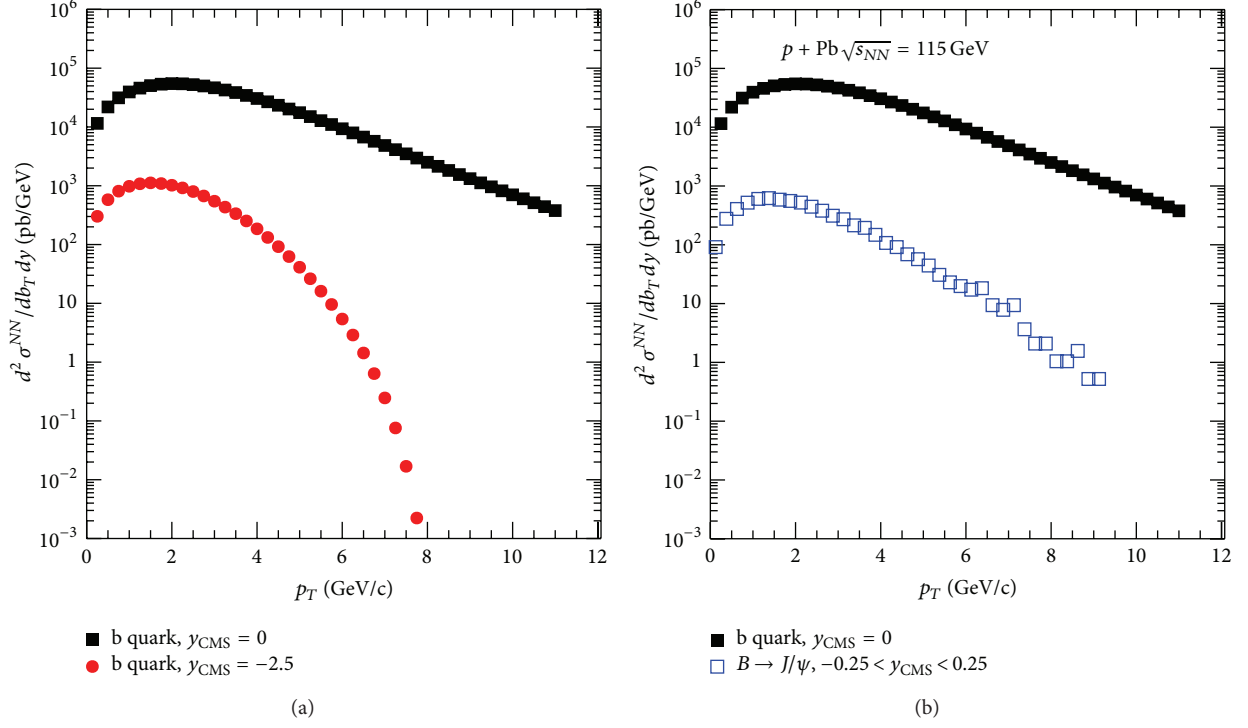


FIGURE 4: Bottom quark differential cross section per nucleon-nucleon collision as a function of p_T in $p + \text{Pb}$ collisions.

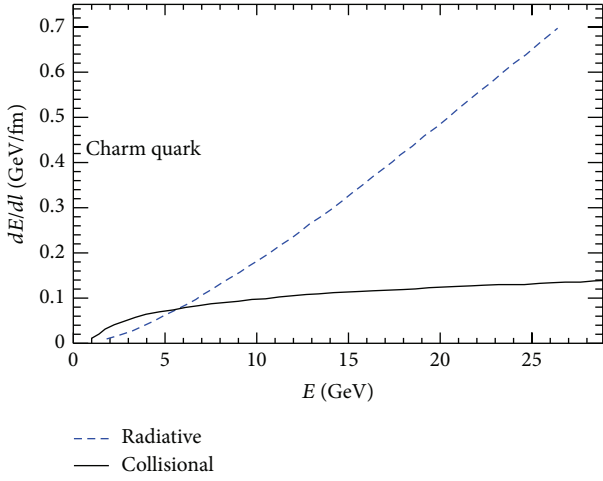


FIGURE 5: Radiative and collisional energy loss for charm quarks from [27] (model I) as a function of charm quark energy. Adopted from [27].

in $\text{Pb} + \text{Pb}$ collisions at $\sqrt{s_{NN}} = 72$ GeV in different rapidity ranges can help to estimate what are the shares of dE/dx_{rad} and dE/dx_{coll} in the observed suppression.

To model charm quark energy loss, we use predictions from [27] for radiative and collisional energy loss of heavy quark. Figure 5 shows the expected energy loss per unit of distance traveled in a nuclear matter for charm quarks from model I in [27] with a coupling constant $\alpha_s = 0.3$, an infrared regulator $\mu = 0.4$ GeV, and temperature $T = 200$ MeV (see

[27] for details). For low energies of heavy quarks, dE/dx_{coll} dominates but the radiative energy loss increases fast with increasing heavy quark energy and dE/dx_{rad} overshadows dE/dx_{coll} for $E > 5$ GeV.

A large acceptance of planned AFTER experiment allows probing different regimes of the energy loss, despite limited D^0 p_T range available experimentally, because charm quark at forward/backward rapidity will have a larger overall energy for the same p_T compared to midrapidity.

To model the suppression of heavy quark production, we assume that the average path length in the nuclear matter $\langle L \rangle$ is approximately equal to the averaged transverse path length $\langle L_{xy} \rangle$ (distance traveled in a plane perpendicular to the beam axis) traversed by a quark from a production point to the edge of the created fireball. We adopted a definition of $\langle L \rangle = \sqrt{\sigma_x^2 + \sigma_y^2}$ from [28], where σ_x^2 and σ_y^2 are variances of x and y positions of the participant nucleons, respectively. σ_x^2 and σ_y^2 are obtained using PHOBOS Glauber Monte Carlo and $\langle L \rangle = 4.104$ fm for 0–10% most central collisions. We use a nuclear modification factor R_{AA} to quantify the modification of the charm quark p_T spectrum due to energy loss:

$$R_{AA}(p_T) = \frac{N_{E_{\text{Loss}}}^{AA}(p_T)}{N_{\text{un.mod}}^{AA}(p_T)}, \quad (1)$$

where $N_{E_{\text{Loss}}}$ is a yield with energy loss applied and $N_{\text{un.mod}}$ is a heavy quark yield without any energy loss for a given centrality class and a given rapidity bin.

Figure 6 shows a nuclear modification factor R_{AA} (central value) at midrapidity (Figure 6(a)) and backward rapidity

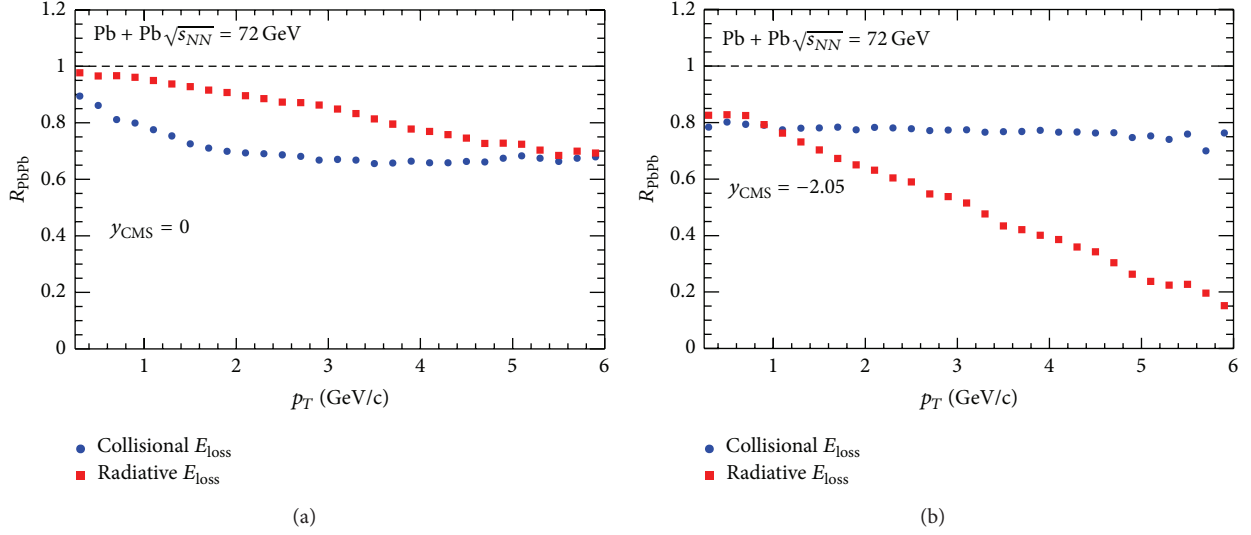


FIGURE 6: Nuclear modification factor R_{AA} (central value) for charm quark in Pb + Pb collisions at $\sqrt{s_{NN}} = 72$ GeV at midrapidity ($y_{CM} = 0$) and forward rapidity ($y_{CM} = -2.05$) for a radiative and collisional energy loss from Figure 5.

(Figure 6(b)) for 0–10% most central Pb + Pb collisions expected for dE/dx_{coll} and dE/dx_{rad} shown in Figure 5. The difference between dE/dx_{rad} and dE/dx_{coll} is more pronounced at backward rapidity, even at relatively low p_T , because quarks have much larger energy due to larger longitudinal momentum. Measurement at these two rapidity ranges simultaneously could help to pin down interplay of these two mechanisms.

4. Nuclear Modification Factors and Elliptic Flow in $p + Pb$ Collisions at $\sqrt{s_{NN}} = 115$ GeV

The sampled luminosity calculation in $p + p$ collisions is a significant source of the uncertainty when an energy loss is studied comparing heavy ion and $p + p$ collisions. Alternatively, we can use a central-to-peripheral ratio R_{CP} to quantify modification of the yields in $p + A$ or $A + A$ collisions:

$$R_{CP}(p_T) = \frac{N_{bin}^{Perip}}{N_{bin}^{Central}} \frac{N^{Central}(p_T)}{N^{Perip}(p_T)}, \quad (2)$$

where $N^{Central}$ and N^{Perip} are yields in central and peripheral $A + A$ collisions, respectively, for a given rapidity range and $N_{bin}^{Central}$ and N_{bin}^{Perip} are the average numbers of binary collisions for central and peripheral collisions. We use 0–10% most central collisions as a central bin and 60–80% bin as a baseline in R_{CP} calculations.

Figure 8(a) shows the expected statistical uncertainties for nuclear modification factor R_{CP} for D^0 at midrapidity and backward rapidity. Figure 7 presents the results for $B \rightarrow J/\psi$. The expected precision will allow a precision study of the cold nuclear matter effects for both charm and bottom for $p_T < 6$ GeV/c. Figure 8(b) shows statistical uncertainties for elliptic flow measurement. High luminosity data expected from AFTER would give a precise answer if there are any signs

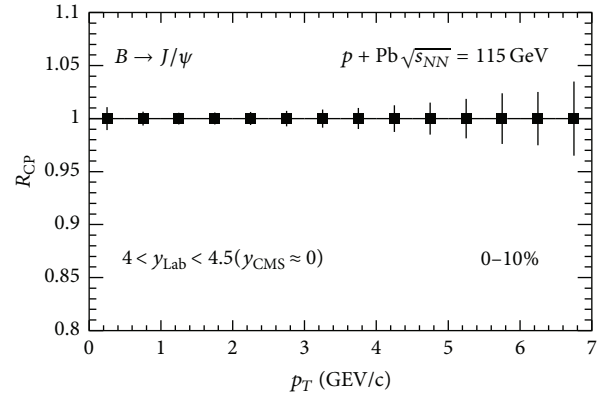


FIGURE 7: Expected statistical uncertainty of R_{CP} for $B \rightarrow J/\psi$ in $p + Pb$ collisions at $\sqrt{s_{NN}} = 115$ GeV.

of collective behavior of charm quarks in $p + A$ collisions at the intermediate energy at RHIC.

5. Nuclear Modification Factor for Charmed Meson in Pb + Pb Collisions at $\sqrt{s_{NN}} = 72$ GeV

Figure 9 shows the expected precision of R_{CP} for charmed meson as a function of p_T at midrapidity and backward rapidity. We show estimates for pure collisional and radiative energy loss scenarios based on Figure 5. The expected integrated luminosity for a single year will allow addressing the question if charm production is suppressed at high transverse momentum at $\sqrt{s_{NN}} = 72$ GeV. The comparison of results at different rapidity ranges will help to pin down the interplay of energy loss mechanisms at this energy range. The measurements of D^0 suppression for various collisions systems (which is feasible in a multiple-year physics program at AFTER) are even more interesting since they will allow

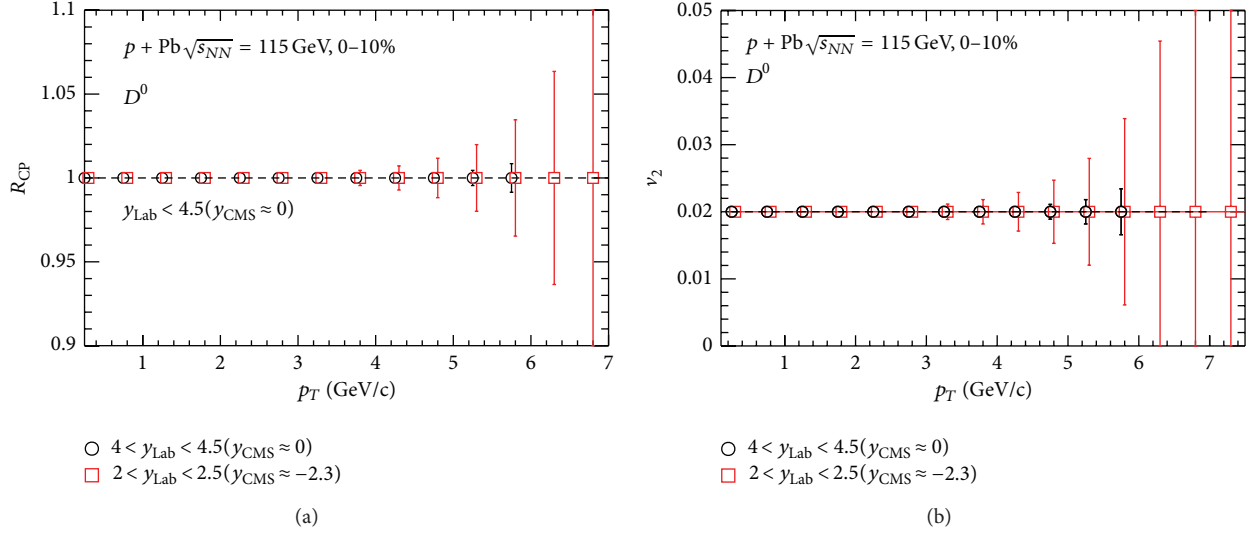


FIGURE 8: Expected statistical uncertainties of (a) D^0 R_{CP} and (b) D^0 elliptic flow in $p + \text{Pb}$ collisions at $\sqrt{s_{NN}} = 115$ GeV.

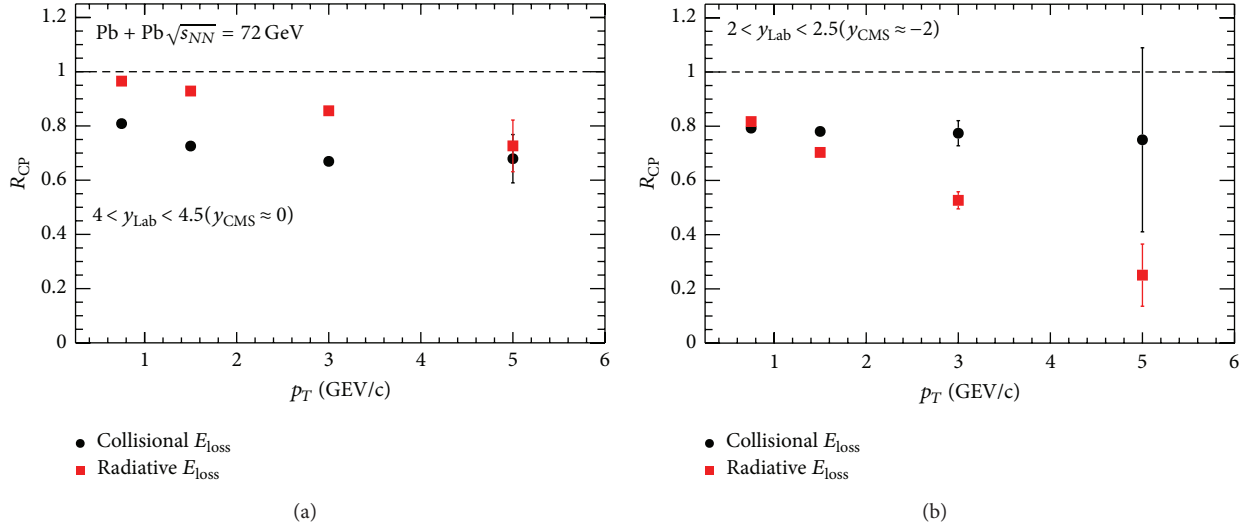


FIGURE 9: Expected statistical uncertainties of nuclear modification factor R_{CP} for D^0 meson in $\text{Pb} + \text{Pb}$ collisions at $\sqrt{s_{NN}} = 72$ GeV.

studying the energy loss as a function of path length and energy density of the created system.

6. Summary

We presented prospects for open charm and bottom production measurements in a fixed target experiment at LHC. We argue that such measurements will address important open issues about interactions of heavy quarks with the nuclear matter. High luminosity $p + A$ and $\text{Pb} + \text{Pb}$ data will help answer questions if there is a collective behavior of heavy quark in $p + A$ collisions at RHIC and what is the mechanism of energy loss of heavy quarks. Measurements at $\sqrt{s_{NN}} = 72$ GeV can shed new light on energy dependence of heavy quark interaction with the nuclear matter and thus on the phase diagram of nuclear matter.

Conflict of Interests

The author declares that there is no conflict of interests regarding the publication of this paper.

Acknowledgment

This work was supported in part by the Foundation for Polish Science Grant HOMING PLUS/2013-7/8.

References

- [1] R. Rapp and H. van Hees, "Heavy quarks in the Quark-Gluon plasma," in *Quark-Gluon Plasma*, vol. 4, chapter 3, p. 111, World Scientific Publishers, 2010, <http://arxiv.org/abs/0903.1096>.

- [2] S. Voloshin and Y. Zhang, “Flow study in relativistic nuclear collisions by Fourier expansion of azimuthal particle distributions,” *Zeitschrift für Physik C*, vol. 70, no. 4, pp. 665–671, 1996.
- [3] L. Adamczyk, J. K. Adkins, G. Agakishiev et al., “Elliptic flow of non-photonic electrons in Au+Au collisions at $\sqrt{s_{NN}} = 200$, 62.4 and 39 GeV,” <http://arxiv.org/abs/1405.6348>.
- [4] A. Adare, C. Aidala, N. N. Ajitanand et al., “Quadrupole anisotropy in dihadron azimuthal correlations in central d+Au Collisions at $\sqrt{s_{NN}} = 200$ GeV,” *Physical Review Letters*, vol. 111, Article ID 212301, 2013.
- [5] S. Chatrchyan, V. Khachatryan, A. M. Sirunyan, and A. Tumasyan, “Multiplicity and transverse momentum dependence of two- and four-particle correlations in pPb and PbPb collisions,” *Physics Letters B*, vol. 724, pp. 213–240, 2013.
- [6] B. I. Abelev, J. Adam, R. A. Bertens et al., “Long-range angular correlations of π , K and p in p-Pb collisions at $\sqrt{s_{NN}} = 5.02$ TeV,” *Physics Letters B*, vol. 726, no. 1–3, pp. 164–177, 2013.
- [7] A. Adare, S. Afanasiev, C. Aidalam et al., “Cold-nuclear-matter effects on heavy-quark production in $d + Au$ collisions at $\sqrt{s_{NN}} = 200$ GeV,” *Physical Review Letters*, vol. 109, Article ID 242301, 2012.
- [8] A. M. Sickles, “Possible evidence for radial flow of heavy mesons in $d + Au$ collisions,” *Physics Letters B*, vol. 731, pp. 51–56, 2014.
- [9] D. Kikola and A. Lipiec, “Estimate of cold nuclear matter effects on bottom production in $d + Au$ collisions at $\sqrt{s_{NN}} = 200$ GeV,” <http://arxiv.org/abs/1410.6503>.
- [10] B. Alver, M. Baker, C. Loizides, and P. Steinberg, “The PHOBOS Glauber Monte Carlo,” <http://arxiv.org/abs/0805.4411>.
- [11] C. Loizides, J. Nagle, and P. Steinberg, “Improved version of the PHOBOS Glauber Monte Carlo,” <http://arxiv.org/abs/1408.2549>.
- [12] A. A. Alves Jr., L. M. A. Filho, A. F. Barbosa et al., “The LHCb detector at the LHC,” *Journal of Instrumentation*, vol. 3, Article ID S08005, 2008.
- [13] A. V. Kozlinskiy, *Outer tracker calibration and open charm production cross section measurement at LHCb [Ph.D. thesis]*, Vrije Universiteit, CERN-THESIS-2012-338, Amsterdam, The Netherlands, 2012.
- [14] R. Aaij, B. Adeva, M. Adinolfi et al., “Measurement of J/ψ production in pp collisions at $\sqrt{s} = 7$ TeV,” *The European Physical Journal C*, vol. 71, article 1645, 2011.
- [15] M. Cacciari, M. Greco, and P. Nason, “The p_T spectrum in heavy-flavour hadroproduction,” *Journal of High Energy Physics*, vol. 1998, no. 5, article 007, 1998.
- [16] M. Cacciari, S. Frixione, N. Houdeau, M. L. Mangano, P. Nason, and G. Ridolfi, “Theoretical predictions for charm and bottom production at the LHC,” *Journal of High Energy Physics*, vol. 2012, no. 10, article 137, 2012.
- [17] P. N. M. Cacciari and S. Frixione, FONLL, version 1.3.3, <http://cacciari.web.cern.ch/cacciari/fonll>.
- [18] P. M. Nadolsky, H.-L. Lai, Q.-H. Cao et al., “Implications of CTEQ global analysis for collider observables,” *Physical Review D*, vol. 78, Article ID 013004, 2008.
- [19] K. Eskola, H. Paukkunen, and C. Salgado, “EPS09—global NLO analysis of nuclear PDFs and their uncertainties,” *Nuclear Physics A*, vol. 830, no. 1–4, pp. 599c–602c, 2009.
- [20] L. Adamczyk, G. Agakishiev, M. M. Aggarwal et al., “Measurements of D^0 and D^+ production in $p + p$ collisions at $\sqrt{s} = 200$ GeV,” *Physical Review D*, vol. 86, Article ID 072013, 2012.
- [21] Z. Ye, “Open charm hadron production in p+p, Au+Au and U+U collisions at STAR,” *Nuclear Physics A*, vol. 931, pp. 520–524, 2014.
- [22] C. Amsler, M. Doser, M. Antonelli et al., “Review of particle physics,” *Physics Letters B*, vol. 667, no. 1–5, pp. 1–6, 2008.
- [23] I. Antcheva, “ROOT—a C++ framework for petabyte data storage, statistical analysis and visualization,” *Computer Physics Communications*, vol. 180, no. 12, pp. 2499–2512, 2009, <http://root.cern.ch>.
- [24] R. Aaij, C. Abellan Beteta, B. Adeva et al., “Measurement of b hadron production fractions in 7 TeV pp collisions,” *Physical Review D*, vol. 85, Article ID 032008, 2012.
- [25] S. J. Brodsky, F. Fleuret, C. Hadjidakis, and J. P. Lansberg, “Physics opportunities of a fixed-target experiment using LHC beams,” *Physics Reports*, vol. 522, no. 4, pp. 239–255, 2013.
- [26] M. Djordjevic, M. Gyulassy, R. Vogt, and S. Wicks, “Influence of bottom quark jet quenching on single electron tomography of Au + Au,” *Physics Letters, Section B: Nuclear, Elementary Particle and High-Energy Physics*, vol. 632, no. 1, pp. 81–86, 2006.
- [27] J. Aichelin, P. B. Gossiaux, and T. Gousset, “Collisional and radiative energy loss of heavy quarks,” *Journal of Physics: Conference Series*, vol. 455, no. 1, Article ID 012046, 2013.
- [28] H. Masui, B. Mohanty, and N. Xu, “Predictions of elliptic flow and nuclear modification factor from 200 GeV U + U collisions at RHIC,” *Physics Letters B*, vol. 679, no. 5, pp. 440–444, 2009.

Research Article

A Gas Target Internal to the LHC for the Study of pp Single-Spin Asymmetries and Heavy Ion Collisions

Colin Barschel,¹ Paolo Lenisa,² Alexander Nass,³ and Erhard Steffens⁴

¹LHCb Collaboration, CERN, 1211 Geneva 23, Switzerland

²University of Ferrara and INFN, 44100 Ferrara, Italy

³Institut für Kernphysik, FZJ, 52425 Jülich, Germany

⁴Physics Institute, Friedrich-Alexander University Erlangen-Nürnberg, 91058 Erlangen, Germany

Correspondence should be addressed to Paolo Lenisa; lenisa@fe.infn.it

Received 19 March 2015; Revised 5 June 2015; Accepted 5 July 2015

Academic Editor: Barbara Trzeciak

Copyright © 2015 Colin Barschel et al. This is an open access article distributed under the Creative Commons Attribution License, which permits unrestricted use, distribution, and reproduction in any medium, provided the original work is properly cited. The publication of this article was funded by SCOAP³.

We discuss the application of an open storage cell as gas target for a proposed LHC fixed-target experiment AFTER@LHC. The target provides a high areal density at minimum gas input, which may be polarized ¹H, ²H, or ³He gas or heavy inert gases in a wide mass range. For the study of single-spin asymmetries in pp interaction, luminosities of nearly 10³³/cm² s can be produced with existing techniques.

Devoted to Professor Willy Haeberli (Wisconsin) on his 90th birthday on June 17, 2015, who presented the first ideas on a polarized storage cell target 50 years ago at the 2nd Polarization Symposium, 1965, in Karlsruhe (Germany) and who pioneered this technique and brought it to maturity

1. Introduction

Colliding beam facilities are indispensable tools for achieving the highest possible collision energies \sqrt{s} . Their range of application may be enlarged by adding a fixed-target experiment, for example, using a thin internal gas target which does not affect the luminosity life time significantly. Experiments based on such targets offer distinct features as compared with collider experiments [1, 2]:

- (1) Accessing the large negative Feynman x_F domain,
- (2) achieving high luminosities with dense targets,
- (3) varying the atomic number A of the target in a wide range,
- (4) polarizing light target atoms (¹H, ²H = D, ³He) with polarization of the nuclear spin s .

The target proposed consists of an open storage cell, a narrow straight tube with thin walls of length L located in the

machine vacuum along the beam axis into which gas is injected at the center in two modes:

- (i) polarized atomic beam (e.g., H) into a feed tube of low gas conductance;
- (ii) unpolarized gas via capillary from a gas handling system.

The gas diffuses through the cell openings into the machine vacuum system, usually a powerful differential pumping system, and constitutes within the cell a density distribution of triangular shape with its maximum ρ_0 [atoms/cm³] at the center. The areal target density θ is then $\theta = \rho_0 \cdot L/2$ (see Section 3). Such kind of gas targets for storage rings is reviewed in [3]. Targets for proton beams at intermediate energies have been applied at the cooler ring COSY (FZ Jülich) [4–6] and at the IUCF Cooler Ring [7]. At the 30 GeV electron ring of the HERA collider (DESY Hamburg), the HERMES H&D target [8] has been operated successfully during 1996–2005. In 1995, prior to the HERMES H&D

target, a polarized ^3He target [9] has been used for the measurement of the neutron spin structure function.

In the following, the design and performance of the HERMES H&D target which may be closest in design to the proposed LHC target are reviewed in Section 2. First ideas of a storage cell target in the LHC are presented in Section 3. The paper is concluded by discussing some of the open problems which need to be subject of further studies.

2. The HERMES Polarized Hydrogen and Deuterium Target

An overview of the HERMES polarized H and D target [8] is presented in Figure 1. It consists of three main components:

- (i) the *Atomic Beam Source* (ABS) for the production of an intense polarized atomic hydrogen beam, consisting of a dissociator with cooled nozzle, a system of sextupole magnets focusing the wanted hfs components¹ into the feed tube of the cell, and adiabatic rf-transitions² for setting and switching the target polarization between states of opposite sign (*Endnotes*^{1,2});
- (ii) the *target chamber* with T-shaped storage cell of 400 mm in length and elliptical cross section with diameters horizontal/vertical of 21 and 9 mm, respectively, and a longitudinal or vertical holding field B up to 350 mT. The cell temperature could be set to values between 50 and 300 K;
- (iii) the *diagnostic system* for analyzing a weak sample beam drawn from the target cell, consisting of the polarimeter (BRP) measuring the substate population and the target gas analyzer (TGA) detecting the molecular fraction and thus the degree of recombination within the cell. From these parameters, the target polarization as seen by the beam is deduced.

For details of the design, operation, and analysis of the data of the diagnostic system the reader is referred to [8] and to the references therein, in particular on the various subsystems. Here a few important details are given, only. The ABS injects a flux of $\approx 6.5 \times 10^{16}$ atoms/s into the feed tube of the target cell, corresponding to a recombined H_2 -flow rate of about $2.5 \cdot 10^{-3}$ mbarl/s into the machine vacuum system. The target particles (H, H_2) are confined by the cell walls to the close vicinity of the beam axis, thus increasing the areal density to values of about $10^{14}/\text{cm}^2$, two orders of magnitude higher than the density of the injected atomic beam. The Al-walls of the cell are cooled to a temperature of about 100 K for two reasons: (i) increasing the density θ by $\sqrt{3}$ and (ii) buildup of a thin layer of frozen water which suppresses wall recombination effectively. The water is produced within the dissociator from a small O_2 admixture to the hydrogen gas and flows with the atomic beam.

A “strong” guide field of sufficient homogeneity is required for the target, either longitudinal for helicity measurements or transverse for transverse spin effects. The strength of about 300 mT = $6 \cdot B_c$ ($B_c = 50.7$ mT is the critical

field of the H atom) for the longitudinal field was chosen such that (i) proton and electron spins are fully decoupled and (ii) there is no depolarizing resonance due to the periodic bunch field of the beam. The target polarization³ is deduced from the data continuously recorded by the diagnostic system. The density-weighted target polarization along z can be related to the sample beam data using assumptions about the relaxation mechanisms which contributes to the error.

The stability of the target is demonstrated in Figure 2, where the raw data of the transverse proton run 2002/03 are shown. For 2002, the average target polarization corrected for guide field and degree of dissociation was $|P_z| = 0.74 \pm 0.06$ only, partly due to a less stable operation of HERA and to a weaker guide field of the normal-conducting transverse magnet, in contrast to the 1996/97 longitudinal proton run with average polarization $|P_z| = 0.851 \pm 0.033$ (see *Endnote*³).

Polarized deuterium has been run in 1999/2000 with longitudinal field. In 2000, a very stable operation had been achieved, resulting in the following parameters: $\theta(\text{D}) = 1.05 \cdot 10^{14}/\text{cm}^2$, with $P_z = +0.851 \pm 0.029$ and -0.840 ± 0.026 and $P_{zz} = +0.891 \pm 0.027$ and -1.656 ± 0.049 [8] (see *Endnote*³).

It should be noted that the same target has been used with unpolarized gas in a broad mass range for the study of the A -dependence of various effects in DIS⁴. The ^3He target [9] run in 1995 had the following characteristics: target density $\theta(^3\text{He}) = 3.3 \cdot 10^{14}/\text{cm}^3$ and polarization $P_z = 0.46 \pm 0.02$. Today, the polarization of such optically pumped targets can reach values of 0.8, that is, 80% of the maximum [12].

3. First Ideas on an LHC Storage Cell Target

3.1. Density Achievable for Polarized Hydrogen. The target density θ depends on the geometry of the storage cell and the gas input. The required aperture at a beam waist may be estimated with safety margin of 1 mm by

$$r = 15\sigma_r + 1 \text{ mm} \quad (r = x, y), \quad (1)$$

with σ_r being the 1σ beam radius in the horizontal and vertical plane. With nominal parameters for the LHC IP⁵ of $\sigma^* = 16 \cdot 10^{-6}$ m and the beta function $\beta^* = 0.55$ m ($*$ = min. values at IP), (1) results in a required aperture of 1.24 mm, dominated by the safety margin. At $z = \pm 0.5$ m the aperture increases slightly to 1.46 mm. It seems unlikely that such small apertures are compatible with a stable LHC operation. Another criterion is required for first estimates on a possible cell target for the LHC.

At the VELO detector [13–15] of LHCb, the two halves can be opened during injection and tuning. In the closed position, a narrow tube of 1 cm in diameter and 100 cm in length is wide enough to guide the LHC beam through the detector. In the following we assume conservatively (see Figure 3) a size of $D_1 = 1.4$ cm and $L_1 = 50$ cm for a cylindrical target cell, that is, a full length of 100 cm, which may have the option to open by being split into two halves. For the feed tube we assume $D_2 = 1.0$ cm and $L_2 = 10$ cm, a geometry for which the HERMES ABS has been optimized.

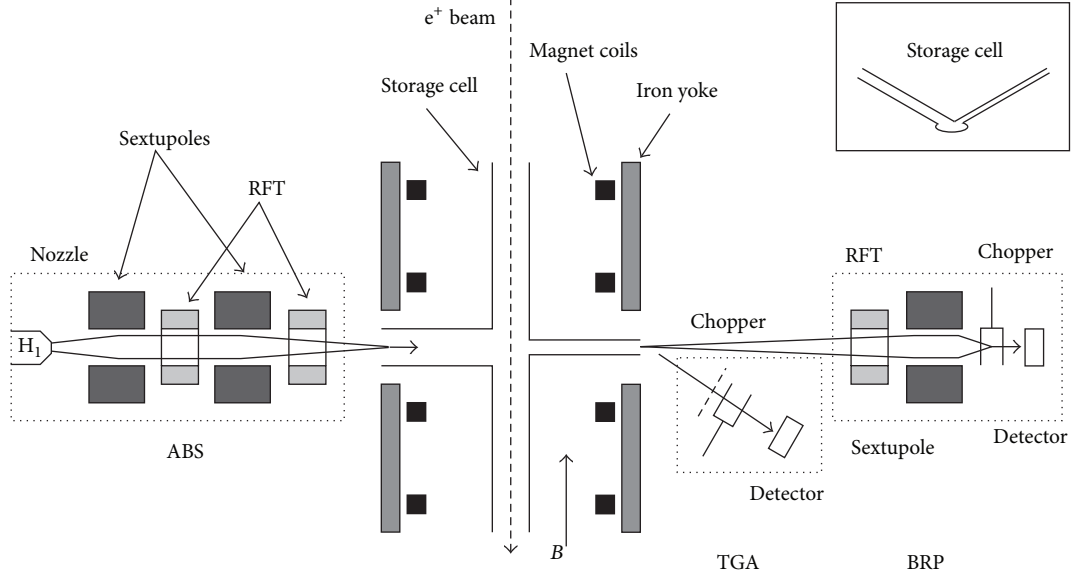


FIGURE 1: Schematic representation (top view) of the HERMES longitudinally polarized target (taken from [8]). From left to right: Atomic Beam Source (ABS), target chamber with cell and SC magnet coils, diagnostic system of target gas analyzer (TGA), and Breit-Rabi polarimeter (BRP).

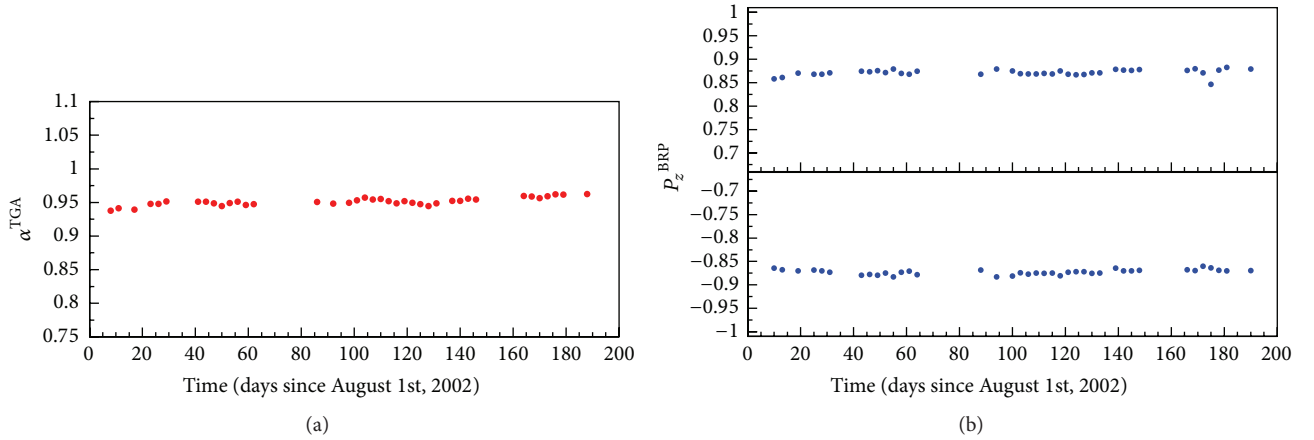


FIGURE 2: Results of the target analysis for the HERMES 2002/03 data taking period with transverse proton polarization as number of days, since August 1, 2002 (taken from [8]): (a) degree of dissociation α measured by the TGA ($\alpha = 1$: no molecules); (b) positive and negative vector polarization P_z of the sampled atomic part as measured by the BRP. During data taking the states of opposite sign are set periodically with a cycle time of the order of 1 min.

The gas conductance of a tube in the molecular-flow regime is given by [3]

$$C_i \text{ [l/s]} = \frac{3.81 \sqrt{(T/M)} D_i^3}{(L_i + 1.33 D_i)}, \quad (2)$$

where T is the temperature in K, $M = 1$ the molecular mass for atomic hydrogen, and L, D are in cm. The total conductance C_{tot} of the cell from the center outwards is then $C_{\text{tot}} = 2C_1 + C_2$ which at $T = 300$ K amounts to $C_{\text{tot}} = 12.81$ l/s. With a flux of polarized hydrogen atoms of $I = 6.5 \cdot 10^{16}$ H/s into the cell, the central density ρ_0 is then

$$\rho_0 = \frac{I}{C_{\text{tot}}} = \frac{5.07 \cdot 10^{12}}{\text{cm}^3}, \quad (3)$$

resulting in an areal polarized hydrogen density of the 100 cm long cell of 1.4 cm i.d. at $T = 300$ K of

$$\theta = \rho_0 L_1 = 2.54 \cdot 10^{14} / \text{cm}^2. \quad (4)$$

The pp luminosity of such a target installed at LHC at nominal proton beam current of $3.6 \cdot 10^{18}$ p/s is then

$$\mathcal{L}_{\text{pp}} = 0.92 \cdot 10^{33} / \text{cm}^2 \text{ s}. \quad (5)$$

For optimizing the cell wall conditions it might be necessary to run the cell at a temperature of 100 K instead of 300 K, as

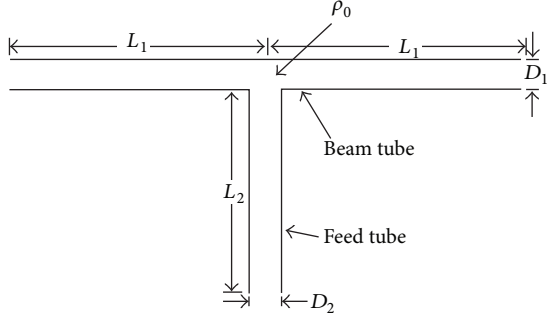


FIGURE 3: Storage cell geometry. The proton beam is traversing the beam tube of total length $2L_1$; the polarized atomic beam enters “ballistically” via the feed tube into the center and diffuses outwards along the three tube elements with a density maximum ρ_0 in the center (figure taken from [3]).

for the HERMES target [8] (see Section 2). This would result in a $\sqrt{3}$ higher target density and a maximum luminosity of $\mathcal{L}_{pp}(100\text{ K}) = 1.59 \cdot 10^{33}/\text{cm}^2\text{ s}$.

If such a target is run in addition to other experiments, it is important to know its effect on the life time τ_p of a stored LHC proton beam. Let us assume a maximum value of $\mathcal{L}_{pp} = 1.6 \cdot 10^{33}/\text{cm}^2\text{ s}$. The loss rate is then given by the product of \mathcal{L}_{pp} with the pp loss cross section at a CM energy of 162 GeV, which we estimate by 0.1 b, resulting in a loss rate $dN/dt = N^* = 1.6 \cdot 10^8\text{ p/s}$. The relative loss rate is N^*/N_p with the number of stored protons $N_p = 3.2 \cdot 10^{14}$, which gives a relative loss rate of $5 \cdot 10^{-7}/\text{s}$, corresponding to a $1/e$ beam life time, the inverse of the relative loss rate, of $2 \cdot 10^6\text{ s}$ or 23 days. We conclude that for the pp case additional beam losses caused by the hydrogen target gas are negligible. The target density given above is limited by the present target technology, for example, the intensity of the source feeding the cell target.

These are first estimates only, which need to be developed further if the details of a fixed-target experiment at LHC are known. The calculated target densities and the resulting luminosities are within a favorable range. Clearly, several aspects need to be investigated to make such estimates more reliable, in particular (i) the amount of target gas the LHC machine vacuum system can accept, (ii) the rôle of frozen layers like water on the inner cell surface and whether they might cause instabilities, (iii) problems of access and reliability of running a complex pumping system in the LHC tunnel, and so forth.

3.2. Density Achievable for Heavy Ion Collisions. As mentioned earlier, heavy unpolarized target gas could be injected into the cell for the study of heavy ion collisions. In principle, the gas flow from a Gas Feed System and thus the density of a cell target can be very high. On the other hand, there will be limitations due to the maximum gas flow the vacuum system at a possible LHC target station can take. Another limit might come from the rate capability of the detector system. Here, we present estimates of a density limit set by the requirement that the cell target filled with a heavy gas

must not shorten the beam life time of a heavy ion beam, for example, a Pb beam, by more than 10%. For the LHC in Pb-Pb collider mode without gas target we assume a beam life time of 10 h. As target gas we assume xenon with average molecular weight $M \approx 131$. As a loss cross section we start with the total hadronic cross section σ_{tot} of Pb on Pb of 7.65 b [16]. By scaling with the nuclear radii, the Pb-Xe loss cross section is estimated to be 6.6 b. We require that the additional “target” life time⁶ $\tau_t = 10 \cdot 10\text{ h} = 3.6 \cdot 10^5\text{ s}$ is related to the loss rate $dN/dt = N^*$ (N = number of stored Pb ions = $4 \cdot 10^{10}$) by

$$\frac{N^*}{N} = \frac{1}{3.6 \cdot 10^5\text{ s}}, \quad (6)$$

$$\text{that is } N^* = \frac{4 \cdot 10^{10}}{3.6 \cdot 10^5\text{ s}} = 1.1 \cdot 10^5/\text{s} = \mathcal{L}_{\text{Pb-Xe}} \cdot \sigma_{\text{tot}}.$$

This results in a maximum Pb-Xe luminosity of $\mathcal{L}_{\text{Pb-Xe}} = 1.7 \cdot 10^{28}/\text{cm}^2\text{ s}$ and a maximum density of Xenon atoms of $\theta_{\text{Xe}} = 3.8 \cdot 10^{13}/\text{cm}^2$. The xenon flow rate into the target cell required to produce this density amounts to a value of $3.2 \cdot 10^{-5}\text{ mbar/l/s}$. It should be noted that the LHC Pb-Pb design luminosity in collider mode is $1 \cdot 10^{27}/\text{cm}^2\text{ s}$. We conclude that for the hypothetical Pb-Xe fixed-target case a high luminosity in the order of the LHC Pb-Pb design luminosity can be produced. The Pb-Xe fixed-target luminosity is not limited by the storage cell technology but rather by other factors like beam life time, detector rate, and so forth.

In Table 1, the results of this study are compared with past or existing targets in storage rings, their main operational parameters, and luminosities achieved.

4. Summary

In this study, the application and expected performance of a storage cell target interacting with the LHC beam are investigated. Using polarized light atoms (^1H , ^2D , and possibly ^3He) from external sources and a proton beam, single-spin asymmetries of various processes for longitudinal or transverse target polarization could be measured at high rate. With unpolarized atoms or molecules in a broad mass range from H_2 to Xe or beyond as target gas, heavy ion collisions could be studied with flexible choice of the target mass and target density. These estimates show that a high luminosity for proton-proton and heavy ion collisions at the LHC can be achieved using the storage cell technique. The optimum density has to be determined taking a number of operational aspects into account.

It should be noted that due to the strongly forward peaked particle emission, the physics accessible by such an ultrarelativistic fixed-target experiment depends very much on the design of the detector. This is not subject of the present study.

In summary, the promising results of this study indicate that a storage cell target combined with the LHC beam may open access to additional physics topics like the gluon contribution to the proton spin, the gluon EMC effect, or

TABLE 1: Comparison of gas targets in storage rings with a hypothetical target for the proposed AFTER@LHC initiative [1, 2]. The target gas ^1H , ^2D , or ^3He is assumed to be spin polarized.

Storage ring	Particle	E_{max} [GeV]	Target type	L [m]	T [K]	L_{max} [1/cm ² s]	Remarks	Reference
HERA-e DESY (term. 2007)	e^\pm pol.	27.6	Cell ^1H , ^2D , ^3He	0.4	100 25	$2.5 \cdot 10^{31}$ $2.5 \cdot 10^{32}$	HERMES exp. 1995–2007	[9]
RHIC-p BNL	p pol.	250	Jet	—	—	$1.7 \cdot 10^{30}$	Absolute p polarimeter	[10]
COSY FZ Jülich	p, d pol.	3.77 $T = 49.3 \text{ MeV}$	Cell ^1H , ^2D Cell ^1H	0.4	300	10^{29} $2.75 \cdot 10^{29}$	ANKE exp. PAX exp.	[4, 5] [11]
LHC CERN (proposed)	p unpol. heavy ions	7,000 $2,760 \cdot A$	Cell ^1H , ^2D Xe $M \approx 131$	1.0	100 ≥ 100	10^{33} $10^{27}-10^{28}$	Based on techn. of HERMES target	this paper

deconfinement studies using the Pb beam with targets of different mass, as discussed in [1, 2].

Conflict of Interests

The authors declare that there is no conflict of interests regarding the publication of this paper.

Acknowledgment

The authors thank Massimiliano Ferro-Luzzi (CERN) for valuable discussions.

Endnotes

1. Hyperfine structure components; see [3].
2. Radio-frequency transitions between hfs components; see [3].
3. The vector polarization P_z is bound to $-1 \leq P_z \leq 1$ and tensor polarization P_{zz} for spin = 1 to $-2 \leq P_{zz} \leq 1$; see [3].
4. Deep inelastic scattering.
5. Interaction point, for example, collision point.
6. Note: the total target life time τ_{tot} is calculated from the individual loss rates N_i^* by $\tau_{\text{tot}} = (1/N_1^* + 1/N_2^* + \dots)^{-1}$.

References

- [1] S. J. Brodsky, F. Fleuret, C. Hadjidakis, and J. P. Lansberg, “Physics opportunities of a fixed-target experiment using LHC beams,” *Physics Reports*, vol. 522, no. 4, pp. 239–255, 2013.
- [2] J. P. Lansberg, M. Anselmino, R. Arnaldi et al., “Spin physics and TMD studies at A Fixed-Target Experiment at the LHC (AFTER@LHC),” *EPJ Web of Conferences*, vol. 85, Article ID 02038, 6 pages, 2015.
- [3] E. Steffens and W. Haeberli, “Polarized gas targets,” *Reports on Progress in Physics*, vol. 66, no. 11, article 1887, 2003.
- [4] M. Mikirtychyants, R. Engels, K. Grigoryev et al., “The polarized H and D atomic beam source for ANKE at COSY-Jülich,” *Nuclear Instruments and Methods in Physics Research A: Accelerators, Spectrometers, Detectors and Associated Equipment*, vol. 721, pp. 83–98, 2013.
- [5] K. Grigoryev, F. Rathmann, R. Engels et al., “Machine studies for the development of storage cells at the ANKE facility of COSY,” *Nuclear Instruments and Methods in Physics Research Section A*, vol. 599, no. 2-3, pp. 130–139, 2009.
- [6] G. Ciullo, “The H and D polarized target for spin-filtering measurements at COSY,” in *Proceedings of the 21st International Symposium on Spin Physics (SPIN '14)*, Beijing, China, October 2014, <http://collaborations.fz-juelich.de/ikp/pax/documents/talks.shtml>.
- [7] W. A. Dezarn, J. Doskow, J. G. Hardie et al., “Polarized internal gas target for hydrogen and deuterium at the IUCF Cooler Ring,” *Nuclear Instruments and Methods in Physics Research Section A*, vol. 362, no. 1, pp. 36–40, 1995.
- [8] A. Airapetian, N. Akopov, Z. Akopov et al., “The HERMES polarized hydrogen and deuterium gas target in the HERA electron storage ring,” *Nuclear Instruments and Methods in Physics Research Section A*, vol. 540, no. 1, pp. 68–101, 2005.
- [9] D. De Schepper, L. H. Kramer, S. F. Pate et al., “The HERMES polarized ^3He internal gas target,” *Nuclear Instruments and Methods in Physics Research A: Accelerators, Spectrometers, Detectors and Associated Equipment*, vol. 419, no. 1, pp. 16–44, 1998.
- [10] A. Poblaguev, “Polarimetry at the AGS,” in *Proceedings of the 15th International Workshop on Polarized Sources, Targets, and Polarimetry (PSTP '13)*, p. 053, Charlottesville, Va, USA, 2013.
- [11] W. Augustyniak, L. Barion, S. Barsov et al., “Polarization of a stored beam by spin-filtering,” *Physics Letters B*, vol. 718, no. 1, pp. 64–69, 2012.
- [12] R. Milner, *Private Communication*, MIT, 2015.
- [13] C. Barschel, *Precision luminosity measurements at LHCb with beam-gas imaging [Ph.D. thesis]*, RWTH Aachen University, Aachen, Germany, 2014, CERN-THESIS-2013-301.
- [14] M. Ferro-Luzzi, “Proposal for an absolute luminosity determination in colliding beam experiments using vertex detection of beam-gas interactions,” *Nuclear Instruments and Methods in Physics Research Section A*, vol. 553, no. 3, pp. 388–399, 2005.

- [15] R. Aaij, C. Abellan Beteta, R. Llull et al., “Precision luminosity measurements at LHCb,” *Journal of Instrumentation*, vol. 9, Article ID P12005, 2014.
- [16] K. Oyama, “Reference cross section measurements with ALICE in pp and Pb-Pb collisions at LHC,” <http://arxiv.org/abs/1305.7044>.

Review Article

A Review of the Intrinsic Heavy Quark Content of the Nucleon

S. J. Brodsky,¹ A. Kusina,² F. Lyonnet,³ I. Schienbein,² H. Spiesberger,^{4,5} and R. Vogt^{6,7}

¹SLAC National Accelerator Laboratory, Stanford University, Stanford, CA 94301, USA

²Laboratoire de Physique Subatomique et de Cosmologie, Université Grenoble-Alpes, CNRS/IN2P3, 53 avenue des Martyrs, 38026 Grenoble, France

³Southern Methodist University, Dallas, TX 75275, USA

⁴PRISMA Cluster of Excellence, Institut für Physik, Johannes Gutenberg-Universität Mainz, 55099 Mainz, Germany

⁵Centre for Theoretical and Mathematical Physics and Department of Physics, University of Cape Town, Rondebosch 7700, South Africa

⁶Nuclear and Chemical Sciences Division, Lawrence Livermore National Laboratory, Livermore, CA 94551, USA

⁷Physics Department, University of California at Davis, Davis, CA 95616, USA

Correspondence should be addressed to I. Schienbein; schien@lpsc.in2p3.fr

Received 17 April 2015; Accepted 15 June 2015

Academic Editor: Gianluca Cavoto

Copyright © 2015 S. J. Brodsky et al. This is an open access article distributed under the Creative Commons Attribution License, which permits unrestricted use, distribution, and reproduction in any medium, provided the original work is properly cited. The publication of this article was funded by SCOAP³.

We present a review of the state of the art of our understanding of the intrinsic charm and bottom content of the nucleon. We discuss theoretical calculations, constraints from global analyses, and collider observables sensitive to the intrinsic heavy quark distributions. A particular emphasis is put on the potential of a high energy and high luminosity fixed target experiment using the LHC beams (AFTER@LHC) to search for intrinsic charm.

1. Introduction

The existence of a nonperturbative intrinsic heavy quark component in the nucleon is a rigorous prediction of Quantum Chromodynamics (QCD). An unambiguous experimental confirmation is still missing and would represent a major discovery. The goal of this paper is to summarize our current understanding of this subject with a particular focus on the potential of a high energy and high luminosity fixed target experiment using the LHC beams (AFTER@LHC) [1–4] to search for intrinsic charm.

Production processes sensitive to the intrinsic heavy quark distributions of protons and nuclei are among the most interesting hadronic physics topics that can be investigated with AFTER@LHC. In contrast to the familiar extrinsic contributions which arise from gluon splitting in perturbative QCD, the intrinsic heavy quarks have multiple connections to the valence quarks of the proton and thus are sensitive to its nonperturbative structure. For example, if the gluon-gluon scattering box diagram, $gg \rightarrow Q\bar{Q} \rightarrow gg$ (the analog of QED light-by-light scattering), is inserted into the proton

self-energy, the cut of this amplitude generates five-quark Fock states of the proton $|uudQ\bar{Q}\rangle$; see Figure 1.

Intrinsic strange, charm, and bottom quarks are thus a fundamental property of the wavefunctions of hadronic bound states [5–8]. While the extrinsic contributions to the heavy quark parton distribution functions (PDFs) are most important at low x and depend logarithmically on the heavy quark mass M_Q , the intrinsic heavy quark contributions are dominant at high x and depend on $1/M_Q^2$. Because the extrinsic heavy quarks are generated by gluon splitting, their PDFs are always softer than those of the parent gluon by a factor of $(1-x)$. In contrast, the high x intrinsic heavy quark contributions are kinematically dominated by the regime where the $|uudQ\bar{Q}\rangle$ state is minimally off shell, corresponding to equal rapidities of the constituent quarks. The resulting momentum and spin distributions of the intrinsic Q and \bar{Q} can be distinct, for example, $s(x) \neq \bar{s}(x)$, since the comoving $uudQ\bar{Q}$ quarks are sensitive to the global quantum numbers of the protons.

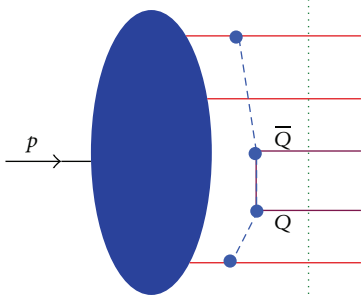


FIGURE 1: Five-quark Fock state $|uudQ\bar{Q}\rangle$ of the proton and the origin of the intrinsic sea.

A finite intrinsic charm contribution to the nucleon has been extracted from lattice QCD. An analysis by the MILC collaboration [9] yields a probability for the charm matrix element $\langle N|c\bar{c}|N\rangle$ in the range of 5-6%, consistent with a four-loop perturbative QCD calculation [10].

While the first experimental evidence of intrinsic heavy quarks came from the EMC measurement of the large x charm structure function [11], a variety of other charm hadrons and charmonium measurements are consistent with the existence of intrinsic charm. Open charm observables in hadroproduction include forward Λ_c production at the ISR [12]. Similarly, the coalescence of comoving b , u , and d quarks from the $|uud\bar{b}b\rangle$ intrinsic bottom Fock state in the proton can explain the high x_F production of the $\Lambda_b(udb)$ baryon, as observed at the ISR [12], and asymmetries between leading and nonleading charms (\bar{D} mesons which share valence quarks with the projectile and D mesons which do not, resp.) measured as functions of x_F and p_T in fixed target experiments, WA89 and WA82 at CERN; E791 and SELEX at Fermilab; see [13–15] and references therein. Previous fixed target J/ψ measurements also give indications of important intrinsic charm contributions, particularly from the nuclear mass, or A , dependence, as measured by NA3 at CERN as well as E772 and, later, E866 at Fermilab; see, for example, [16]. Indeed, the A dependence, proportional to A^α , is quite different than the $\alpha \sim 1$ expected from extrinsic-type production [17]. At large x_F , there are indications of $A^{2/3}$ dependence, consistent with a nuclear surface-type interaction instead of the volume dependence of pQCD. In addition, the NA3 collaboration measured double J/ψ production at forward x_F in πA interactions, difficult to explain without an intrinsic charm mechanism [18]. All of these observables can be studied with higher energies and luminosities at AFTER@LHC, making precision measurements possible for the first time.

In addition to the typical observables for intrinsic heavy quarks, these intrinsic heavy quarks also contribute to a number of more exotic observables and inclusive and diffractive Higgs production $pp \rightarrow ppH$, in which the Higgs boson carries a significant fraction of the projectile proton momentum [19, 20]. There are also important implications for intrinsic charm and bottom quarks in Standard Model physics, as in the weak decays of the B -meson [21] and a novel

solution to the $J/\psi \rightarrow \rho\pi\pi$ problem [22]. AFTER@LHC could also shed light on these topics.

The rest of this paper is organized as follows. In Section 2, we give an overview of the theoretical models predicting the x -shape (but not the normalization) of the intrinsic charm and bottom parton distribution functions. In Section 3, we discuss the constraints on the normalization of the intrinsic charm (IC) obtained in global analyses of PDFs. Section 4 is devoted to the intrinsic bottom (IB) content of the nucleon, for which there are currently no quantitative constraints. In Section 5 we review collider observables sensitive to an intrinsic charm or bottom PDF. Finally, in Section 6 we present our conclusions.

2. Theoretical Models

The QCD wavefunction of a hadron can be represented as a superposition of quark and gluon Fock states. For example, at fixed light-front time, a hadron wavefunction can be expanded as a sum over the complete basis of free quark and gluon states: $|\Psi_h\rangle = \sum_m |m\rangle \psi_{m/h}(x_i, k_{T,i})$ where the color-singlet states, $|m\rangle$, represent the fluctuations in the hadron wavefunction with the Fock components $|q_1 q_2 q_3\rangle$, $|q_1 q_2 q_3 g\rangle$, $|q_1 q_2 q_3 c\bar{c}\rangle$, and so forth. The boost-invariant light-front wavefunctions, $\psi_{m/h}(x_i, k_{T,i})$, are functions of the relative momentum coordinates $x_i = k_i^+/P^+$ and $k_{T,i}$ where k_i denotes the parton momenta and P the hadron momentum. Momentum conservation demands $\sum_{i=1}^n x_i = 1$ and $\sum_{i=1}^n \vec{k}_{T,i} = 0$ where n is the number of partons in state $|m\rangle$. For example, as predicted by Brodsky and collaborators, in the BHPS model intrinsic charm fluctuations [5, 23] can be liberated by a soft interaction which breaks the coherence of the Fock state [24] provided the system is probed during the characteristic time that such fluctuations exist.

Microscopically, the intrinsic heavy quark Fock component in the proton wavefunction, $|uudc\bar{c}\rangle$, is generated by virtual interactions such as $gg \rightarrow Q\bar{Q}$ where the gluons couple to two or more valence quarks. The probability for $c\bar{c}$ fluctuations to exist in a hadron is higher twist since it scales as $1/m_c^2$ relative to the extrinsic, EC, leading-twist production by photon-gluon fusion [18].

The dominant Fock state configurations are not far off shell and thus have minimal invariant mass, $M^2 = \sum_i \hat{m}_i^2/x_i$, where $\hat{m}_i^2 = m_i^2 + \langle \vec{k}_{T,i}^2 \rangle$ is the square of the average transverse mass of parton i . The general form of the Fock state wavefunction for a hadron with mass m_h appropriate to any frame at fixed light-front time is

$$\Psi(x_i, \vec{k}_{\perp i}) = \frac{\Gamma(x_i, \vec{k}_{\perp i})}{m_h^2 - M^2}, \quad (1)$$

where Γ is a vertex function, expected to be a slowly varying, decreasing function of $m_h^2 - M^2$. The particle distributions are then controlled by the light-front energy denominator and phase space. This form for the higher Fock components is applicable to an arbitrary number of light and heavy partons. Intrinsic $c\bar{c}$ Fock components with minimum invariant mass correspond to configurations with equal rapidity

constituents. Thus, unlike extrinsic heavy quarks generated from a single parton, intrinsic heavy quarks carry a larger fraction of the parent momentum than the light quarks in the state [5, 23].

The parton distributions reflect the underlying shape of the Fock state wavefunction. Assuming that it is sufficient to use $\langle k_T^2 \rangle$ for the transverse momentum, the probability distribution as a function of x in a general n -particle intrinsic $c\bar{c}$ Fock state is

$$\frac{dP_{IC}}{dx_i \cdots dx_n} = N_n \frac{\delta(1 - \sum_{i=1}^n x_i)}{(m_h^2 - \sum_{i=1}^n (\hat{m}_i^2/x_i))^2}, \quad (2)$$

where N_n normalizes the n -particle Fock state probability.

At LO in the heavy quark limit, $\hat{m}_c, \hat{m}_{\bar{c}} \gg m_h, \hat{m}_q$,

$$\frac{dP_{IC}}{dx_i \cdots dx_n} = N_n \frac{x_c^2 x_{\bar{c}}^2}{(x_c + x_{\bar{c}})^2} \delta\left(1 - \sum_{i=1}^n x_i\right), \quad (3)$$

leading to

$$\begin{aligned} F_{2c}^{\text{ICLO}}(x) &= \frac{8}{9} x c(x) \\ &= \frac{8}{9} x \int dx_1 \cdots dx_{\bar{c}} \frac{dP_{IC}}{dx_i \cdots dx_{\bar{c}} dx_c}. \end{aligned} \quad (4)$$

There are many applications of intrinsic charm in charm hadron production. See, for example, [13–16, 18] for more details.

Paiva et al. have also calculated an intrinsic charm component of the nucleon sea within the context of the meson cloud model [25]. They assumed that the nucleon can fluctuate into $\bar{D}\Lambda_c$. The \bar{c} distribution in the nucleon is then

$$x\bar{c}_N(x) = \int_x^1 dy f_{\bar{D}}(y) \frac{x}{y} \bar{c}_{\bar{D}}\left(\frac{x}{y}\right), \quad (5)$$

where

$$f_{\bar{D}}(y) = \frac{g_{\bar{D}N\Lambda_c}^2}{16\pi^2} y \int_{-\infty}^{t_{\max}} dt \frac{[-t + (m_{\Lambda_c} - m_N)^2]}{[t - m_{\bar{D}}^2]^2} F^2(t), \quad (6)$$

with $F(t)$ being a form factor at the $DN\Lambda$ vertex and $t_{\max} = m_N^2 y - m_{\Lambda_c}^2 y/(1 - y)$. In this case they chose a monopole form factor with $\Lambda_m = 1.2$ GeV. The coupling constant was assumed to be $g_{\bar{D}N\Lambda_c} = -3.795$. From heavy quark effective theories [26], the \bar{c} distribution in the \bar{D} is expected to be hard because, in the bound state, the \bar{c} exchanges momenta much less than m_c . They make the extreme assumption that the entire \bar{D} momentum is carried by the charm quark, $\bar{c}_{\bar{D}} = x\delta(x - y)$.

Next, Steffens et al. investigated all the charm structure function data with two variants of intrinsic charm [27]. The first was that of (4), called IC1 in their paper, while the second was a meson cloud model, IC2. In the second approach, the \bar{c}

distribution is obtained from the light-front distribution of \bar{D}^0 mesons in the nucleon:

$$\begin{aligned} \bar{c}^{\text{IC2}}(x) &\approx f_{\bar{D}}(x) = \frac{1}{16\pi^2} \int_0^\infty dk_\perp^2 \\ &\cdot \frac{g^2(x, k_\perp^2)}{x(1-x)(s_{\bar{D}\Lambda_c} - m_N^2)^2} \\ &\cdot \frac{k_\perp^2 + (m_{\Lambda_c} - (1-x)m_N)^2}{1-x}. \end{aligned} \quad (7)$$

A hard charm momentum distribution was assumed in the \bar{D} , similar to that of [25]. The vertex function $g^2(x, k_\perp^2)$ is parameterized as $g^2 = g_0^2(\Lambda^2 + m_N^2)/(\Lambda^2 + s_{\bar{D}\Lambda_c})$ where $s_{\bar{D}\Lambda_c}$ is the square of the center-of-mass energy of the $\bar{D}\Lambda_c$ system and g_0^2 the coupling constant at $s_{\bar{D}\Lambda_c} = m_N^2$. For an intrinsic charm probability of 1%, $\Lambda \approx 2.2$ GeV. The charm distribution is then

$$c^{\text{IC2}}(x) \approx \frac{3}{2} f_{\Lambda_c} \left(\frac{3x}{2} \right), \quad (8)$$

where the charm distribution in the Λ_c is assumed to be $c_{\Lambda_c} \sim \delta(x - 2/3)$ and $f_{\Lambda_c}(x) = f_{\bar{D}}(1 - x)$.

Pumplin [28] considered a model where a point scalar particle of mass m_0 couples with strength g to N scalar particles with mass m_1, m_2, \dots, m_N . The probability density is then

$$\begin{aligned} dP &= \frac{g^2}{(16\pi^2)^{N-1} (N-2)!} \prod_{j=1}^N dx_j \delta\left(1 - \sum_{j=1}^N x_j\right) \int_{s_0}^\infty ds \\ &\cdot \frac{(s - s_0)^{N-2}}{(s - m_0^2)^2} |F(s)|^2, \end{aligned} \quad (9)$$

where $s_0 = \sum_{j=1}^N (m_j^2/x_j)$. The form factor $F(s)$ suppresses higher mass state contributions. If the quark transverse momenta are neglected, with m_c much greater than all other mass scales, and $F(s) = 1$, then the BHPS model is recovered. Two types of form factors were studied, an exponential $|F(s)|^2 = \exp[-(s - m_0^2)/\Lambda^2]$ and a power law $|F(s)|^2 = 1/(s + \Lambda^2)^n$ where the cutoff Λ is varied between 2 and 10 GeV.

Hobbs et al. employed a meson cloud type approach but specified the spin and parity of all lowest mass charm meson-baryon combinations from the 5-particle $|uudc\bar{c}\rangle$ Fock states of the proton [29]. They pointed out that treating quarks as scalar point-like particles, as in, for example, [28], does not conserve spin and parity. They calculated the appropriate meson-baryon splitting functions for the meson-baryon combinations and found that the production of charm mesons would be almost entirely through D^* mesons. To study the phenomenological distributions of charm mesons and baryons in this approach, they studied exponential and confining vertex functions, $\propto \exp[-(s - m_D^2)/\Lambda^2]$ and $(s - m_D^2)\exp[-(s - m_D^2)/\Lambda^2]$, respectively. They used these results to compare to the Λ_c distribution from the ISR [30] and the $\Lambda_c/\bar{\Lambda}_c$ asymmetry from SELEX [31]. See [29] for details.

3. Global Analyses of PDFs with Intrinsic Charm

In the standard approach employed by almost all global analyses of PDFs, the heavy quark distributions are generated *radiatively*, according to DGLAP evolution equations [32–34], starting with a perturbatively calculable boundary condition [35, 36] at a scale of the order of the heavy quark mass. In other words, there are no free fit parameters associated with the heavy quark distribution and it is entirely related to the gluon distribution function at the scale of the boundary condition. As a consequence, also the PDF uncertainties for the heavy quark and the gluon PDFs are strongly correlated as has been discussed in the context of inclusive Higgs production at the Tevatron and the LHC [37]. However, a purely perturbative treatment might not be adequate in particular for the charm quark with a mass $m_c \approx 1.3$ GeV which is not much bigger than typical hadronic scales but also for the bottom quark with a mass $m_b \approx 4.5$ GeV. Indeed, as discussed above, light-front models predict a nonperturbative (“intrinsic”) heavy quark component in the proton wavefunction [5, 23]. Motivated by the theoretical predictions of the BHPS light-front model, analyses of the charm distribution in the proton going beyond the common assumption of purely radiatively generated charm date back almost as far as the BHPS predictions themselves. For definiteness, in the following we refer to the radiatively generated charm by $c_0(x, Q)$ and to the intrinsic charm by $c_1(x, Q)$. The full charm parton distribution is then given by the sum $c(x, Q) = c_0(x, Q) + c_1(x, Q)$. Strictly speaking, this decomposition is defined at the initial scale $Q_0 \approx m_c$ of the DGLAP evolution but holds to a good approximation at any scale since the intrinsic component c_1 is governed (to a very good approximation) by a standalone nonsinglet evolution equation [38]. A similar decomposition is understood for the bottom quark which will be discussed in Section 4.

The BHPS model of the $|uudc\bar{c}\rangle$ Fock state predicts a simple form for $F_{2c}(x)$:

$$F_{2c}^{\text{IC}}(x) = \left(\frac{8}{9}x\right) \frac{1}{2} N_5 x^2 \left[\frac{1}{3} (1-x) (1+10x+x^2) + 2x(1+x) \ln x \right]. \quad (10)$$

If there is a 1% intrinsic charm contribution to the proton PDF, $N_5 = 36$.

Hoffmann and Moore incorporated mass effects and introduced next-to-leading order corrections as well as scale evolution [39]. They compared their result to the EMC F_{2c} data from muon scattering on iron at high x and Q^2 with the intrinsic charm contribution added to the leading order calculation of F_{2c} by photon-gluon fusion.

A complete next-to-leading order analysis of both the “extrinsic” radiatively generated charm component and the intrinsic component was later carried out by Harris et al. [7]. The EMC data with $\bar{\nu} = Q^2/2m_p\bar{x} = 53, 95, \text{ and } 168$ GeV were fit by a sum of the extrinsic and intrinsic components

[7]. The normalization of the two components was left as free parameters:

$$F_{2c}(x, \mu^2, m_c^2) = \epsilon F_{2c}^{\text{yp}}(x, \mu^2, m_c^2) + \delta F_{2c}^{\text{IC}}(x, \mu^2, m_c^2), \quad (11)$$

with the scale $\mu = \sqrt{m_{c\bar{c}}^2 + Q^2}$. The parameter ϵ , typically larger than unity, was considered to be an estimate of the NNLO contribution to the extrinsic contribution. Since a 1% normalization of the IC component was assumed in (11), the fitted value of δ is the fraction of this normalization. Given the quality of the data, no statement could be made about the intrinsic charm content of the proton when $\bar{\nu} = 53$ and 95 GeV. However, with $\bar{\nu} = 168$ GeV an intrinsic charm contribution of $(0.86 \pm 0.60)\%$ was indicated. These results were consistent with those of the original analysis by Hoffmann and Moore [39].

The BHPS light-front model assumes that $c_1(x) = \bar{c}_1(x)$. Meson cloud models, introduced later, treat the 5-particle Fock state as a combination of (predominantly) $\bar{D}^0 \Lambda_c^+$. In this case, of course, $c_1(x) \neq \bar{c}_1(x)$ with the \bar{c} quark in the \bar{D}^0 carrying more momentum than the c quark in the charm baryon. An analysis by Steffens et al. in the context of the meson cloud model and using a hybrid scheme to interpolate between massless evolution at high Q^2 and “extrinsic” production at low Q^2 found a limit of $\sim 0.4\%$ [27].

Regardless of whether or not the models predict $\bar{c}_1(x) - c_1(x) > 0$, intrinsic charm should provide the dominant contribution to the charm density in the proton at large x [28].

For some time, no other analyses of the charm structure function were made. The EMC data remain the only measurement of the charm structure function in the relevant (x, Q^2) regime and are the only DIS data cited as evidence for intrinsic charm. The HERA data on F_{2c} were at too low x to address the issue.

The first global analyses of the proton PDFs with an intrinsic charm contribution included were performed by members of the CTEQ collaboration [40, 41]. In addition to the BHPS and meson cloud approaches, they also allowed for a “sea-like” contribution with the same shape as the radiatively generated charm distribution. They characterized the magnitude of the intrinsic charm component ($c_1(x, Q^2)$) by the first moment of the charm distribution at the input scale $Q_0 = m_c = 1.3$ GeV (Note that at $Q_0 = m_c$ the radiatively generated charm component ($c_0(x, Q^2)$) vanishes at NLO in the $\overline{\text{MS}}$ scheme so that $c(x, Q_0^2) = c_1(x, Q_0^2)$):

$$c_1(N=1, Q_0^2) = \int_0^1 dx c_1(x, Q_0^2) = 0.01, \quad (12)$$

which translates into a momentum fraction

$$\langle x \rangle_{c_1+\bar{c}_1} = \int_0^1 dx x [c_1(x, Q_0^2) + \bar{c}_1(x, Q_0^2)] = 0.0057. \quad (13)$$

They found that the global analyses of hard-scattering data provided no evidence for or against the existence of intrinsic charm up to $\langle x \rangle_{c_1+\bar{c}_1} = 0.0057$; that is, the quality of the fit is insensitive to $\langle x \rangle_{c_1+\bar{c}_1}$ in this interval. They also

found that the allowed range was greatest for the sea-like IC expected since this shape is rather easily interchangeable with other sea quark components while the other, harder, charm distributions are not [40]. In addition, they concluded that the enhancement due to IC relative to analyses without it persisted up to scales of ~ 100 GeV and could have an influence on charm-initiated processes at the LHC, as is discussed later. The CTEQ6.6C proton PDFs were generated as a result of this analysis [41].

There are two recent updates to the global analyses, reaching different conclusions about the importance of intrinsic charm. The first, by Dulat et al. [42], follows the previous work in the context of the CTEQ collaboration [40, 41]. The second, by Jimenez-Delgado et al. [43], included more lower energy data than the previous global analyses.

The result of Dulat et al. [42] was based on the CT10 NNLO parton densities. Here the strong coupling, $\alpha_s(Q^2)$, the evolution equations, and the matrix elements are calculated at NNLO. Only the inclusive jet data still required NLO expressions. Their analysis included DIS data from BCDMS, NMC, CDHSW, and CCFR; SIDIS data from NuTeV and CCFR; the combined DIS and F_{2c} data from HERA; Drell-Yan production; the W charge asymmetry and Z^0 rapidity from CDF and D0; and the inclusive jet measurements from CDF and D0; see [42] for a complete list.

Two models of IC were considered: the BHPS light-front model and the sea-like IC introduced in [40]. They found a broader possible probability range for IC in this analysis, $\langle x \rangle_{IC} = \langle x \rangle_{c_1 + \bar{c}_1} (Q_0^2) \leq 0.025$ for BHPS and $\langle x \rangle_{IC} \leq 0.015$ for the sea-like IC, summarized in Figure 2. This finding differs from the previous work which found a larger upper limit on IC for the sea-like model. They believe that the difference is caused by the improved treatment of the charm quark mass in the later study [42].

In addition to the global fit, they also tested the sensitivity of their result to individual experiments by introducing a penalty factor, $T_2(i)$, for each experiment i . This penalty factor is designed to increase more rapidly than the χ_i^2 for that experiment when χ_i^2 goes beyond the 90% confidence level. The penalty factor employs an equivalent Gaussian variable S_n which measures the goodness of fit for each individual data set. Values of $S_n \leq |1|$ are considered good fits, $S_n > 3$ is considered to be a poor fit, and values of $S_n < -3$ are better fits than expected from usual statistical analyses. Using the S_n dependence on $\langle x \rangle_{IC}$, they determined which of the data sets used in the global analyses are most sensitive to intrinsic charm. The upper limit on the BHPS value of $\langle x \rangle_{IC}$ comes from the CCFR structure function data while the HERA combined charm data sets the upper limit on IC from the sea-like model [42].

They also studied the sensitivity of their sea-like result to the charm quark mass and found that if the charm quark mass was raised from 1.3 GeV, as in the CT10 fits, to 1.67 GeV, then the minimum χ^2 for the global analyses would support $\langle x \rangle_{IC} = 0.01$ rather than 0 although the global χ^2 is worse for the larger charm mass [42]. Finally, they showed how W and Z production at the LHC might be affected by a nonzero IC contribution.

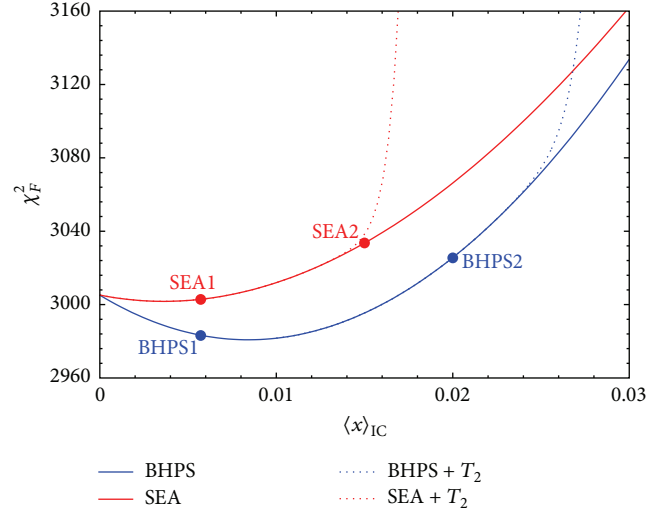


FIGURE 2: The global chi-square function versus charm momentum fraction $\langle x \rangle_{IC}$. The two curves are determined from fits with many values of $\langle x \rangle_{IC}$. Two exemplary fits for each IC model are shown as dots. Blue dots denote the BHPS model; the dots have $\langle x \rangle_{IC} = 0.57\%$ and 2% , which are denoted as BHPS1 and BHPS2. Red denotes SEA model; the dots have $\langle x \rangle_{IC} = 0.57\%$ and 1.5% , which are denoted as SEA1 and SEA2. Additionally the dotted lines show global chi-square function with additional penalty, $T_2(i)$, used to set the upper limits on the allowed IC component (figure taken from [42]).

In the most recent study, Jimenez-Delgado et al. [43] included the full range of high energy scattering data by using looser kinematic cuts $Q^2 \geq 1 \text{ GeV}^2$ and $W^2 \geq 3.5 \text{ GeV}^2$. In particular, they included the lower energy SLAC fixed target data which did not pass the more stringent standard DIS cuts on the (Q^2, W^2) plane applied in the previous work [40–42]. The EMC F_{2c} data, cited as the strongest evidence for intrinsic charm in DIS, are used as a consistency check. The low energy, high x , fixed target data lie precisely in the region where IC is expected to be most important. Thus including these data could enhance the sensitivity of the global fit to IC. Note, however, that some of these newly added data are on heavier targets than the deuteron and thus target mass corrections, nuclear corrections for $A > 2$, and higher-twist effects need to be taken into account [43].

They followed the framework of the JR14 [44] global fit which decomposed F_2 into light and heavy components. The charm component is itself separated into the “extrinsic” and intrinsic charm components. The fixed-flavor number scheme is used to compute the extrinsic contribution. In this scheme, the charm quark mass enters the PDF evolution only indirectly through the running of α_s [43]. They employed a charm quark mass of 1.3 GeV, as did Dulat et al. [42]. They used all three intrinsic charm models previously considered: BHPS, the meson cloud model (this time including pseudoscalar and vector mesons as well as spin 1/2 and spin 3/2 charm baryons—the CTEQ analyses only included the scalar $\bar{D}\Lambda_c$ fluctuation), and the sea-like component [43]. The IC contribution was evolved up to NLO.

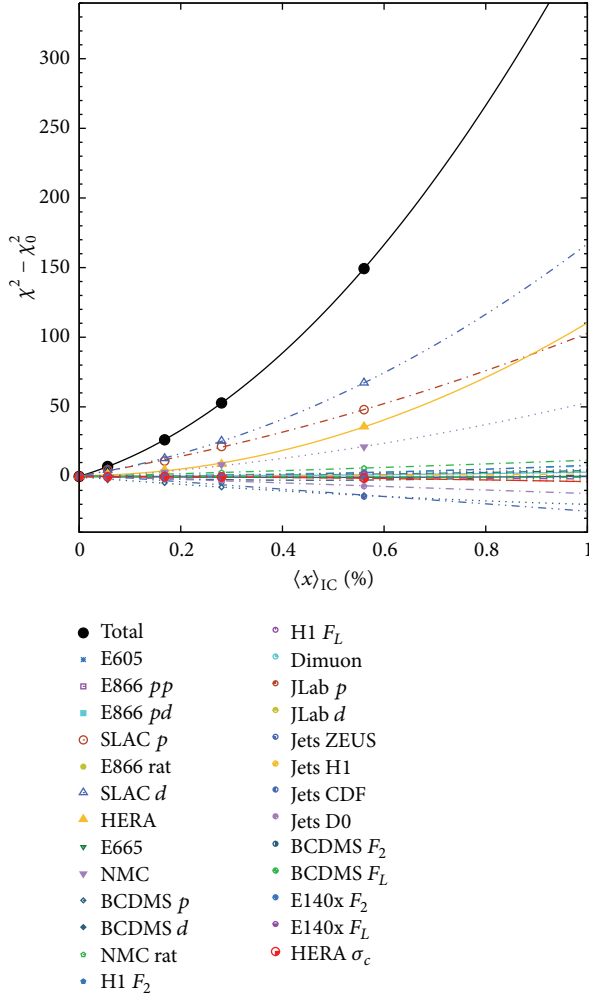


FIGURE 3: Contributions to the total χ^2 (black circles), relative to the value χ_0^2 for no IC, of various data sets as a function of the momentum fraction $\langle x \rangle_{IC}$ (figure taken from [43]).

They found that the total χ^2 is minimized for $\langle x \rangle_{IC} = 0$ with $\langle x \rangle_{IC} < 0.1\%$ at the 5σ level. When a hadron suppression factor to suppress charm contributions near threshold is applied, they find a minimum χ^2 at $\langle x \rangle_{IC} = (0.15 \pm 0.09)\%$ for the full data set. The SLAC F_2 (large x), NMC cross sections (medium x), and HERA F_{2c} (low x) display the greatest sensitivity to IC; see Figure 3 for details. However, fits without the SLAC data still give a low IC contribution [43]. The difference between their results and previous results is in part due to the very different tolerance criteria, $\Delta\chi^2 = 1$ for their fit and $\Delta\chi^2 = 100$ for Dulat et al. [42]. Increasing the tolerance to $\Delta\chi^2 = 100$ would also accommodate $\langle x \rangle_{IC} = 1\%$ at the 1σ level [43]. (For a critical discussion of the analysis in [44] and in particular of the tolerance criterion $\Delta\chi^2 = 1$ see [45, 46].)

When checked against the EMC F_{2c} data, a clear preference for IC is found, as expected, for the highest x data. (The EMC μ - p data have not been included in some global analyses because of a possible conflict with HERA e - p data at very low x ; however, the relative suppression of the low

x and low Q^2 EMC data could be accounted for by nuclear shadowing, suppressed evolution, higher twist, and other effects.)

Given that the two most recent analyses set significantly different limits on IC, it is important to collect further large x data, particularly on F_{2c} to try and place greater confidence on the limit of IC in the nucleon. This would be an important measurement at the future electron-ion collider.

4. Predictions for Intrinsic Bottom

In contrast to the case of intrinsic charm, there is currently no global analysis available that investigates the possibility of an intrinsic bottom (IB) content of the nucleon. The main reason for this is the lack of experimental data that could constrain it. The BHPS light-front model [5] predicts the existence of IB with an x -shape very similar to the one of IC given in (10) but with a normalization which is parametrically suppressed by the ratio m_c^2/m_b^2 . This fact, together with the observation that the IB PDF is governed (to an excellent approximation) by an independent nonsinglet evolution equation [38], can be used to investigate IB in a flexible way without the need of a dedicated global analysis. Such a study has been done in [38] where a set of decoupled IB (and IC) PDFs has been provided and used together with the CTEQ6.6 PDFs [41] to estimate the impact of the IB on new physics searches at the LHC. The advantage of this approach is that the provided IB (IC) PDF can be used with any standard set of PDFs and the normalization of the intrinsic component can be freely adjusted. This is especially useful for studies of possible IB effects, as, in that case, there are no experimental limits on what amount of IB is allowed.

In the following we show some of the results found in [38]. In this work, the boundary condition for the IB distribution was modeled using the IC distributions in the CTEQ analyses [40, 41] scaled down by the mass factor m_c^2/m_b^2 . The result of such an intrinsic bottom distribution $b_1(x, Q^2)$, with normalization $\int_0^1 dx b_1(x, m_c^2) = 0.01 \times m_c^2/m_b^2$, is shown in Figure 4, where the ratio of the intrinsic (b_1) and the radiatively generated (b_0) component of the bottom PDF is plotted. As always in the light-front models the intrinsic component is mostly present at large x values. We can see that for low scales $Q \sim 10$ GeV the modification of the bottom PDF, $\kappa_b = 1 + b_1/b_0$, can reach $\kappa_b = 2.5$. However, it decreases rapidly with the rising scale. Since b_1 evolves independently of the other PDFs the change in the normalization of the IB component in Figure 4 can be done by simply rescaling the curves in the figure. If we allowed for a $0.035 \times m_c^2/m_b^2$ normalization of the IB the modification of the bottom PDF would be given by $\kappa_b = 1 + b_1/b_0 \times 3.5$, which for high x and $Q \sim 10$ GeV would result in an enhancement of the bottom PDF by a factor ~ 6.25 . However, at a scale of around 100 GeV and x below 0.2–0.3, even with the higher IB normalization, the effect is becoming negligible.

In Figure 5 we show the sum of the intrinsic bottom PDF b_1 and the dynamically generated PDF b_0 from CTEQ6.6 for different normalizations of the IB component, namely, 0.01 and $0.035 \times m_c^2/m_b^2$. We compare this sum to the asymmetric

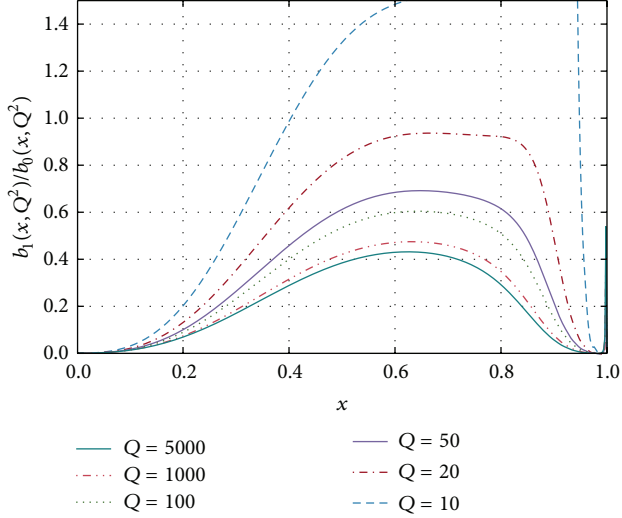


FIGURE 4: Ratio of intrinsic (b_1) and dynamically generated (b_0) bottom PDFs for various Q scales. The perturbative bottom PDF from CTEQ6.6c0 [41] is used; the normalization of the IB is taken to be such that $\int_0^1 dx b_1(x, m_c^2) = 0.01 \times m_c^2/m_b^2$ (figure taken from [38]).

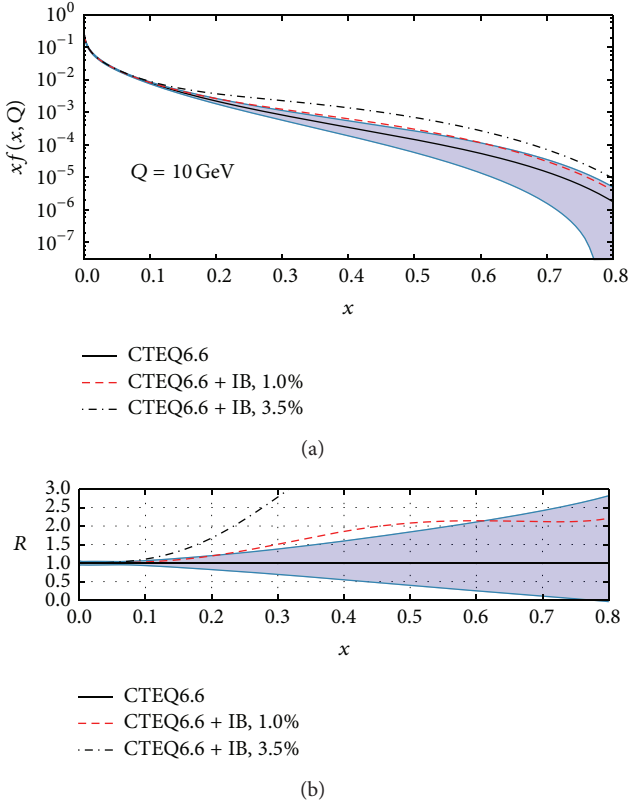


FIGURE 5: CTEQ6.6 + b_1 for different normalizations of the intrinsic bottom quark PDF at the scale $Q = 10$ GeV, compared to the asymmetric PDF errors from the same set (a). Also shown is the ratio of the same PDF sets to the central value of CTEQ6.6 (b).

uncertainties (The asymmetric errors are computed following [47, 48].) of the CTEQ6.6 PDF set (a). In the same figure is also shown the ratio of the same PDFs to the central value of CTEQ6.6 (b). As can be seen, the IB curve with the $0.035 \times m_c^2/m_b^2$ normalization clearly lies outside the uncertainty band whereas the one with the smaller normalization is marginally outside the band (up to $x \leq 0.6$).

If we are looking for new physics with couplings proportional to the mass, the suppression of IB compared to the IC would be partly compensated by the square of the coupling. For a more detailed study of the relevant parton-parton luminosities please see [38].

5. Collider Observables

Several collider observables receive large contributions from heavy quark initiated subprocesses and are hence potentially sensitive to an intrinsic charm content in the nucleon. In order to expect optimal effects the heavy quark PDF should be probed at large $x \gtrsim 0.2$ (for light-front models) and not too large factorization scales. This kinematic region is best accessible at lower energies in the center-of-mass system (cms) and/or large rapidities. Therefore, a fixed target experiment like AFTER@LHC [1–4] operating at cms energy $\sqrt{s} = 115$ GeV with a high luminosity is ideally suited for searches of IC effects. In the following we review some of the collider processes which have been studied in the literature in this respect.

5.1. Open Heavy Flavor Production. Inclusive charm hadron ($D^0, D^+, D^{*+}, \Lambda_c, \dots$) production in hadronic collisions was advocated in [49] as a laboratory to probe IC inside the colliding hadrons. In this analysis, predictions for the differential cross section in dependence on the transverse momentum p_T were obtained in the general-mass variable-flavor-number scheme (GM-VFNS) [50–52] at next-to-leading order (NLO). In this scheme, the charm quark is an active parton and the differential cross sections of inclusive charm meson production depend heavily on the PDF of the charm quark. The sensitivity of these cross sections to IC was studied for the Tevatron at cms energy of 1960 GeV and the Relativistic Heavy Ion Collider (RHIC) at cms energies of 200 GeV (RHIC200) and 500 GeV (RHIC500). The different IC models from the CTEQ6.5c global analysis [40] were employed together with the fragmentation functions for charm mesons from [53]. While the effects at the Tevatron were found to be very moderate and likely not testable, large enhancements were found at RHIC200 reaching values of ~ 3 at $p_T = 20$ GeV. Unfortunately, the measurements at RHIC200 are limited by the luminosity. At RHIC500 the cross section is increased by about a factor 3.6. However, the sensitivity to IC for the light-front models is greatly reduced.

More recently, the GM-VFNS was applied to obtain predictions for the production of inclusive D mesons at the LHC for cms energy of 7 TeV (LHC7) [54]. It was found that the production cross sections at large rapidities $y \gtrsim 4$ are sensitive to an IC component. These predictions can be tested by measurements at forward rapidities with the LHCb detector.

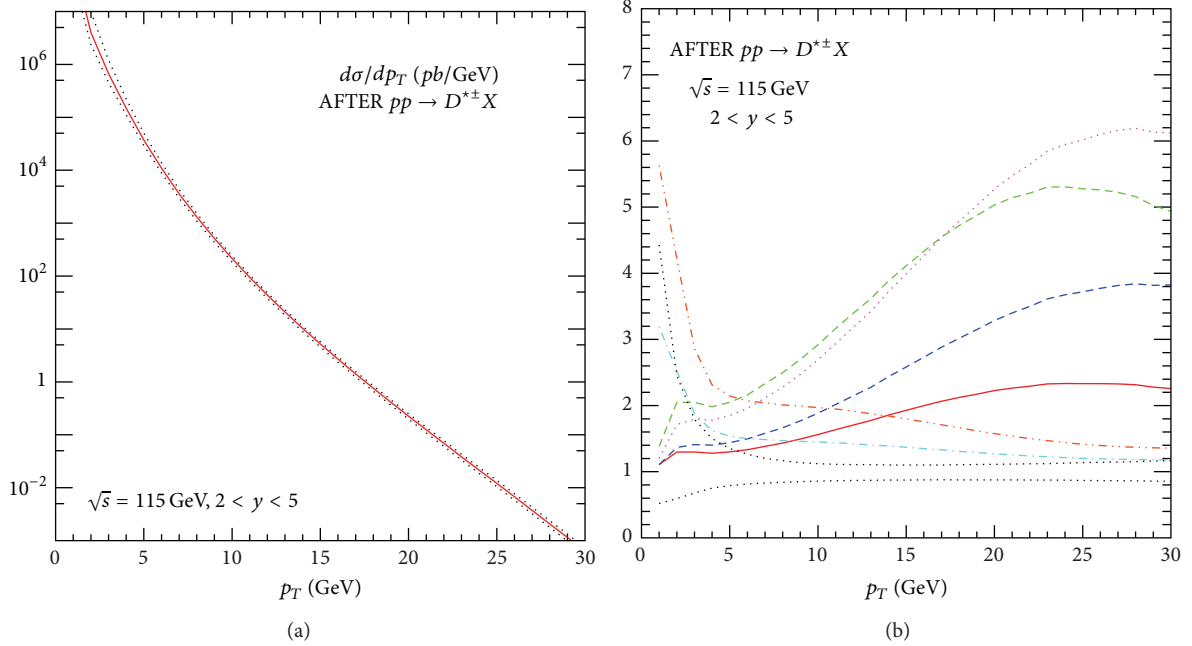


FIGURE 6: NLO predictions for inclusive D^* meson production at AFTER@LHC versus the transverse momentum of the D meson. (a) Differential cross section on an absolute scale without intrinsic charm. (b) Ratio with respect to the central prediction of (a). Shown are results using the IC parametrizations from [40] for $n = 1$ (red, solid line), 2 (violet, dotted line), 3 (blue, dashed line), 4 (green, long dashed line), 5 (cyan, dot-dashed line), and 6 (orange, double-dot-dashed line). In both figures, the black dotted lines have been obtained by varying the renormalization scale around the central choice ($\mu_R = m_T$) to $\mu_R = m_T/2$ (upper line) and $\mu_R = 2m_T$ (lower line).

The ideal experiment to search for the effects of IC would be a high luminosity fixed target experiment such as AFTER@LHC operating at cms energy of 115 GeV. In Figure 6 we show results for inclusive D^* meson production as a function of the transverse momentum of the D^* meson integrated over the rapidity range $2 < y < 5$ (in the laboratory frame) in essentially the same setup as in [49] to which we refer for details. The only difference is that, following [55], the default choice for the renormalization and factorization scales is $\mu_R = m_T$, $\mu_F = \mu'_F = m_T/2$, where $m_T = \sqrt{p_T^2 + m^2}$ is the transverse mass. The theoretical predictions are shown on an absolute scale in Figure 6(a) and as a ratio with respect to the default results in Figure 6(b). In both figures, the black dotted lines have been obtained by varying the renormalization scale around the central choice to $\mu_R = m_T/2$ (upper line) and $\mu_R = 2m_T$ (lower line). In Figure 6(b) we repeat the calculation of the central prediction in turn with PDF sets CTEQ6.5Cn for $n = 1, \dots, 6$ and normalize the outcome to the default prediction with zero IC of Figure 6(a). We observe that the ratios for $n = 1, 2, 3, 4$ corresponding to the BHPS ($n = 1, 2$) or meson cloud ($n = 3, 4$) models become very large at large p_T . Indeed, the default cross section can be increased by more than a factor 5 at $p_T = 20$ GeV in scenarios with maximally allowed intrinsic charm ($n = 2, 4$). Even for the IC sets with smaller normalization ($n = 1, 3$) corresponding to $\langle x \rangle_{c+\bar{c}_1} = 0.57\%$ and $\langle x \rangle_{c_1+\bar{c}_1} = 0.96\%$ the cross section would be enhanced by a factor larger than 2 (red solid line) or 3 (blue dashed line) at $p_T = 20$ GeV. It is also interesting to note that the phenomenological models for a sea-like IC ($n = 5, 6$) lead to a significant enhancement of the cross section at

small $p_T \sim m_c$ which would be probed at AFTER@LHC as well.

5.2. Production of a Photon in Association with a Charm Quark. Another process with a wide range of phenomenological applications in pp , pA , and AA collisions [56–58] which is very sensitive to the heavy quark PDF is the associated production of a photon with a heavy quark. A dedicated study of this process at the LHC operating at $\sqrt{s} = 8$ TeV (LHC8) was performed in [59, 60] where it was demonstrated that the existence of IC in the proton can be visible at large transverse momenta of the photons and heavy quark jets at rapidities $1.5 < |y_\gamma| < 2.4$, $|y_c| < 2.4$. Indeed, for the BHPS model the cross section can be enhanced by a factor of 2-3 for $p_T^\gamma > 200$ GeV (see Figure 5 in [60]). This comes with the penalty that the cross section falls rapidly with increasing transverse momentum so that this measurement will be limited by statistics.

Again, as for open heavy flavor production, the lower cms energy together with the high luminosity makes a fixed target experiment like AFTER@LHC the ideal place to discover IC using $\gamma + c$ production. This can be seen in Figure 7, where the differential cross section is enhanced by a factor 5 at $p_T^\gamma = 20$ GeV (b) with a not too small cross section (a).

5.3. Vector Boson Production. Dulat et al. [42] studied the sensitivity of W^\pm and Z^0 production to the presence of IC. Vector boson production at the LHC is an interesting testing ground for IC because they are produced at relatively large x and $Z^0 \rightarrow l^+ l^-$ is a rather clean final state. They did a NNLO

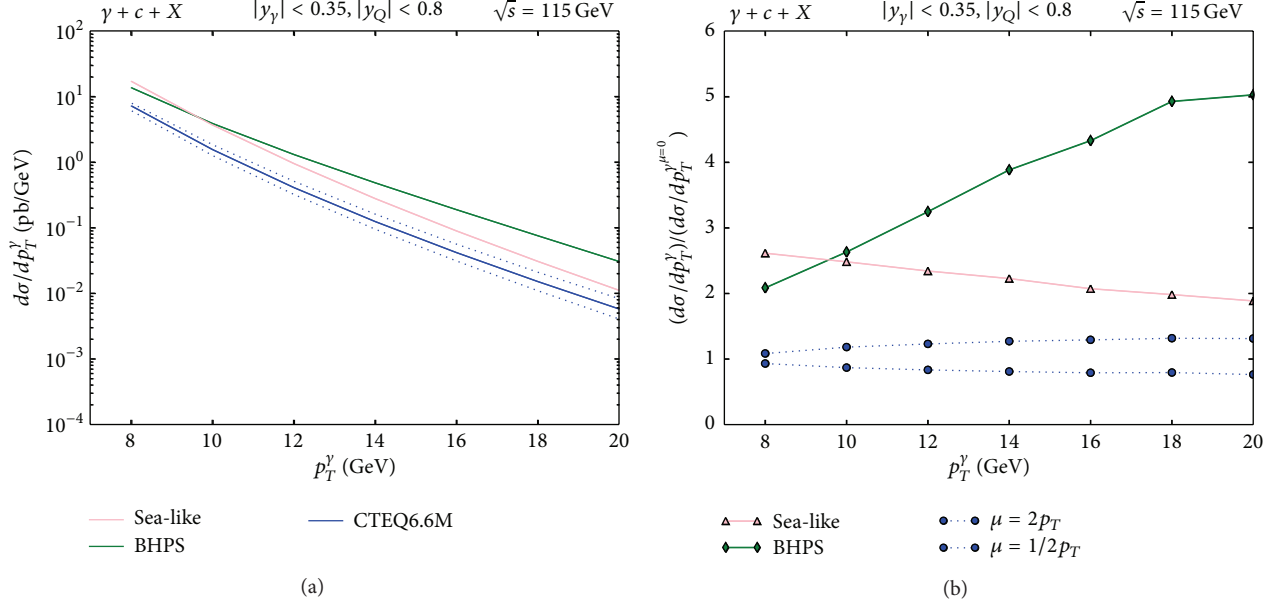


FIGURE 7: (a) NLO predictions for the production of a prompt photon in association with a charm quark jet in pp collisions at AFTER@LHC versus the transverse momentum of the photon. Shown are results for a BHPS and a sea-like intrinsic charm using the CTEQ6.6c PDFs. For comparison, the predictions without an IC using the CTEQ6.6M PDFs are shown as well together with the uncertainty band obtained by varying the central factorization scale $\mu_F = p_T^\gamma$ by a factor 2 up and down (blue, dotted curves). (b) Depicting the ratio of the curves in (a) with respect to the central prediction without intrinsic charm.

calculation of W and Z production including IC based on their global fits at $\sqrt{s} = 8$ and 14 TeV. They also studied the ratio $d\sigma_{W^+ + W^-}(y)/d\sigma_{Z^0}(y)$ relative to the result with no IC. Neither of these calculations showed an effect larger than the uncertainties due to the CT10 sets themselves. However, when the Z^0 p_T distribution with IC was compared to that without, they saw a factor of two enhancement at $p_T \sim 500$ GeV for $\sqrt{s} = 8$ TeV in the range $|\eta| < 2.1$. The corresponding enhancement at 14 TeV was smaller at the same p_T because the x value reached is reduced at the higher energy [42].

We show a simple test case here for W and Z production to NLO at $\sqrt{s} = 7$ TeV. We use only the BHPS IC parameterization for the five-particle Fock state, shown in (10). We assume a 1% normalization and no Q^2 evolution to maximize the possible effect at forward rapidity. The p_T -integrated rapidity distribution is shown in Figure 8, as is the ratio of the result with IC to that without as a function of rapidity. The rapidity distributions without IC are given by the solid curves while the dashed curves are the calculations with the BHPS IC contribution to the charm parton density. With BHPS IC, one expects enhancement only at forward rapidity. The enhancement from IC appears for $|y| > 2.5$. Note that if the sea-like IC would be used instead, the enhancement would be small but finite over all rapidity.

The W^+ cross section is largest and most forward peaked, because of the $u\bar{d}$ contribution. The contribution from the $c\bar{d}$ part is a very small addition since the u valence contribution is large and peaks at large x , making the y distribution larger at $|y| \sim 2$ than at $y = 0$. Indeed, it gives the smallest IC contribution. The W^- distribution should have the largest possible contribution from IC because both $d\bar{u}$ and $d\bar{c}$ peak at low x and because the d valence distribution peaks at lower x

so that the W^- rapidity distribution has a maximum at $y = 0$. At $|y| \sim 4$, the IC enhancement is $\sim 40\%$. Finally, the Z^0 distribution, with a plateau over $|y| < 1.5$, also has a very small IC contribution because the charm enhancement only comes through $c\bar{c}$.

Such IC enhancements are only visible outside the midrapidity acceptance of the collider detector coverage of CMS and ATLAS. However, LHCb or ALICE covers this forward rapidity range with muons and could detect forward Z^0 . They could also look at the lepton rapidity asymmetry $(W^+ - W^-)/(W^+ + W^-)$ at forward rapidity. The statistical accuracy of the measurement would need to be high to distinguish an IC enhancement from the no IC result, especially since the 1% BHPS IC is likely an upper limit on this enhancement. Note that the higher energy of LHC Run 2 will reduce the potential enhancement even though it would increase the rates.

6. Conclusions

The existence of nonperturbative intrinsic charm and bottom components is a fundamental prediction of QCD. In this paper, we have reviewed the current status of our understanding of this intrinsic heavy quark content of the nucleon which yet remains to be confirmed experimentally. In particular, after introducing theoretical models predicting the intrinsic heavy quark distributions we have turned to a summary of the available information on intrinsic charm coming from global analyses of parton distribution functions. There are no global analyses of intrinsic bottom available and we have described how IB can be modeled in order to explore its impact on collider observables keeping in mind that bottom quark initiated subprocesses play an important

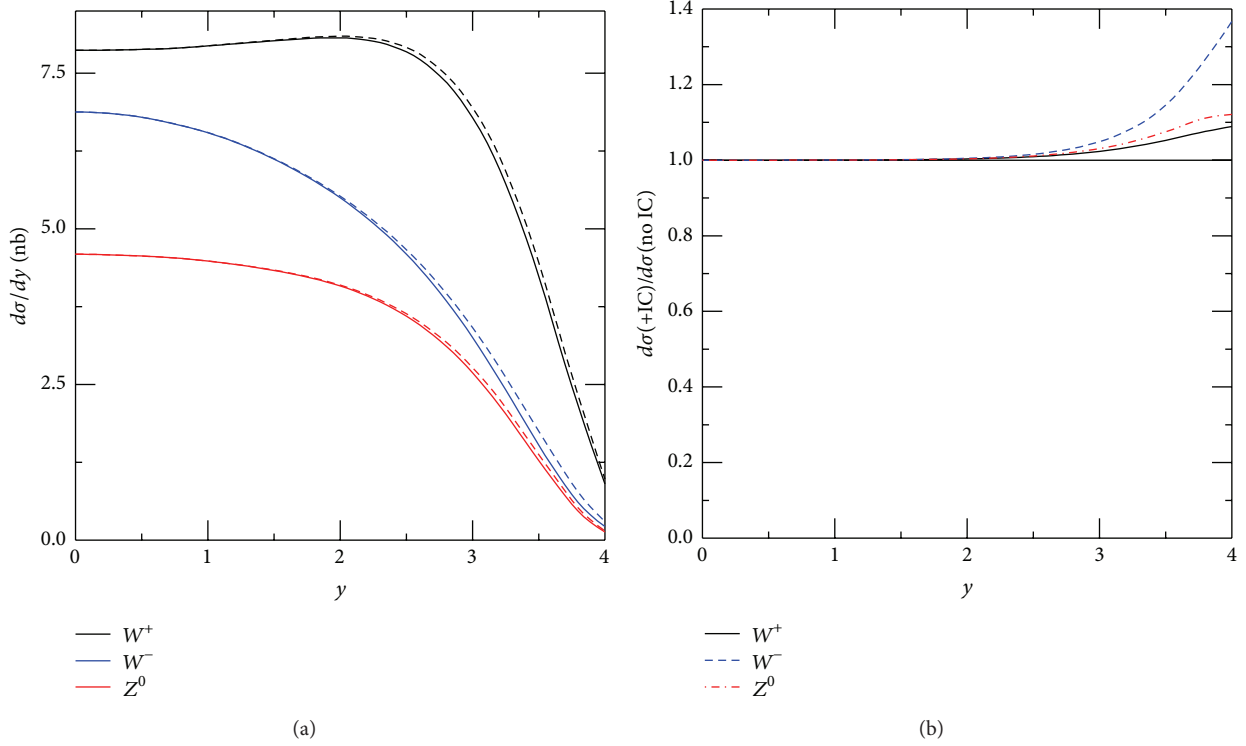


FIGURE 8: The W^+ (black), W^- (blue), and Z^0 (red) rapidity distributions (a). The solid curves are the results without IC while the dashed curves include 1% BHPS IC. The ratios of the dashed curves to the solid curves showing the enhancement of the rapidity distributions due to IC for W^+ (solid black), W^- (blue dashed), and Z^0 (red dot dashed) are shown in (b).

role in certain electroweak observables and in models for physics beyond the Standard Model. We then have turned to a discussion of collider processes where IC could be discovered. Generally, the effects of IC are larger at colliders with a lower center-of-mass energy and for hard processes with moderate factorization scales. Therefore, a high luminosity fixed target experiment like AFTER@LHC operating at a center-of-mass energy $\sqrt{s} = 115$ GeV would be ideally suited to discover or constrain IC.

Conflict of Interests

The authors declare that there is no conflict of interests regarding the publication of this paper.

Acknowledgments

The authors are grateful to T. Stavreva for providing Figure 7. The work of S. J. Brodsky was supported by the Department of Energy Contract no. DE-AC02-76SF00515. The work of R. Vogt was performed under the auspices of the US Department of Energy by Lawrence Livermore National Laboratory under Contract DE-AC52-07NA27344.

References

- [1] S. J. Brodsky, F. Fleuret, C. Hadjidakis, and J. P. Lansberg, "Physics opportunities of a fixed-target experiment using LHC beams," *Physics Reports*, vol. 522, no. 4, pp. 239–255, 2013.
- [2] J. P. Lansberg, S. J. Brodsky, F. Fleuret, and C. Hadjidakis, "Quarkonium physics at a fixed-target experiment using the LHC Beams," *Few-Body Systems*, vol. 53, no. 1-2, pp. 11–25, 2012.
- [3] J. Lansberg, R. Arnaldi, S. Brodsky et al., "AFTER@LHC: a precision machine to study the interface between particle and nuclear physics," *EPJ Web of Conferences*, vol. 66, Article ID 11023, 4 pages, 2014.
- [4] A. Rakotozafindrabe, M. Anselmino, R. Arnaldi et al., "Studying the high x frontier with a fixed-target experiment at the LHC," in *Proceedings of the 21st International Workshop on Deep-Inelastic Scattering and Related Subject (DIS '13)*, p. 250, Marseille, France, April 2013.
- [5] S. J. Brodsky, P. Hoyer, C. Peterson, and N. Sakai, "The intrinsic charm of the proton," *Physics Letters B*, vol. 93, no. 4, pp. 451–455, 1980.
- [6] S. J. Brodsky, J. C. Collins, S. D. Ellis, J. F. Gunion, and A. H. Mueller, "Intrinsic chevrons at the SSC," in *Proceedings of the 1984 Summer Study on the SSC*, Snowmass, Colo, USA, June–July 1984, Edited by R. Donaldson and J. G. Morfin (AIP, New York, NY, USA, 1985).
- [7] B. Harris, J. Smith, and R. Vogt, "Reanalysis of the EMC charm production data with extrinsic and intrinsic charm at NLO," *Nuclear Physics B*, vol. 461, pp. 181–196, 1996.
- [8] M. Franz, M. V. Polyakov, and K. Goeke, "Heavy quark mass expansion and intrinsic charm in light hadrons," *Physical Review D*, vol. 62, Article ID 074024, 2000.
- [9] W. Freeman and D. Toussaint, "Intrinsic strangeness and charm of the nucleon using improved staggered fermions," *Physical Review D*, vol. 88, no. 5, Article ID 054503, 18 pages, 2013.

- [10] A. Kryjevski, “Heavy quark $\bar{q}q$ matrix elements in the nucleon from perturbative QCD,” *Physical Review D*, vol. 70, Article ID 094028, 2004.
- [11] J. J. Aubert, G. Bassompierre, K. H. Becks et al., “Production of charmed particles in 250 GeV μ^+ -iron interactions,” *Nuclear Physics B*, vol. 213, no. 1, pp. 31–64, 1983.
- [12] G. Bari, M. Basile, G. Bruni et al., “The Λ_b^0 beauty baryon production in proton-proton interactions at $\sqrt{s} = 62$ GeV: a second observation,” *Il Nuovo Cimento A*, vol. 104, no. 12, pp. 1787–1800, 1991.
- [13] R. Vogt, S. J. Brodsky, and P. Hoyer, “Systematics of charm production in hadronic collisions,” *Nuclear Physics B*, vol. 383, no. 3, pp. 643–684, 1992.
- [14] R. Vogt and S. J. Brodsky, “Charmed hadron asymmetries in the intrinsic charm coalescence model,” *Nuclear Physics B*, vol. 478, no. 1-2, pp. 311–332, 1996.
- [15] T. Gutierrez and R. Vogt, “Leading charm in hadron-nucleus interactions in the intrinsic charm model,” *Nuclear Physics B*, vol. 539, pp. 189–214, 1999.
- [16] R. Vogt, S. J. Brodsky, and P. Hoyer, “Systematics of J/ψ production in nuclear collisions,” *Nuclear Physics B*, vol. 360, no. 1, pp. 67–96, 1991.
- [17] P. Hoyer, M. Vanttinen, and U. Sukhatme, “Violation of factorization in charm hadroproduction,” *Physics Letters B*, vol. 246, pp. 217–220, 1990.
- [18] R. Vogt and S. J. Brodsky, “Intrinsic charm contribution to double quarkonium hadroproduction,” *Physics Letters B*, vol. 349, no. 4, pp. 569–575, 1995.
- [19] S. J. Brodsky, B. Kopeliovich, I. Schmidt, and J. Soffer, “Diffractive Higgs production from intrinsic heavy flavors in the proton,” *Physical Review D*, vol. 73, no. 11, Article ID 113005, 13 pages, 2006.
- [20] S. J. Brodsky, A. S. Goldhaber, B. Z. Kopeliovich, and I. Schmidt, “Higgs hadroproduction at large Feynman x ,” *Nuclear Physics B*, vol. 807, no. 1-2, pp. 334–347, 2009.
- [21] S. J. Brodsky and S. Gardner, “Evading the CKM hierarchy: intrinsic charm in B decays,” *Physical Review D*, vol. 65, Article ID 054016, 2002.
- [22] S. Brodsky, G. de Teramond, and M. Karliner, “Puzzles in hadronic physics and novel quantum chromodynamics phenomenology,” *Annual Review of Nuclear and Particle Science*, vol. 62, pp. 1–35, 2012.
- [23] S. J. Brodsky, C. Peterson, and N. Sakai, “Intrinsic heavy-quark states,” *Physical Review D*, vol. 23, no. 11, p. 2745, 1981.
- [24] S. J. Brodsky, P. Hoyer, A. H. Mueller, and W.-K. Tang, “New QCD production mechanisms for hard processes at large x ,” *Nuclear Physics B*, vol. 369, no. 3, pp. 519–542, 1992.
- [25] S. Paiva, M. Nielsen, F. S. Navarra, F. O. Duraes, and L. L. Barz, “Virtual meson cloud of the nucleon and intrinsic strangeness and charm,” *Modern Physics Letters A*, vol. 13, no. 34, pp. 2715–2724, 1998.
- [26] M. Neubert, “Heavy-quark symmetry,” *Physics Reports*, vol. 245, no. 5-6, pp. 259–395, 1994.
- [27] F. M. Steffens, W. Melnitchouk, and A. W. Thomas, “Charm in the nucleon,” *The European Physical Journal C—Particles and Fields*, vol. 11, no. 4, pp. 673–683, 1999.
- [28] J. Pumplin, “Light-cone models for intrinsic charm and bottom,” *Physical Review D*, vol. 73, Article ID 114015, 2006.
- [29] T. Hobbs, J. Londergan, and W. Melnitchouk, “Phenomenology of nonperturbative charm in the nucleon,” *Physical Review D*, vol. 89, Article ID 074008, 2014.
- [30] P. Chauvat, R. Cousins, K. Hayes et al., “Production of Λ_c with large X_F at the isr,” *Physics Letters B*, vol. 199, no. 2, pp. 304–310, 1987.
- [31] F. Garcia, G. Alkhazov, A. G. Atamantchouk et al., “Hadronic production of Λ_c from 600 GeV/ π^- , Σ^- and p beams,” *Physics Letters B*, vol. 528, no. 1-2, pp. 49–57, 2002.
- [32] G. Altarelli and G. Parisi, “Asymptotic freedom in parton language,” *Nuclear Physics B*, vol. 126, pp. 298–318, 1977.
- [33] V. N. Gribov and L. N. Lipatov, “Deep inelastic ep scattering in perturbation theory,” *Soviet Journal of Nuclear Physics*, vol. 15, p. 438, 1972.
- [34] Y. L. Dokshitzer, “Calculation of the structure functions for deep inelastic scattering and e^+e^- annihilation by perturbation theory in quantum chromodynamics,” *Soviet Physics—JETP*, vol. 46, pp. 641–653, 1977.
- [35] J. C. Collins and W.-K. Tung, “Calculating heavy quark distributions,” *Nuclear Physics B*, vol. 278, no. 4, pp. 934–950, 1986.
- [36] M. Buza, Y. Matiounine, J. Smith, and W. L. van Neerven, “Charm electroproduction viewed in the variable-flavour number scheme versus fixed-order perturbation theory,” *The European Physical Journal C*, vol. 1, no. 1-2, pp. 301–320, 1998.
- [37] A. Belyaev, J. Pumplin, W.-K. Tung, and C. P. Yuan, “Uncertainties of the inclusive Higgs production cross section at the tevatron and the LHC,” *Journal of High Energy Physics*, vol. 2006, no. 1, article 069, 2006.
- [38] F. Lyonnet, A. Kusina, T. Ježo et al., “On the intrinsic bottom content of the nucleon and its impact on heavy new physics at the LHC,” *Journal of High Energy Physics*, <http://arxiv.org/abs/1504.05156>.
- [39] E. Hoffmann and R. Moore, “Sub-leading contributions to the intrinsic charm of the nucleon,” *Zeitschrift für Physik C*, vol. 20, no. 1, pp. 71–82, 1983.
- [40] J. Pumplin, H. L. Lai, and W. K. Tung, “Charm parton content of the nucleon,” *Physical Review D*, vol. 75, Article ID 054029, 2007.
- [41] P. M. Nadolsky, H.-L. Lai, Q.-H. Cao et al., “Implications of CTEQ global analysis for collider observables,” *Physical Review D*, vol. 78, no. 1, Article ID 013004, 21 pages, 2008.
- [42] S. Dulat, T.-J. Hou, J. Gao et al., “Intrinsic charm parton distribution functions from CTEQ-TEA global analysis,” *Physical Review D*, vol. 89, no. 7, Article ID 073004, 18 pages, 2014.
- [43] P. Jimenez-Delgado, T. J. Hobbs, J. T. Londergan, and W. Melnitchouk, “New limits on intrinsic charm in the nucleon from global analysis of parton distributions,” *Physical Review Letters*, vol. 114, Article ID 082002, 2015.
- [44] P. Jimenez-Delgado and E. Reya, “Delineating parton distributions and the strong coupling,” *Physical Review D*, vol. 89, no. 7, Article ID 074049, 17 pages, 2014.
- [45] S. J. Brodsky and S. Gardner, “Comment on ‘New limits on intrinsic charm in the nucleon from global analysis of parton distributions’,” <http://arxiv.org/abs/1504.00969>.
- [46] P. Jimenez-Delgado, T. J. Hobbs, J. T. Londergan, and W. Melnitchouk, “Reply to comment on ‘new limits on intrinsic charm in the nucleon from global analysis of parton distributions’,” <http://arxiv.org/abs/1504.06304>.
- [47] D. Stump, J. Huston, J. Pumplin et al., “Inclusive jet production, parton distributions, and the search for new physics,” *Journal of High Energy Physics*, vol. 2003, no. 10, article 046, 2003.
- [48] P. M. Nadolsky and Z. Sullivan, “PDF uncertainties in WH production at Tevatron,” <http://arxiv.org/abs/hep-ph/0110378>.

- [49] B. A. Kniehl, G. Kramer, I. Schienbein, and H. Spiesberger, "Open charm hadroproduction and the charm content of the proton," *Physical Review D*, vol. 79, no. 9, Article ID 094009, 10 pages, 2009.
- [50] B. A. Kniehl, G. Kramer, I. Schienbein, and H. Spiesberger, "Inclusive $D^{*\pm}$ production in $p\bar{p}$ collisions with massive charm quarks," *Physical Review D*, vol. 71, Article ID 014018, 2005.
- [51] B. A. Kniehl, G. Kramer, I. Schienbein, and H. Spiesberger, "Collinear subtractions in hadroproduction of heavy quarks," *The European Physical Journal C—Particles and Fields*, vol. 41, no. 2, pp. 199–212, 2005.
- [52] B. A. Kniehl, G. Kramer, I. Schienbein, and H. Spiesberger, "Hadroproduction of D and B mesons in a massive VFNS," in *Proceedings of the 13th International Workshop on Deep Inelastic Scattering (DIS '05)*, Madison, Wis, USA, April 2005.
- [53] T. Kneesch, B. Kniehl, G. Kramer, and I. Schienbein, "Charmed-meson fragmentation functions with finite-mass corrections," *Nuclear Physics B*, vol. 799, no. 1-2, pp. 34–59, 2008.
- [54] B. Kniehl, G. Kramer, I. Schienbein, and H. Spiesberger, "Inclusive charmed-meson production at the CERN LHC," *The European Physical Journal C*, vol. 72, article 2082, 2012.
- [55] B. Kniehl, G. Kramer, I. Schienbein, and H. Spiesberger, "Inclusive B-meson production at small p_T in the general-mass variable-flavor-number scheme," *The European Physical Journal C*, vol. 75, p. 140, 2015.
- [56] T. P. Stavreva and J. F. Owens, "Direct photon production in association with a heavy quark at hadron colliders," *Physical Review D*, vol. 79, Article ID 054017, 2009.
- [57] T. Stavreva, I. Schienbein, F. Arleo et al., "Probing gluon and heavy-quark nuclear PDFs with $\gamma + Q$ production in pA collisions," *Journal of High Energy Physics*, vol. 2011, no. 1, article 152, 2011.
- [58] T. Stavreva, F. Arleo, and I. Schienbein, "Prompt photon in association with a heavy-quark jet in Pb-Pb collisions at the LHC," *Journal of High Energy Physics*, vol. 2013, no. 2, article 072, 2013.
- [59] V. Bednyakov, M. Demichev, G. Lykasov, T. Stavreva, and M. Stockton, "Searching for intrinsic charm in the proton at the LHC," *EPJ Web of Conferences*, vol. 60, Article ID 20047, 3 pages, 2013.
- [60] V. A. Bednyakov, M. A. Demichev, G. I. Lykasov, T. Stavreva, and M. Stockton, "Searching for intrinsic charm in the proton at the LHC," *Physics Letters, Section B: Nuclear, Elementary Particle and High-Energy Physics*, vol. 728, no. 1, pp. 602–606, 2014.

Research Article

Near-Threshold Production of W^\pm , Z^0 , and H^0 at a Fixed-Target Experiment at the Future Ultrahigh-Energy Proton Colliders

J. P. Lansberg,¹ R. Mikkelsen,^{1,2} and U. I. Uggerhøj²

¹IPNO, Université Paris-Sud, CNRS/IN2P3, 91406 Orsay, France

²Department of Physics and Astronomy, Aarhus University, 8000 Aarhus, Denmark

Correspondence should be addressed to R. Mikkelsen; rune@phys.au.dk

Received 25 March 2015; Revised 5 July 2015; Accepted 18 August 2015

Academic Editor: Luca Stanco

Copyright © 2015 J. P. Lansberg et al. This is an open access article distributed under the Creative Commons Attribution License, which permits unrestricted use, distribution, and reproduction in any medium, provided the original work is properly cited. The publication of this article was funded by SCOAP³.

We outline the opportunities to study the production of the Standard Model bosons, W^\pm , Z^0 , and H^0 , at “low” energies at fixed-target experiments based on possible future ultrahigh-energy proton colliders, that is, the High-Energy LHC, the Super proton-proton Collider, and the Future Circular Collider hadron-hadron. These can be indeed made in conjunction with the proposed future colliders designed to reach up to $\sqrt{s} = 100$ TeV by using bent crystals to extract part of the halo of the beam which would then impinge on a fixed target. Without disturbing the collider operation, this technique allows for the extraction of a substantial amount of particles in addition to serving for a beam-cleaning purpose. With this method, high-luminosity fixed-target studies at centre-of-mass energies above the W^\pm , Z^0 , and H^0 masses, $\sqrt{s} \approx 170$ –300 GeV, are possible. We also discuss the possibility offered by an internal gas target, which can also be used as luminosity monitor by studying the beam transverse shape.

1. Introduction

In this paper, we consider the possibility of performing fixed-target experiments with the beams of the proposed high-energy LHC (HE-LHC) (see, e.g., [1]), the Future Circular Collider hadron-hadron (FCC-hh) (see, e.g., [2]), and the Super proton-proton Collider (SppC) (see, e.g., [3]), which, as their names indicate, are primarily intended for collider physics. The beam energy of these possible future facilities ranges from 16.5 up to 50 TeV, allowing for fixed-target collisions at centre-of-mass system (c.m.s.) energies ranging from 175 to 300 GeV.

Just as lower energy beams, these can in principle be extracted over the course of about a meter by using the channelling of particles in a bent crystal. This phenomenon is well documented (see, e.g., [4–8]) and has been experimentally studied for protons and heavy ions at energies per nucleon up to 900 GeV. Recently, studies performed at SLAC have shown that the beam bending by means of bent crystals is also possible for high-energy positrons and electrons [9]. In [10], it was discussed specifically for the LHC beams.

Channelling experiments at the LHC have been proposed [11], are installed [12, 13], and will be performed during Run-2 for beam collimation studies. The bent crystal extraction technique allows for the extraction of particles from the beam halo only, so that the collider experiments can be kept running simultaneously. These particles would anyway be lost to collimation and would not be used in the collider mode.

In [14], a comprehensive list of physics opportunities offered by the use of the multi-TeV proton and lead LHC beams on a fixed target was presented. Let us recall the critical assets of the fixed-target mode as compared to the collider mode, that is,

- (i) a quasi unlimited target-species versatility,
- (ii) a full access to the target rapidity, which corresponds to the far backward region in the centre-of-mass frame,
- (iii) the possibility to polarise the target,
- (iv) very large luminosities with modest beam intensity thanks to the high target density.

These advantages already translate, with the proton and lead LHC beams, into an impressive list of possible physics studies [14] beyond their respective state of the art, in particular as regards precision studies of spin-related observables with a polarised target and of quark-gluon plasma formation in lead-nucleus collisions in the target rapidity region at c.m.s. energies between those of SPS and RHIC and of QCD at large momentum fractions x in proton-proton, proton-deuteron, and proton-nucleus collisions, and so forth. We refer to [15] for the more specific case of quarkonium studies, to [16–19] for spin physics, and to [15, 20, 21] for heavy-ion physics. First simulation studies at the generator level have been presented in [22] and have demonstrated the great potential for both charmonium and bottomonium studies at $\sqrt{s} = 72$ and 115 GeV at a fixed-target experiment with the LHC beams (thereafter referred to as AFTER@LHC).

With beams of higher energies at future facilities, the available c.m.s. energies can nearly be three times as large as at AFTER@LHC and allow for even more systematic studies of systems whose masses are well above that of the bottomonia, that is, 10 GeV. At fixed-target LHC energies, W and Z production, sometimes generically referred to as the Drell-Yan-like processes, is just reachable with very low expected rates but with the advantage of potentially providing unique information about the nucleon structure at momentum fractions x close to unity ($x \simeq M/\sqrt{s}e^{\pm y_{\text{c.m.s.}}}$) and about QCD corrections near the threshold (let us note here that the production of heavy Beyond-the-Standard-Model particles produced at the LHC in the collider mode might also be subject to similar QCD threshold corrections) and the advantage of offering interesting information on hadronic W decays. With beams of higher energies, rates would significantly be larger allowing, among other things, for rapidity dependent measurements. In general, the combination of high-luminosity hadron-hadron collisions at \sqrt{s} well above 100 GeV and a backward c.m.s. coverage provide the opportunity to study the interplay between the—genuinely nonperturbative—confinement of partons at large momentum fractions x and the perturbative behaviour of the short-distance parton scatterings. Such extremely hard reactions are indeed believed to be well understood within the perturbative regime of QCD. Using a polarised target allows one to advance further the precision and the refinements of such studies of the hadron inner structure with information on the helicity of the partons and on their angular momentum when they carry most of the hadron momentum. The confinement properties of Quantum Chromodynamics, the theory of strong interaction, is still an open problem which deserves novel and innovative studies, even at high-energy facilities.

Although, exactly as for AFTER@LHC, the potential for physics studies go well beyond that of Drell-Yan-like studies in the mass region of W and Z bosons, we wish to focus on it here as an illustrative example of the gain offered by even higher energy beams—in what we believe to be the very first paper on the use of ultrahigh-energy beam in the fixed-target mode. The case for such W and Z studies is clear. So far, the production of W^\pm and Z bosons at RHIC could only be performed at $\sqrt{s} = 500$ GeV (see, e.g., [23, 24]) with a couple of thousand W^\pm candidates and less than one

hundred Z counts. Studies at lower energies, in order to reach x higher than 0.2 and measure the \bar{d}/\bar{u} flavour asymmetry at larger x and high Q^2 , require luminosities on the order of an inverse femtobarn which is out of reach at RHIC in particular if operated at $\sqrt{s} = 200$ GeV where its luminosity is significantly lower. In addition, the most accessible region in the fixed-target mode at high energies is that of backward c.m.s. rapidities, where x in the target can even be larger. Of course, H^0 production has so far only been observed at the LHC at 7 and 8 TeV [25, 26] and it is of interest to have a look at the conditions in which it could be studied not far from the threshold.

The structure of this paper is thus as follows. In Section 2, we discuss the beam extraction in a parasitic mode using the bent crystal technique at ultrahigh energies. In Section 3, we recall the main characteristics of possible future colliders as they are currently discussed and derive reasonable expectations for luminosities in the fixed-target mode. In Section 4, we discuss the case of the weak boson production as a benchmark of what can be achieved with luminosities up to 100 times larger than at RHIC. In addition to the expected rates, we briefly discuss the potential backgrounds whose precise size can however only be assessed with a proposed detector setup. Section 5 gathers our conclusions.

2. Beam Extraction by Means of a Bent Crystal with Ultrahigh-Energy Protons

As previously mentioned, these possible future collider facilities would use proton beams from 16.5 up to 50 TeV. The bending of GeV beams of protons and ions has been studied extensively during the past three decades. As a first approximation, one may calculate the approximate deflection efficiency as a function of crystal length as, for example, done in [6]. For example, at a deflection angle of 0.5 mrad, as approximately required for the passage of a septum blade downstream required for further extraction, the efficiency (excluding surface transmission) in Si (110) is 84% for a 50 TeV beam. This efficiency is obtained at the optimum crystal length of $L/L_D = 0.085$ (see Figure 1), corresponding to a length of 1.6 m.

However, the optimal distance calculated in this simulation may significantly be overestimated because it does not take into account the probability for dechanneled particles to get extracted on a later encounter with the crystal. Several studies have shown that this multipass mechanism may result in a significant shortening of the optimal distance. The optimal crystal thickness also depends on the beam optics used. Results of the order 20–30 cm are certainly not unrealistic.

3. Main Parameters of Future Colliders and Their Corresponding Characteristics in the Fixed-Target Mode

In order to derive the luminosities which can reasonably be expected in the fixed-target mode with the beams of future colliders, we start by recalling their main parameters as currently discussed. Indeed, efforts are now being made in

TABLE 1: Beam parameters for the proposed next-generation colliders and the corresponding fixed-target energies along with the boost ($\gamma_{\text{c.m.s.}}^{\text{lab}}$) and the rapidity shift ($\Delta y_{\text{c.m.s.}}^{\text{lab}}$) between the centre-of-mass frame of the fixed-target collision and the laboratory frame, which identifies to the centre-of-mass frame in the collider mode.

	SppC-1	SppC-2	HE LHC	FCC-hh
Beam energy (E_p) [TeV]	20	45	16.5	50
Fixed-target centre-of-mass energy ($\sqrt{2E_p m_N}$) [GeV]	194	291	176	307
Number of bunches stored	3000	6000	1404 (50 ns spacing)	10600/53000 (25 and 5 ns spacing)
Number of protons (N_p) per bunch [10^{11}]	$1.7 \cdot 10^{-3}$	$0.98 \cdot 10^{-3}$	1.3	1/0.2
$\gamma_{\text{c.m.s.}}^{\text{lab}} = \frac{\sqrt{s}}{2m_p}$	103	155	94	163
$\Delta y_{\text{c.m.s.}}^{\text{lab}} = \ln \left(\gamma_{\text{c.m.s.}}^{\text{lab}} + \sqrt{(\gamma_{\text{c.m.s.}}^{\text{lab}})^2 - 1} \right)$	5.3	5.7	5.2	5.8

investigating the best location and technology for future collider projects. These proposed circular colliders have circumferences of 50 to 100 km and the ability to circulate protons with 15 to 50 TeV energies. We list their most relevant characteristics in Table 1. In particular, we consider phases one and two of the SppC, denoted by SppC-1 and SppC-2, as discussed in [3]. We also consider the High-Energy Large Hadron Collider (HE LHC) [1] and the Future Circular Collider hadron-hadron (FCC-hh) [2].

With colliding beams of equal energies, the c.m.s. frame obviously corresponds to the laboratory frame. In the fixed-target mode, with the LHC 7 TeV protons, for instance, the boost ($\gamma_{\text{c.m.s.}}^{\text{lab}}$) and the rapidity shift ($\Delta y_{\text{c.m.s.}}^{\text{lab}}$) between the c.m.s. frame of the fixed-target collision and the laboratory frame are, respectively, $\gamma_{\text{c.m.s.}}^{\text{lab}} = \sqrt{s}/(2m_p) \approx 60$ and $\Delta y_{\text{c.m.s.}}^{\text{lab}} = \ln(\gamma_{\text{c.m.s.}}^{\text{lab}} + \sqrt{(\gamma_{\text{c.m.s.}}^{\text{lab}})^2 - 1}) \approx 4.8$. The region of central c.m.s. rapidities, $y_{\text{c.m.s.}} \approx 0$, is thus highly boosted at an angle with respect to the beam axis of about one degree in the laboratory frame. The entire backward hemisphere, $y_{\text{c.m.s.}} < 0$, is thus easily accessible with standard experimental techniques. With the future facilities, the rapidity shift is on the order of 5-6; see Table 1. A detector covering $\eta_{\text{lab}} \in [2, 6]$ would thus cover nearly half of the physical phase space of the fixed-target mode.

As we discussed in the previous section, the extraction of such high-energy beams by a bent crystal should not pose more challenges than at the LHC where it will be tested in the coming year. In this case, the main accelerator parameter fixing the luminosities achievable is the flux of the extracted beam. In the following discussion, we will assume (see [14] for a discussion on the LHC conditions where it corresponds to half of the beam loss) that it amounts to 5% of the protons stored in the beam over a fill lasting 10 hours. In the case of the LHC, such a parasitic mode corresponds to a proton flux of 5×10^8 per second and, on the average, to the extraction of minibunches of about 15 protons per bunch per pass with a 25 ns bunch spacing. In such a case, with a target thickness of 5–10% of interaction length, which is the case we consider here, the pileup is not an issue. The corresponding numbers for future facilities are given in Table 2.

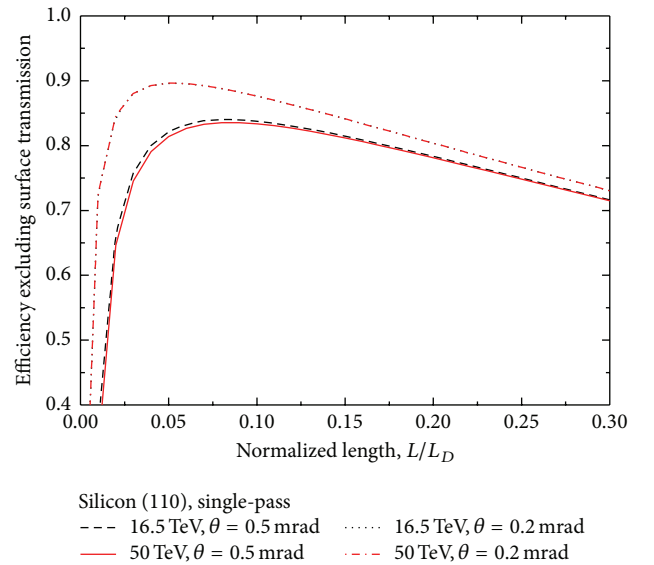


FIGURE 1: Single-pass efficiency, excluding surface transmission, calculated as in [6]. The angles and energies are given in the legends.

Yet, it may not be necessary to extract the beam from the collider to perform fixed-target experiments. By injecting a small amount of gas into the detector region of a running collider, one can sufficiently increase the probability of beam-gas interactions such as to reach decent luminosities yet without affecting at all the beam lifetime. At the LHC, the LHCb experiment has implemented such a system initially to monitor the beam luminosity [34–36] referred to as SMOG for System for Measuring Overlap with Gas (SMOG). SMOG has so far proved to be functioning well while not disturbing the primary beam. LHCb is currently analysing data in proton-neon and lead-neon collisions taken during beam tests in 2012 and 2013. In [19], the corresponding luminosities are given for the LHC. One may think that switching from a dense solid or liquid target to a dilute (10^{-9} Bar) gas necessarily decreases the luminosity. In fact, it may not be always so. Indeed, this decrease is compensated since the entire collider beam, amounting to a current close to an ampere for the LHC, traverses the gas cell, as opposed to the extraction beam which is similar to the beam loss.

TABLE 2: Luminosities reachable in the fixed target mode. The proton flux is calculated by assuming that 5% of the beam is used per fill of 10 hours. The luminosities are calculated for the case of targets that are 1 cm thick. The three values displayed represent luminosities for three different targets: liquid hydrogen, beryllium, and tungsten. The gas-target values are calculated using the same parameters as in [19] for a perfect gas at a pressure of 10^{-9} Bar in a zone of 100 cm.

	SppC-1	SppC-2	HE LHC	FCC-hh
Extracted beam				
Proton flux	$7.1 \cdot 10^5$	$8.1 \cdot 10^5$	$2.5 \cdot 10^8$	$1.5 \cdot 10^9$
$\mathcal{L}(\mu\text{b}^{-1}\text{s}^{-1})$	0.028/0.088/0.044	0.032/0.10/0.05	10/31/15	30/93/45
$\int dt \mathcal{L}(\text{pb}^{-1}\text{yr}^{-1})$	0.28/0.88/0.44	0.32/1.0/0.5	100/310/155	300/930/450
Gas target				
$\mathcal{L}(\mu\text{b}^{-1}\text{s}^{-1})$	0.014	0.016	5	30
$\int dt \mathcal{L}(\text{pb}^{-1}\text{yr}^{-1})$	0.14	0.16	50	300

Table 2 summarises all these numbers for 1 cm thick targets in the case of an extracted beam with a bent crystal and an internal gas target of 1 meter. In the former case and for light target materials, the luminosity can be increased by using a target much thicker/longer than 1 cm: NA51 at SPS used, for instance, a 1.2 m long hydrogen and deuterium target [37] with 450 GeV protons, E866 at Fermilab used 3 target cells of 50 cm [38] with 900 GeV protons, and COMPASS at SPS uses [39, 40] a 110 cm polarised NH_3 target with 160 GeV pions. In such a case, one can obtain luminosities *per annum* well above the inverse femtobarn. Even in this case, the thickness of the target does not reach more than 10% of interaction length.

Much higher luminosities could be achieved by using the full amount of the remaining protons stored in the beam at the end of each fill. Such a “dumping” mode, which could last an hour without unreasonably impacting the schedule of the machine, would of course provide luminosities orders-of-magnitude higher, probably up to 3, than the ones quoted in Table 2. However, this would also be done at the cost of carrying out the experiment in a highly activated environment, which may not be feasible in practice, and at the cost of a significant pileup. For some specific studies to look for rare events with very large momentum tracks, the latter may however not be an unsolvable issue.

4. Fixed-Target Mode and Boson Production

4.1. Expected Signal Rates. As announced we have decided to focus on the production of SM bosons production as an illustrative example of what the high luminosities reachable with the fixed-target mode can allow for. Physicswise, by measuring the production of Standard Model bosons W^\pm and Z^0 , the distribution of quarks and antiquarks at large x can be probed both in the proton with a hydrogen target and in the nuclei with nuclear targets. In particular, it allows one to determine the \bar{d}/\bar{u} flavour asymmetry at large x and large scales. The study of these reactions not far from the threshold also allows one to validate the theoretical methods to account for the so-called threshold resummation effects (see [41] for W production at RHIC).

To evaluate the cross section at NLO accuracy, we used the library MCFM [28] and set the $\mu_F = \mu_R$ equal to the boson mass. Since we are mainly interested in illustrating how

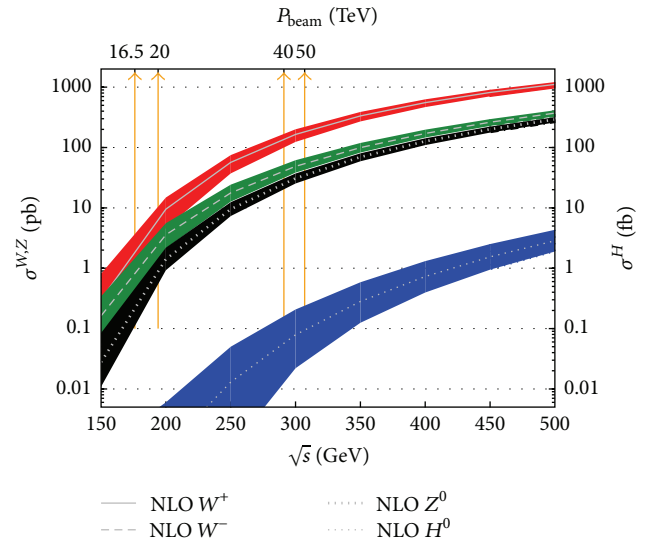


FIGURE 2: Cross sections for Standard Model boson production in proton-proton collisions at various centre-of-mass (lower x -axis) and corresponding beam energies in the fixed-target mode (upper x -axis). The color bands indicate the $1\text{-}\sigma$ values coming from the PDF uncertainty. The NLO calculations were performed with CT10NLO [27] by using MCFM [28] with $\mu_F = \mu_R$ set to the mass of the produced particle. The 4 orange arrows point at the beam energy of the 4 setups which we have considered.

such a measurement would help to better constrain parton distribution (PDF), we only show the theoretical uncertainty from these as they are currently determined. To this end, we use the NLO PDF set CT10 [27] and its associated eigenvector sets. MCFM takes all these into account and provide a $1\text{-}\sigma$ uncertainty which we have depicted on Figure 2. One observes an increasing PDF uncertainty for decreasing energies. With a 20 TeV beam, the uncertainty of W^+ production is as large as a factor of 3 for a total cross section about 10 pb.

If one sticks to the conventional leptonic decay channels, the branching is on the order of 10%. At 200 GeV, with a detector covering pseudorapities from 2 to 6—a detector similar to LHCb [42] with a slightly more forward coverage, for instance—and imposing the lepton transverse momentum

(as well as the missing transverse momentum carried by the neutrino) to be larger than 20 GeV as usually done to cut the background (see later), a quick evaluation shows that the acceptance is on the order of 45% for the W as well as for the Z , although with a smaller branching ratio it is on the order of 3%. The central values for the cross sections times the corresponding leptonic branching at $\sqrt{s} = 200$ GeV in this fiducial volume ($P_{T,\ell,\nu_\ell} > 20$ GeV, $2 < \eta_{\ell,\nu_\ell} < 6$) are therefore 400, 150, and 20 fb, respectively, for the W^+ , W^- , and Z .

Relying on the performance of LHCb for similar studies [43], the efficiency including that of the triggering, the tracking, and additional selections (for the W : the lepton isolation, a cut on the energy deposit to limit the punch-through, the absence of a second lepton with a minimum P_T , and a vertex cut to remove the heavy-flavour decays) is around 40% for the W and 67% for the Z .

With a yearly luminosity of 15 fb^{-1} using, for instance, a 50 cm long liquid hydrogen target at a facility similar to a FCC-hh (see Table 2) one would expect a couple of thousands of W^+ events to be measured at 200 GeV. It would be one order of magnitude more at 300 GeV.

Z boson production is also at reach at 200 GeV with 200 dimuon events, especially if the rather clean environment associated with the rather low centre-of-mass energy allows for the use—and the study—of hadron decay channels. With a detector such as LHCb, both electron and muon decay channels can be used (see, e.g., [44]).

For the H^0 , the situation is very different with much smaller rates (on Figure 2, the cross sections for H^0 are shown in fb for readability). Since the process is dominated by gluon fusion—and we have checked that the vector-boson-fusion contribution is negligible down to low energies—the PDF uncertainties are very large. Fixed-target luminosities of 100 fb^{-1} seem to be needed to be able to have a hope to see a H^0 signal even with the 50 TeV FCC-hh proton beams.

For the W and Z bosons, with a very successful experiment, one may however be able to access regions more backward than $y_{\text{c.m.s.,V}} = \ln(M_V/\sqrt{s})$ and hence to probe the quark distribution in the target for x larger than unity in the nuclear case (the yields in proton-nucleus collisions with a 1 cm thick gold or lead target should be similar to that in proton-proton collisions with a 1 m long liquid hydrogen target).

4.2. Expected Background. At such low energies, very few processes can mimic a dilepton pair of a mass around 90 GeV or an isolated lepton of a transverse momentum around 40 GeV accompanied with a missing transverse energy of a similar size. In fact, one expects the main background to be of electroweak origin such as the $Z \rightarrow \ell\ell$ for the $W \rightarrow \ell\nu_\ell$ channel where one lepton from the Z is lost. $W \rightarrow \tau\nu_\tau$ is also known to sometimes mimic a $\mu\nu_\mu$ final state, although usually at lower P_T . These should be tractable with data. As compared to studies at the LHC or at RHIC, QCD backgrounds are in general expected to be smaller.

For the W^\pm , Figure 3 illustrates that, even without any specific cuts usually used to reduce the background (see below), the P_T spectrum from heavy-flavour-decay electrons

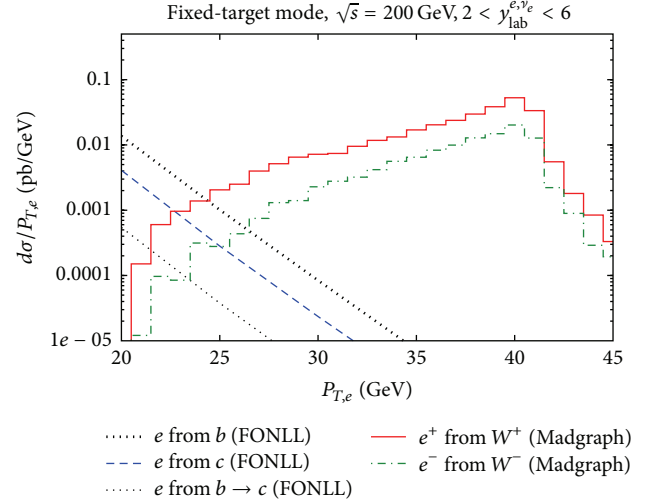


FIGURE 3: P_T spectra for heavy-flavour-decay electrons (and positrons) as predicted by FONLL compared to that from the predicted signal from W^\pm decays obtained with Madgraph 4 [29] at $\sqrt{s} = 200$ GeV. The FONLL cross sections have been evaluated with the default setup of <http://www.lpthe.jussieu.fr/~cacciari/fonll/fonll-form.html> along the lines of [30–32] with the PDFs CTEQ6.6M [33].

is extremely suppressed at large P_T and the electron yield close to $m_W/2$ is essentially purely from W decays. The same holds for muons. Let us however stress the fact that the main QCD background in the LHCb study of [43] is from hadron decay-in-flight which contributes less than 10%. Overall the purity of their W^\pm yield is 78%.

At RHIC, electron channels were used both by STAR [45, 46] and PHENIX [23, 47] and they required its isolation. Since PHENIX has an incomplete azimuthal coverage, the requirement for a missing transverse energy could not be imposed. Yet, the signal could be extracted. Once these requirements are applied, the W peak in the electron P_T spectrum around 40 GeV is evident. Let us note here that the background electron spectra reported in Figure 3 would severely be reduced once cuts for a missing transverse energy, for the isolation of the electron and for a maximum distance from the primary vertex, are imposed. Conversely, these could be measured—and then subtracted—by selecting displaced leptons.

With muons, it is even possible not to impose any lepton isolation to extract the W signal as demonstrated by the CMS study [48] in the very busy lead-lead environment at 2.76 TeV. At lower P_T , QCD backgrounds contribute essentially converted photons from π^0 and η decays, whereas muons from converted photon are usually negligible. The P_T spectrum of this background can be evaluated from dedicated simulations at the detector level but its size is however very difficult to predict without a precise knowledge of the hadron detector response. Usually the normalisation of such a background is simply adjusted on the data. In any case, it always has been found to be smaller than the signal at electron P_T above 30 GeV. We also note that the STAR detector is rather slow as compared to the LHCb detector, for instance, and tracks of

particles produced in earlier collisions can pile up in the data acquisition system, which further increases the background.

In the Z case [43], the main background at LHC energies is that of heavy-flavour decays with on average 3 background events per thousand! At lower energies, it should also be even more suppressed [23]. At 200 GeV, for instance, $\sigma_{b\bar{b}}$ ($2 < \eta_b < 6$; $P_{T,b} > 20$ GeV, $m_{b\bar{b}} > 80$ GeV) ~ 220 fb. Even if one neglects the momentum difference between the b quark, the beauty hadron, and the lepton, which is however a far too conservative approximation, one should multiply it by $f(B \rightarrow \ell) \simeq 0.1$ squared. The dilepton background from b decays is thus in any case much smaller than 2 fb whereas the signal size, accounting for the acceptance, is 20 fb. As regards the uncorrelated background from hadrons, no same-sign dimuon was found by LHCb with 40 pb^{-1} of data [43] and, with 1 fb^{-1} of data, they determined [49] it to be 0.2% of the signal with an overall purity of more than 0.99. At 500 GeV, STAR did not report any same-sign events [45] although with a, necessary less clean, dielectron sample.

Given the likely smaller background at energies below 500 GeV, the fact that the muon channel, with smaller background than that for RHIC studies, would be preferred with a much reduced background and the likely strong dependence of any background simulation on specific detector performances, we chose not to perform any generator level simulation and tend to advocate in view of past experiments at higher energies that, using conventional cuts resulting in tractable acceptances and efficiencies (see above), such signals should easily be extractable.

5. Conclusions

The current planning of future proton colliders necessitates a discussion of whether these facilities could also be used in a fixed-target mode. There is a long list of physics arguments that supports this case at the LHC. We have shown calculations specific to Standard Model bosons at the HE-LHC, SppC, and FCC-hh. This next generation of fixed-target experiments would provide access to high-luminosity measurements at unique laboratory energies and momentum transfers. Using a bent crystal is a viable option to extract high-energy beams of protons and perform—in a parasitic mode—fixed-target experiment at $\sqrt{s} \simeq 170\text{--}300$ GeV with annual luminosities on the order of tens of inverse femtobarn, that is, with high enough rates to produce a significant amount of Standard Model bosons. Although it offers a priori smaller luminosities, an internal gas target is an option which probably requires less civil engineering.

Conflict of Interests

The authors declare that there is no conflict of interests regarding the publication of this paper.

Acknowledgment

This work is supported in part by the CNRS via Grants PICS-06149 Torino-IPNO and PEPS4AFTER2.

References

- [1] R. Assmann, R. Bailey, O. Brüning et al., “First thoughts on a higher-energy LHC,” Tech. Rep. CERN-ATS-2010-177, 2010.
- [2] A. Ball, M. Benedikt, L. Bottura et al., “Future circular collider study hadron collider parameters,” Tech. Rep. FCC-1401101315-DSC, 2014.
- [3] Q. Qin, J. Y. Tang, Y. W. An et al., “Preliminary accelerator design of a circular Higgs factory in China,” in *Proceedings of the North American Particle Accelerator Conference (PAC '13)*, p. 523, Pasadena, Calif, USA, September-October 2013.
- [4] K. Elsener, G. Fidecaro, M. Gyr et al., “Proton extraction from the CERN SPS using bent silicon crystals,” *Nuclear Instruments and Methods in Physics Research Section B: Beam Interactions with Materials and Atoms*, vol. 119, no. 1-2, pp. 215–230, 1996.
- [5] G. Arduini, C. Biino, M. Clément et al., “Deflection and extraction of Pb ions up to 33 TeV/c by a bent silicon crystal,” *Physical Review Letters*, vol. 79, no. 21, article 4182, 1997.
- [6] A. Baurichter, C. Biino, M. Clément et al., “Channeling of high-energy particles in bent crystals—experiments at the CERN SPS,” *Nuclear Instruments and Methods in Physics Research Section B: Beam Interactions with Materials and Atoms*, vol. 164-165, pp. 27–43, 2000.
- [7] V. M. Biryukov, V. N. Chepegin, Y. A. Chesnokov, V. Guidi, and W. Scandale, “Crystal collimation as an option for the large hadron colliders,” *Nuclear Instruments and Methods in Physics Research Section B: Beam Interactions with Materials and Atoms*, vol. 234, no. 1-2, pp. 23–30, 2005.
- [8] W. Scandale, G. Arduini, R. Assmann et al., “Comparative results on collimation of the SPS beam of protons and Pb ions with bent crystals,” *Physics Letters B*, vol. 703, no. 5, pp. 547–551, 2011.
- [9] U. Wienands, T. W. Markiewicz, J. Nelson et al., “Observation of deflection of a beam of multi-GeV electrons by a thin crystal,” *Physical Review Letters*, vol. 114, no. 7, Article ID 074801, 6 pages, 2015.
- [10] E. Uggerhøj and U. I. Uggerhøj, “Strong crystalline fields—a possibility for extraction from the LHC,” *Nuclear Instruments and Methods in Physics Research Section B: Beam Interactions with Materials and Atoms*, vol. 234, no. 1-2, pp. 31–39, 2005.
- [11] W. Scandale, G. Arduini, R. Assmann et al., “LHC collimation with bent crystals—LUA9,” Tech. Rep. CERN-LHCC-2011-007, 2011.
- [12] LHC Committee, Minutes of the 107th meeting, CERN/LHCC 2011-010.
- [13] W. Scandale, Talk at 173th meeting of the LHC Machine Committee, slides.
- [14] S. J. Brodsky, F. Fleuret, C. Hadjidakis, and J. P. Lansberg, “Physics opportunities of a fixed-target experiment using LHC beams,” *Physics Reports*, vol. 522, no. 4, pp. 239–255, 2013.
- [15] J. P. Lansberg, S. J. Brodsky, F. Fleuret, and C. Hadjidakis, “Quarkonium physics at a fixed-target experiment using the LHC beams,” *Few-Body Systems*, vol. 53, no. 1-2, pp. 11–25, 2012.
- [16] C. Lorcé, M. Anselmino, R. Arnaldi et al., “Spin and diffractive physics with a fixed-target experiment at the LHC (AFTER@LHC),” *AIP Conference Proceedings*, vol. 1523, p. 149, 2012.
- [17] A. Rakotozafindrabe, M. Anselmino, R. Arnaldi et al., “Spin physics at a fixed-target experiment at the LHC (AFTER@LHC),” *Physics of Particles and Nuclei*, vol. 45, no. 1, pp. 336–337, 2014.

- [18] J. P. Lansberg, M. Anselmino, R. Arnaldi et al., “Spin physics and TMD studies at a fixed-target Experiment at the LHC (AFTER@LHC),” *EPJ Web of Conferences*, vol. 85, Article ID 02038, 6 pages, 2015.
- [19] L. Massacrier, M. Anselmino, R. Arnaldi et al., “Studies of transverse-momentum-dependent distributions with a fixed-target Experiment using the LHC beams (AFTER@LHC),” *International Journal of Modern Physics: Conference Series*, In press.
- [20] A. Rakotozafindrabe, R. Arnaldi, S. J. Brodsky et al., “Ultra-relativistic heavy-ion physics with AFTER@LHC,” *Nuclear Physics A*, vol. 904–905, pp. 957c–960c, 2013.
- [21] J. P. Lansberg, R. Arnaldi, S. J. Brodsky et al., “AFTER@LHC: a precision machine to study the interface between particle and nuclear physics,” *EPJ Web of Conferences*, vol. 66, Article ID 11023, 4 pages, 2014.
- [22] L. Massacrier, B. Trzeciak, F. Fleuret et al., “Feasibility studies for quarkonium production at a fixed-target experiment using the LHC proton and lead beams (AFTER@LHC),” <http://arxiv.org/abs/1504.05145>.
- [23] A. Adare, S. Afanasiev, C. Aidala et al., “Cross section and parity-violating spin asymmetries of W^\pm boson production in polarized $p + p$ collisions at $\sqrt{s} = 500$ GeV,” *Physical Review Letters*, vol. 106, Article ID 062001, 2011.
- [24] M. M. Aggarwal, Z. Ahammed, A. V. Alakhverdyants et al., “Measurement of the parity-violating longitudinal single-spin asymmetry for W^\pm Boson production in polarized proton-proton collisions at $\sqrt{s} = 500$ GeV,” *Physical Review Letters*, vol. 106, no. 6, Article ID 062002, 6 pages, 2011.
- [25] G. Aad, T. Abajyan, B. Abbott et al., “Observation of a new particle in the search for the Standard Model Higgs boson with the ATLAS detector at the LHC,” *Physics Letters B*, vol. 716, no. 1, pp. 1–29, 2012.
- [26] S. Chatrchyan, V. Khachatryan, A. M. Sirunyan et al., “Observation of a new boson at a mass of 125–GeV with the CMS experiment at the LHC,” *Physics Letters B*, vol. 716, no. 1, pp. 30–61, 2012.
- [27] H. L. Lai, M. Guzzi, J. Huston et al., “New parton distributions for collider physics,” *Physical Review D*, vol. 82, no. 7, Article ID 074024, 24 pages, 2010.
- [28] J. M. Campbell and R. K. Ellis, “Radiative corrections to $Zb\bar{b}$ production,” *Physical Review D*, vol. 62, Article ID 114012, 2000.
- [29] J. Alwall, P. Demin, S. de Visscher et al., “MadGraph/MadEvent v4: the new web generation,” *Journal of High Energy Physics*, vol. 2007, no. 9, article 028, 2007.
- [30] M. Cacciari, M. Greco, and P. Nason, “The p_T spectrum in heavy-flavour hadroproduction,” *Journal of High Energy Physics*, vol. 5, article 007, 1998.
- [31] M. Cacciari, S. Frixione, and P. Nason, “The p_T spectrum in heavy-flavour photoproduction,” *Journal of High Energy Physics*, vol. 2001, no. 3, article 006, 2001.
- [32] M. Cacciari, P. Nason, and R. Vogt, “QCD predictions for charm and bottom quark production at RHIC,” *Physical Review Letters*, vol. 95, no. 12, Article ID 122001, 4 pages, 2005.
- [33] P. M. Nadolsky, H. L. Lai, Q. H. Cao et al., “Implications of CTEQ global analysis for collider observables,” *Physical Review D*, vol. 78, Article ID 013004, 2008.
- [34] C. Barschel and M. Ferro-Luzzi, *Precision luminosity measurement at LHCb with beam-gas imaging [Ph.D. thesis]*, RWTH Aachen University, Aachen, Germany, 2014, CERN-THESIS-2013-301.
- [35] M. Ferro-Luzzi, “Proposal for an absolute luminosity determination in colliding beam experiments using vertex detection of beam-gas interactions,” *Nuclear Instruments and Methods in Physics Research Section A: Accelerators, Spectrometers, Detectors and Associated Equipment*, vol. 553, no. 3, pp. 388–399, 2005.
- [36] The LHCb Collaboration, “Precision luminosity measurements at LHCb,” *Journal of Instrumentation*, vol. 9, Article ID P12005, 2014.
- [37] A. Baldit, C. Barrière, J. Castor et al., “Study of the isospin symmetry breaking in the light quark sea of the nucleon from the Drell-Yan process,” *Physics Letters B*, vol. 332, no. 1-2, pp. 244–250, 1994.
- [38] L. Y. Zhu, P. E. Reimer, B. A. Mueller et al., “Measurement of Y production for $p + p$ and $p + d$ interactions at 800 GeV/c,” *Physical Review Letters*, vol. 100, Article ID 062301, 2008.
- [39] COMPASS Collaboration, COMPASS-II Proposal, CERNSPSC-2010-014.
- [40] M. Chiosso, “COMPASS-II,” *Physics of Particles and Nuclei*, vol. 44, no. 6, pp. 882–885, 2013.
- [41] A. Mukherjee and W. Vogelsang, “Threshold resummation for W -boson production at BNL RHIC,” *Physical Review D*, vol. 73, 2006.
- [42] A. A. Alves Jr., L. M. Andrade Filho, A. F. Barbosa et al., “The LHCb Detector at the LHC,” *Journal of Instrumentation*, vol. 3, Article ID S08005, 2008.
- [43] R. Aaij, C. A. Beteta, A. Adametz et al., “Inclusive W and Z production in the forward region at $\sqrt{s} = 7$ TeV,” *Journal of High Energy Physics*, vol. 2012, no. 6, article 058, 2012.
- [44] R. Aaij, B. Adeva, M. Adinolfi et al., “Measurement of forward $Z \rightarrow e^+e^-$ production at $\sqrt{s} = 8$ TeV,” *Journal of High Energy Physics*, vol. 2015, no. 5, article 109, 2015.
- [45] L. Adamczyk, G. Agakishiev, M. M. Aggarwal et al., “Measurement of the $W \rightarrow e\nu$ and $Z/\gamma^* \rightarrow e^+e^-$ production cross sections at mid-rapidity in proton-proton collisions at $\sqrt{s} = 500$ GeV,” *Physical Review D*, vol. 85, Article ID 092010, 2012.
- [46] L. Adamczyk, J. K. Adkins, G. Agakishiev et al., “Measurement of longitudinal spin asymmetries for weak boson production in polarized proton-proton collisions at RHIC,” *Physical Review Letters*, vol. 113, Article ID 072301, 2014.
- [47] A. Adare, C. Aidala, N. N. Ajitanand et al., “Measurement of parity-violating spinasymmetries in W^\pm production at midrapidity in longitudinally polarized $p+p$ collisions,” <http://arxiv.org/abs/1504.07451>.
- [48] S. Chatrchyan, V. Khachatryan, A. M. Sirunyan et al., “Study of W boson production in PbPb and pp collisions at $\sqrt{s_{NN}} = 2.76$ TeV,” *Physics Letters B*, vol. 715, no. 1–3, pp. 66–87, 2012.
- [49] R. Aaij, B. Adeva, M. Adinolfi et al., “Measurement of the forward Z boson production cross-section in pp collisions $\sqrt{s} = 7$ TeV,” *Journal of High Energy Physics*, vol. 2015, article 39, 2015.